

Electronic Thesis and Dissertation Repository

12-13-2017 2:45 PM

Study of Motion of Agglomerates Through a Fluidized Bed

Muhammad Owais Iqbal Bhatti, *The University of Western Ontario*

Supervisor: Briens, Cedric, *The University of Western Ontario*

Co-Supervisor: Berruti, Franco, *The University of Western Ontario*

A thesis submitted in partial fulfillment of the requirements for the Master of Engineering
Science degree in Chemical and Biochemical Engineering

© Muhammad Owais Iqbal Bhatti 2017

Follow this and additional works at: <https://ir.lib.uwo.ca/etd>

 Part of the [Other Chemical Engineering Commons](#)

Recommended Citation

Bhatti, Muhammad Owais Iqbal, "Study of Motion of Agglomerates Through a Fluidized Bed" (2017).
Electronic Thesis and Dissertation Repository. 5066.
<https://ir.lib.uwo.ca/etd/5066>

This Dissertation/Thesis is brought to you for free and open access by Scholarship@Western. It has been accepted for inclusion in Electronic Thesis and Dissertation Repository by an authorized administrator of Scholarship@Western. For more information, please contact wlsadmin@uwo.ca.

Abstract

Formation of agglomerates in Fluid Cokers™ can cause operating problems, such as excessive shed fouling, which can lead to premature unit shut down. Better understanding of how agglomerates move through a fluidized bed can help improve the design and operation of Fluid Cokers™ and minimize the risk of agglomerates reaching regions where they cause problems.

To identify key factors in agglomerates motion in a fluidized bed, a new two-dimensional (2D) Radioactive Particle Tracking (RPT) method was developed which tracks model agglomerates motion. In conjunction, a tribo-electric method was used to determine bubble flow distribution in the fluidized bed.

This thesis outlines the effects of bed hydrodynamics and agglomerate properties on agglomerate motion. It was found that agglomerates produced by liquid injection in the fluidized bed were of similar density. Agglomerates larger than 9500 μm segregated near the bottom of the fluidized bed and all agglomerates spent more time in regions of low bubble flow.

Keywords

Fluid Coking, Fluidized Bed, Radioactive Particle Tracking, Motion of Agglomerates, Agglomerate Segregation, Tribo-Electric, Core Annulus Flow

Co-Authorship Statement

Chapter 3

Article Title: Preliminary Study on Behavior of Agglomerates formed by Liquid Injection
Authors: Muhammad Owais Iqbal Bhatti, Cedric Briens, Franco Berruti, Jennifer McMillan.
Article Status: Unpublished
Contributions: Muhammad Owais Iqbal Bhatti wrote the manuscript who also conducted all the experimental work and data analysis. Cedric Briens and Franco Berruti jointly supervised the work. Cedric Briens, Franco Berruti and Jennifer McMillan reviewed several drafts of the chapter.

Chapter 4

Article Title: Development of a New Two-Dimensional Radioactive Particle Tracking (RPT) System to Study the Motion of Agglomerates
Authors: Muhammad Owais Iqbal Bhatti, Francisco J. Sanchez, Cedric Briens, Franco Berruti, Jennifer McMillan.
Article Status: Unpublished
Contributions: Muhammad Owais Iqbal Bhatti wrote the manuscript who also conducted all the experimental work and data analysis. Francisco J. Sanchez provided assistance and guidance in setting up the RPT system. Cedric Briens, Franco Berruti and Jennifer McMillan reviewed several drafts of the chapter. Cedric Briens and Franco Berruti jointly supervised the work.

Chapter 5

Article Title: Study of the Impact of Radial Fluidization Gas Profile on Agglomerates Motion

Authors: Muhammad Owais Iqbal Bhatti, Cedric Briens, Franco Berruti, Jennifer McMillan.

Article Status: Unpublished

Contributions:

Muhammad Owais Iqbal Bhatti wrote the manuscript who also conducted all the experimental work and data analysis. Cedric Briens and Franco Berruti jointly supervised the work. Cedric Briens, Franco Berruti and Jennifer McMillan reviewed several drafts of the chapter.

Acknowledgments

Conducting research at ICFAR was one of the toughest challenges of my life so far and this journey would not have been possible without the incredible people who guided and supported me during this time.

I could not be more grateful to my supervisors, Dr. Cedric Briens and Dr. Franco Berruti, for giving me the prestigious opportunity to work at ICFAR. Both of whom not only shared their expertise and in-depth knowledge with me but also provided the guidance, constructive criticism and constant motivation that was needed to complete this challenging task.

I would like to thank Syncrude Canada Limited and Natural Sciences and Engineering Research Council (NSERC) of Canada for the financial support. Also, I am grateful to Province of Ontario and The University of Western Ontario for providing me with the funds through Queen Elizabeth II – Graduate Scholarship in Science and Technology (QEII-GSST).

I am especially indebted to Dr. Francisco J. Sanchez and Majid Jahanmiri, who both put in countless efforts in helping me setup the equipment required for the research. I would also like to thank Thomas Johnston and Cody Ruthman (from University Machine Services) for helping me with the modifications in the unit and navigating through the technical problems. I would also like to express my gratitude and appreciation to all my friends, colleagues and personnel at ICFAR, especially Saber, Dhiraj, Cher, Afsana, Chiara, Marina, Luanna, Muhammad, Tracy and Stefano for all the great memories I would cherish my whole life.

In the end, this wonderful voyage would be meaningless if it wasn't for my parents and family. I am very fortunate to get all the love, support and courage from my Papa Mr. Muhammad Iqbal Bhatti, my Ammi Mrs. Shahida Iqbal, my beloved sister Sidra Iqbal and my brothers Junaid Iqbal, Fahad Iqbal, Saad Iqbal and Abdur-Rehman Iqbal.

This page would be incomplete without mentioning my best friends Nazim Hussain, Faizan Siddiqui, Danish Ali, Sana Zahid, Baber Rahim, Kiran Baber, Tauseef, Manzar, Sufyan Khan and Shereen Sufyan for their great friendship and providing the most needed support system.

Table of Contents

Abstract.....	i
Co-Authorship Statement.....	ii
Acknowledgments.....	iv
Table of Contents.....	v
List of Tables.....	ix
List of Figures.....	x
List of Appendices.....	xx
Nomenclature.....	xxi
Chapter 1.....	1
1 Introduction.....	1
1.1 Bitumen.....	1
1.2 Coking.....	2
1.3 Fluid Coking.....	2
1.3.1 Fouling.....	4
1.3.2 Sheds.....	4
1.4 Agglomeration.....	5
1.4.1 Formation of Agglomerates.....	6
1.5 Models for the Study of Agglomerate Formation.....	7
1.6 Tribo-Electric Method for Bubble Flow Distribution.....	8
1.6.1 Theory and Background.....	8
1.7 Radioactive Particle Tracking.....	9
1.7.1 Theory and Background.....	9
1.7.2 Factors Affecting Strength of Radioactive Source.....	10
1.7.3 Working Principle of Scintillation Detectors.....	11

1.7.4	Rendition Techniques	13
1.8	Research Objectives and Outline	14
Chapter 2	16
2	Experimental Setup and Methodology.....	16
2.1	Equipment.....	16
2.2	Fluidized Bed	17
2.3	Liquid Injection System.....	18
2.4	Agglomerates Recovery.....	19
2.5	Agglomerates Analysis	20
2.6	Tribo-Electric Method	21
2.6.1	Analysis of Triboelectric Signals.....	23
2.7	Radioactive Particle Tracking (RPT) System.....	23
2.7.1	Radioactive Particle/Source	24
2.7.2	Scintillation Detectors.....	24
2.7.3	Experimental Setup.....	27
Chapter 3	30
3	Preliminary Study on Behavior of Agglomerates formed by Liquid Injection.....	30
3.1	Bubble Flow Distribution in the Fluidized Bed.....	30
3.2	Experimental Setup and Procedure.....	30
3.2.1	Data Acquisition for Triboelectric Method.....	33
3.3	Results and Discussion	33
3.3.1	Results for Vertical Distribution of Agglomerates	33
3.3.2	Results for Lateral Distribution of Agglomerates.....	43
3.3.3	Density of Agglomerates	49
3.3.4	Gas Bubble Flow Distribution using Tribo-Electric Method	50
3.4	Conclusion	57

Chapter 4.....	58
4 Development of a New Two-Dimensional Radioactive Particle Tracking System to Study the Motion of Agglomerates	58
4.1 Experimental Setup and Procedure.....	58
4.1.1 Development of a New Method for 2D RPT System	59
4.1.2 Preparation of Model Agglomerates.....	68
4.1.3 Experimental Procedure.....	70
4.2 Results and Discussion	70
4.2.1 Results for Model Agglomerate-2 (12500 μm)	70
4.2.2 Results for Model Agglomerate-1 (5500 μm)	78
4.2.3 Comparison of Results Obtained with Agglomerates formed by Liquid Injection Experiments with RPT Results.....	86
4.3 Conclusion	92
Chapter 5.....	94
5 Study of the Impact of Radial Fluidization Gas Profile on Agglomerates Motion.....	94
5.1 Experimental Setup and Procedure.....	94
5.2 Results and Discussion	95
5.2.1 Gas Bubble Flow Distribution using Tribo-Electric Method	95
5.2.2 Results for Liquid Injection Experiments.....	99
5.2.3 Results for Radioactive Particle Tracking	105
5.2.4 Comparison of Results obtained with Agglomerates formed by Liquid Injection Experiments, and Radioactive Particle Tracking.....	111
5.3 Conclusion	119
Chapter 6.....	120
6 Conclusions and Recommendations	120
6.1 Conclusions.....	120
6.2 Recommendations.....	121

References.....	123
Appendices.....	126
Curriculum Vitae	130

List of Tables

Table 3-1: Ratio of gas distributor pressure drop to the bed pressure drop	51
Table 4-1: R^2 -values for curve fitting for location coordinates of model agglomerate	64
Table 4-2: Index of Segregation for bottom (IS_B) compared for different cases for a fluidization time of 4 min	87
Table 5-1: Gas velocity provided by the two sections of the gas distributor.....	95
Table 5-2: Index of Segregation for bottom (IS_B) compared for MA2.....	112
Table A-1: Combinations of sonic nozzles that can be utilized to achieve a range of desired velocities	126

List of Figures

Figure 1-1: Schematic of a Fluid Coker™ Reactor (Prociw, 2014)	2
Figure 1-2: Fouling caused by unwanted coke deposition on the sheds and walls of the Fluid Coker™ stripper section (Adopted from Bi et al., 2005)	5
Figure 1-3: An example of a calibration curve for a detector (Javier Sanchez, 2013)	12
Figure 2-1: Equipment used for fluidizing 150 kg of sand using air as fluidization gas	16
Figure 2-2: Silica sand particle size distribution (190 μm Sauter mean diameter).....	17
Figure 2-3: Sonic nozzle banks upstream of gas distributors which provide the fluidization air	18
Figure 2-4: Liquid injection system.....	19
Figure 2-5: Bilateral Flow Conditioner (BFC) pre-mixer.....	19
Figure 2-6: Array of triboelectric rods comprised of 3 rows and 12 columns inserted half way in the fluidized bed.....	22
Figure 2-7: A triboelectric rod	22
Figure 2-8: Decay scheme of Sc-46.....	24
Figure 2-9: NaI(Tl) scintillation crystal used for the current research work (Saint-Gobain Crystals Inc.).....	26
Figure 2-10: Scintillation detector mounted on data acquisition (DAQ) base.....	27
Figure 2-11: Schematic showing the arrangement of scintillation detectors	28
Figure 2-12: Scintillation detectors arranged in 3 x 4 matrix in a 2D plane.....	29
Figure 2-13: Data acquisition center showing all 13 computers connected with 12 scintillation detectors in the back.....	29

Figure 3-1: Experimental setup for runs with liquid injection.....	32
Figure 3-2: Layers and sections in which bed solids were divided	34
Figure 3-3: Agglomerates larger than 12500 μm collected from the bottom layer at 0.06 m/s fluidization gas velocity	34
Figure 3-4: Agglomerates larger than 12500 μm collected from the bottom layer on a 12500 μm sieve at 0.60 m/s fluidization gas velocity.....	35
Figure 3-5: Proportion of agglomerates in each layer at $V_g = 0.06$ m/s at $t_f = 0$ min.....	36
Figure 3-6: Proportion of agglomerates in each layer at $V_g = 0.06$ m/s at $t_f = 10$ min.....	37
Figure 3-7: Index of Segregation for Bottom and Top layers when the bed was slumped at $t_f = 0$ min at 0.06 m/s gas velocity	38
Figure 3-8: Index of Segregation for Bottom layer vs. size of agglomerates at 0.06 m/s fluidization gas velocity	40
Figure 3-9: Index of Segregation for Top layer vs. size of agglomerates at 0.06 m/s fluidization gas velocity	40
Figure 3-10: Index of Segregation for Bottom layer vs. fluidization time at 0.06 m/s fluidization gas velocity	41
Figure 3-11: Index of Segregation for Top layer vs. fluidization time at 0.06 m/s fluidization gas velocity	41
Figure 3-12: Index of Segregation for Bottom layer vs. size of agglomerates at 0.60 m/s fluidization gas velocity	42
Figure 3-13: Index of Segregation for Top layer vs. size of agglomerates at 0.60 m/s fluidization gas velocity	43
Figure 3-14: Lateral distribution of agglomerates for Bottom layer at 0.06 m/s and for a fluidization time of 2 min	44

Figure 3-15: Lateral distribution of agglomerates for Top layer at 0.06 m/s and for a fluidization time of 2 min.....	45
Figure 3-16: Lateral distribution of agglomerates for Bottom layer at 0.06 m/s and for a fluidization time of 4 min	45
Figure 3-17: Lateral distribution of agglomerates for Top layer at 0.06 m/s and for a fluidization time of 4 min.....	46
Figure 3-18: Lateral distribution of agglomerates for Bottom layer at 0.06 m/s and for a fluidization time of 7 min	46
Figure 3-19: Lateral distribution of agglomerates for Top layer at 0.06 m/s and for a fluidization time of 7 min.....	47
Figure 3-20: Lateral distribution of agglomerates for Bottom layer at 0.60 m/s and for a fluidization time of 0 min	47
Figure 3-21: Lateral distribution of agglomerates for Top layer at 0.60 m/s and for a fluidization time of 0 min.....	48
Figure 3-22: Lateral distribution of agglomerates for Bottom layer at 0.60 m/s and for a fluidization time of 4 min	48
Figure 3-23: Lateral distribution of agglomerates for Top layer at 0.60 m/s and for a fluidization time of 4 min.....	49
Figure 3-24: Gas bubble profile for $V_g = 0.06$ m/s (Bottom: $h = 12$ cm; Middle: $h = 32$ cm; Top: $h = 52$ cm)	52
Figure 3-25: Gas bubble profile for $V_g = 0.10$ m/s (Bottom: $h = 12$ cm; Middle: $h = 32$ cm; Top: $h = 52$ cm)	52
Figure 3-26: Gas bubble profile for $V_g = 0.20$ m/s (Bottom: $h = 12$ cm; Middle: $h = 32$ cm; Top: $h = 52$ cm)	53

Figure 3-27: Gas bubble profile for $V_g = 0.35$ m/s (Bottom: $h = 12$ cm; Middle: $h = 32$ cm; Top: $h = 52$ cm)	53
Figure 3-28: Gas bubble profile for $V_g = 0.35$ m/s with adjusted y-scale (Bottom: $h = 12$ cm; Middle: $h = 32$ cm; Top: $h = 52$ cm).....	54
Figure 3-29: Gas bubble profile for $V_g = 0.50$ m/s (Bottom: $h = 12$ cm; Middle: $h = 32$ cm; Top: $h = 52$ cm)	54
Figure 3-30: Gas bubble profile for $V_g = 0.60$ m/s (Bottom: $h = 12$ cm; Middle: $h = 32$ cm; Top: $h = 52$ cm)	55
Figure 3-31: Gas bubble profile for Bottom Row for all velocities.....	55
Figure 3-32: Gas bubble profile for Middle Row for all velocities	56
Figure 3-33: Gas bubble profile for Top Row for all velocities	56
Figure 4-1: Map of 290 source locations for calibration	63
Figure 4-2: Error on X for all calibration runs: Predicted values of X vs actual values of X	66
Figure 4-3: Error on Y for all calibration runs: Predicted values of Y vs actual values of Y	66
Figure 4-4: Standard deviation for X-coordinate of location of radioactive particle	67
Figure 4-5: Standard deviation for Y-coordinate of location of radioactive particle	68
Figure 4-6: Nylon balls of different sizes	69
Figure 4-7: Model Agglomerate-1 (MA1).....	70
Figure 4-8: Tracer locations and gas bubble flow distribution for MA2 at 0.06 m/s and room temperature	72
Figure 4-9: Tracer locations and gas bubble flow distribution for MA2 at 0.10 m/s and room temperature	72

Figure 4-10: Tracer locations and gas bubble flow distribution for MA2 at 0.35 m/s and room temperature	73
Figure 4-11: Tracer locations and gas bubble flow distribution for MA2 at 0.50 m/s and room temperature	73
Figure 4-12: Tracer locations and gas bubble flow distribution for MA2 at 0.60 m/s and room temperature	74
Figure 4-13: Tracer locations and gas bubble flow distribution for MA2 at 0.06 m/s and 120 °C	74
Figure 4-14: Tracer locations and gas bubble flow distribution for MA2 at 0.35 m/s and 120 °C	75
Figure 4-15: Tracer locations and gas bubble flow distribution for MA2 at 0.60 m/s and 120 °C	75
Figure 4-16: Probability distribution of particle presence for MA2 at 0.06 m/s and room temperature	76
Figure 4-17: Probability distribution of particle presence for MA2 at 0.10 m/s and room temperature	76
Figure 4-18: Probability distribution of particle presence for MA2 at 0.35 m/s and room temperature	77
Figure 4-19: Probability distribution of particle presence for MA2 at 0.50 m/s and room temperature	77
Figure 4-20: Probability distribution of particle presence for MA2 at 0.60 m/s and room temperature	77
Figure 4-21: Probability distribution of MA2 presence at 0.06 m/s and 120 °C	78
Figure 4-22: Probability distribution of MA2 presence at 0.35 m/s and 120 °C	78

Figure 4-23: Probability distribution of MA2 presence at 0.60 m/s and 120 °C	78
Figure 4-24: Tracer locations and gas bubble flow distribution for MA1 at 0.06 m/s and room temperature	79
Figure 4-25: Tracer locations and gas bubble flow distribution for MA1 at 0.10 m/s and room temperature	80
Figure 4-26: Tracer locations and gas bubble flow distribution for MA1 at 0.35 m/s and room temperature	80
Figure 4-27: Tracer locations and gas bubble flow distribution for MA1 at 0.50 m/s and room temperature	81
Figure 4-28: Tracer locations and gas bubble flow distribution for MA1 at 0.60 m/s and room temperature	81
Figure 4-29: Tracer locations and gas bubble flow distribution for MA1 at 0.06 m/s and 120 °C	82
Figure 4-30: Tracer locations and gas bubble flow distribution for MA1 at 0.35 m/s and 120 °C	82
Figure 4-31: Tracer locations and gas bubble flow distribution for MA1 at 0.60 m/s and 120 °C	83
Figure 4-32: Probability distribution of particle presence for MA1 at 0.06 m/s and room temperature	84
Figure 4-33: Probability distribution of particle presence for MA1 at 0.10 m/s and room temperature	84
Figure 4-34: Probability distribution of particle presence for MA1 at 0.35 m/s and room temperature	84
Figure 4-35: Probability distribution of particle presence for MA1 at 0.50 m/s and room temperature	85

Figure 4-36: Probability distribution of particle presence for MA1 at 0.60 m/s and room temperature	85
Figure 4-37: Probability distribution of MA1 presence at 0.06 m/s and 120 °C	85
Figure 4-38: Probability distribution of MA1 presence at 0.35 m/s and 120 °C	86
Figure 4-39: Probability distribution of MA1 presence at 0.60 m/s and 120 °C	86
Figure 4-40: Index of Segregation for Bottom vs. fluidization time at 0.60 m/s.....	88
Figure 4-41: Index of Segregation for Top vs. fluidization time at 0.60 m/s	88
Figure 4-42: Vertical distribution of 12500 μm at 0.60 m/s.....	89
Figure 4-43: Vertical distribution of 5500 μm at 0.60 m/s.....	89
Figure 4-44: Lateral distribution of 12500 μm in Bottom layer at 0.60 m/s	90
Figure 4-45: Lateral distribution of 5500 μm in Bottom layer at 0.60 m/s	91
Figure 4-46: Lateral distribution of 12500 μm in Top layer at 0.60 m/s	91
Figure 4-47: Lateral distribution of 5500 μm in Top layer at 0.60 m/s.....	92
Figure 5-1: Gas bubble profile for $V_g = 0.35$ m/s in both halves of the fluidized bed (Bottom: h = 12 cm; Middle: h = 32 cm; Top: h = 52 cm)	96
Figure 5-2: Gas bubble profile for 0.60 m/s in left and 0.10 m/s in right half of the fluidized bed (Bottom: h = 12 cm; Middle: h = 32 cm; Top: h = 52 cm)	96
Figure 5-3: Gas bubble profile for 0.10 m/s in left and 0.60 m/s in right half of the fluidized bed (Bottom: h = 12 cm; Middle: h = 32 cm; Top: h = 52 cm)	97
Figure 5-4: Gas bubble profile for Bottom row (h = 12 cm) for all velocities	97
Figure 5-5: Gas bubble profile for Middle row (h = 32 cm) for all velocities.....	98
Figure 5-6: Gas bubble profile for Top row (h = 52 cm) for all velocities.....	98

Figure 5-7: Cumulative mass of all collected agglomerates in the bed	100
Figure 5-8: Index of Segregation for the Bottom layer.....	100
Figure 5-9: Index of Segregation for the Top layer	101
Figure 5-10: Lateral distribution of agglomerates for Bottom layer for 0.35 m/s in both halves of the bed.....	102
Figure 5-11: Lateral distribution of agglomerates for Top layer for 0.35 m/s in both halves of the bed.....	102
Figure 5-12: Lateral distribution of agglomerates for Bottom layer for 60L-10R	103
Figure 5-13: Lateral distribution of agglomerates for Top layer for 60L-10R	103
Figure 5-14: Lateral distribution of agglomerates for Bottom layer for 10L-60R	104
Figure 5-15: Lateral distribution of agglomerates for Top layer for 10L-60R	104
Figure 5-16: Tracer locations and gas bubble flow distribution for MA2 at 0.35 m/s in both halves of the bed	106
Figure 5-17: Tracer locations and gas bubble flow distribution for MA2 at 0.60 m/s in the left and 0.10 m/s in the right side of the bed	106
Figure 5-18: Tracer locations and gas bubble flow distribution for MA2 at 0.10 m/s in the left and 0.60 m/s in the right side of the bed	107
Figure 5-19: Probability distribution of particle presence for MA2 at 0.35 m/s in both halves of the bed.....	107
Figure 5-20: Probability distribution of particle presence for MA2 at 0.60 m/s in the left and 0.10 m/s in the right side of the bed.....	108
Figure 5-21: Probability distribution of particle presence for MA2 at 0.10 m/s in the left and 0.60 m/s in the right side of the bed.....	108

Figure 5-22: Tracer locations and gas bubble flow distribution for MA1 at 0.35 m/s in both halves of the bed	109
Figure 5-23: Tracer locations and gas bubble flow distribution for MA1 at 0.60 m/s in the left and 0.10 m/s in the right side of the bed	109
Figure 5-24: Tracer locations and gas bubble flow distribution for MA1 at 0.10 m/s in the left and 0.60 m/s in the right side of the bed	110
Figure 5-25: Probability distribution of particle presence for MA1 at 0.35 m/s in both halves of the bed.....	110
Figure 5-26: Probability distribution of particle presence for MA1 at 0.60 m/s in the left and 0.10 m/s in the right side of the bed.....	111
Figure 5-27: Probability distribution of particle presence for MA1 at 0.10 m/s in the left and 0.60 m/s in the right side of the bed.....	111
Figure 5-28: Vertical distribution of 12500 μm for the base case (0.35 m/s gas velocity in both sides of the bed)	112
Figure 5-29: Vertical distribution of 12500 μm for the 60L-10R case (0.60 m/s gas velocity in the left side of the bed and 0.10 m/s in the right side of the bed)	113
Figure 5-30: Vertical distribution of 12500 μm for the 10L-60R case (0.10 m/s gas velocity in the left side of the bed and 0.60 m/s in the right side of the bed)	113
Figure 5-31: Vertical distribution of 5500 μm for the base case (0.35 m/s gas velocity in both sides of the bed)	114
Figure 5-32: Vertical distribution of 5500 μm for the 60L-10R case (0.60 m/s gas velocity in the left side of the bed and 0.10 m/s in the right side of the bed)	114
Figure 5-33: Vertical distribution of 5500 μm for the 10L-60R case (0.10 m/s gas velocity in the left side of the bed and 0.60 m/s in the right side of the bed)	115

Figure 5-34: Lateral distribution of 12500 μm in Bottom layer for the base case (0.35 m/s gas velocity in both sides of the bed)	116
Figure 5-35: Lateral distribution of 12500 μm in Bottom layer for the 60L-10R case	116
Figure 5-36: Lateral distribution of 12500 μm in Bottom layer for the 10L-60R case	117
Figure 5-37: Lateral distribution of 5500 μm in Bottom layer for the base case (0.35 m/s in both halves of the bed)	117
Figure 5-38: Lateral distribution of 5500 μm in Bottom layer for the 60L-10R case	118
Figure 5-39: Lateral distribution of 5500 μm in Bottom layer for the 10L-60R case	118
Figure A-1: Calibration curves for different combinations of sonic nozzles to supply fluidization gas to the right side of the bed.....	129
Figure A-2: Calibration curves for different combinations of sonic nozzles to supply fluidization gas to the left side of the bed.....	129

List of Appendices

Appendix A: Calibration for Sonic Nozzle Banks..... 126

Nomenclature

A_0	Initial activity of radioactive source (nuclei/s)
A_D	Activity of source after t seconds (nuclei/s)
t	time elapsed (s)
h	half-life (s)
I	Intensity of radiation (W/m^2)
r	distance between source and detector (m)
A_s	Activity of source before attenuation (nuclei/s)
ω	Mass attenuation coefficient (m^2/kg)
ρ_i	Density of medium (kg/m^3)
L_i	Length of medium (m)
x	coordinate x from tracer particle (m)
x_i	coordinate x from detector i (m)
y	coordinate y from tracer particle (m)
y_i	coordinate y from detector i (m)
z	coordinate z from tracer particle (m)
z_i	coordinate z from detector i (m)
V_g	Fluidization gas velocity (m/s)
$d_{aggl.}$	Size of agglomerate (μm)
d_p	size of an individual sand particle (μm)

t_f	Fluidization time (min)
q_b	Bubbles gas flux (m/s)
q_{bi}	Local bubbles gas flux (m/s)
ΔP_{grid}	Gas distributor grid pressure drop (kPa)
ΔP_{bed}	Fluidized bed pressure drop (kPa)

Chapter 1

1 Introduction

Canada has the largest bitumen reserves in the world that are extracted from oil sands. Fluid CokersTM are an essential part of upgrading facilities to produce synthetic crude oil by thermal cracking of bitumen, which can be pumped through pipelines and processed in oil refineries. Agglomerates, which consist of particles bound together by liquid, are formed when bitumen is injected in Fluid CokersTM. When wet agglomerates reach the stripper region, they bring wet/sticky coke and vapor. The coke depositing on sheds in the stripper section (lower section of Fluid CokerTM) results in reduction in open area for solids circulation which eventually leads to de-fluidized zones that causes stripper fouling. Sheds fouling in the stripper section can lead to premature shutdown of the unit.

The aim of the research work presented in this thesis is to describe the behavior of agglomerates to develop a better understanding of how bed hydrodynamics and agglomerate properties affect the motion of agglomerates in a fluidized bed in the context of Fluid CokingTM technology. However, this work is applicable to other processes as well which utilize fluidized beds. This chapter introduces key concepts and literature background related to the research work.

1.1 Bitumen

Bitumen is a type of heavy crude oil that has a viscosity $> 1000\text{cP}$ and an API gravity $< 10^\circ$ (Hein, 2017). It is extracted from oil sands in Alberta, Canada. Complex long-chain hydrocarbon (HC) molecules make up a large fraction of bitumen which need to be broken to produce lighter, higher-value products.

The vast resources of bitumen in oil sands in Western Canada require extensive processing to produce transportation fuels. The fraction of vacuum residue in bitumen is 50-60 wt %. Coking is one of the key technologies for processing vacuum residue, which is converted to valuable distillable liquids, gases, and solid coke residues (Gray et al., 2003).

1.2 Coking

Coking is a continuous thermal cracking process for the conversion of heavy hydrocarbons into synthetic crude oil. It produces coke and gases as by-products. Numerous processes have been developed to thermally crack bituminous materials including visbreaking, delayed coking, Fluid CokingTM and FlexicokingTM (Javier Sanchez, 2013). Fluid CokingTM is of particular interest in context of the research work presented in this thesis.

1.3 Fluid Coking

Fluid CokingTM is an upgrading process in which bitumen is injected via spray nozzles into a fluidized bed of heated coke particles to thermally crack it into more valuable lighter hydrocarbon products. Preheated feed at 350 °C is injected into the fluidized bed of coke at 500 °C to 550 °C through steam atomization spray nozzles. The bed temperature should be maintained such that production of low-value permanent gases by over-cracking is avoided. Figure 1-1 shows a schematic of a Fluid CokerTM.

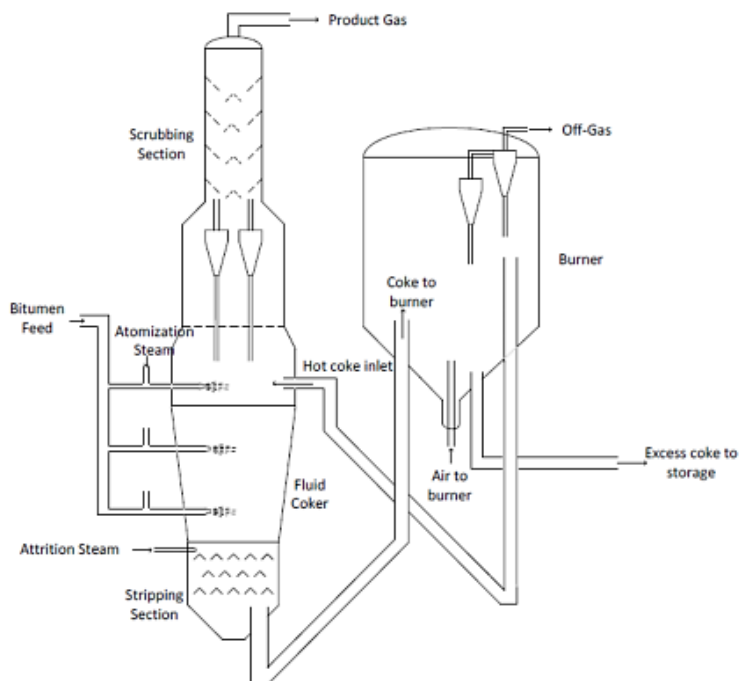


Figure 1-1: Schematic of a Fluid CokerTM Reactor (Prociw, 2014)

When feedstock is injected in a downward-flowing bed of hot coke particles, it heats up and cracks into smaller vapor molecules. Vapors move upward through the bed while the particles move down to stripper region where valuable vapor product trapped between the coke particles is recovered through steam stripping. The stripper is equipped with sheds (baffles) to enhance the removal of hydrocarbon vapors from fluidized coke particles. The down-moving coke particles are then conveyed to a burner where partial combustion is used to reheat the coke particles and recirculate them back to the reactor. This provides the heat required for the endothermic thermal cracking process. Excess coke particles are then removed, quenched and stockpiled.

The hydrocarbon feed is dispersed into very fine droplets when sprayed into the fluidized bed which significantly enhances the phase contact area in the reactor and provides a proper cracking environment for the bitumen feed, without major heat and mass transfer limitations. The even distribution of droplets improves the heat transfer, for a rapid and effective process (Base et al., 1999).

Gray et al. (2003) mentioned that the time required for Athabasca bitumen to completely react is around 24 s at 503 °C. Furthermore, the adhesive forces caused by reacting material are only significant when the film is still liquid and capable to form liquid bridges between coke particles. Particles can grow either by normal growth by laying down product coke on the individual particles or by coke-particles agglomerating.

The stripper displaces hydrocarbons in the interstitial voids between the coke particles by using countercurrent contact with steam. Stripping is most effective in a dense, moving fluidized bed. When the steam is injected at the bottom of the stripper, bubbles rise opposite to the down-flowing coke stream entering from the top (Wiens, 2010). To enhance the contact between steam and the coke particles, baffles known as “shed decks” or simply sheds, are employed in the stripping section of the reactor (Blaser et al., 1986; Graf & Janssen, 1985; Luckenbanch, 1969).

1.3.1 Fouling

One of the most common issues encountered in Fluid CokingTM is fouling of the stripper section of the reactor because of solid coke deposits. The build-up of undesirable material on the surfaces of process equipment is usually referred to as fouling. The rate of fouling can be defined by the change of rate of deposition and the rate of removal. When fouling arises in a process, there are two likely scenarios that can occur:

1. The deposition rate is always greater than the removal rate and a complete barrier to the flow will be formed after some time
2. Equilibrium will be reached after a certain period when the removal rate is equal to the deposition rate

In a Fluid CokerTM, the deposition rate is always greater than the removal rate and a complete barrier to the flow is eventually formed. Fouling impacts negatively on yield and throughput of the unit, and reduces the total run-time between shutdowns.

1.3.2 Sheds

Fluidization can be improved by breaking and re-distributing the bubbles by using internals (Javier Sanchez, 2013) such as baffles, especially with Group B powders (Geldart, 1973). Bubble size plays an important role for gas/solid mass transfer in bubbling fluidized beds. The coke particles in the wake around the bubbles interact with the gas inside the bubbles resulting in mass transfer between gas and solid. This mass transfer can be improved by decreasing the bubble size and renewing the wake around the bubble by exchanging the gas components from the emulsion phase (Yang, 2003).

A schematic diagram of a small section of sheds in the stripper section in a Fluid CokerTM is shown in Figure 1-2. The open area for solids circulation reduces when coke particles are deposited on the sheds. This phenomenon is called fouling.

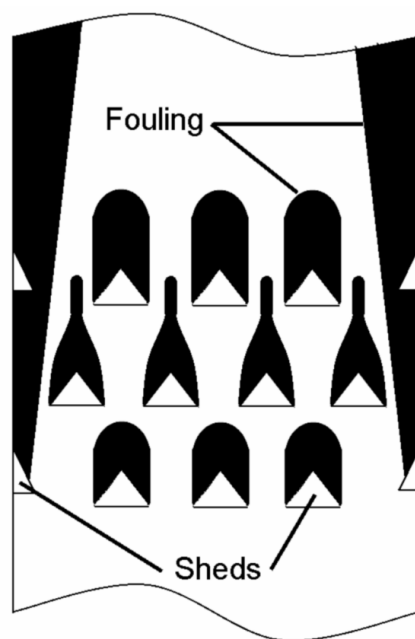


Figure 1-2: Fouling caused by unwanted coke deposition on the sheds and walls of the Fluid Coker™ stripper section (Adopted from Bi et al., 2005)

Coke gradually deposits on the surface of the sheds. When the coke gathered on the middle row reaches the top row of the sheds, the flow of coke particles is increasingly restricted until the shutdown of the Fluid Coker™ for cleaning becomes unavoidable. To avoid the premature shutdown of the unit, it is very important that coke deposits on the sheds is minimized.

1.4 Agglomeration

The phenomenon of particles sticking to each other is called agglomeration. In some processes, agglomeration is desirable such as in pharmaceuticals and fertilizer industries where dustiness can be reduced by agglomeration (Weber, 2009). However, in processes such as Fluid Coking™, agglomeration is highly undesirable as it reduces the production yield when agglomerates with considerable amount of high value unreacted hydrocarbons leave the Coker to be burned in the burner. In Fluid Cokers™, agglomeration causes both mass transfer and heat transfer limitations. Mass transfer limitations prevent the cracked products from moving to the vapor phase in the bed resulting in the formation of coke, whereas heat transfer limitations lead to a reduction in the cracking rate, causing liquid

accumulation in the bed and further agglomeration which increases the risk of bogging and de-fluidization (House, 2007). Agglomeration also causes fouling of the internals and surfaces such as sheds/baffles (Javier Sanchez, 2013).

1.4.1 Formation of Agglomerates

When liquid is injected in a fluidized bed, it does not vaporize instantaneously even if the bed is operated above the boiling point of the liquid. Agglomerates are almost immediately formed when particles and liquid jet come in contact. These agglomerates then move around the rest of the fluidized bed.

Ariyapadi et al. (2003) studied the agglomerate formation using X-ray imaging. An opaque radio liquid tracer with ethanol was injected to visualize the jet cavity. It was observed that agglomerates formed because of coalescence of liquid droplets and solid particles at the end of the jet cavity.

A study by Schaefer & Mathiesen (1996) showed that there are two mechanisms by which initial contact between liquid droplets and particles occur,

1. When droplets are small, wetting is caused by the distribution of droplets on individual solid particulates. This leads to coalescence between wet solid particles.
2. When droplets are large, wetting is caused by the immersion of large number of solid particles in the liquid.

House (2007) showed using open air experiments that the first mechanism occurs in Fluid CokersTM. The results showed that the Sauter mean diameter of the liquid droplets is equivalent to the Sauter mean diameter of the coke particles, hence, leading to the result that the first mechanism is prevalent in Fluid CokerTM.

For agglomeration to occur, the viscosity of the liquid and contact angle are two key factors that are independent of fluidization gas velocity (McDougall et al., 2005). A low contact angle between the liquid and solid surface results in well wetted particles. When the particles are well wetted by the liquid, the agglomerate formation occurs if the liquid has a

high viscosity. However, when the contact angle is high, agglomerate formation will always take place (McDougall et al., 2005).

1.5 Models for the Study of Agglomerate Formation

Several experimental models are available to generate agglomerates by liquid injection in a fluidized bed under conditions that simulate agglomerate formation in Fluid CokersTM. Such models include the PlexiglasTM experimental model developed by Morales (2013) and the Gum Arabic model developed by Reyes (2015). Both models produce an agglomerate distribution that matches the agglomerate distribution obtained in a pilot plant Fluid CokerTM (Reyes, 2015).

The model developed by Morales (2013) uses Plexiglas as a binder dissolved in a mixture of acetone and pentane, and sand as fluidized solids. Since the acetone-pentane mixture can form combustible mixtures with air or in some cases explosive mixtures, nitrogen had to be used as fluidization gas for this model which is quite expensive compared to air. The experiments were conducted at 68 °C. The experimental technique also required a complex procedure to measure the initial concentration of liquid in agglomerates (Soxhlet extraction) that caused the measurements to be conducted on small proportions of the agglomerates. The flammable and toxic acetone and pentane also posed health and environmental hazards.

The advantages of the Gum Arabic model developed by Reyes (2015) is that it can be operated at 120 °C and while it provides a similar distribution of agglomerates formed, is more flexible in terms of operation, control and complexity as it does not form explosive mixtures with air and does not need a complex procedure to determine the initial liquid content of the recovered agglomerates. The binder solution for the model developed by Reyes (2015) requires a mixture of Gum Arabic (as binder), food dye (tracer) and water (solvent) that causes no environmental or health impact. Also, the measurement procedure to estimate concentration of the binder in the solution is accurate thanks to the use of food dye. For this reason, the Gum Arabic model was used for agglomerates formation by liquid injection for this study. Another advantage of the Gum Arabic model is that it uses water

as the solvent. Water wets sand particles well as bitumen wets coke particles in Fluid Cokers™ (Prociw, 2014).

In either case, agglomerates were generated by injecting the binder solution into the fluidized bed. The agglomerates were then collected and analyzed to determine the size distribution and the initial binder concentration.

1.6 Tribo-Electric Method for Bubble Flow Distribution

The particles in a fluidized bed move when bubbles of fluidization gas move through the bed. The local gas bubble flux varies greatly over the bed cross-section. The motion of agglomerates is also affected by the distribution of gas bubble flux.

Various methodologies have been developed by scientists to visualize or quantify the bubble flow distribution. Some of the methodologies include direct visualization using image analysis, X-ray image analysis, X-ray tomography, optical probes etc. Jahanmiri (2017), developed a novel tribo-electric method to quantify the gas bubbles distribution in a fluidized bed.

1.6.1 Theory and Background

Some materials become electrically charged after a frictional contact with another material. This phenomenon is known as the triboelectric effect. Jahanmiri (2017) showed that in a fluidized bed, triboelectric probes can be used reliably to determine the fluidization gas bubble flow distribution. The triboelectric probes generate electric current when solids in the wake of the bubbles interact with the triboelectric probe. This electric signal enables us to determine the local bubble flux from the characteristics of the signals, i.e. power and average frequency, obtained from a triboelectric probe. The signals can be analyzed using a data analysis tool such as power spectrum.

For the research work presented here, an array of 12 x 3 triboelectric rods was used to determine the fluidization gas bubble flow distribution in the fluidized bed (Figure 2-5). The advantage of triboelectric rods over optical or conductance probes is that triboelectric rods can be used even when the fluidized bed is operated at higher fluidization gas

velocities such as 1 m/s without bending or breaking. They also require minimal maintenance.

1.7 Radioactive Particle Tracking

Radioactive Particle Tracking (RPT) is a non-intrusive technique to track the motion of a single radioactive particle (source) in a vessel without disrupting the flow inside (Shehata et al., 2007). The concept was first developed by Kondukov in 1965. However, Lin et al. (1985) were the first to successfully attain their objectives to study the motion of solids inside a fluidized bed and observe a change in direction of solids motion as the gas velocity was increased. Moslemian et al. (1992) then made data sampling faster and easier by introducing digital pulse counters. RPT has been improved significantly since its conception by various scientists and several new applications have been found for this method (Ayatollahi, 2016).

1.7.1 Theory and Background

RPT works on the principle that a radioactive particle releases γ -rays. These γ -rays can be detected using scintillation detectors and, hence, the distance can be measured from the source as a function of radiation strength. Based on the distances from different scintillation detectors, location coordinates of the radioactive source in a fluidized bed can be determined. Scintillation detectors should be placed around the controlled volume in such a way that they provide sufficient redundancy to calculate the location of the tracer particle.

Radioactive nuclei can emit alpha, beta and gamma radiations. The selection of scintillation material depends on the type of radiation to be detected and the type of radiation to be detected is determined by the radioactive isotope used. For example, a NaI scintillation detector is used to detect gamma radiation whereas a ZnS scintillation detector can be used to detect alpha radiation. Each type of radiation has a different penetration capability (alpha with the lowest and gamma with the highest), therefore, the selection of radio-isotope depends on the system that needs to be observed. In this case, the highest penetrating radiation was needed i.e. gamma rays. Hence, the radio-isotope and the detection system were selected accordingly; details are presented in Section 2.7.

1.7.2 Factors Affecting Strength of Radioactive Source

Several factors affect the strength of the radioactive source including time (half-life), distance of detector from the source and mass attenuation due to media present between the detector and the source etc. Hence, a correction is required for each factor when calculating the intensity of radiation.

1.7.2.1 Half Life

The number of parent nuclei of radioisotope decreases when they undergo disintegration and release nuclear radiation. The time elapsed, while the number of parent nuclei reduce to half of the initial value, is called half-life. For example, the half-life of Scandium-46 is 83.79 days which means approximately 50 of the 100 initial parent nuclei will be left after 83.79 days and so on. Reduction in number of parent nuclei reduces the activity of the radioactive source (number of radioactive disintegrations per second) in the same proportion. Equation (1.1) represents the correlation to determine the radioactivity of a source after any given time.

$$A_D = A_o \cdot (1/2)^{t/h} \quad (1.1)$$

In this equation, h is the half-life of the radioactive material.

1.7.2.2 Effect of Distance on Radiation Strength

The radiation strength reduces as the source moves away from the detector. (Javier Sanchez, 2013) The effect of distance on radiation strength can be determined by the Inverse Square Law as given by Equation (1.2).

$$I \propto \frac{1}{r^2} \quad (1.2)$$

1.7.2.3 Attenuation

The radiation emitted from radioactive source loses its intensity when it passes through a medium or a series of media due to interaction between radiation and the medium it passes through. This phenomenon is known as attenuation. The attenuation of the radiation in the

medium is characteristic of the type of medium (i.e. mass attenuation coefficient) and its length (Ayatollahi, 2016). The absorption of radiation in a series of different media can be determined using the generalized Beer-Lambert law in Equation (1.3) which gives the radioactivity corrected for the attenuation.

$$A_D = A_S \cdot \exp(-\sum_i \omega_i \rho_i L_i) \quad (1.3)$$

The energy of gamma rays emitted by the source should be high enough so that it can be detected by the detector after attenuation through the system.

1.7.3 Working Principle of Scintillation Detectors

A scintillator is a material which, when struck by an incoming radiation source, absorbs the energy of the incoming radiation. The absorbed energy is re-emitted by the scintillator as a photon of visible light after a certain decay time. Decay time can vary from a few nanoseconds to several hours depending on the material of the scintillator. In this case, a scintillator with a very small decay time was needed to create an RPT system with a considerable short sampling time.

By coupling a scintillator to an electronic light sensor, such as photomultiplier (PMT), a scintillation detector is obtained. When a PMT absorbs a photon, it re-emits the energy as an electric pulse due to photoelectric effect. Hence, a scintillation detector counts the incident radiations in two steps. In the first step, a photon is generated by the scintillator when the scintillator is struck by a radiation source. In the second step, this photon goes to the PMT and strikes a thin metal foil, also known as photocathode, causing an electron to eject from the photocathode. The ejected electron is electrostatically accelerated to a high energy and strikes a series of metal cups which are located just past the photocathode. This successive collision with metal cups generates secondary electrons resulting in an amplified electric pulse in the end which can be measured by the electronic circuit. The intensity of the radiation can be determined by measuring the number of electric pulses generated per unit time.

The external photons can affect the ionization events caused by incident radiation if the scintillator is not shielded from the ambient light. A thin opaque foil, such as aluminized

mylar, is often used to shield the scintillator. However, the foil thickness should be selected in a way that it minimizes the attenuation of the incident radiation.

1.7.3.1 Calibration of Scintillation Detectors

The effect of distance on the strength of radiation source can be corrected if the distance between the source and detector is known. The coordinates of the detector are known as the detector has a fixed known location, but the location coordinates of a radioactive particle are not known when the RPT system is used to track the motion of a particle. It means the distance between the source and detector is unknown and correction due to strength cannot be known. Calibration of scintillation detectors is carried out to eliminate this problem. A calibration curve is generated by placing the radioactive source at several known locations and measuring the intensity of radiation from the source (Javier Sanchez, 2013).

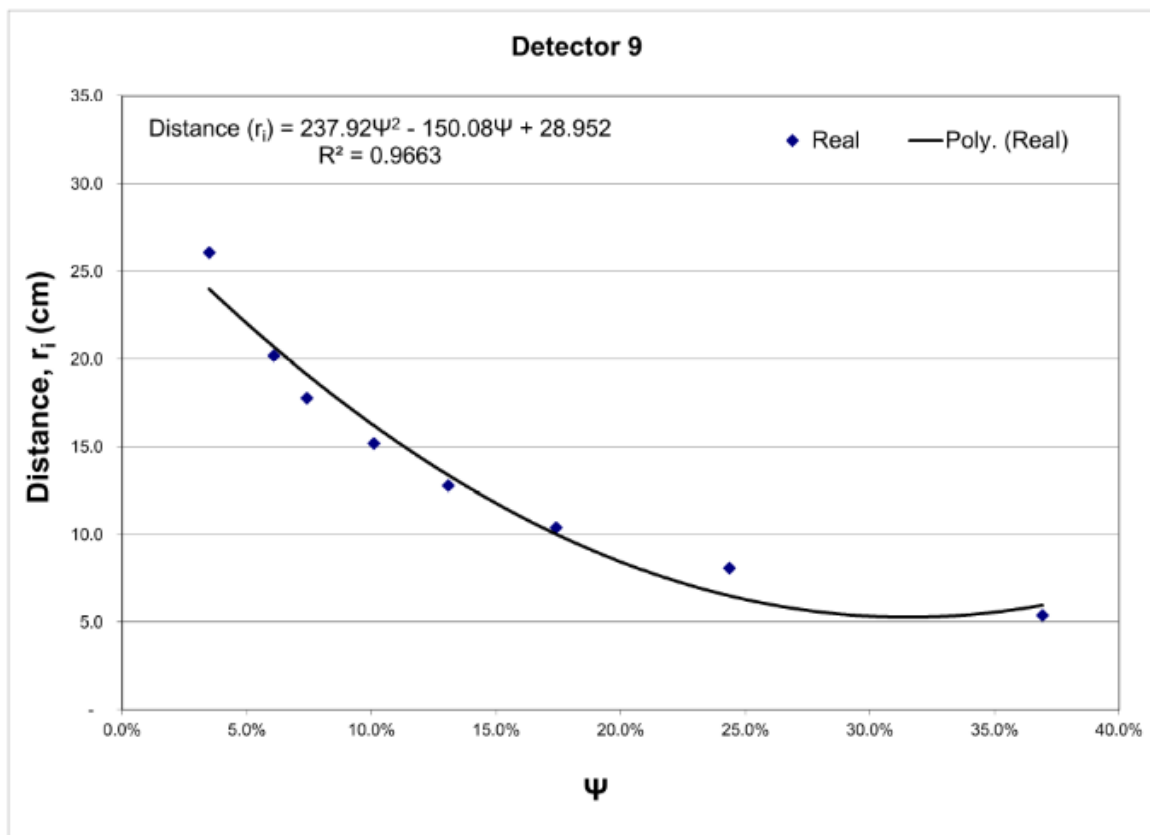


Figure 1-3: An example of a calibration curve for a detector (Javier Sanchez, 2013)

Figure 1-3 shows an example of a calibration curve which provides distance between the center of detector and radioactive particle as a function of normalized radiation data. It is clear from the calibration curve that the closer the particle, the higher the intensity of the radiation. Hence, distance can be obtained from the above curve, if radiation data from the detector is available. For more information on calibration, please refer to Chapter 4 (Section 4.1.1).

1.7.4 Rendition Techniques

Several rendition techniques can be used to obtain the location coordinates of a radioactive source as a function of time in a fluidized bed. The most common methods used are,

1. Computer Aided Radioactive Particle Tracking (CARPT)
2. Monte Carlo Simulation

1.7.4.1 Computer Aided Radioactive Particle Tracking (CARPT)

This method was first introduced by Lin et al. (1985). Before the position of tracer can be determined, an in-situ calibration must be conducted by placing the tracer at several known positions and measuring the radiation intensity by each detector. A calibration curve is established for each detector from the obtained information to correlate the intensity measured by the detector to the distance between the tracer and the center of the detector surface. The calibration curve can have different shape and order. The calibration curve usually is developed by curve fitting of the raw data and the fitted curve. Several polynomial fits of different orders are used to determine the relationship of distance versus γ -rays counts (Chaouki et al., 1997).

The distance between the i^{th} detector (x_i, y_i, z_i) and the source (x, y, z) can be measured using the two-points distance formula given in Equation (1.4).

$$r_i^2 = (x - x_i)^2 + (y - y_i)^2 + (z - z_i)^2 \quad (1.4)$$

Where r is the distance that is attained from the polynomial fitting. Since the data is available from many scintillation detectors, it results in the redundancy of the data for

location determination. Lin et al. (1985) used a weighted least-square exact linearization method to take advantage of the available redundancy.

The main advantages of the CARPT method are simplicity of the mathematics and less amount of processing time required. The disadvantages of this method are that it needs an extensive calibration and still the model does not consider the angle between the tracer and a horizontal axis through the center of the scintillation detector.

1.7.4.2 Monte Carlo Rendition Technique

This method was developed by Dr. Chaouki and his group at École Polytechnique de Montréal. This method takes into account both the geometry and effect of radiations in RPT. This eliminates the need for the extensive in-situ calibration, but increases the computer processing time. The determination of the tracer location from the detectors counts involves the development of a map of counts as a function of the possible coordinates of the source. Since a certain fraction of the γ -rays are absorbed by the fluidized material and by the vessel walls, a new map is needed whenever the density of the medium to be studied changes (Chaouki et al., 1997).

The unfortunate disadvantage of using this method is that it requires high computation time due to complex mathematics. One coordinate per second is the approximate rate to obtain the position. It means it will take around 11 days to calculate coordinates from the data if one million data points are present in the data. This would take 5 minutes when CARPT method is used (Javier Sanchez, 2013).

1.8 Research Objectives and Outline

The main objective of the research work conducted in this thesis is to develop a better understanding of how agglomerates move through a fluidized bed, and how their motion is affected by bed hydrodynamics. To achieve this target, model agglomerates were manufactured with a radioactive source so that they can be tracked when they move in the fluidized bed unit. But before model agglomerates could be manufactured, the properties of such agglomerates needed to be determined in a separate set of experiments. Hence, the main objective was divided into following three sub-objectives:

Chapter-3: A preliminary study was conducted to determine which agglomerates segregate in a fluidized bed and their properties such as size and density. Preliminary experiments were conducted by injecting a binder liquid solution of Gum Arabic (GA) in a fluidized bed of sand and air. The cold model developed by Reyes (2015) was adopted for these experiments, as Reyes (2015) showed that the GA model gives an agglomerate distribution similar to that of a pilot Fluid CokerTM. The agglomerates produced in these experiments were collected and their properties were determined. Agglomerates that segregated were also identified in these experiments. Gas bubble flow distribution was also measured using the tribo-electric method to study the impact of bubbles distribution on segregation.

Chapter-4: This chapter describes the development of new method for a 2D RPT system. Initially, CARPT method was used to determine the location coordinates of a radioactive model agglomerate in a fluidized bed, but it did not work because all the detectors were in a 2D plane for the RPT setup. CARPT method is applicable for a system with detectors in a 3D plane. After the development of the new method, the motion of model agglomerates was investigated for various velocities at room temperature and 120 °C. The size of model agglomerates was based on the properties of actual agglomerates that were found important in the preliminary studies (Chapter-3).

Chapter-5: After successful implementation of the new method for our 2D RPT system, experiments were conducted with split gas velocities. It was achieved by creating two different gas velocities in two halves of the bed as fluidization air can be supplied to both halves independently. The purpose of this investigation was to determine how agglomerates behave when one half of the bed has a higher gas velocity or more gas bubbles, which simulates the core-annular flow observed in Fluid CokersTM. Experiments were also conducted with the GA model, to obtain preliminary segregation results and agglomerate properties to compare with the experiments with same gas velocities in both halves of the fluidized bed, and the tribo-electric method was used to measure the gas bubbles distribution in the bed.

Chapter 2

2 Experimental Setup and Methodology

This chapter describes the equipment setup used for all the experiments. It describes the methodologies used for the experiments conducted as well, but each chapter will also provide experimental procedures specific to those chapters.

2.1 Equipment

For all experiments, the same equipment was used for the fluidized bed. However, some minor changes were made in the equipment during the research work. A schematic diagram of the equipment with its dimensions is presented in Figure 2-1.

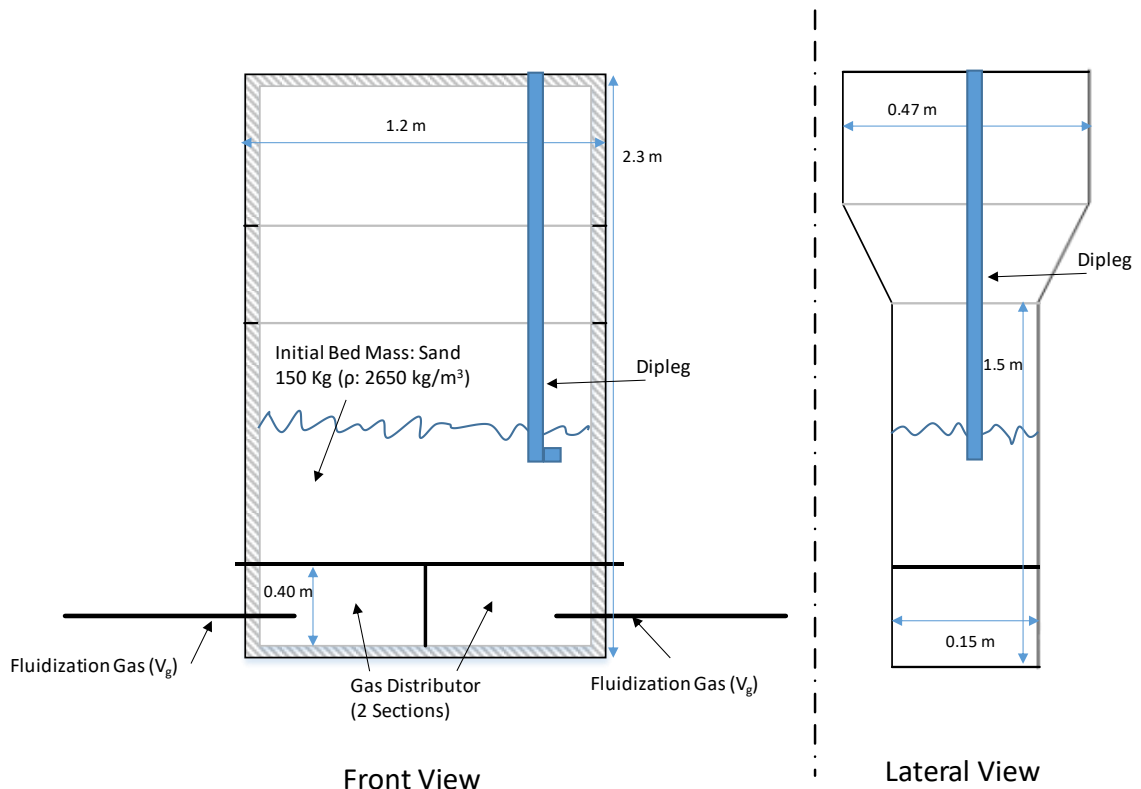


Figure 2-1: Equipment used for fluidizing 150 kg of sand using air as fluidization gas

The equipment used was 2.3 m high with a cross section of 1.2 m by 0.15 m. It had an expansion zone of cross sectional area of 1.2 m by 0.47 m at the height of 1.5 m. Fluidization gas was provided by two independent gas distributors. The mass flow of fluidization gas to the gas distributors could be controlled independently using two banks of sonic nozzles, one for each distributor. It was also equipped with one primary cyclone and one secondary cyclone. The dipleg from the primary cyclone recycled the collected particles back to the bed.

2.2 Fluidized Bed

Silica sand with a Sauter mean diameter of $190\ \mu\text{m}$ and a particle density of $2650\ \text{kg/m}^3$ was used as fluidized solids. For all experiments, 150 kg of silica sand was used making a fixed bed with a height of 0.54 m. Figure 2-2 shows the particle size distribution for the silica sand used in this study.

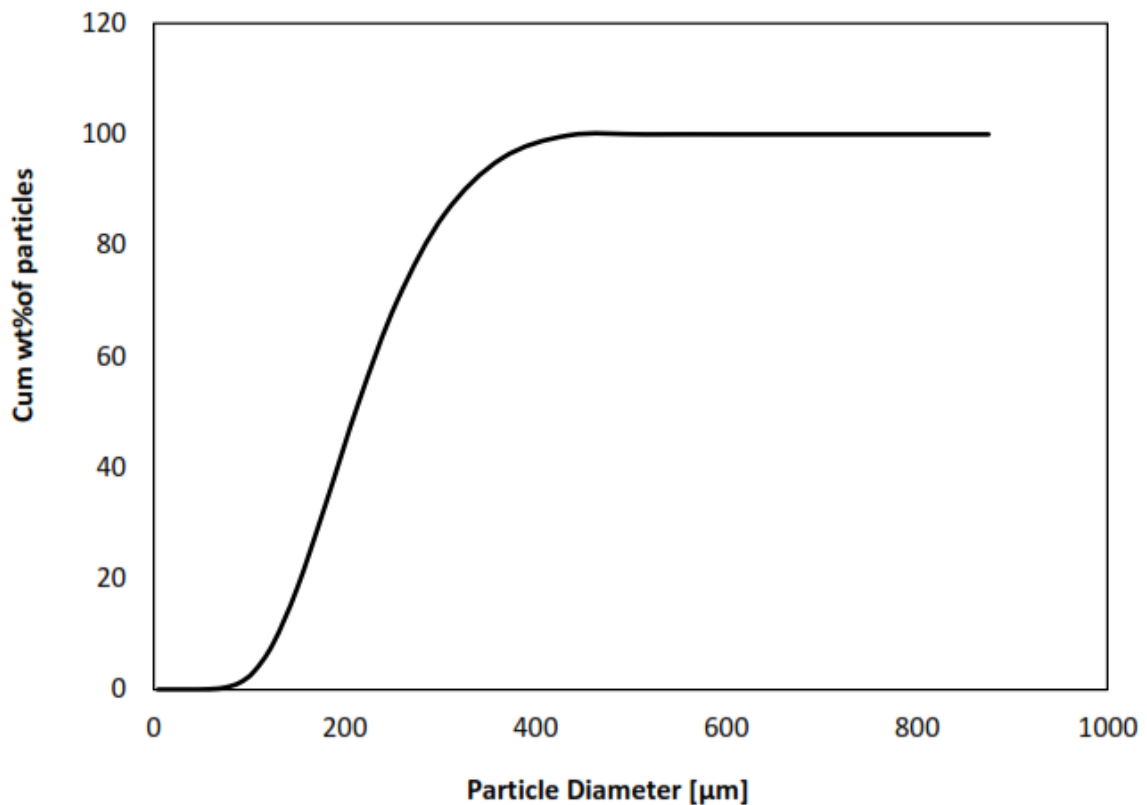


Figure 2-2: Silica sand particle size distribution ($190\ \mu\text{m}$ Sauter mean diameter)

Air was used as fluidization gas which was provided by the two gas distributors. The air flow was controlled by the two banks of sonic nozzles upstream of the fluidization gas distributors as shown in Figure 2-3. Air was used as fluidization gas as it is compatible with the binder liquid solution injected for agglomerates formation. The calculated minimum fluidization velocity for this system is 0.04 m/s.

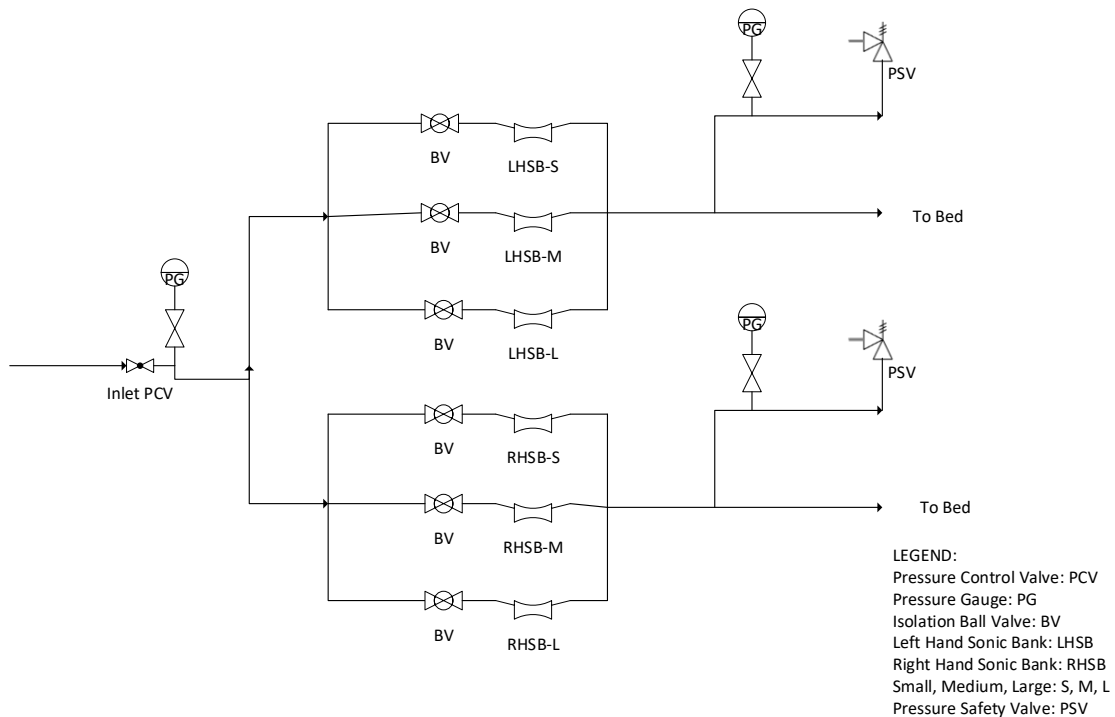


Figure 2-3: Sonic nozzle banks upstream of gas distributors which provide the fluidization air

Before experiments were conducted, the sonic nozzle banks were calibrated to obtain the data of mass flow rates for the given upstream operating pressures. The detailed operating and calculation procedure is provided as Appendix A.

2.3 Liquid Injection System

The liquid binder solution was injected at constant flowrate from a blow tank, pressurized with nitrogen, into the fluidized bed. A spray nozzle, with exit diameter of 2.7 mm, that used nitrogen gas to atomize the liquid into small droplets was used to inject the liquid in the fluidized bed in the form of a jet of small droplets (Figure 2-4). A Bilateral Flow

Conditioner (BFC) pre-mixer was used to mix the atomizing nitrogen gas and liquid binder solution upstream of the spray nozzle. The liquid solution was mixed with the atomizing gas at an angle of 30° as shown in Figure 2-5.

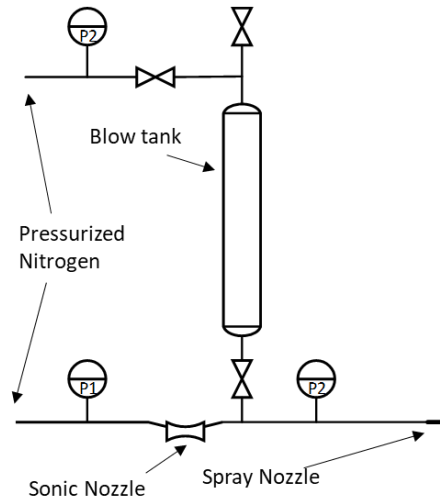


Figure 2-4: Liquid injection system

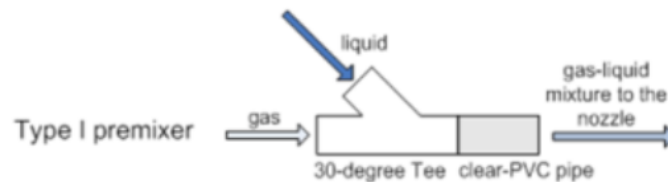


Figure 2-5: Bilateral Flow Conditioner (BFC) pre-mixer

Open air experiments were conducted to adjust all the pressure transducers such that the liquid injection system injects 30 g/s of liquid binder solution with a Gas to Liquid Ratio (GLR) of 2 wt%.

2.4 Agglomerates Recovery

Once an experimental run had been completed and the bed had been de-fluidized and cooled, the agglomerates were collected by sieving the bed mass as established by Morales (2013). The total bed mass recovered is categorized into three groups: macro-agglomerates ($\geq 600 \mu\text{m}$), micro-agglomerates ($< 600 \mu\text{m}$) and individual solid bed particles. Since there were no individual bed particles larger than $600 \mu\text{m}$ before liquid injection, macro-

agglomerates were, therefore, obtained by sieving the mass of all bed solids. Macro-agglomerates were then sieved into following size cuts:

$$\begin{aligned}
 & d_{\text{aggl}} \geq 12500 \text{ } \mu\text{m} \\
 & 12500 \text{ } \mu\text{m} > d_{\text{aggl}} \geq 9500 \text{ } \mu\text{m} \\
 & 9500 \text{ } \mu\text{m} > d_{\text{aggl}} \geq 4750 \text{ } \mu\text{m} \\
 & 4750 \text{ } \mu\text{m} > d_{\text{aggl}} \geq 4000 \text{ } \mu\text{m} \\
 & 4000 \text{ } \mu\text{m} > d_{\text{aggl}} \geq 2000 \text{ } \mu\text{m} \\
 & 2000 \text{ } \mu\text{m} > d_{\text{aggl}} \geq 1400 \text{ } \mu\text{m} \\
 & 1400 \text{ } \mu\text{m} > d_{\text{aggl}} \geq 850 \text{ } \mu\text{m} \\
 & 850 \text{ } \mu\text{m} > d_{\text{aggl}} \geq 600 \text{ } \mu\text{m}
 \end{aligned}$$

Because individual particles smaller than 600 μm were also present in the bed, retrieval of just micro-agglomerates free of individual particles was not possible. Therefore, the quantity and properties of micro-agglomerates were estimated from a representative sample that was taken after macro-agglomerates were recovered. The representative sample was then sieved to collect following size cuts:

$$\begin{aligned}
 & 600 \text{ } \mu\text{m} > d_p \geq 500 \text{ } \mu\text{m} \\
 & 500 \text{ } \mu\text{m} > d_p \geq 425 \text{ } \mu\text{m} \\
 & 425 \text{ } \mu\text{m} > d_p \geq 355 \text{ } \mu\text{m}
 \end{aligned}$$

In this thesis, each size cut is identified by its smallest value. For example, agglomerates of the size cut $425 \text{ } \mu\text{m} > d_p \geq 355 \text{ } \mu\text{m}$ are recognized as agglomerates of size 355 μm .

2.5 Agglomerates Analysis

The mass and density of macro-agglomerates were determined for each size cut after sieving. The procedure of estimation of mass and liquid to solid ratio (L/S) for micro-agglomerates is very well described by Reyes (2015). In summary, it consists of the following steps:

1. Recovery of micro-agglomerates (mixed with smaller individual bed particles)

2. Estimation of dye (tracer) in the micro-agglomerates using UV – spectroscopy (helped determining the L/S for both macro and micro-agglomerates)
3. Determination of mass of fine particles in agglomerates with the help of laser diffraction method

It was observed during preliminary studies that micro agglomerates did not segregate, therefore, micro-agglomerates were not analyzed for all later experiments.

2.6 Tribo-Electric Method

A total of 36 triboelectric rods were used to measure the gas bubble flow at 36 locations in the fluidized bed at the same time (Figure 2-6). The rods were inserted halfway into the bed to measure the time-averaged gas bubble flow. As the rods were inserted half way in the bed, they measured the tribo-electricity generated over the length of the rod that was inside the bed. Since 12 rods are placed in one row to measure the lateral bubbles distribution, the radial direction in which one rod is inserted is not important (later radial dimension or z-axis was also ignored for Radioactive Particle Tracking or RPT). This approach is different than the strategy used by Jahanmiri (2017). He inserted and moved the rod (covered with tygon coating exposing only 12 mm tip to measure local bubble flux) in the lateral direction to measure the local bubble flow at various locations. In our case, placing the 12 rods eliminated the need of moving the rods in any direction and enabled to obtain the 12 measurements in one row at the same time.

One of the triboelectric rods used is shown in Figure 2-7. The electric current generated by the triboelectric rods was then converted to voltage and amplified by a multirange amplifier which converted an input of 0-200 nA to an output of 0-10.4 V. The amplifier was linked to a data acquisition system that recorded the amplified signal every millisecond (sampling time of 1 ms) for 300 seconds. The experiments were conducted at room temperature for various gas velocities as described in Chapter 3 and Chapter 5.

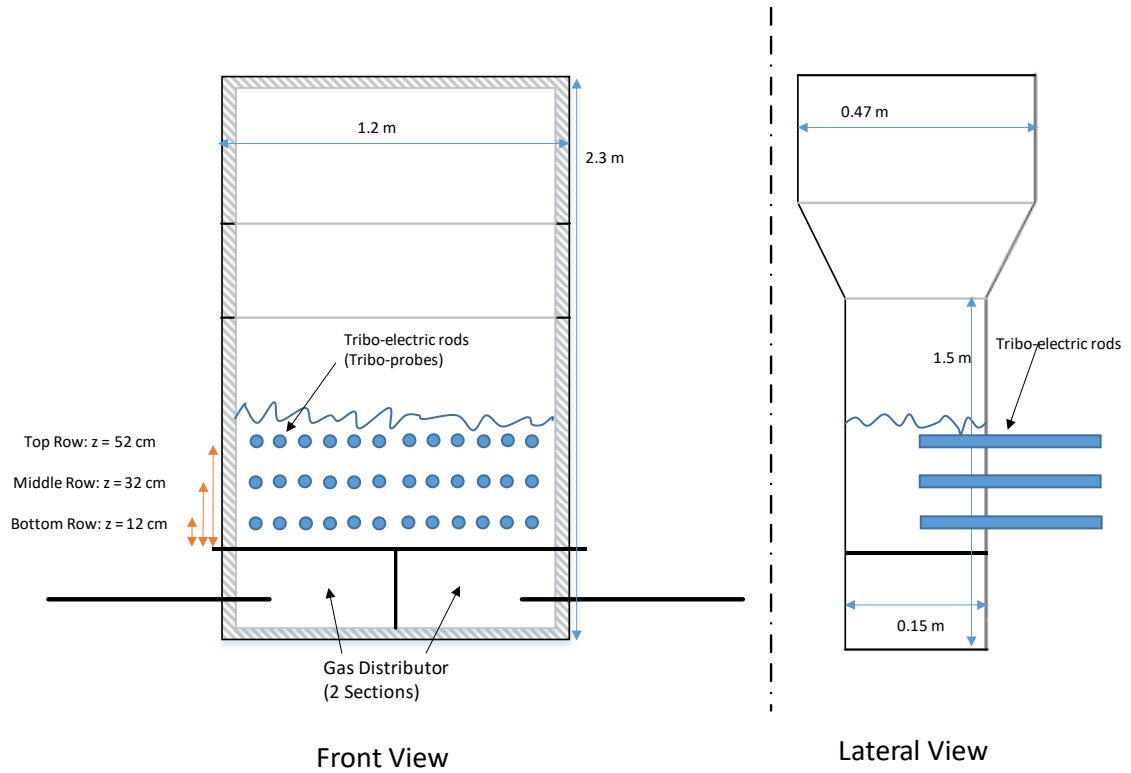


Figure 2-6: Array of triboelectric rods comprised of 3 rows and 12 columns inserted half way in the fluidized bed

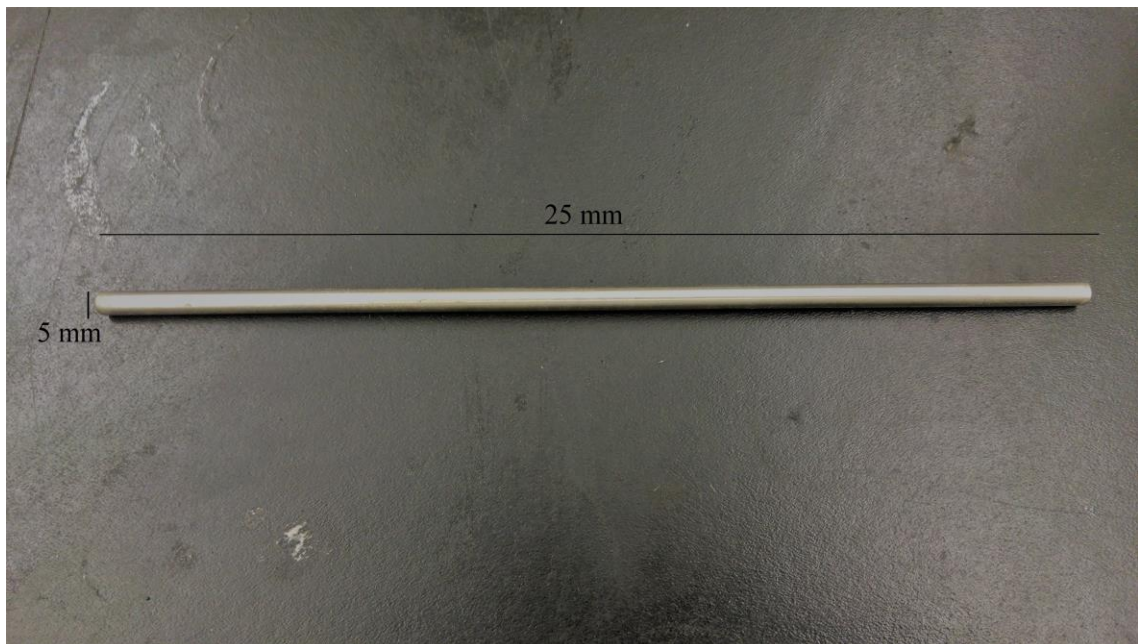


Figure 2-7: A triboelectric rod

2.6.1 Analysis of Triboelectric Signals

Jahanmiri (2017) showed that the best results for signal analysis were obtained when a correlation for gas bubble flux based on two variables was used by combining the power and average frequency, hence, the power spectrum of a signal. The average frequency and power of the signals can be calculated by the Equations (2.1) and (2.2), where f is the frequency and $P(f).df$ is the power between the frequencies $(f-df/2)$ and $(f+df/2)$, as determined with the Fast Fourier Transform:

$$\text{Average Frequency } (f_{avg.}) = \frac{\int_0^{25} P(f).f.df}{\int_0^{25} P(f).df} \quad (2.1)$$

$$\text{Average Power } (P) = \frac{1}{25} \int_0^{25} P(f).df \quad (2.2)$$

The local gas bubble flux (q_{bi}) can be calculated using the average frequency (f_i) and power (P_i) obtained from the above equations, using the Equation (2.3):

$$q_{bi} = a.P_i^b.f_i^c \quad (2.3)$$

The values of a , b and c were determined for the obtained data for each flowrate by minimizing the error between the experimental values and measured values as explained by Jahanmiri (2017).

2.7 Radioactive Particle Tracking (RPT) System

As described in Section 1.7, the development of the Radioactive Particle Tracking (RPT) system will depend on the type of radiation suitable for the intended application. In this case, the equipment wall was made of quarter inch iron sheet with a fluidized bed of silica sand inside. Therefore, alpha and beta radiations would not be able to penetrate the fluidized bed of sand and the equipment wall because of attenuation in radiation strength of the radioactive source. Hence, a radioactive source (further termed as source) with gamma decay was needed to make the RPT system work because of the non-disruptive nature of gamma rays and their ability to travel through various media.

2.7.1 Radioactive Particle/Source

Before actual experiments could be performed, calibration of the system was required by placing the particle inside the fluidized bed at known locations and recording the radiation strength for each location. It was estimated that it would take more than 3 months to complete the calibration of the system, therefore, a radioactive source with significant half-life was needed which would be environmental friendly as well. For this reason, Scandium-46 (Sc-46) isotope with a half-life of 83.79 days was chosen. Another advantage of Sc-46 is that it disintegrates into Titanium-46 (Ti-46) which does not pose any environmental or biological hazards.

The decay scheme of Sc-46 into Ti-46 is given in Figure 2-8.

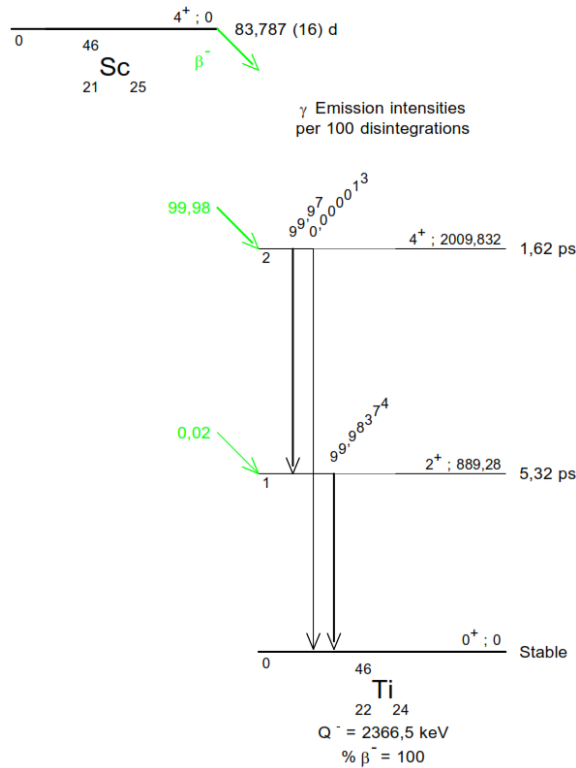


Figure 2-8: Decay scheme of Sc-46

2.7.2 Scintillation Detectors

Scintillation detectors consist of a scintillator and a photomultiplier (PMT). Selection of a scintillation detector is, therefore, based on the type of scintillator needed. For this system,

a scintillation detector with the capability of detecting gamma rays was required. For selection of a scintillation detector, the decay time is very important as it defines the minimum sampling time for the system (This decay time is not the same as half-life or radioactive decay. Please refer to Section 1.7.3 for further information). For this system, a scintillation detector with minimum decay time was required.

Sodium Iodide with activated Thallium [NaI(Tl)] is a commonly used scintillator with a decay time of only 0.23 μ s which was highly desirable for this work. The scintillation detector used to obtain intensities of gamma rays for the research work presented in this thesis was 2M2/2 (Saint-Gobain Crystals, USA). The cylindrical NaI scintillator was of 2" x 2" size with 0.2% thallium (Tl) impurity as activator. Thallium in the crystal structure of NaI converted the energy absorbed in the crystal by the radiation into visible light. The visible light generated by thallium was then converted and amplified by an integrally mounted photomultiplier tube (PMT) into a measurable electrical pulse (Figure 2-9).

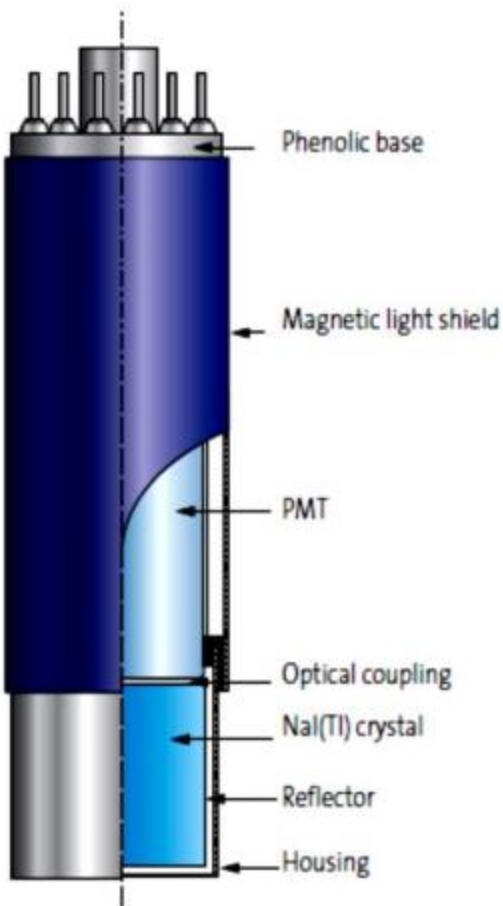


Figure 2-9: NaI(Tl) scintillation crystal used for the current research work (Saint-Gobain Crystals Inc.)

The NaI scintillation detector was coupled with an ORTEC digiBASE (Figure 2-10) externally which was used for data acquisition and processing through CONNECTION-32 and MAESTRO®-32 programs. This base consisted of a preamplifier and a powerful digital Multichannel Buffer (MCB).



Figure 2-10: Scintillation detector mounted on data acquisition (DAQ) base

Each scintillation detector was connected to a computer (also called Client computer) via a USB cable. The client computer measured the detector signal every 6 ms using a program on LabWindows CVI (National Instruments, Austin, TX) platform. This program was developed by Javier Sanchez (2013). Sanchez also found that by placing a USB hub between each detector and client computer speeds up data transmission from digiBase to client computer which reduced the sampling time from 62 ms to 6 ms.

2.7.3 Experimental Setup

The current RPT system at the Institute for Chemicals and Fuels from Alternative Resources (ICFAR) includes:

- A single radioactive source (Sc-46) emitting γ -rays
- 12 scintillation detectors arranged in a 2D plane to count the radiations emitted
- One computer for each scintillation detector along with a master computer to record, process and analyze data

- Sampling time (time to record 1 event) was 6-10 ms

A Server computer (Server) synchronized all 12 client computers along with timestamping the acquired data to make sure that all the data was acquired from the detectors at the same known time. The server communicated with client computers through an Ethernet hub.

A schematic of the experimental setup is shown in Figure 2-11, followed by actual pictures of the scintillation detectors and data acquisition (DAQ) system in Figures 2-12 and 2-13.

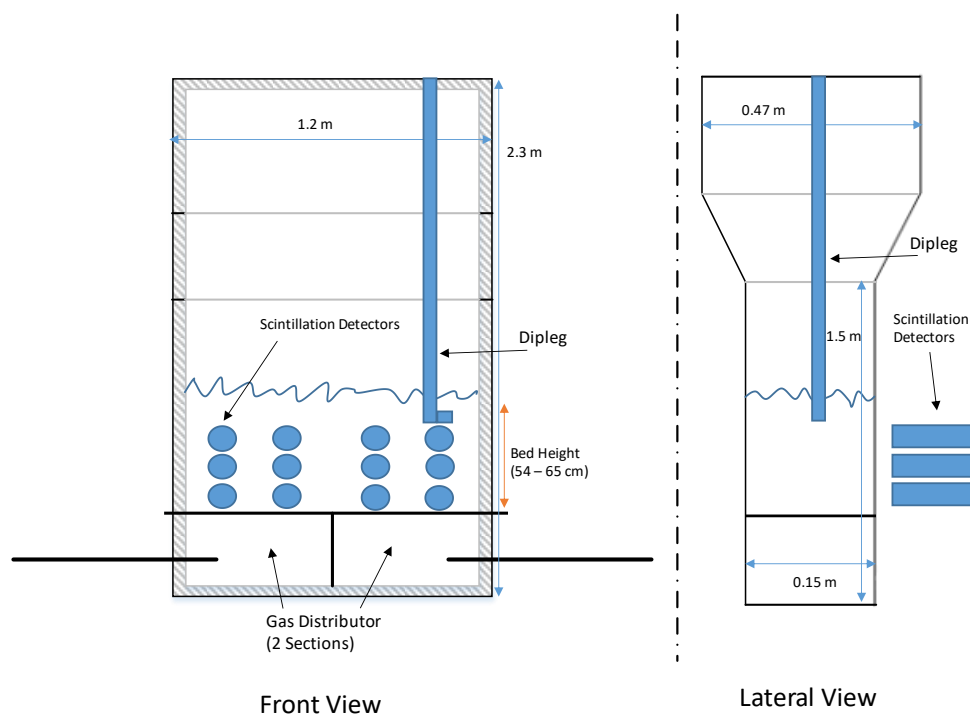


Figure 2-11: Schematic showing the arrangement of scintillation detectors



Figure 2-12: Scintillation detectors arranged in 3 x 4 matrix in a 2D plane



Figure 2-13: Data acquisition center showing all 13 computers connected with 12 scintillation detectors in the back

Chapter 3

3 Preliminary Study on Behavior of Agglomerates formed by Liquid Injection

To determine the properties for the model agglomerates for Radioactive Particle Tracking (RPT), experiments were conducted to generate agglomerates by injecting a liquid binder solution in a fluidized bed of sand and air. As mentioned in Chapter 2, a liquid binder solution composed of Gum Arabic (binder), blue color food dye (tracer) and water (solvent) was used for injection in the fluidized bed. The liquid to solid ratio (L/S) can be measured by analyzing the tracer in the agglomerates.

Another purpose of the experiments with liquid injection was to identify the agglomerates that would segregate. Liquid injection experiments were, thus, performed for two different velocities spanning the range of velocities expected in Fluid CokersTM so that agglomerates that would segregate over a range of hydrodynamic conditions could be identified.

To check whether the agglomerates segregated or not, the bed was divided into layers as it was progressively removed from the unit after experiments. The bed was divided into 8 horizontal layers with a height of 7 cm.

3.1 Bubble Flow Distribution in the Fluidized Bed

Jahanmiri (2017) showed that the local bubble flux can be evaluated from the triboelectric current produced by the interaction between bed solids and a triboelectric rod. Hence, several rods can be used together to measure the gas bubble flow distribution inside a fluidized bed as described in Section 2.6. The gas bubble flow distribution was measured to determine whether agglomerate segregation was affected by the bubble flow distribution. Triboelectric measurements were conducted separately from the liquid injection experiments.

3.2 Experimental Setup and Procedure

Agglomerates were generated by injecting a liquid binder solution into a fluidized bed of sand that was fluidized by air. The fluidized bed was operated at 120 °C. The fluidized bed

was equipped with one liquid injection system comprised of a blow tank (for liquid), a sonic nozzle, a pre-mixer and an atomizing spray nozzle (Figure 3-1). The spray nozzle used nitrogen as the atomizing gas. The blow tank was pressurized with nitrogen once it had been filled with the liquid. 300 g of liquid was injected into 150 kg of sand for each experiment. The particle density (ρ_p) of the silica sand was 2650 kg/m^3 . The liquid solution was composed of 6 wt% Gum Arabic, 2 wt% blue color dye, 92 wt% water and a few drops of sulphuric acid to reduce the pH to 3.0. Reducing the pH adjusted the viscosity of the gum Arabic solution in the range of viscosity of bitumen at injection conditions (Reyes, 2015). The injection nozzle was installed on one of the 0.15 m walls (Figure 3-1). For all experiments, liquid was injected at a rate of 30 g/s for total 10 s of injection time with a gas to liquid ratio (GLR) of 2 %. GLR was maintained by adjusting the pressure of nitrogen in the blow tank and upstream of the sonic nozzle.

The fluidization gas (air) was provided through two gas distributors, with each distributor supplying one half of the bed (Figure 3-1). The flow of air to these distributors could be controlled independently by two banks of sonic nozzles that were calibrated prior to the experiments. Each sonic bank consisted of 3 sonic nozzles of different sizes. A wide range of air flow rates could be provided by operating these sonic nozzles individually or in combination. Two heaters were installed on the air pipes to heat the air before entering the fluidized bed so that the fluidized bed could be heated to and maintained at $120 \text{ }^\circ\text{C}$. For this chapter, experiments were conducted at two gas velocities (V_g) i.e. 0.06 m/s and 0.6 m/s .

Hence, the overall procedure was as follows:

The bed was fluidized and preheated to $120 \text{ }^\circ\text{C}$. The gas velocity (V_g) was adjusted to 0.06 or 0.6 m/s . Liquid was injected for 10 s at a rate of 30 g/s. The bed was kept fluidized for a set duration of time i.e. $t_f = 0, 2, 4, 7, 10$ or 15 min after the liquid injection had been completed. The fluidization gas was then shut off to slump the bed so that the agglomerates froze at that moment and stopped moving. After that, the bed was cooled with gas well below the minimum fluidization velocity. A section of the bed wall was then removed (Figure 3-2) and a vacuum cleaner was used to remove the bed solids layer by layer. For

some selected experiments, the top and bottom layers were further divided into 4 lateral sections so that the lateral distribution of agglomerates could be measured. The collected bed solids were then sieved to recover agglomerates in size cuts as mentioned in Section 2.4. For all experiments, the procedure remained the same, except for the gas velocity and the time after liquid injection when the bed was de-fluidized.

Initially, the bed solids were sieved in 9 size cuts. But later two screen sizes with openings of 12500 μm and 4750 μm were added to increase the resolution of the size distribution of macro-agglomerates.

A schematic of the equipment setup for the experiments for liquid injection is given in Figure 3-1:

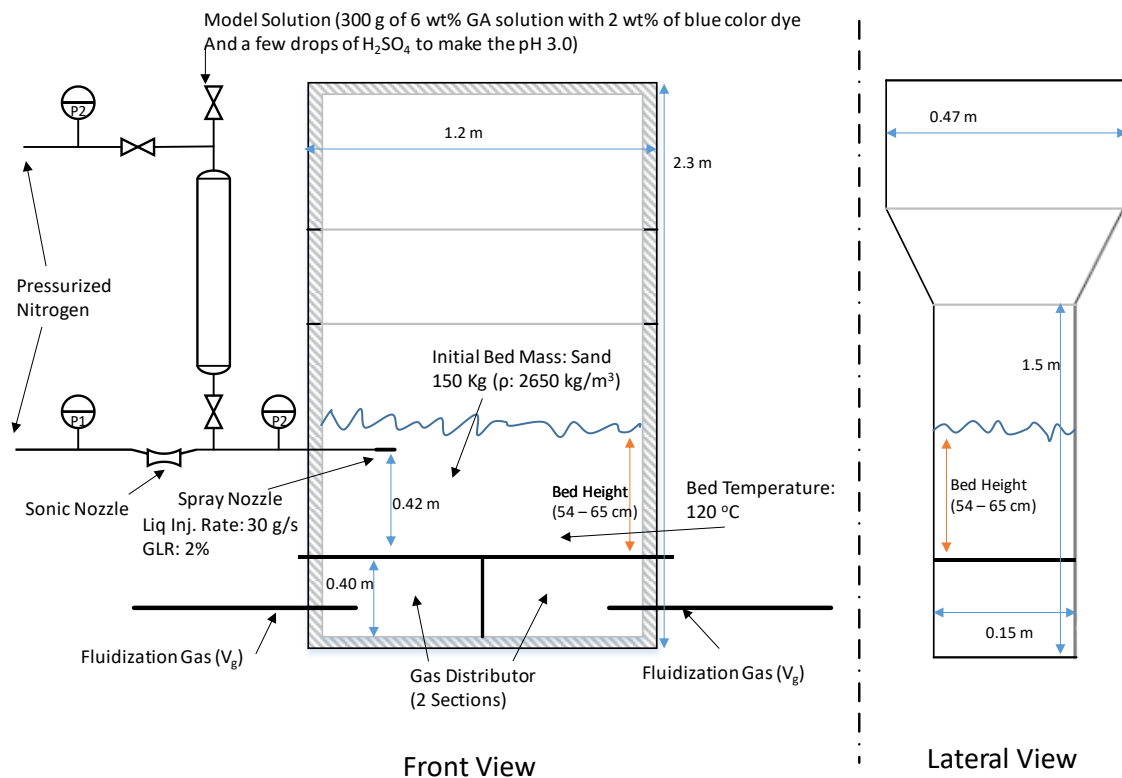


Figure 3-1: Experimental setup for runs with liquid injection

3.2.1 Data Acquisition for Triboelectric Method

Bubble flow distribution was measured in the fluidized bed by using 36 triboelectric rods arranged in 3 rows and 12 columns (Figure 2-5). The distance between the adjacent rows was 20 cm whereas the distance between the columns was 10 cm. The three rows were named Top, Middle and Bottom rows. Hence, local bubble flux was measured at 36 locations at the same time. Each rod was 5 mm in diameter and 25 cm in length. The rods were inserted half way in the bed to measure the average radial gas bubble flow through that location. Each run was conducted for 5 min. The acquired data was then processed by power spectrum using Signal Analysis software by Dr. Cedric Briens at ICFAR. The power spectrum provided the average frequency and power of the collected data, for frequencies below 25 Hz. Using the correlation and calibration method developed by Jahanmiri (2017), the local bubble flux was calculated for each rod as a function of two variables as described in Section 2.6.1. The data of local bubble flux was then combined to generate the gas bubble flow distribution in the fluidized bed.

3.3 Results and Discussion

3.3.1 Results for Vertical Distribution of Agglomerates

To check the segregation of agglomerates, two preliminary experiment were conducted at $V_g = 0.06$ m/s. For the first experiment, the bed was slumped right after liquid injection was completed i.e. at $t_f = 0$ min and for the second experiment, the bed was slumped 10 min after the injection was completed. Figure 3-2 shows how bed solids were collected in layers and sections. For selected experiments, the Top (Layer-8) and Bottom (Layer-1) layers were divided into 4 more sections.

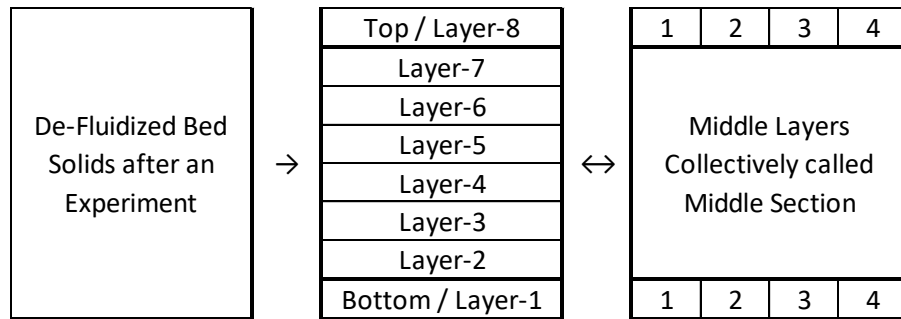


Figure 3-2: Layers and sections in which bed solids were divided

Figure 3-3 and 3-4 show some of the agglomerates that were collected while recovering the agglomerates.



Figure 3-3: Agglomerates larger than 12500 μm collected from the bottom layer at 0.06 m/s fluidization gas velocity



Figure 3-4: Agglomerates larger than 12500 μm collected from the bottom layer on a 12500 μm sieve at 0.60 m/s fluidization gas velocity

The total mass of the agglomerates in each size cut was measured for all the layers. Since the layers were collected by vacuuming the bed solids, the mass of each layer was not exactly the same. Results for each agglomerate size cut were reported as:

- Concentration of agglomerates of that size cut in the layer.

$$C_{i,j} = \frac{\text{mass of agglomerates for } i \text{ cut in } j \text{ layer (g)}}{\text{mass of bed solids in } j \text{ layer (kg)}} \quad (3.1)$$

Here, “i” is the size cut i.e. 9500 μm , 600 μm etc. and “j” defines the number of layer

- Average concentration of agglomerates of a size cut in the whole bed:

$$C_i = \frac{\sum_{j=0}^8 \text{mass of agglomerates for } i \text{ cut in the layer (g)}}{\sum_{j=0}^8 \text{mass of bed solids in the layer (kg)}} = \frac{\text{Total mass of agglomerates in the bed for a size cut}}{\text{Total mass of bed solids}} \quad (3.2)$$

- Average proportion of agglomerates of a size cut i in the layer j:

$$r = \frac{c_{i,j}}{c_i} \quad (3.3)$$

The plots generated from the above calculations for the first two runs are given in Figures 3-5 and 3-6.

Figures 3-5 and 3-6 show that, for the 0.06 m/s superficial gas velocity, the agglomerates larger than 9500 μm quickly segregated near the bottom of the fluidized bed, as there was already significant segregation of these agglomerates at $t_f = 0$ min. It was also interesting that, at $t_f = 0$ min (Figure 3-5), the proportion of mid-size agglomerates near the top of the fluidized bed was higher than the bed average. At $t_f = 10$ min (Figure 3-6), this effect had dissipated and the mid-size agglomerates (smaller than 9500 μm) had become fairly well distributed throughout the bed, with some accumulation in the bottom layer.

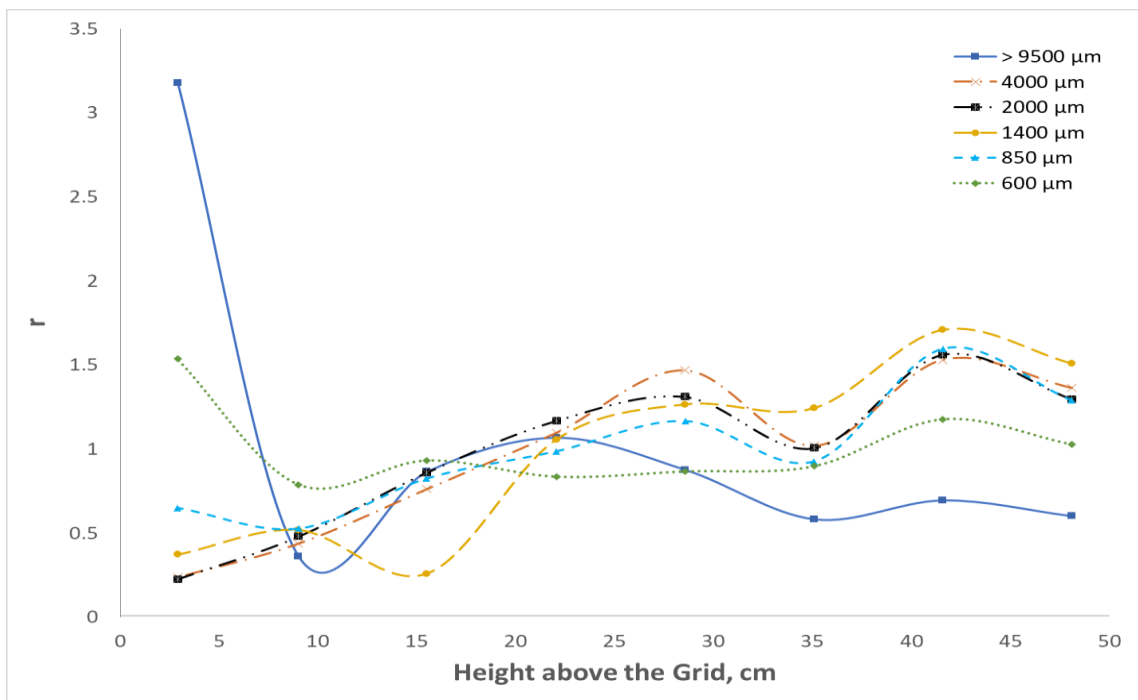


Figure 3-5: Proportion of agglomerates in each layer at $V_g = 0.06$ m/s at $t_f = 0$ min

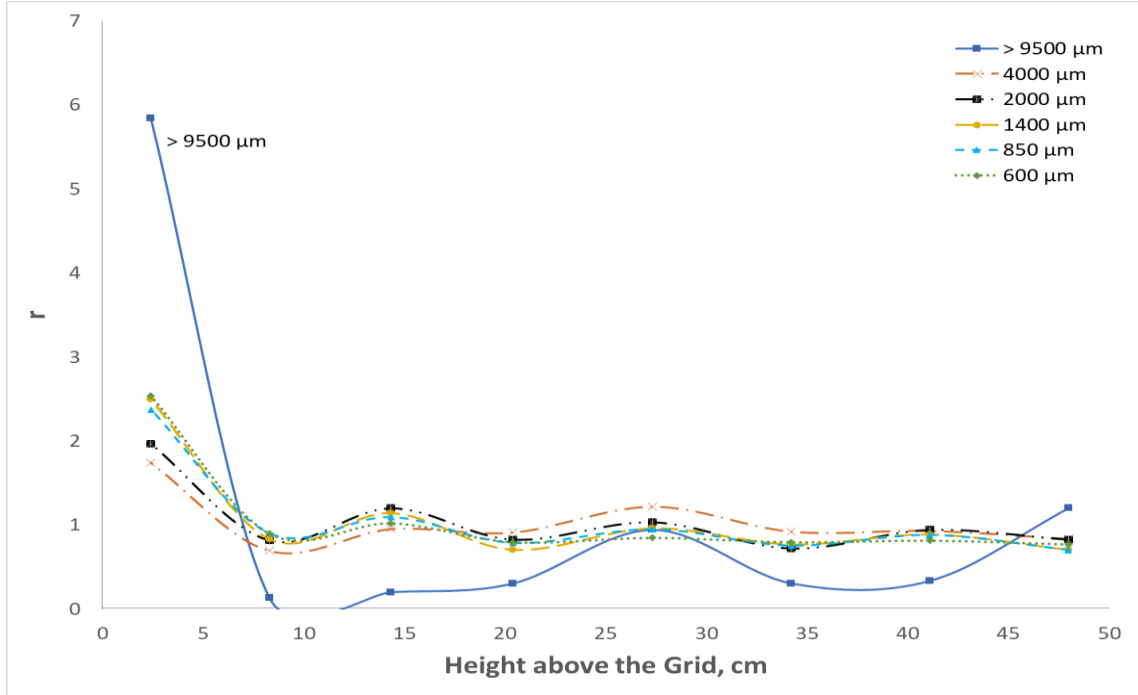


Figure 3-6: Proportion of agglomerates in each layer at $V_g = 0.06$ m/s at $t_r = 10$ min

Since the results indicated that most of the segregation occurred in the bottom and top layers, the results were summarized with two new dimensionless Indices of Segregation:

- Index of Segregation for Bottom Layer (IS_B): Ratio of concentration of agglomerates in the bottom later to the average concentration of the agglomerates in middle layers.

$$IS_B = \frac{\text{Concentration of agglomerates of a size cut in Bottom layer}}{\text{Average concentration of agglomerates of the same size cut in layer 2 to layer 7}} \quad (3.4)$$

- Index of Segregation for Top Layer (IS_T): Ratio of concentration of agglomerates in the top later to the average concentration of the agglomerates in middle layers.

$$IS_T = \frac{\text{Concentration of agglomerates of a size cut in Top layer}}{\text{Average concentration of agglomerates of the same size cut in layer 2 to layer 7}} \quad (3.5)$$

This simplified the representation of the data and made it easy to interpret the results as shown in Figure 3-7.

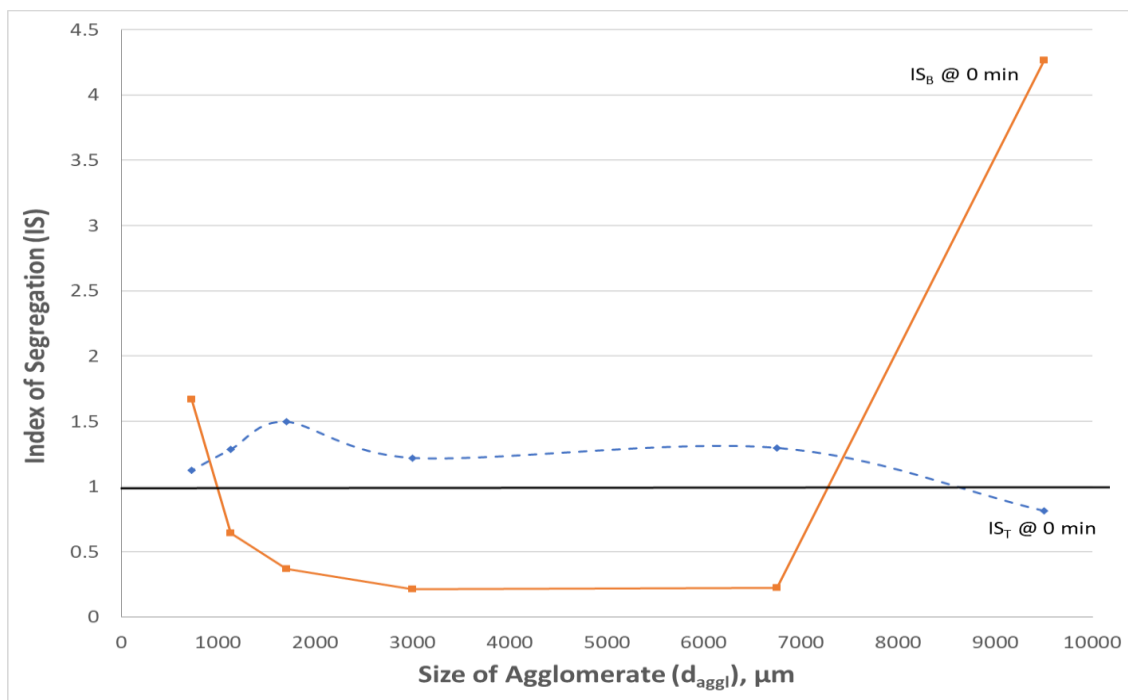


Figure 3-7: Index of Segregation for Bottom and Top layers when the bed was slumped at $t_f = 0$ min at 0.06 m/s gas velocity

A value higher than 1 identifies a higher proportion in the layer than in the middle section of the bed, indicating segregation in that layer. A higher value of the index signifies a more pronounced segregation. A value of 1 or smaller means no segregation.

Figure 3-7 shows that agglomerates larger than 9500 μm segregated significantly in the bottom layer when the bed is slumped right after liquid injection was completed at $V_g = 0.06$ m/s. Figure 3-7 also shows that slightly more mid-sized agglomerates were found in the top layer as compared to the middle layers.

Figures 3-8 to 3-15 report the indices of segregation at two different velocities and different fluidization times (t_f) after the liquid injection was finished. The time mentioned on all the graphs in this chapter represent the time duration for which bed was kept fluidized (t_f) after liquid injection was completed. The fluidized bed was slumped after the end of that time. For example, 10 min means the bed was kept fluidized for $t_f = 10$ min after the liquid injection and then slumped (de-fluidized).

Figure 3-8 shows the index of segregation for the bottom layer at the 0.06 m/s gas velocity. It clearly shows that at low velocity the agglomerates larger than 9500 μm segregated significantly. For runs with 2, 4 and 7 min of fluidization time, two more size cuts were used to increase the resolution of agglomerates distribution to check whether agglomerates larger than 9500 μm and smaller than 12500 μm segregate as well. Figure 3-8 shows that the agglomerates $12500 \mu\text{m} > d_{\text{aggl}} \geq 9500 \mu\text{m}$ segregated as well.

Interestingly, Figure 3-9 shows that, at the 0.06 m/s gas velocity, for fluidization times greater than 2 minutes, the proportion of agglomerates larger than 9500 μm in the top layer was slightly higher than their proportion in the middle layers. On the other hand, the proportion of mid-size agglomerates (i.e. smaller than 9500 μm) was smaller than their bed average (Figure 3-9) because of their moderate segregation in the bottom layer (Figure 3-8).

Plotting the indices of segregation for the bottom layer against fluidization time at 0.06 m/s in Figure 3-10, it shows that the segregation of agglomerates larger than 3000 μm gradually increased with the fluidization time. Figure 3-11 shows that, for the same gas velocity, segregation in the top layer quickly stabilized, which suggests that different physical phenomena drive the segregations in the top and bottom layers.

Micro-agglomerates ($d_{\text{aggl.}} \leq 600 \mu\text{m}$) were not considered for analysis as small agglomerates do not segregate based on preliminary tests.

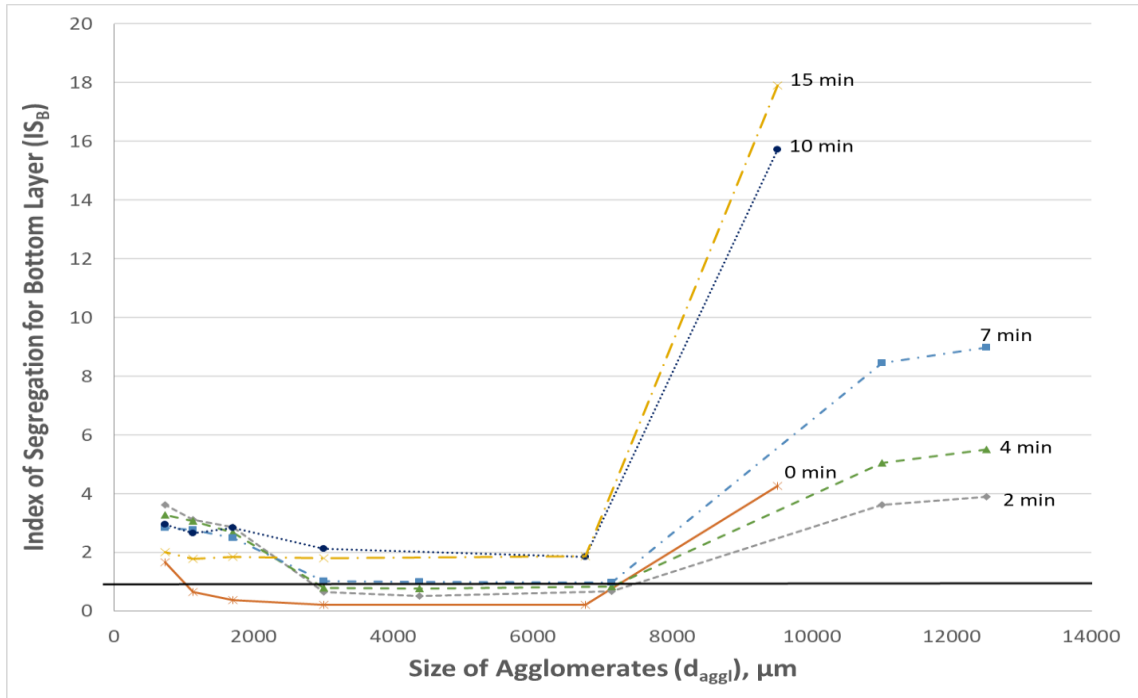


Figure 3-8: Index of Segregation for Bottom layer vs. size of agglomerates at 0.06 m/s fluidization gas velocity

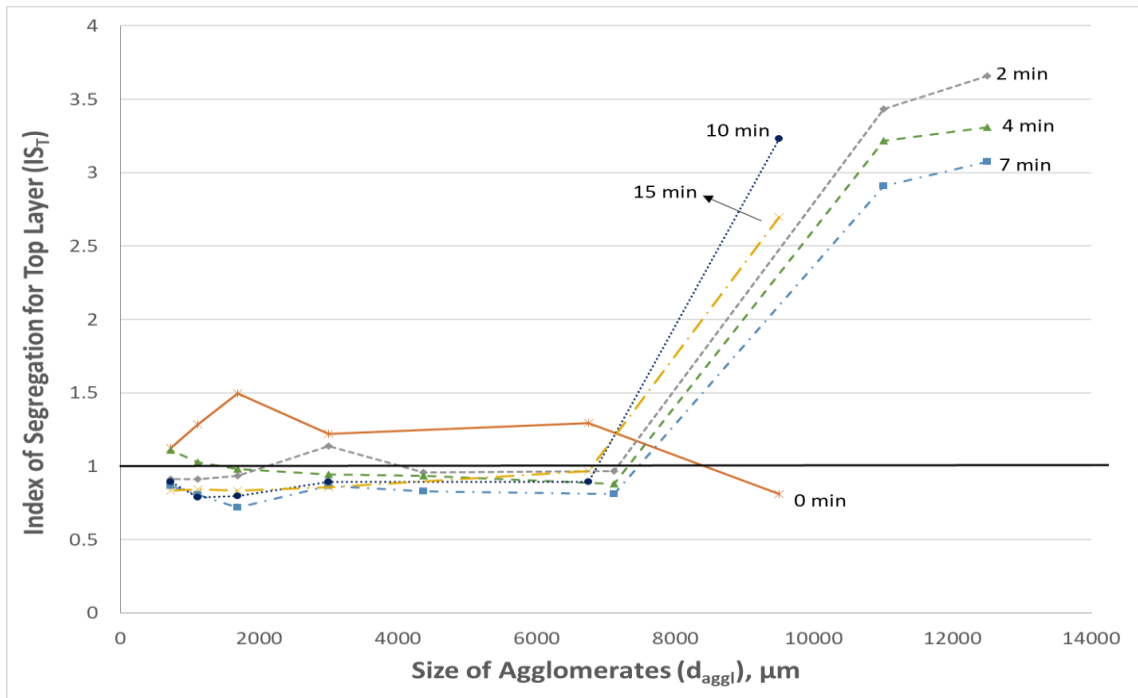


Figure 3-9: Index of Segregation for Top layer vs. size of agglomerates at 0.06 m/s fluidization gas velocity

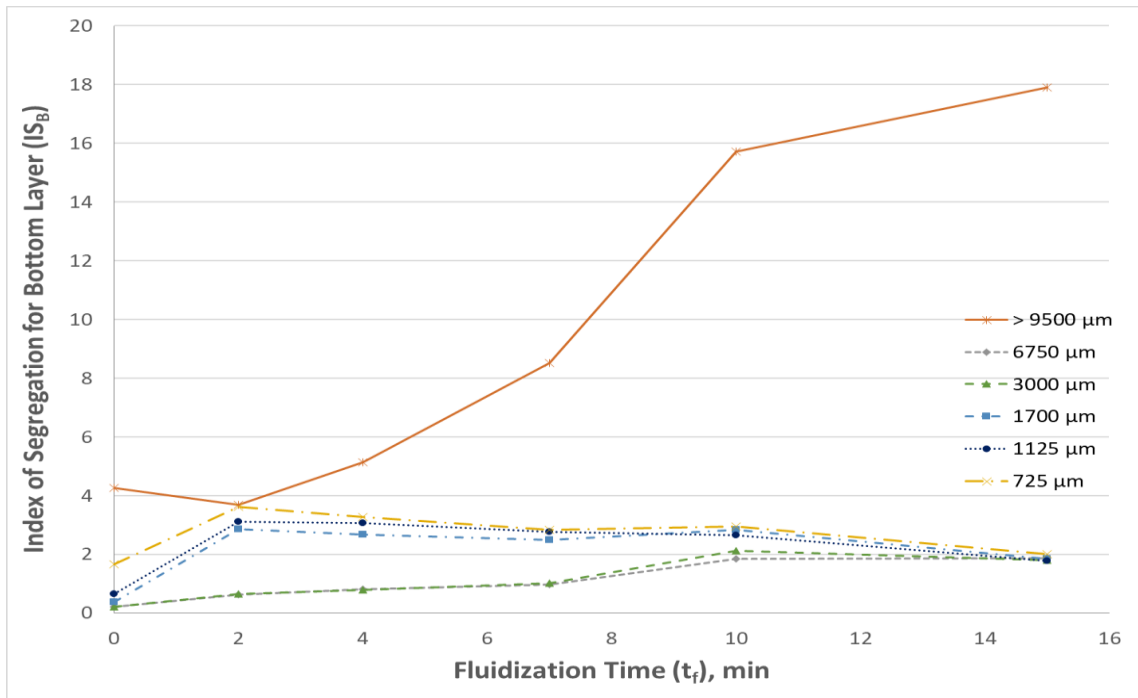


Figure 3-10: Index of Segregation for Bottom layer vs. fluidization time at 0.06 m/s fluidization gas velocity

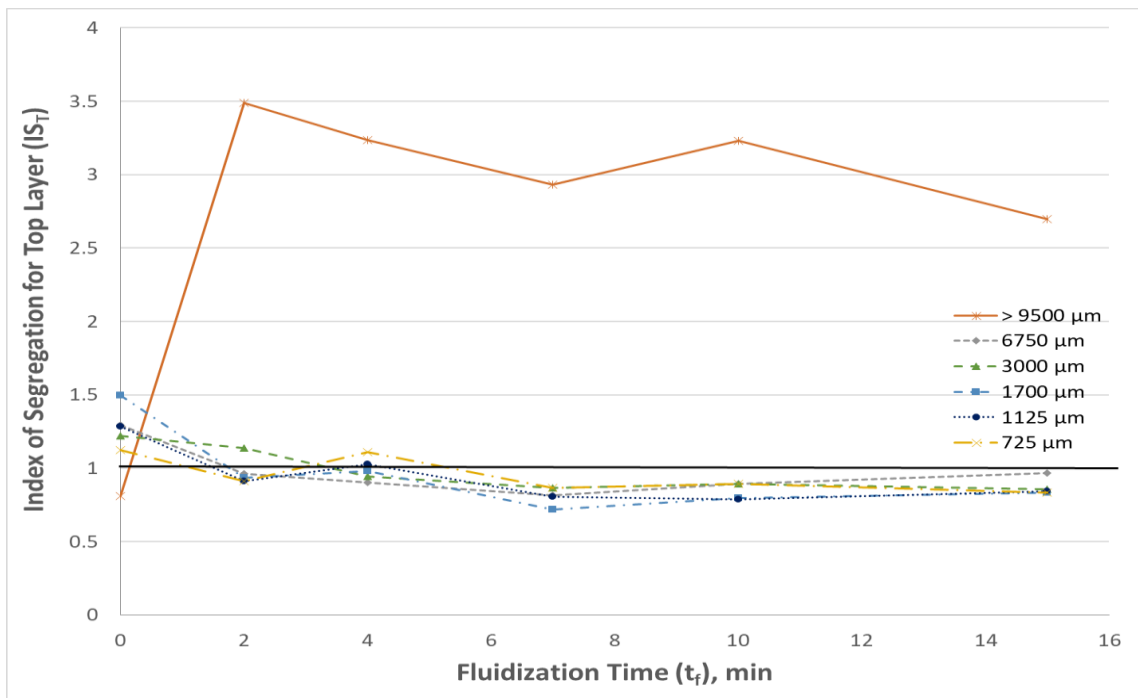


Figure 3-11: Index of Segregation for Top layer vs. fluidization time at 0.06 m/s fluidization gas velocity

Figure 3-12 shows the index of segregation for the bottom layer at the 0.60 m/s gas velocity. It shows that at high velocity the agglomerates larger than 9500 μm segregated but not as significantly as they segregated at the lower velocity of 0.06 m/s. There was no significant segregation for other agglomerates.

Figure 3-13 shows that the proportion of agglomerates larger than 9500 μm was lower in the top layer than in the rest of the bed. However, the proportion of mid-size agglomerates (i.e. smaller than 3000 μm) was slightly higher in the top layer than in the rest of the bed.

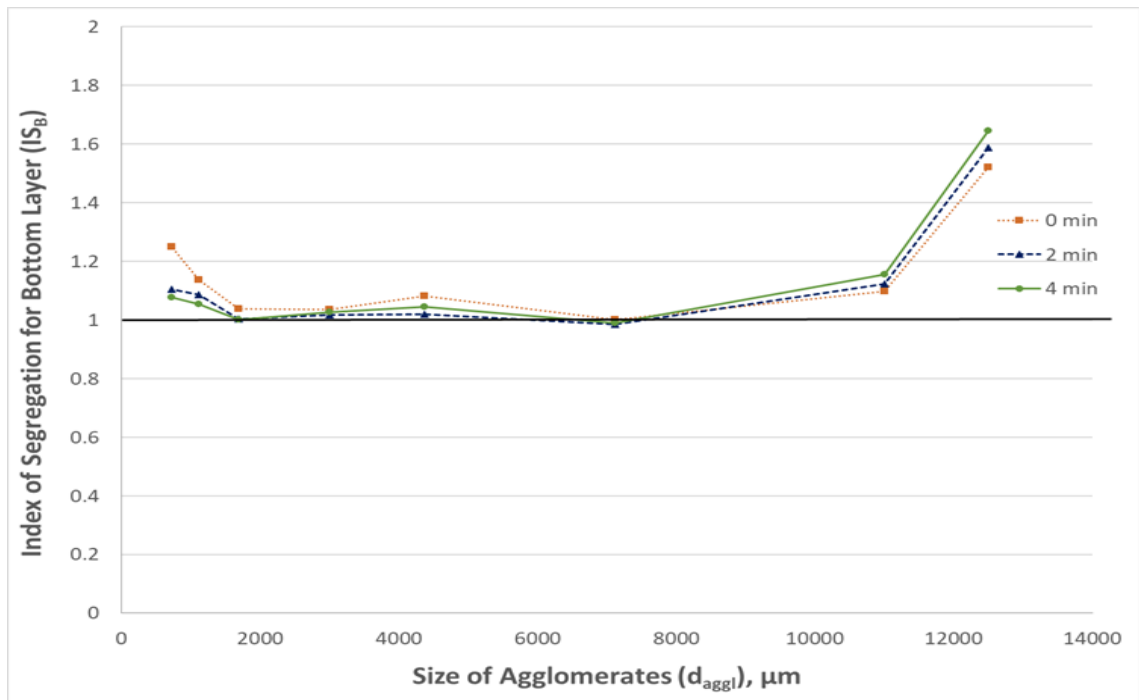


Figure 3-12: Index of Segregation for Bottom layer vs. size of agglomerates at 0.60 m/s fluidization gas velocity

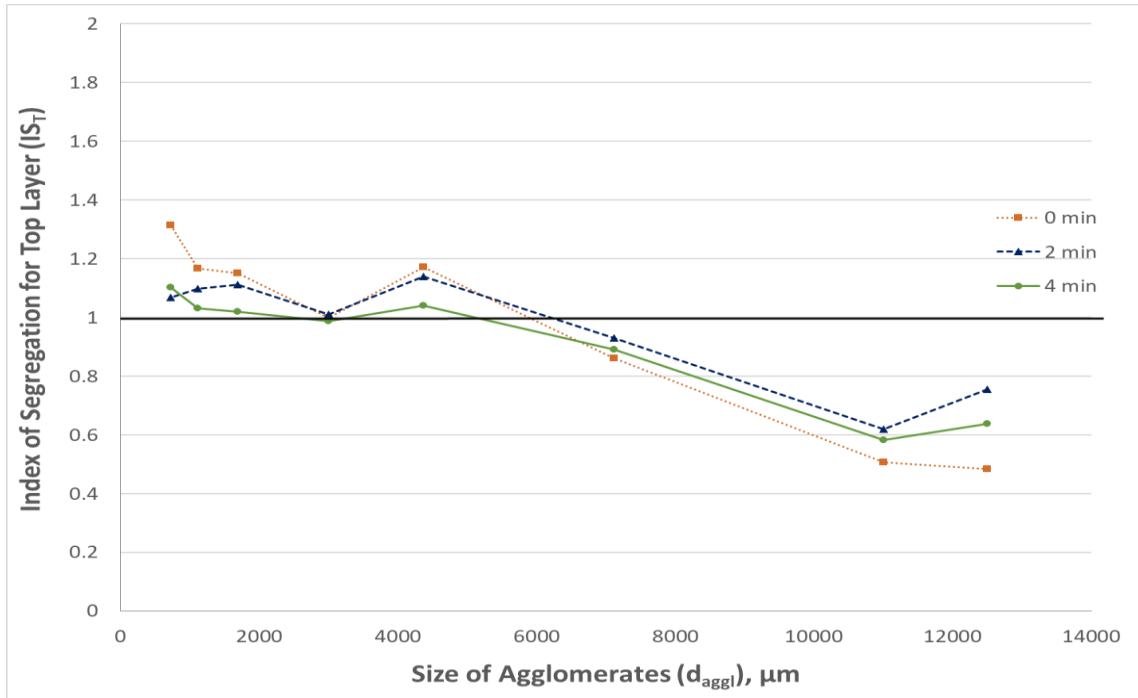


Figure 3-13: Index of Segregation for Top layer vs. size of agglomerates at 0.60 m/s fluidization gas velocity

3.3.2 Results for Lateral Distribution of Agglomerates

The top and bottom layers were further divided in four lateral sections, for selected experiments at 2 gas velocities, as shown in Figure 3-2.

To measure the distribution of agglomerates in a layer, a new dimensionless ratio term ‘ α ’ was introduced. α is defined as the ratio of concentration of agglomerates of a size cut in a section to the average concentration of agglomerates of that size cut in the layer.

$$\alpha_{i,k} = \frac{\text{Concentration of agglomerates of size cut } i \text{ in } k \text{ section}}{\text{Average concentration of agglomerates of size cut } i \text{ in the layer}} \quad (3.6)$$

The ratio ‘ α ’ for each section was plotted together against the horizontal distance (X) from a reference wall (side of the bed/wall with injection nozzle) to generate the lateral distribution of agglomerates. The results were plotted in the graphs shown in Figure 3-14 to Figure 3-23.

The agglomerates were distributed poorly at low velocity but there was no trend in lateral distribution as shown in Figure 3-14 to Figure 3-19. Except for large agglomerates in the bottom layer for fluidization times of 4 min and 7 min. Higher concentrations of large agglomerates were found in the right half of the bed as compared to the left. This might be a result of poor gas bubbles distribution in the bed at low velocity. Very large agglomerates did not move around much once they were settled in the bottom. Gas bubble flow distribution was analyzed using the triboelectric method for further investigation. The results for gas flow distribution are presented in Section 3.4.4.

However, the results for lateral distribution of agglomerates at 0.60 m/s, show that agglomerates were well distributed laterally at high velocity. Graphs in Figures 3-20 to 3-23 show that the concentration of agglomerates for all size cuts was uniform laterally as the values of ' α ' are close to 1 for all size cuts.

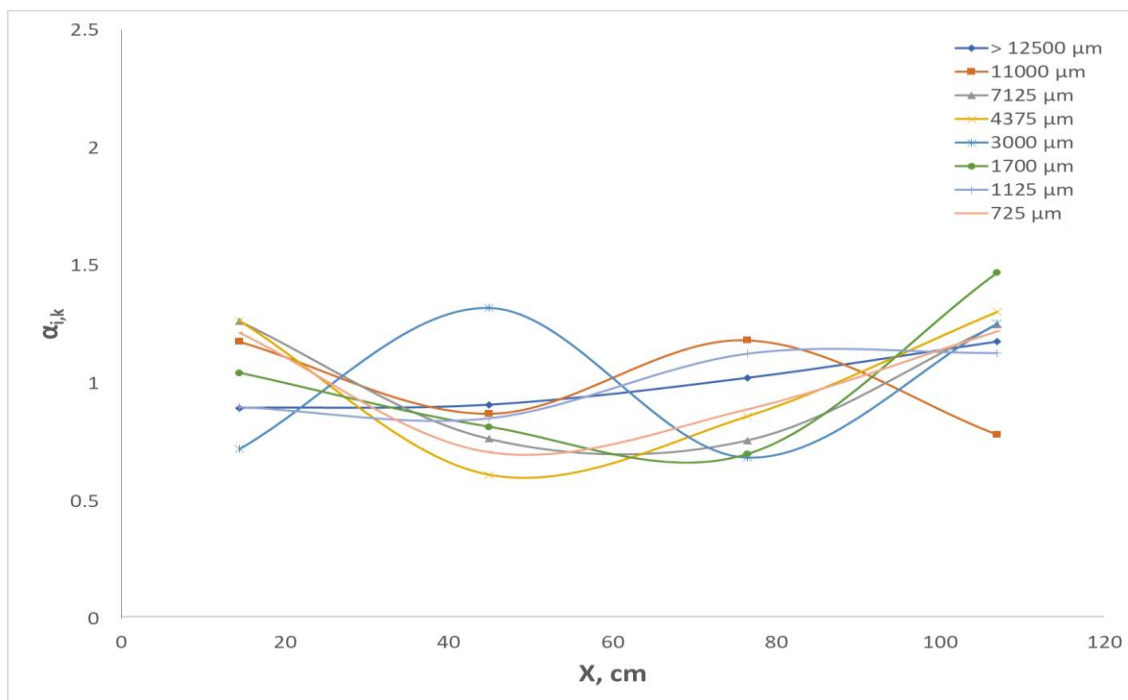


Figure 3-14: Lateral distribution of agglomerates for Bottom layer at 0.06 m/s and for a fluidization time of 2 min

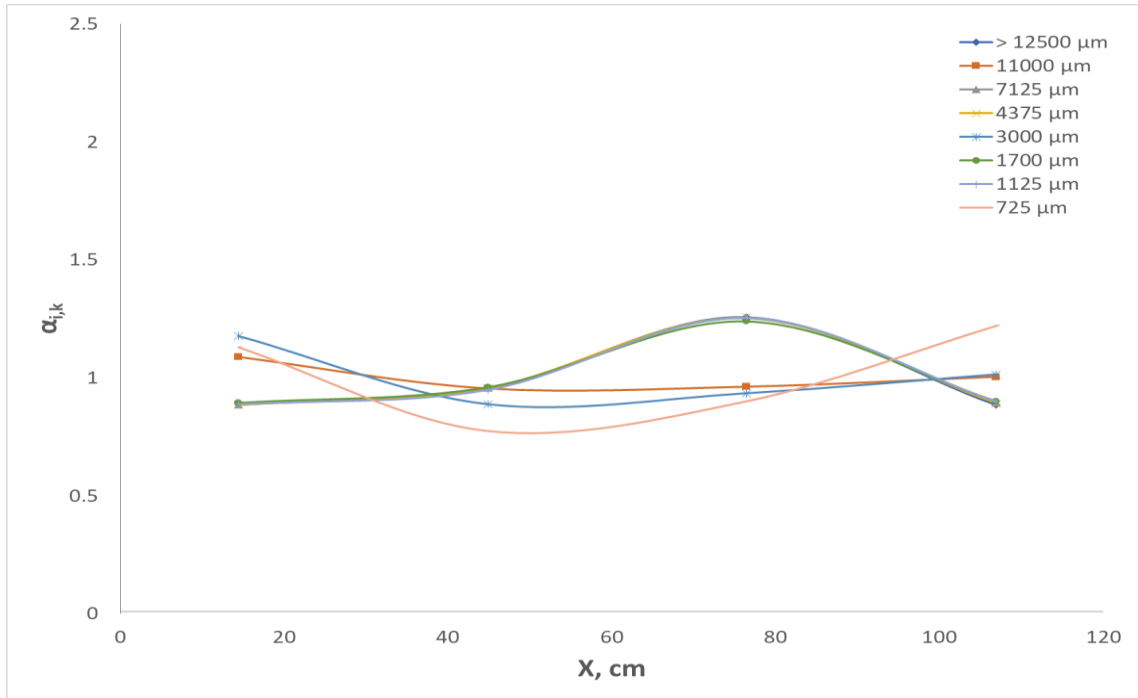


Figure 3-15: Lateral distribution of agglomerates for Top layer at 0.06 m/s and for a fluidization time of 2 min

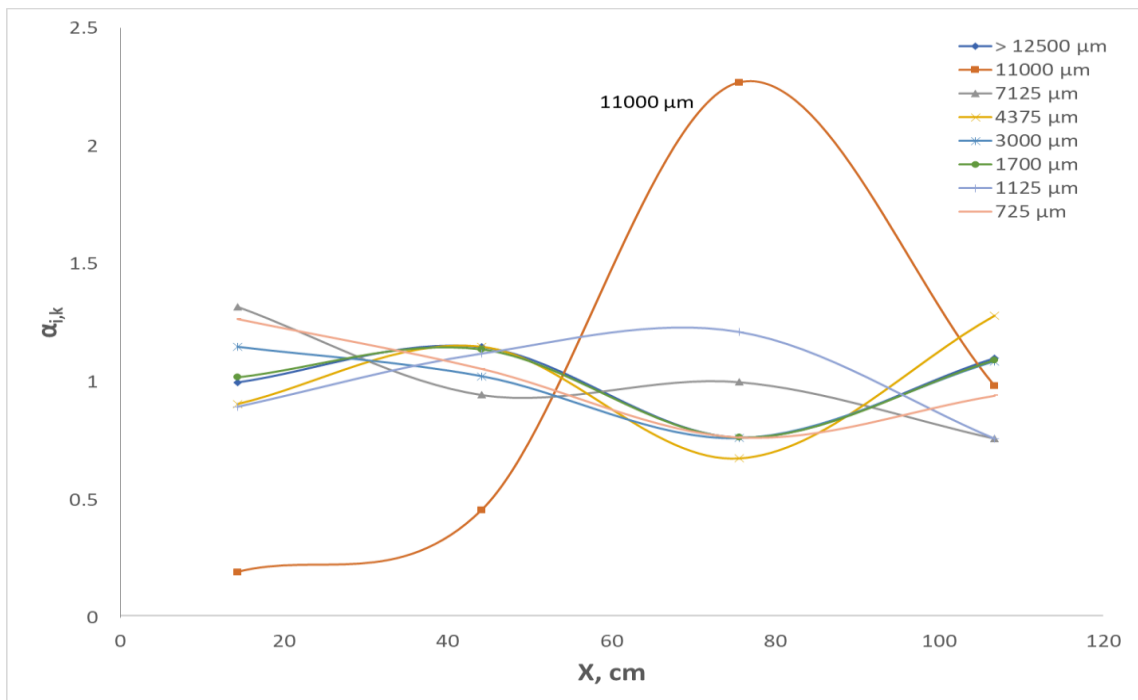


Figure 3-16: Lateral distribution of agglomerates for Bottom layer at 0.06 m/s and for a fluidization time of 4 min

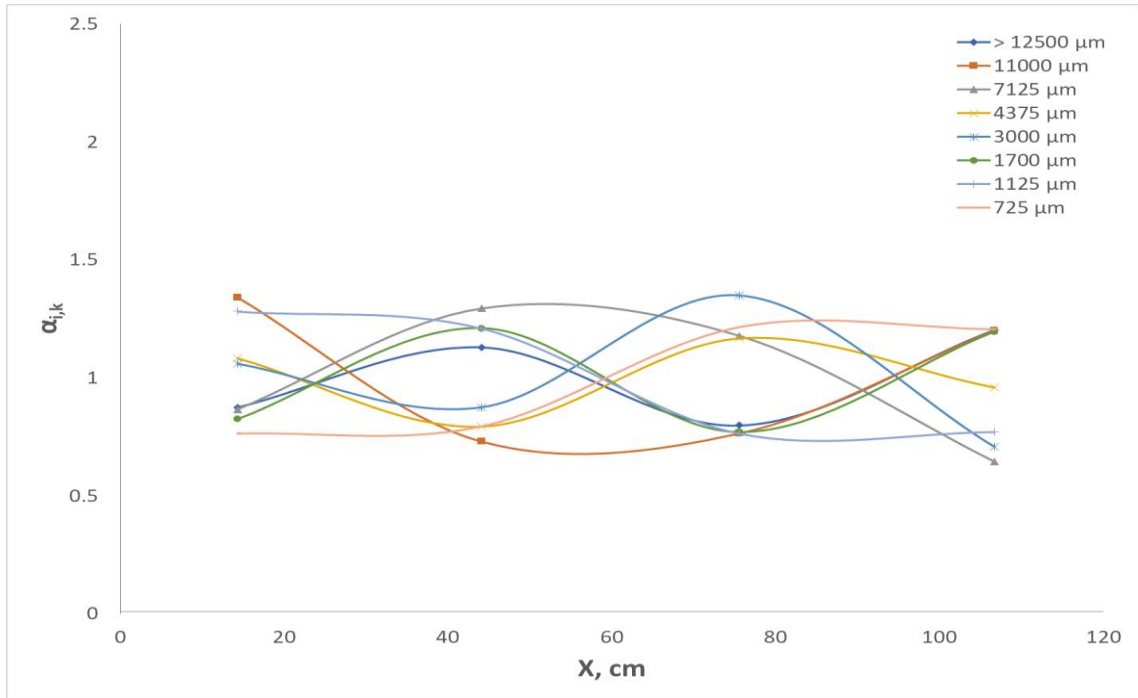


Figure 3-17: Lateral distribution of agglomerates for Top layer at 0.06 m/s and for a fluidization time of 4 min

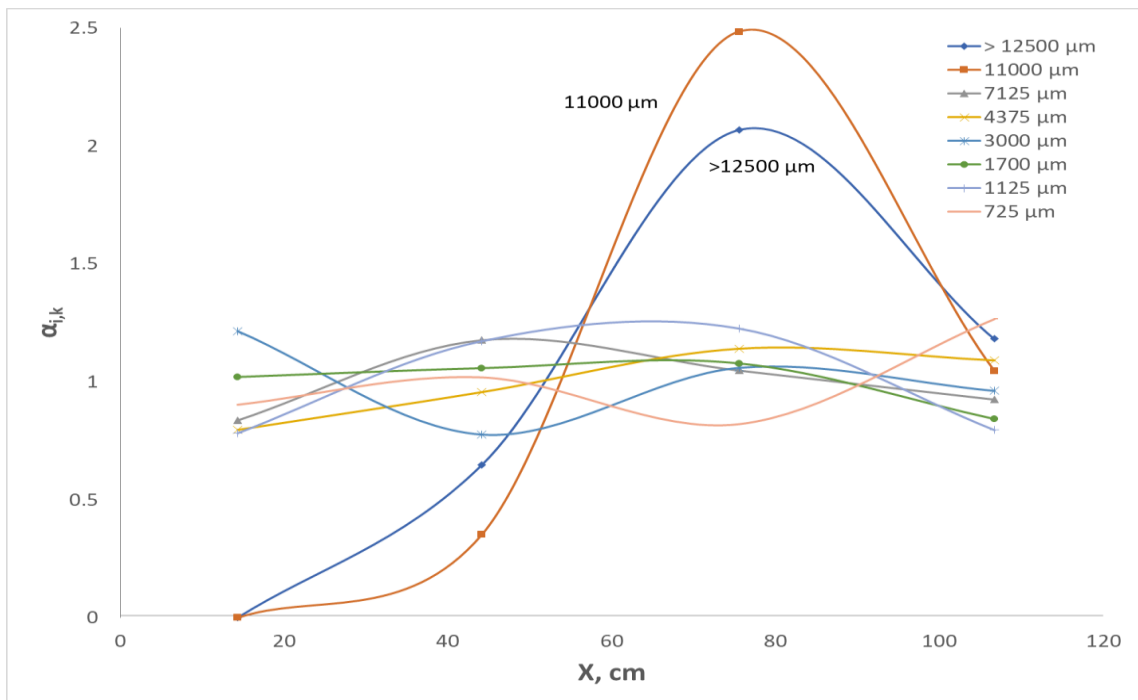


Figure 3-18: Lateral distribution of agglomerates for Bottom layer at 0.06 m/s and for a fluidization time of 7 min

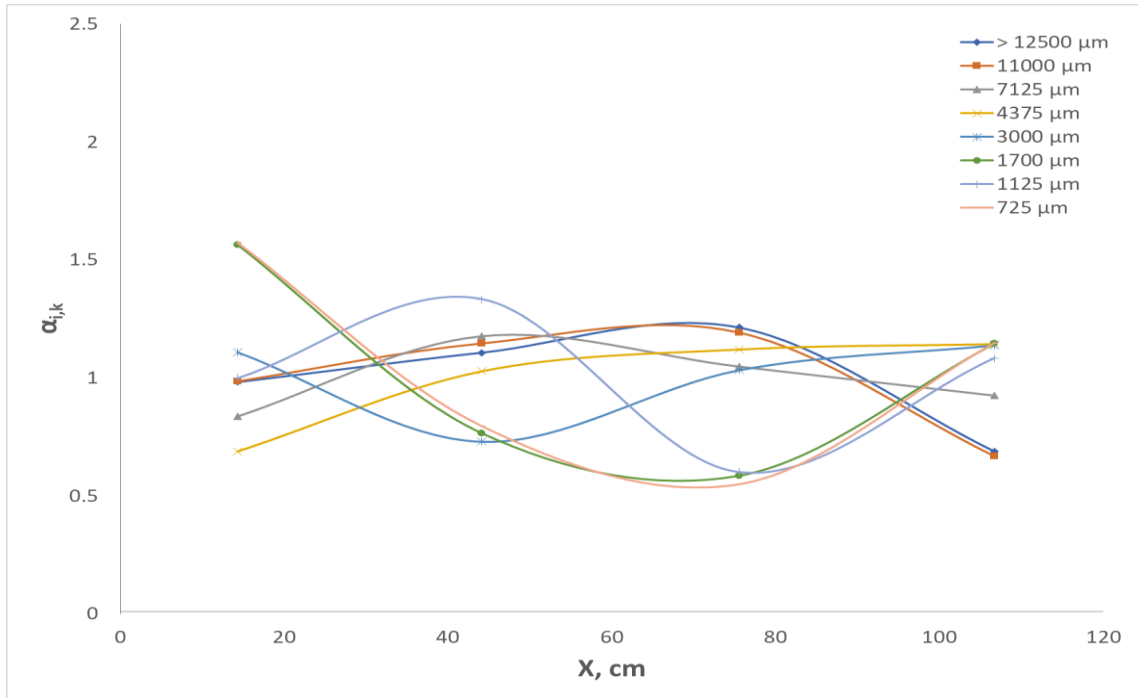


Figure 3-19: Lateral distribution of agglomerates for Top layer at 0.06 m/s and for a fluidization time of 7 min

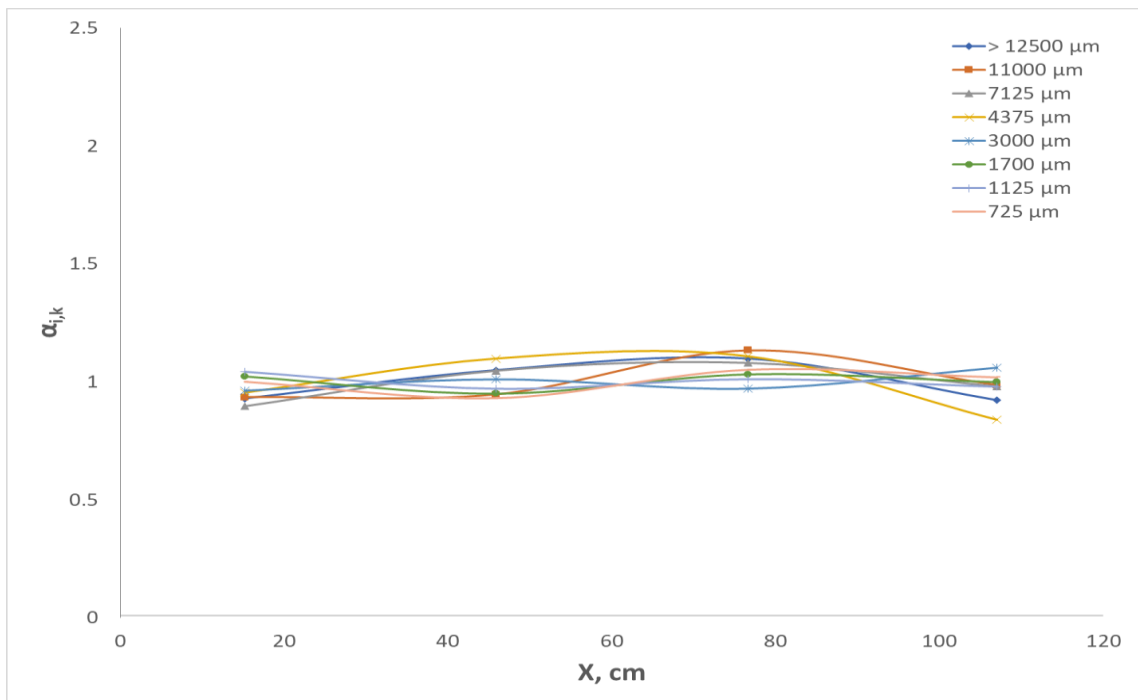


Figure 3-20: Lateral distribution of agglomerates for Bottom layer at 0.60 m/s and for a fluidization time of 0 min

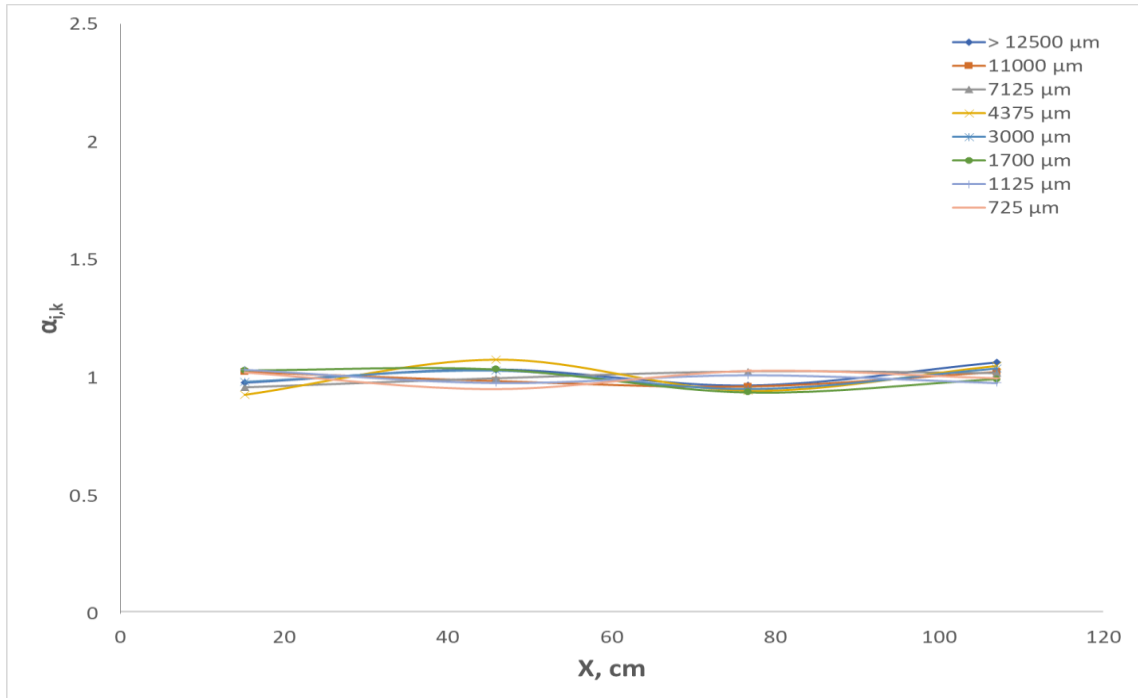


Figure 3-21: Lateral distribution of agglomerates for Top layer at 0.60 m/s and for a fluidization time of 0 min

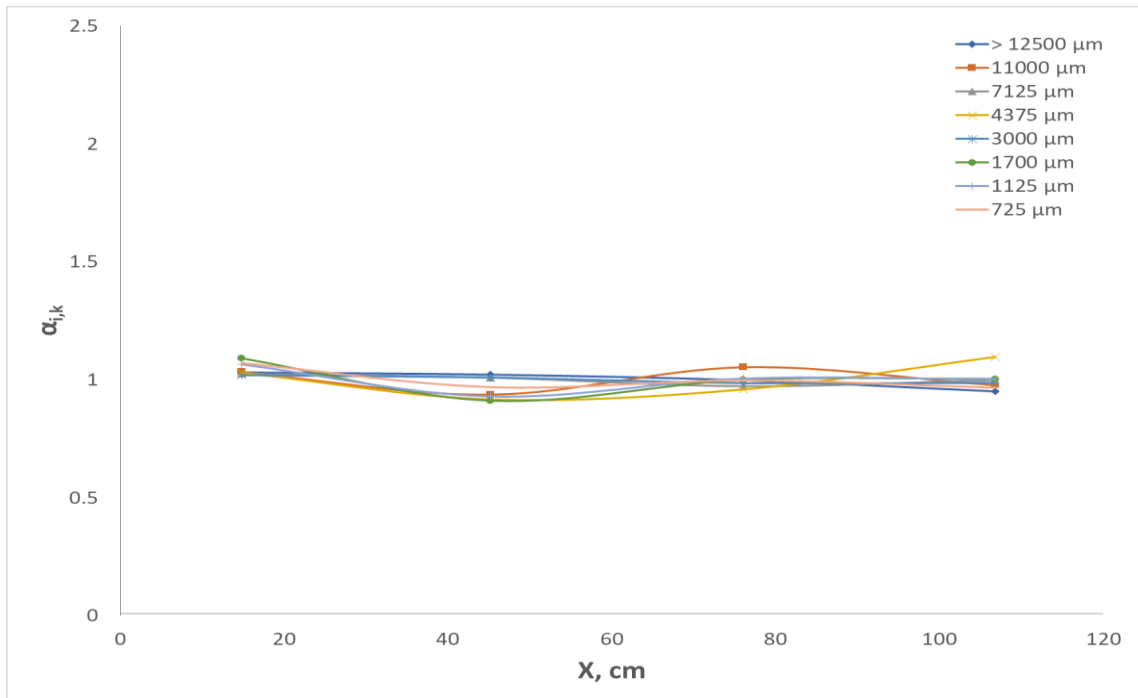


Figure 3-22: Lateral distribution of agglomerates for Bottom layer at 0.60 m/s and for a fluidization time of 4 min

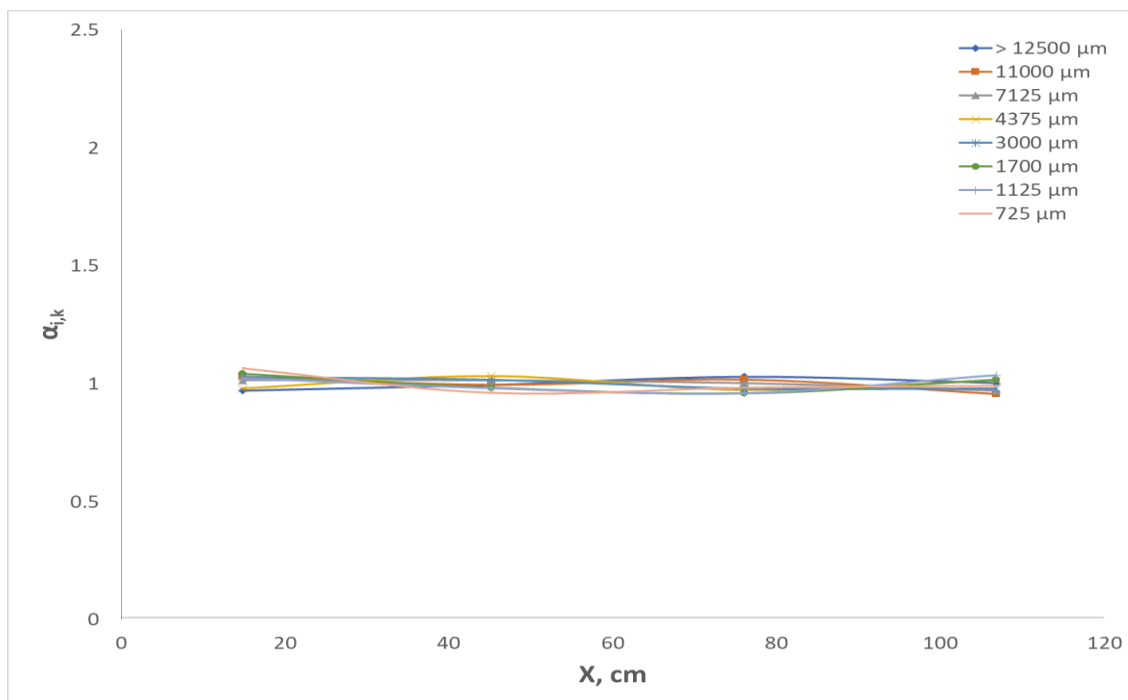


Figure 3-23: Lateral distribution of agglomerates for Top layer at 0.60 m/s and for a fluidization time of 4 min

3.3.3 Density of Agglomerates

Knowing the density of the agglomerate was required to manufacture the model tracer agglomerate for the Radioactive Particle Tracking experiments. The agglomerates generated by liquid injection were porous and the agglomerate pores needed to be sealed before the density could be measured by liquid pycnometry. Agglomerates were coated with epoxy resin to seal their pores.

The density of the sealed agglomerates was measured by pycnometry with vegetable oil, as water would have dissolved the gum Arabic. Since only large agglomerates were relevant for further study, the density was only measured for agglomerates larger than 9500 μm .

The density of all the measured agglomerates was within the range of 1350 kg/m^3 to 1450 kg/m^3 .

3.3.4 Gas Bubble Flow Distribution using Tribo-Electric Method

The gas bubbles distribution was analyzed at different gas velocities to determine if there was any impact of bubble flow distribution on agglomerates distribution in the bed. Jahanmiri (2017) developed a reliable triboelectric method to measure the gas bubbles distribution in a fluidized bed (Section 1.6 and 2.6).

An array of 36 rods arranged in 3 rows and 12 columns was used to determine the local bubble flux at 36 locations (Figure 2-5). The triboelectric current was measured in the form of the voltage output from the amplifier every millisecond (sampling time, $t_s = 1$ ms) for 300 seconds. The data was analyzed with the Fast Fourier Transform to calculate its power spectrum and determine the average power and frequency of the data. The average and frequency were used to calculate the local bubble flux for each location using the correlation developed by Jahanmiri (2017) given in Equation (3.7). The values of a , b and c were determined using excel solver to minimize the error square between the experimental values and measured values as explained by Jahanmiri (2017). To determine the gas bubbles distribution for each location, the ratio of local bubble flux (q_{bi}) to the cross-sectional average bubble flux (q) at the same height was calculated. This ratio was plotted against the distance from the wall (X) to generate the distribution of the gas bubbles in the bed.

$$q_{bi} = a \cdot P_i^b \cdot f_i^c \quad (3.7)$$

Figures 3-24 to 3-30 show the gas bubbles distribution for 3 heights above the distributor grid at different gas velocities. Figure 3-24 shows that the gas bubbles distribution at 0.06 m/s was very poor, especially for the bottom location. Most of the gas passed through the mid-section of the bed with much less flow through the sides. This explains the high proportion of large agglomerates in the right half of the bottom layer of the bed (Figure 3-8, 3-19 and 3-18). It might be possible that the bed was not fully fluidized at 0.06 m/s as bubbles distribution shows low bubble fraction in the right side of the bed. More than one third of the spray jet was in right section, therefore, it is possible that agglomerates were pushed to the other side of the bed. The spray nozzle penetration was 30 cm and jet penetration was 47 cm.

As the gas velocity was increased, the gas bubbles distribution became less erratic as shown in Figures 3-25 to Figure 3-30. Gas bubbles distribution for higher velocities (0.35 m/s, 0.50 m/s and 0.60 m/s) was not uniform, however, the ratio of gas bubbles in the right half to the gas bubbles in the left half is close to 1 which means the gas flow in two halves of the bed was similar. The gas bubbles distribution in the bed is similar for 0.35 m/s, 0.50 m/s and 0.60 m/s. In each case, there is a dip in bubble flux in the top row near 110 cm which is due to the presence of the cyclone dipleg in that area (Figure 2-1). Table 3-1 shows the ratio of distributor pressure drop (ΔP_{grid}) to the bed pressure drop (ΔP_{bed}) for each velocity. The value of the ratio of grid to bed pressure drop should be higher than 0.10 for good fluidization. However, for 0.06 m/s and 0.10 m/s, the grid to bed pressure drop is below the recommended value.

V_g	0.06 m/s	0.10 m/s	0.35 m/s	0.50 m/s	0.60 m/s
$\Delta P_{\text{grid}} / \Delta P_{\text{bed}}$	0.082	0.105	0.298	0.365	0.429

Table 3-1: Ratio of gas distributor pressure drop to the bed pressure drop

Figure 3-31 to Figure 3-33 compare the gas bubbles distribution for each row for different gas velocities. These figures show that at 0.06 m/s and 0.10 m/s, gas bubbles are poorly distributed in each row as compared to higher gas velocities which might be a result of low grid to bed pressure drop at low velocities as shown in Table 3-1. This explains the poor vertical distribution of agglomerates in the bed at 0.06 m/s (Figure 3-5).

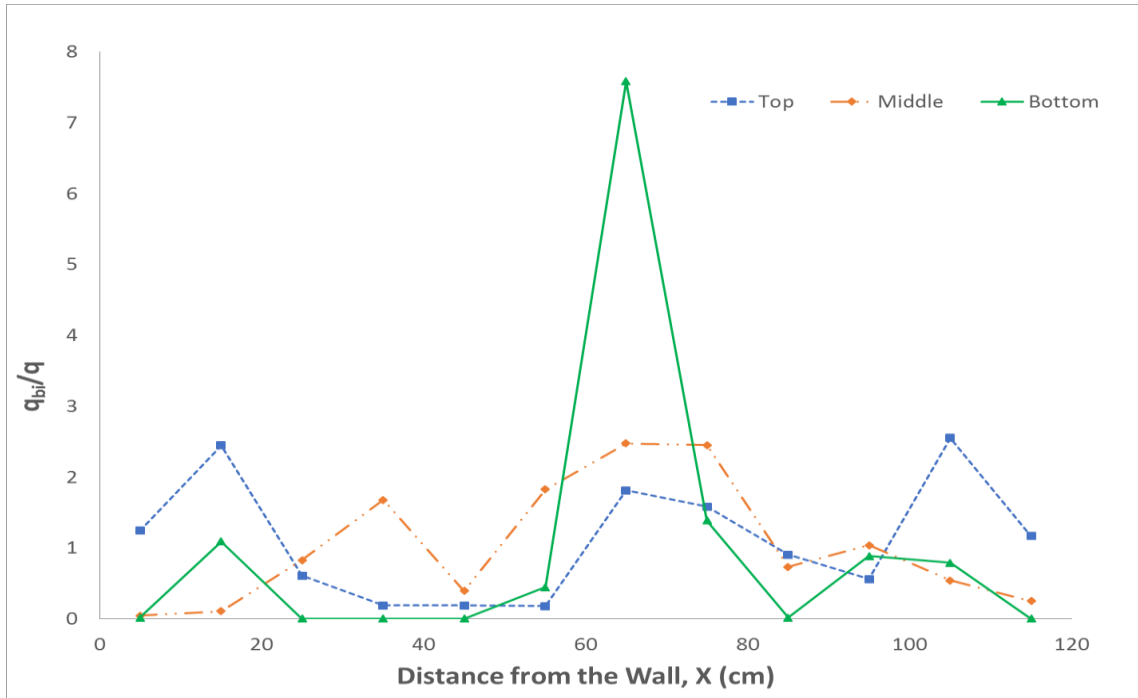


Figure 3-24: Gas bubble profile for $V_g = 0.06$ m/s (Bottom: $h = 12$ cm; Middle: $h = 32$ cm; Top: $h = 52$ cm)

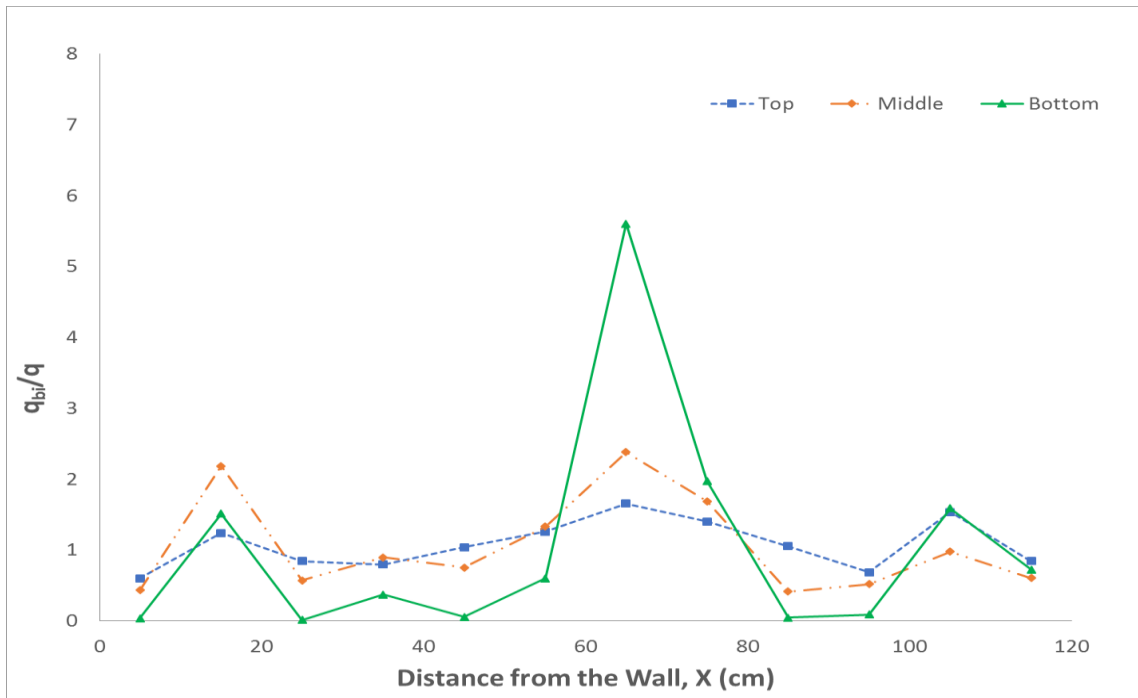


Figure 3-25: Gas bubble profile for $V_g = 0.10$ m/s (Bottom: $h = 12$ cm; Middle: $h = 32$ cm; Top: $h = 52$ cm)

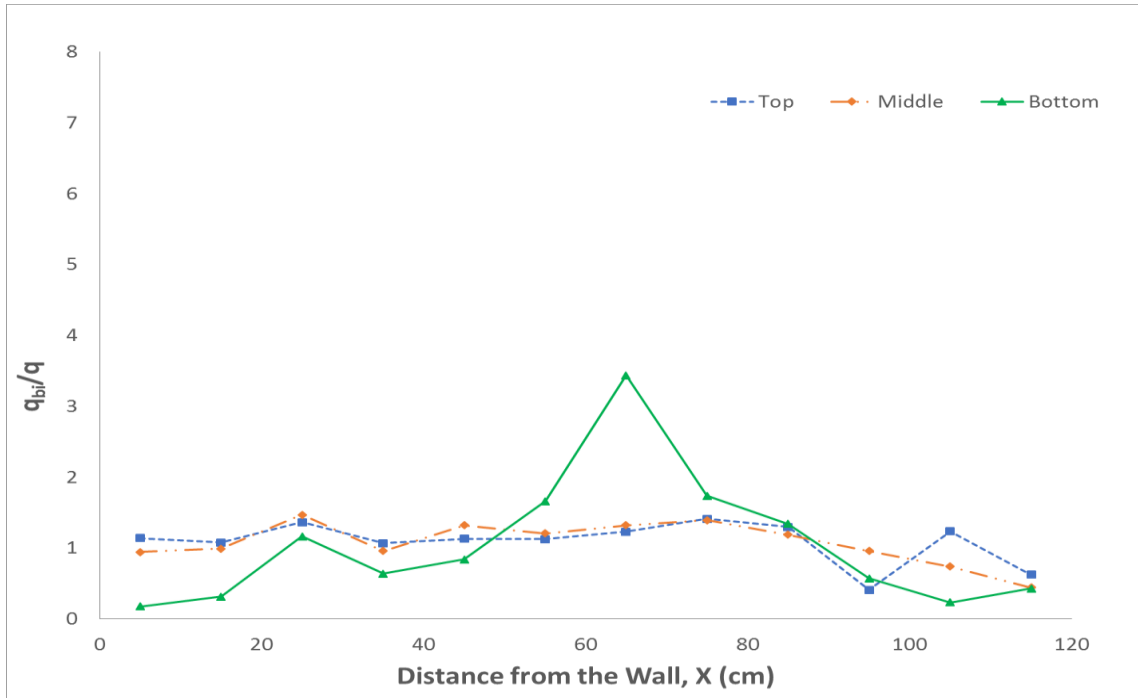


Figure 3-26: Gas bubble profile for $V_g = 0.20$ m/s (Bottom: $h = 12$ cm; Middle: $h = 32$ cm; Top: $h = 52$ cm)

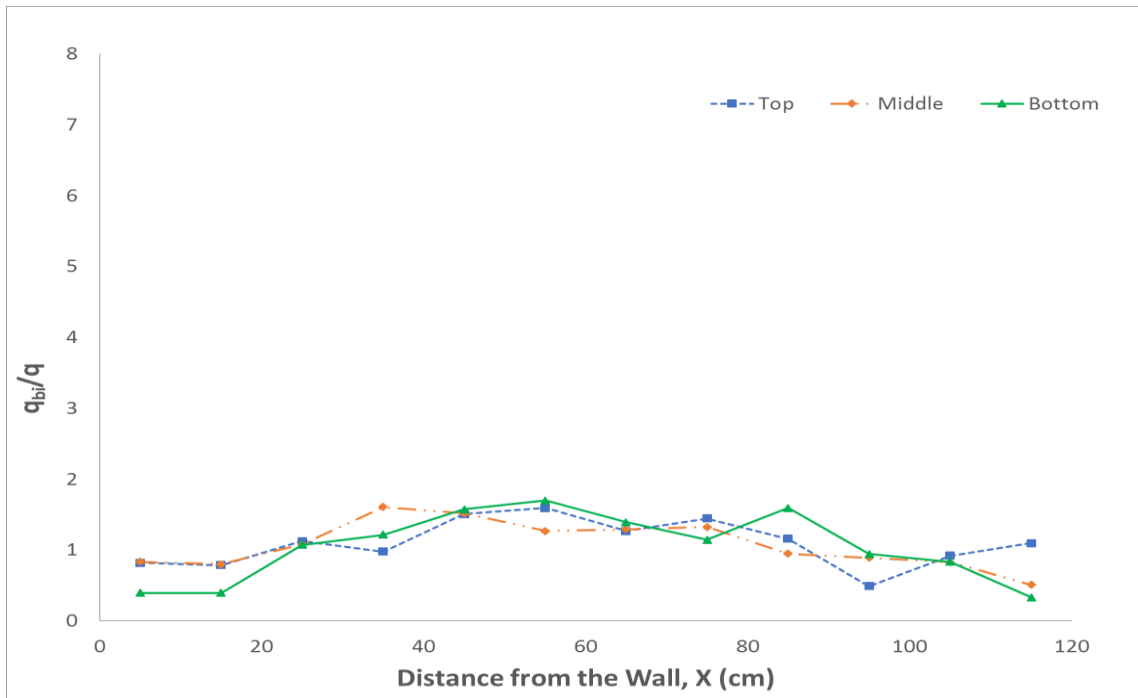


Figure 3-27: Gas bubble profile for $V_g = 0.35$ m/s (Bottom: $h = 12$ cm; Middle: $h = 32$ cm; Top: $h = 52$ cm)

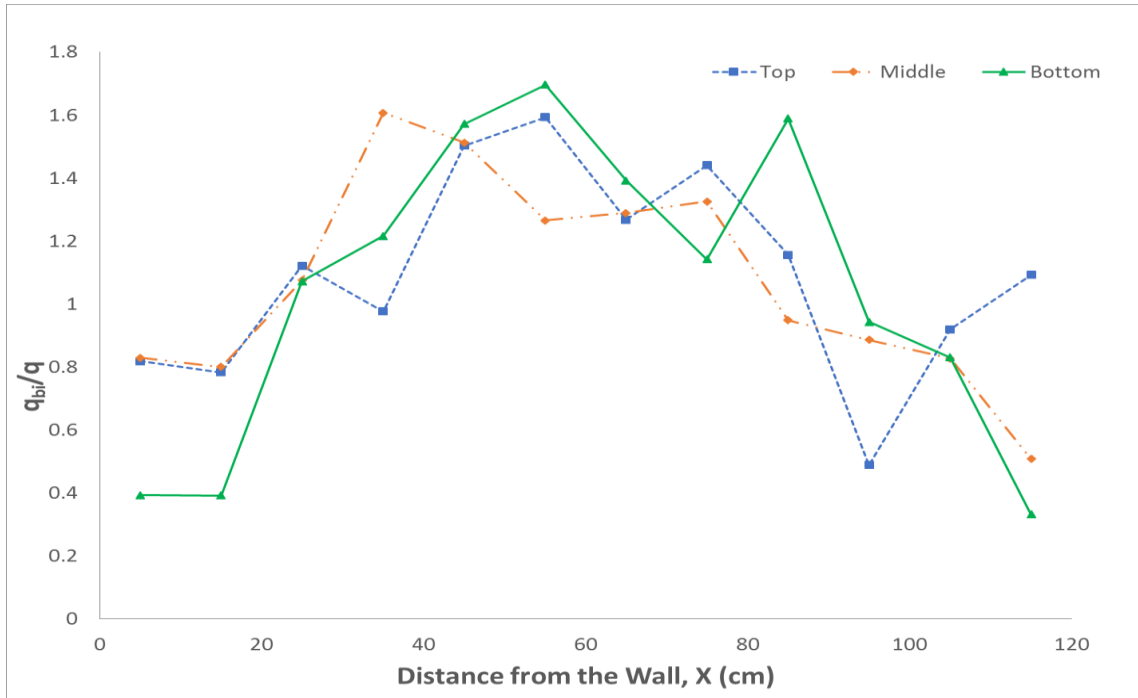


Figure 3-28: Gas bubble profile for $V_g = 0.35$ m/s with adjusted y-scale (Bottom: $h = 12$ cm; Middle: $h = 32$ cm; Top: $h = 52$ cm)

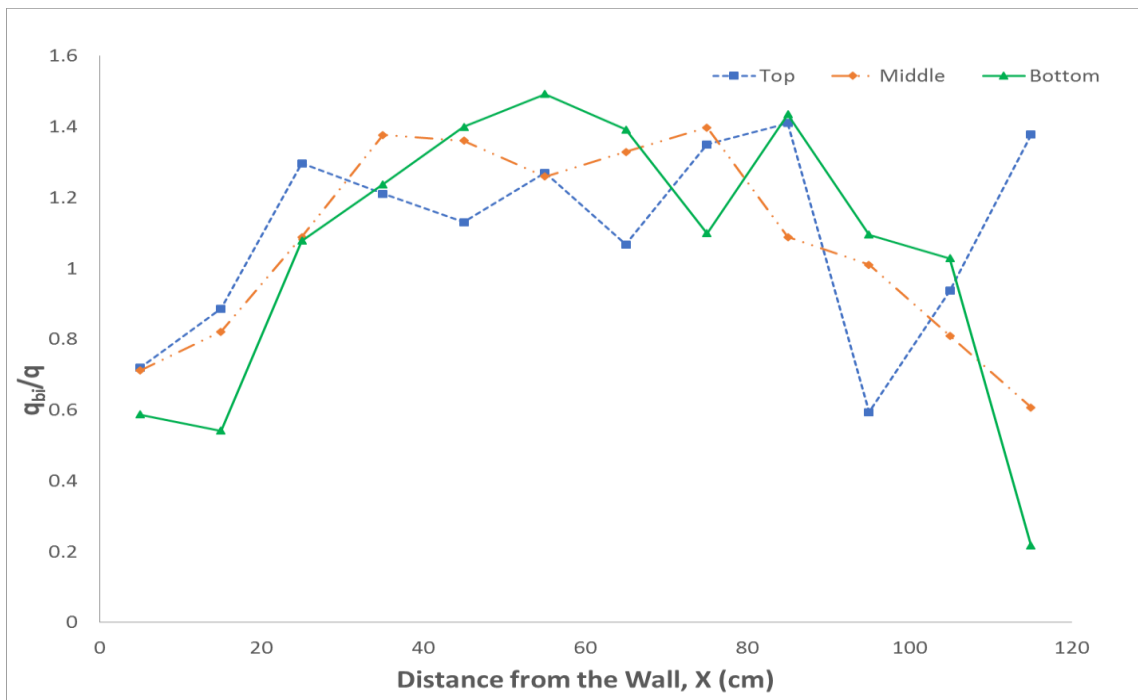


Figure 3-29: Gas bubble profile for $V_g = 0.50$ m/s (Bottom: $h = 12$ cm; Middle: $h = 32$ cm; Top: $h = 52$ cm)

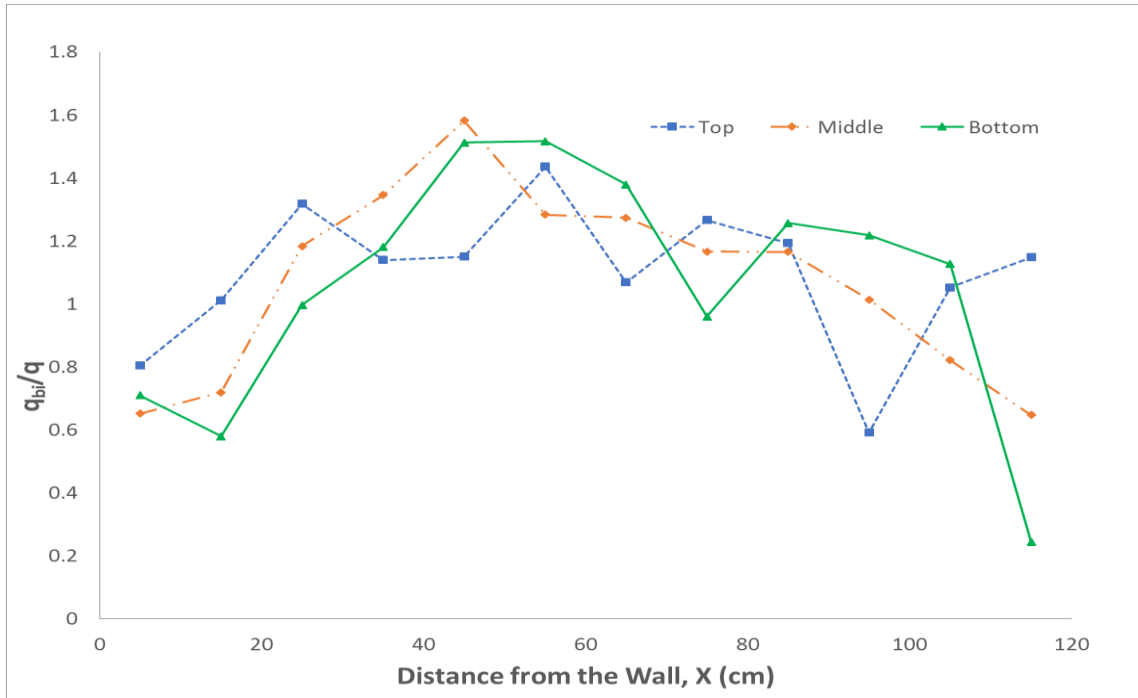


Figure 3-30: Gas bubble profile for $V_g = 0.60$ m/s (Bottom: $h = 12$ cm; Middle: $h = 32$ cm; Top: $h = 52$ cm)

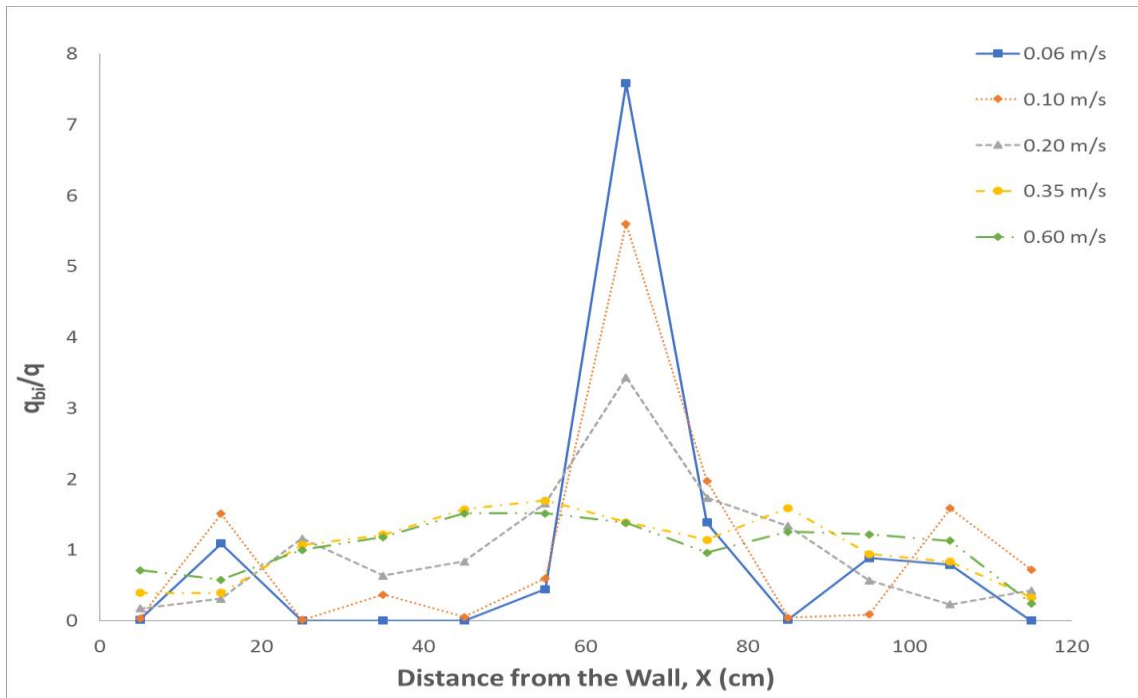


Figure 3-31: Gas bubble profile for Bottom Row for all velocities

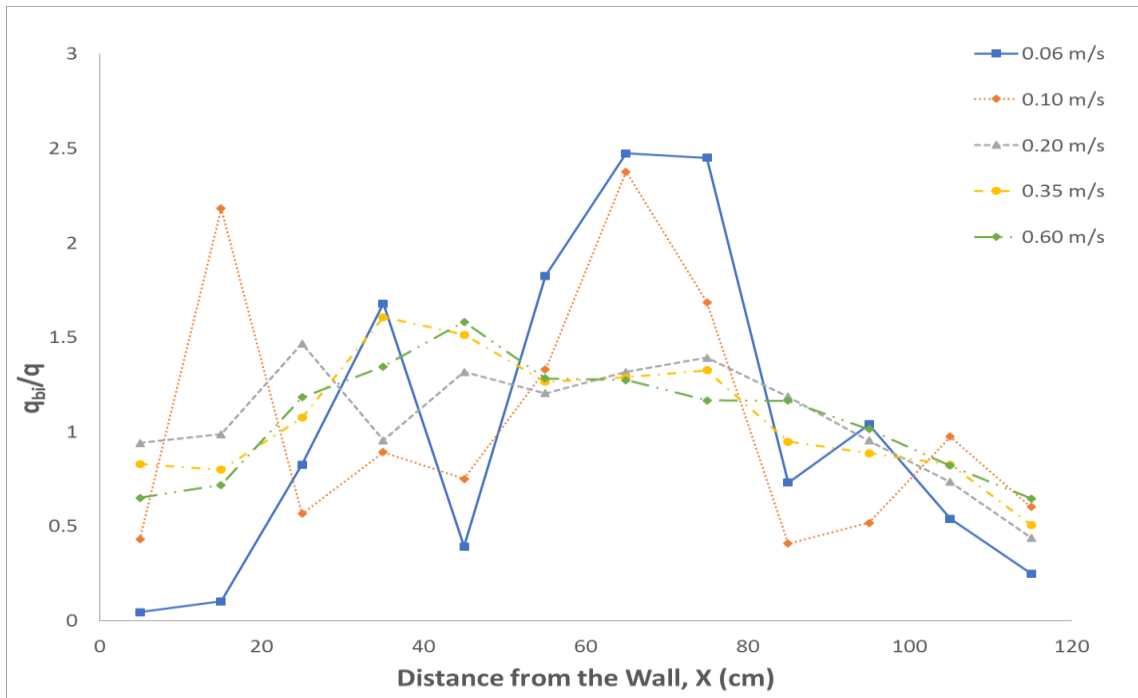


Figure 3-32: Gas bubble profile for Middle Row for all velocities

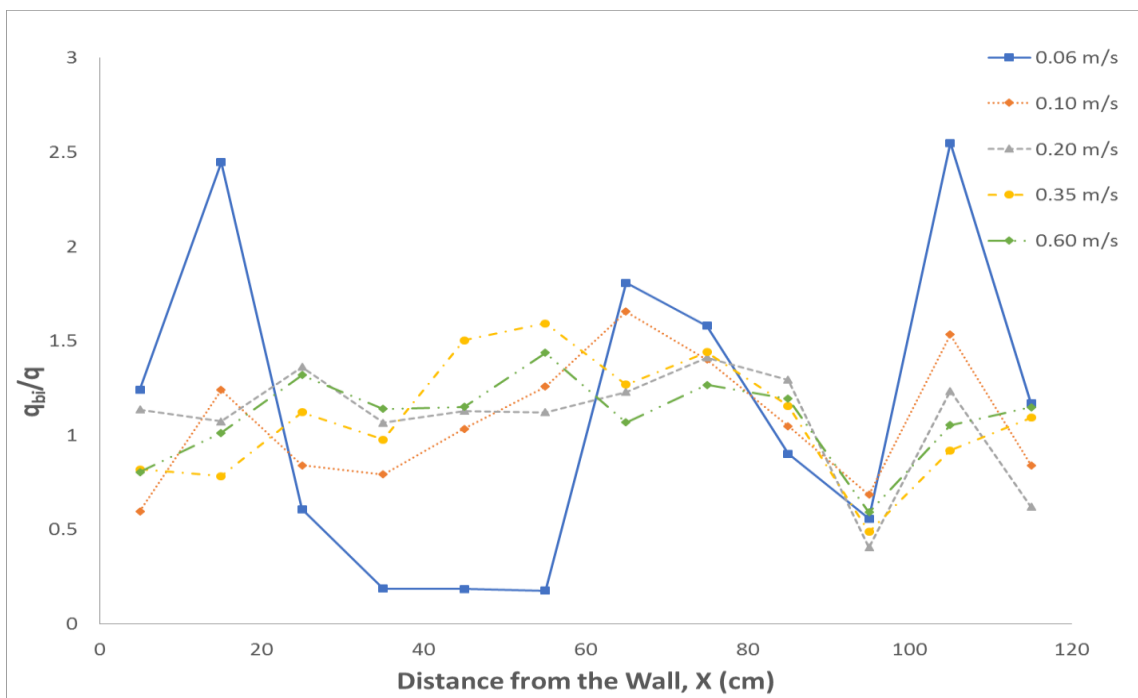


Figure 3-33: Gas bubble profile for Top Row for all velocities

3.4 Conclusion

Agglomerates were generated in a fluidized bed of sand and air by injecting a liquid binder solution of Gum Arabic, blue dye and water with a spray nozzle. These experiments were conducted to determine the size and density for model agglomerates to be used in a more detailed series of measurements with Radioactive Particle Tracking (RPT).

Vertical and lateral distributions of agglomerates were measured to determine agglomerate segregation. It was found that the fluidization velocity has a strong impact on agglomerate segregation. At low velocity (0.06 m/s), agglomerates larger than 600 μm segregated but segregation of agglomerates larger than 9500 μm was more significant. At high velocity (0.60 m/s), only agglomerates larger than 9500 μm segregated near the bottom. The segregation of agglomerates at 0.60 m/s was very low as compared to 0.06 m/s. However, the segregation results for agglomerates larger than 9500 μm are significant and this agglomerate size should be further investigated. The agglomerates were well distributed laterally at both 0.06 m/s and 0.60 m/s except for agglomerates larger than 9500 μm at 0.06 m/s.

The density of agglomerates was determined for agglomerate size larger than 9500 μm to find the density for the model agglomerate for RPT. The density of those agglomerates was between 1350 kg/m^3 to 1450 kg/m^3 . Hence, the size of the model agglomerates for RPT should be 9500 μm or larger with a density of 1450 kg/m^3 .

A triboelectric method was used to measure the gas bubble distribution in the fluidized bed. There seems to be an impact of the gas bubble distribution on the agglomerates distribution in the bed. The connection between gas bubble distribution and agglomerate motion and segregation will be studied more thoroughly with Radioactive Particle Tracking.

Chapter 4

4 Development of a New Two-Dimensional Radioactive Particle Tracking System to Study the Motion of Agglomerates

The purpose of this study is to simulate the motion of agglomerates in a fluidized bed. The motion of agglomerates can be simulated by tracking a single radioactive particle within a model agglomerate in the fluidized bed using Radioactive Particle Tracking (RPT). The properties of the model agglomerate were determined in Chapter 3 by generating agglomerates by injecting a liquid binder solution in a fluidized bed.

When agglomerates were generated by liquid injection in the fluidized bed, it was found that agglomerates larger than $9500\ \mu\text{m}$ are relevant to this study as they segregate both at low and highly velocities. It was decided to simulate a mid-size agglomerate ($5500\ \mu\text{m}$) as well.

4.1 Experimental Setup and Procedure

The RPT system tracks a radioactive particle by means of detecting the intensity of the gamma rays emitted by the particle inside a tracer or carrier. For the current study, a single radioactive source of Scandium-46 (Sc-46) was tracked by 12 scintillation detectors arranged in a 2D plane to detect and count the radiations emitted as shown in Figure 2-9. The Sc-46 source was radiated in a nuclear reactor (Material Test Reactor at McMaster University, Ontario, Canada) to get an initial strength of $200\ \mu\text{Ci}$. Details of the experimental setup are provided in Section 2.7.

Each scintillation detector was connected to a client computer to acquire and process the scintillation data. All client computers were synchronized by a Server computer by communicating through an Ethernet hub. For this research, several arrangements of scintillation detectors were considered initially, but only one configuration was found suitable. Detectors could not be placed facing the sides of the bed. Since the length of the bed is 1.22 m, the radiation detection after attenuation was too small to be significant for accurate calculation of location coordinates of the radioactive source. Hence, for the given

setup, all 12 detectors were placed in one plane covering 0.60 m of the height and 1.22 m of the length of the bed.

Ayatollahi (2016) has discussed various sources that may contribute to the errors in the location coordinates of the radioactive tracer, which include,

- Statistical nature of gamma rays due to randomness of radionuclide disintegration
- Variation of sampling time due to hardware or software
- Electrical noise caused by equipment used for electrical signal acquisition or processing in the RPT system
- Experimental error caused by experimenter
- Change in tracer location due to movement of particle during sampling time
- Fluctuation in gas and solid holdup in the fluidized bed

4.1.1 Development of a New Method for 2D RPT System

To determine the location coordinates of the particle tracer with respect to time, two methods are widely used i.e. Computer Aided Radioactive Particle Tracking (CARPT) and Monte Carlo Simulation of Radioactive Particles. The intensity of gamma rays detected depends on the distance from the source, attenuation due to the density of the fluidized bed and reactor walls and strength of the radioactive source used. Due to the inhomogeneous nature of the fluidized bed, it is essential to conduct an in-situ calibration of the system (Lin et al., 1985). Monte Carlo Simulation, on the other hand, requires less calibration as compared to the CARPT method and effects of geometry and radiations are taken into account mathematically (Chaouki et al., 1997). However, the computing time to calculate the coordinates is far greater than CARPT due to complex calculations. To take advantage of the lower computation time and simple mathematics, CARPT method is preferred over Monte Carlo Simulation.

4.1.1.1 Challenges with CARPT Method

In order to avoid complex calculations for the determination of the coordinates of the radioactive tracer, in-situ calibration is first carried out by placing the tracer at several hundred known locations throughout the fluidized bed. Counts are registered for each

detector for a certain period of time from which a calibration curve is generated for each detector by curve fitting. The calibration curve provides distance between the center of detector and radioactive particle as a function normalized radiation data. Since the position of the radioactive source and detectors are known, a map of distances between the radioactive source and the detectors is generated. Once the calibration equations are obtained, a weighted regression scheme can be used to determine the coordinates of a particle for a particular instance (Lin et al., 1985). The solution of the system of equations can be obtained by using the weighted linearized regression as defined by Lin et al. (1985). The accuracy of the location coordinates depends on the resolution of the calibration mesh (Rados, 2003).

Determination of location coordinates for the radioactive tracer in the bed using CARPT method as developed by Lin et al. (1985) includes the following mathematical steps. The distance of the source from each detector is first determined from the calibration curves. Coordinates of the detectors are known as their positions are fixed. The distance between the i^{th} detector (x_i, y_i, z_i) and source (X, Y, Z) can be given as,

$$r_i^2 = (X - x_i)^2 + (Y - y_i)^2 + (Z - z_i)^2 \quad (4.1)$$

Equation 4.1 can be expanded to obtain Equation 4.2,

$$\mu - 2Xx_i - 2Yy_i - 2Zz_i = r_i^2 - x_i^2 - y_i^2 - z_i^2 \quad (4.2)$$

Where μ is given as,

$$\mu \equiv X^2 + Y^2 + Z^2 \quad (4.3)$$

For 'n' number of detectors, the system of equations developed using Equation 4.2 can be written in matrix form as,

$$\begin{bmatrix} 1 & -2x_1 & -2y_1 & -2z_1 \\ 1 & -2x_2 & -2y_2 & -2z_2 \\ \vdots & \vdots & \vdots & \vdots \\ 1 & -2x_n & -2y_n & -2z_n \end{bmatrix}_{n \times 4} \times \begin{bmatrix} \mu \\ X \\ Y \\ Z \end{bmatrix}_{4 \times 1} = \begin{bmatrix} r_1^2 - x_1^2 - y_1^2 - z_1^2 \\ r_2^2 - x_2^2 - y_2^2 - z_2^2 \\ \vdots \\ r_n^2 - x_n^2 - y_n^2 - z_n^2 \end{bmatrix}_{n \times 1} \quad (4.4)$$

Where,

$$\alpha = \begin{bmatrix} 1 & -2x_1 & -2y_1 & -2z_1 \\ 1 & -2x_2 & -2y_1 & -2z_2 \\ \vdots & \vdots & \vdots & \vdots \\ 1 & -2x_n & -2y_n & -2z_n \end{bmatrix}_{n \times 4} \quad (4.5)$$

$$\beta = \begin{bmatrix} \mu \\ X \\ Y \\ Z \end{bmatrix}_{4 \times 1} \quad (4.6)$$

$$\gamma = \begin{bmatrix} r_1^2 - x_1^2 - y_1^2 - z_1^2 \\ r_2^2 - x_2^2 - y_2^2 - z_2^2 \\ \vdots \\ r_n^2 - x_n^2 - y_n^2 - z_n^2 \end{bmatrix}_{n \times 1} \quad (4.7)$$

By replacing matrices in Equation 4.4, it would become,

$$|\alpha||\beta| = |\gamma| \quad (4.8)$$

The coordinates of the tracer can be determined by transforming Equation 4.8 as,

$$|\beta| = |\alpha|^{-1}|\gamma| \quad (4.9)$$

To calculate the inverse of α , determinant of α is required. For the given system, all the detectors are placed in a 2D plane, therefore, the z-coordinate for all the detectors is same.

Determinant for α would become,

$$|\alpha| = \begin{vmatrix} 1 & -2x_1 & -2y_1 & -2z \\ 1 & -2x_2 & -2y_1 & -2z \\ \vdots & \vdots & \vdots & \vdots \\ 1 & -2x_n & -2y_n & -2z \end{vmatrix}_{n \times 4} \quad (4.10)$$

Taking $-2z$ as common would give a determinant with 2 columns which are the same, hence, resulting in a zero determinant.

$$|\alpha| = -2z \begin{vmatrix} 1 & -2x_1 & -2y_1 & 1 \\ 1 & -2x_2 & -2y_1 & 1 \\ \vdots & \vdots & \vdots & \vdots \\ 1 & -2x_n & -2y_n & 1 \end{vmatrix}_{n \times 4} = 0 \quad (4.11)$$

Rotation matrices were used to virtually rotate the plane of detectors, but the determinant still resulted in a value close to zero due to which a mathematical solution was not feasible. Due to this reason, CARPT method as developed by Lin et al. (1985) could not be used to track a model agglomerate in the fluidized bed for a 2D RPT system. Therefore, it was decided to use multilinear regression to develop equations for location coordinates of the model agglomerate in the fluidized bed from the data obtained by calibration of the 2D RPT system.

4.1.1.2 Calibration of RPT System

The density of the fluidized bed is of significant importance as denser material causes higher attenuation of the gamma rays. Accurate accountability of attenuation is important to get location coordinates of the radioactive tracer with a minimum of error. Therefore, in-situ calibration was necessary to take into account the effect of fluctuations in bed density on the attenuation of gamma radiations due to change in gas and solids holdups, bubble flow through the fluidized bed and the metallic wall of the equipment. The result of the calibration was a map between the radiation counts and location of source which was used to develop the empirical equations for the X, Y and Z coordinates of the model agglomerates in the fluidized bed (Figure 4-1).

The 12 detectors were placed in one plane covering 0.60 m of the height and 1.22 m of the length of the bed. To map the complete bed, the source was placed at 290 locations in the bed. Figure 4-1 shows a map of all the locations at which the source was placed. From the front, the bed was divided into 12 columns (x-axis) and 5 rows (y-axis). The column to column and row to row distances were 0.10 m. For each front location, calibration was carried out at 5 depths (z-axis). Due to the presence of the dipleg, the source could not be placed at 10 locations resulting in 290 locations instead of 300. Calibration was conducted at 4 velocities i.e. 0.06 m/s, 0.10 m/s, 0.35 m/s and 0.60 m/s which enabled the gas velocity or bed density to be taken into account in the multilinear regression. For each calibration run, counts were registered for 20,000 events at one location. The system could register the radiation counts for a minimum sampling time of 6 to 10 ms. The data collected during the sampling time (6 to 10 ms) interval was termed as one event. Detectors received 8 to 10,000 photon counts per event depending on the distance and the strength of the source. A total

of 1160 (290 locations x 4 gas velocities) runs were carried out for the complete calibration of the system.

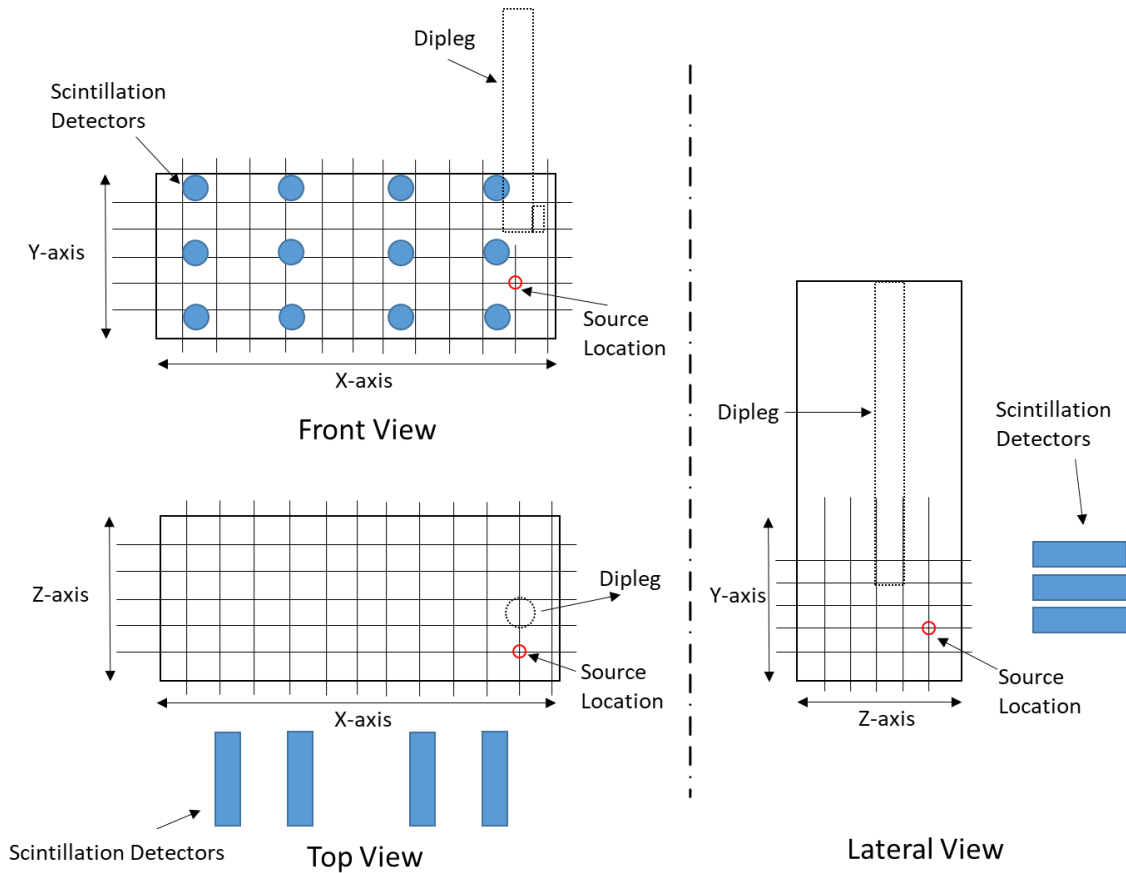


Figure 4-1: Map of 290 source locations for calibration

4.1.1.3 Development of Empirical Equations by Multilinear Regression

Normalized counts for a detector were obtained by taking a ratio of the absolute counts measured by a detector (C_i , counts/s) for each time interval (an event) to the total sum of absolute counts measured by all detectors (C_{sum} , counts/s) for that time interval (event).

$$\text{Normalized Counts for a Detector for a given time interval (event)} (S_i) = \frac{\text{Absolute Counts Detected during Sampling Time for this time interval (event)} (C_i)}{\text{Sum of Absolute Counts Measured by All Detectors for this time interval (event)} (\sum_{i=1}^{12} C_i)} \quad (4.12)$$

Once calibration was complete, average normalized counts (relative counts) were calculated for each detector for each calibration run or location. Hence, 1160 data points (average normalized counts) were obtained for each detector. This data was then used to develop an empirical equation for each coordinate as a function of gas velocity and normalized counts measured by 12 detectors (13 variables). Empirical equations were obtained by multilinear regression using three different regression software i.e. Minitab, Excel and Signal Analysis® by Dr. Cedric Briens which are presented in Equations (4.13) to (4.21). Table 4-1 shows the R²-values for the curve fit for X, Y and Z coordinates. The results for X and Y coordinates were satisfactory, but the fit for Z coordinate was not good.

X	Excel	R-Square
		0.9959
	Minitab	R-Square
0.9959		
Cedric's Software	R-Square	
	0.9958	
Y	Excel	R-Square
		0.9923
	Minitab	R-Square
0.9923		
Cedric's Software	R-Square	
	0.9923	
Z	Excel	R-Square
		0.0088
	Minitab	R-Square
0.0088		
Cedric's Software	R-Square	
	0.0091	

Table 4-1: R²-values for curve fitting for location coordinates of model agglomerate

$$X_{Minitab} = -43.4 + 0.0054 V_g + 220.18 S_{01} + 74.65 S_{02} + 120.29 S_{03} - 0.56 S_{04} + 157.83 S_{05} + 99.57 S_{06} + 94.7 S_{07} + 46.5 S_{08} + 242.77 S_{09} + 70.34 S_{10} + 124.3 S_{11} \quad (4.13)$$

$$X_{Excel} = 3.13 + 0.0054 V_g + 173.65 S_{01} + 28.12 S_{02} + 73.76 S_{03} - 47.09 S_{04} + 111.3 S_{05} + 53.04 S_{06} + 48.17 S_{07} + 196.24 S_{09} + 23.8 S_{10} + 77.79 S_{11} - 46.53 S_{12} \quad (4.14)$$

$$X_{Cedric} = 39.91 + 132.67 S_{01} + 33.44 S_{03} - 81.62 S_{04} + 83.87 S_{05} + 18.46 S_{07} - 40.25 S_{08} + 152.77 S_{09} + 35.19 S_{11} - 80.12 S_{12} \quad (4.15)$$

$$Y_{Minitab} = 77.71 - 0.005 V_g - 111.05 S_{01} - 108.77 S_{02} - 123.83 S_{03} - 98.03 S_{04} - 22.89 S_{05} - 25.64 S_{06} - 21.6 S_{07} - 32.5 S_{08} + 9.63 S_{09} + 6.84 S_{10} + 15.26 S_{11} \quad (4.16)$$

$$Y_{Excel} = 45.21 - 0.005 V_g - 78.54 S_{01} - 76.27 S_{02} - 91.32 S_{03} - 65.52 S_{04} + 9.61 S_{05} + 6.87 S_{06} + 10.9 S_{07} + 42.13 S_{09} + 39.34 S_{10} + 47.76 S_{11} + 32.5 S_{12} \quad (4.17)$$

$$Y_{Cedric} = -32.37 - 0.0049 V_g - 13.16 S_{03} + 11.75 S_{04} + 85.38 S_{05} + 86.62 S_{06} + 87.6 S_{07} + 78 S_{08} + 120.91 S_{09} + 115.36 S_{10} + 126.01 S_{11} + 109.77 S_{12} \quad (4.18)$$

$$Z_{Minitab} = -14.67 - 0.005 V_g - 0.2 S_{01} - 6.7 S_{02} - 4.7 S_{03} - 4.04 S_{04} - 26.3 S_{05} - 5.8 S_{06} - 13.15 S_{07} - 13.1 S_{08} + 6.2 S_{09} - 7.3 S_{10} - 6.6 S_{11} \quad (4.19)$$

$$Z_{Excel} = 1.55 - 0.005 V_g + 12.92 S_{01} + 6.42 S_{02} + 8.44 S_{03} + 9.09 S_{04} - 13.2 S_{05} + 7.28 S_{06} - 0.02 S_{07} + 19.28 S_{09} + 5.81 S_{10} + 6.55 S_{11} + 13.13 S_{12} \quad (4.20)$$

$$Z_{Cedric} = 55916.9 - 0.0004 V_g - 55902.6 S_{01} - 55908.9 S_{02} - 55906.8 S_{03} - 55906.5 S_{04} - 55982.3 S_{05} - 55908.4 S_{06} - 55915.7 S_{07} - 55915.2 S_{08} - 55896.4 S_{09} - 55909.4 S_{10} - 55908.6 S_{11} - 55902.4 S_{12} \quad (4.21)$$

Results obtained by Minitab were selected for further calculations as regression from Minitab provided the smallest standard errors in coefficients. The empirical equations were validated by calculating the coordinates of a tracer particle at several known locations. Figures 4-2 and 4-3 show that the X and Y coordinates can be predicted with the empirical equations obtained from regression.

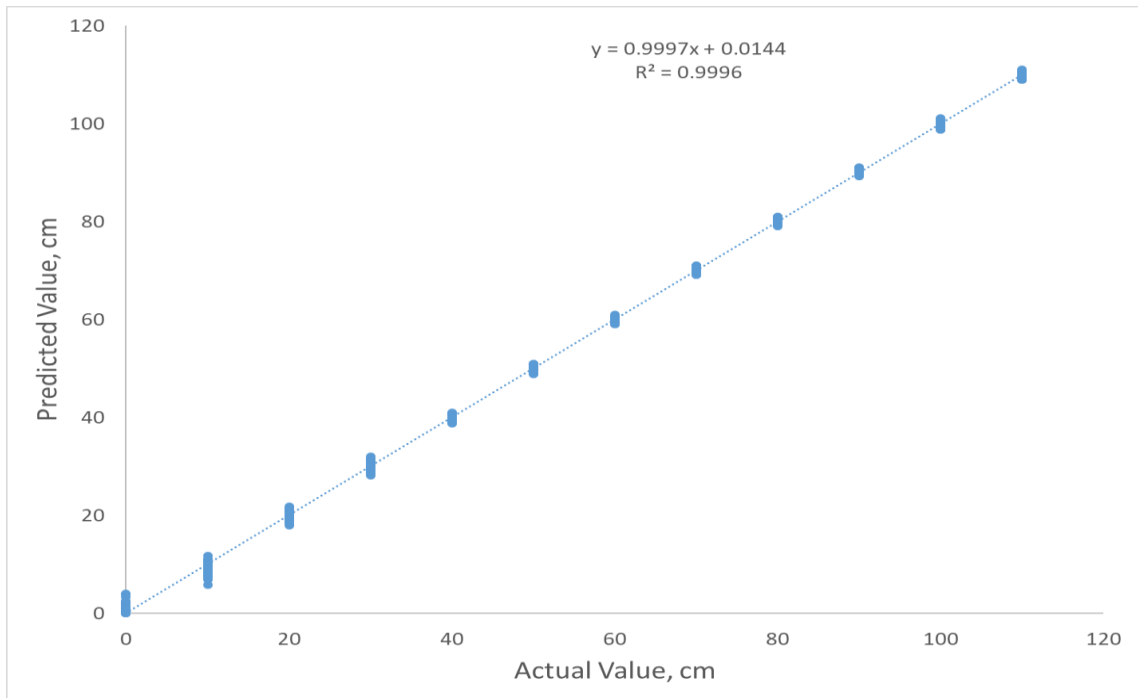


Figure 4-2: Error on X for all calibration runs: Predicted values of X vs actual values of X

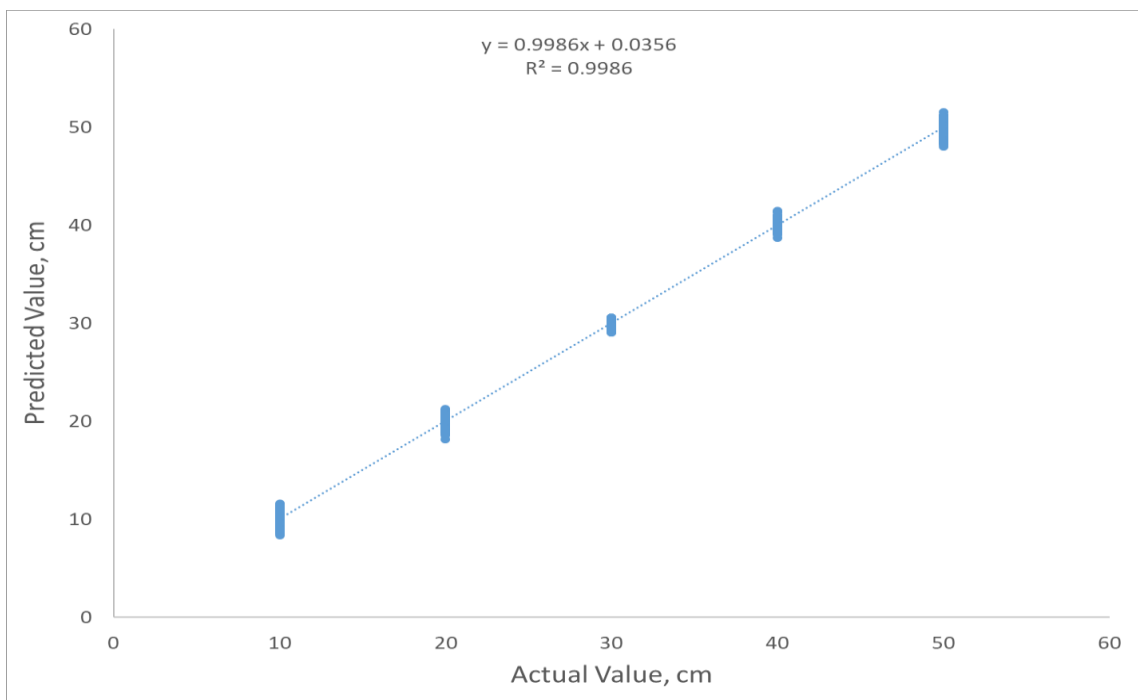


Figure 4-3: Error on Y for all calibration runs: Predicted values of Y vs actual values of Y

A major contribution to the error in the predicted values of X and Y is the random nature of the radioactive decay. This error can be reduced by combining the normalized counts of two or more time intervals or events to increase the effective sample time. Figures 4-4 and 4-5 show the reduction in standard deviation for X and Y coordinates, respectively when sample time is increased. The counts were measured for several thousand events (6-10 ms of time interval per event) while the particle stayed in one location so that variability of the data due to the random nature of radioactivity can be determined.

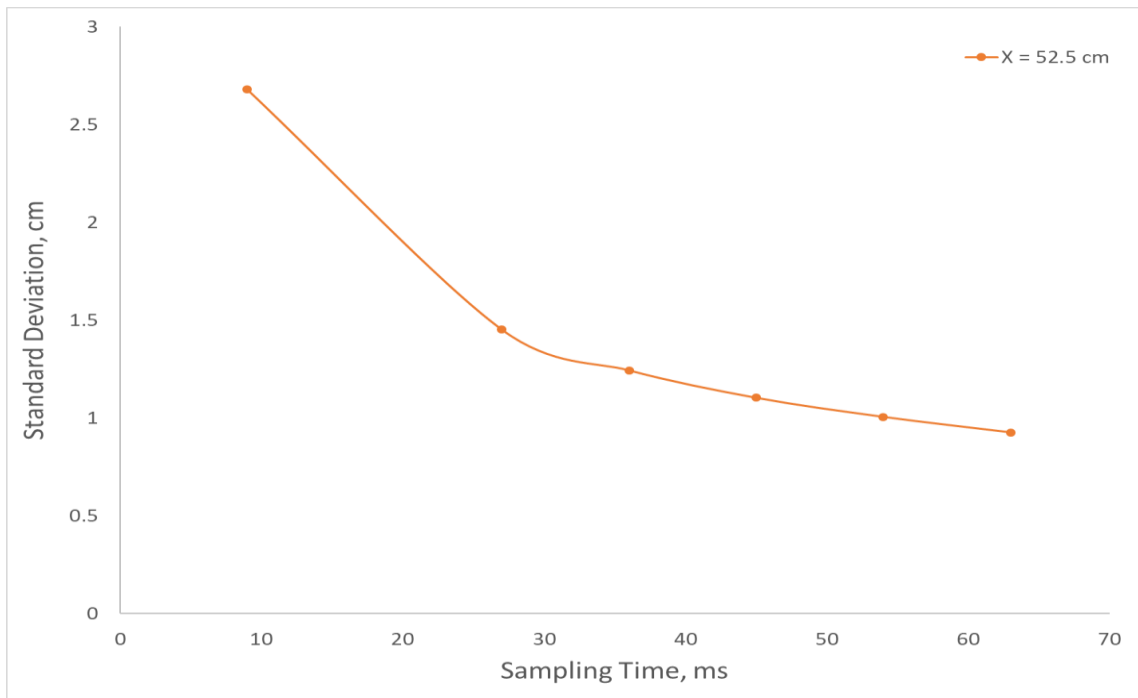


Figure 4-4: Standard deviation for X-coordinate of location of radioactive particle

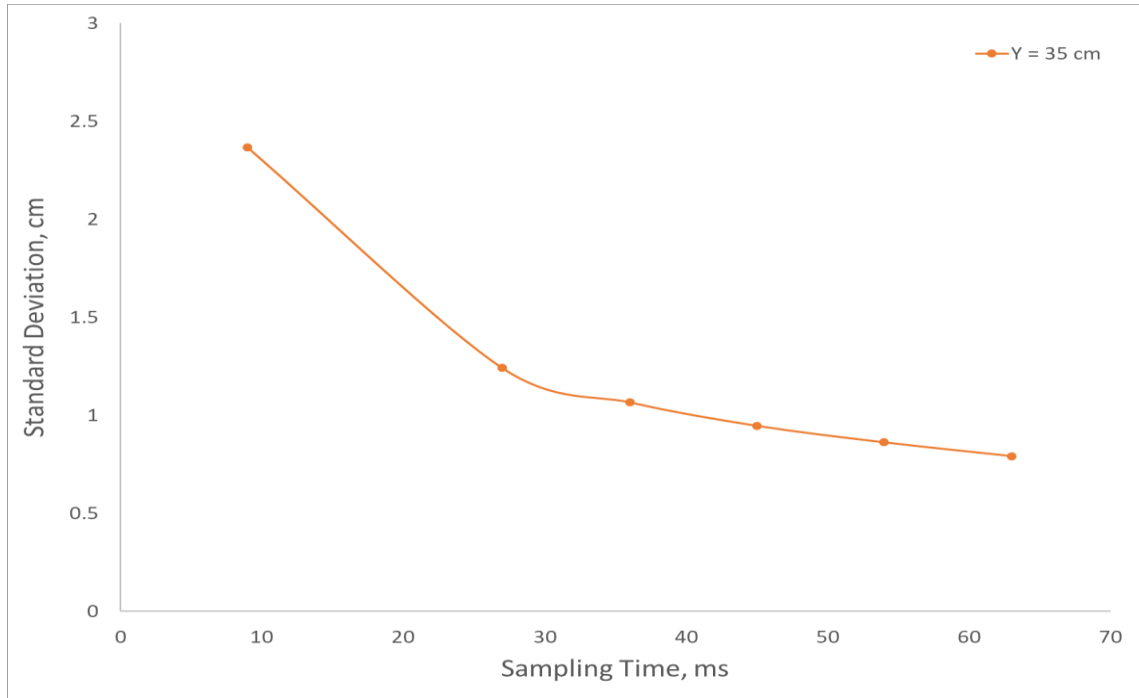


Figure 4-5: Standard deviation for Y-coordinate of location of radioactive particle

Figures 4-4 and 4-5 suggest that a sampling time of 36 ms may be suitable to reduce the errors, since further increases in sampling do not yield major error reductions. However, for a moving particle, increasing the sample time reduces the time resolution. For a larger sample time, the coordinates obtained correspond to the average location during that time interval rather than the nearly instantaneous location coordinates that would be obtained for a much shorter sample time.

For the current research, the focus is to better understand the motion of agglomerates and to determine if they segregate. Since the profile along the Z coordinate is not important for this study (width was small as compared to the bed length and height), the Z-coordinate was ignored for further results.

4.1.2 Preparation of Model Agglomerates

Model agglomerates were manufactured using a Nylon ball as the carrier for the radioactive source. The source was placed in an orifice drilled in the Nylon ball. The orifice was sealed using an epoxy putty. Tungsten powder with a density 19250 kg/m^3 was used to adjust the density of model agglomerates to the desired value. The model agglomerates were then

wrapped with shrink wrap to prevent contamination of bed solids by radioactive material caused by any breakage or disintegration of the model agglomerate. The final density of both model agglomerates was 1450 kg/m^3 . Two sizes of model agglomerates were prepared: $5500 \text{ }\mu\text{m}$ (MA1) and $12500 \text{ }\mu\text{m}$ (MA2). These sizes were used because Nylon balls of size $4750 \text{ }\mu\text{m}$ and $9500 \text{ }\mu\text{m}$ were not available. However, the selected sizes fulfill the needs of the study. Figure 4-6 shows some Nylon balls that were available for experiments.

Model Agglomerate-1 (MA1) was prepared by placing the source in an orifice in a $5500 \text{ }\mu\text{m}$ Nylon ball, sealing it with epoxy putty and wrapping it with shrink wrap (Figure 4-7). After completing the experiments with MA1, its shrink wrap was removed and the source was placed in a $12500 \text{ }\mu\text{m}$ Nylon ball to prepare Model Agglomerate-2 (MA2). MA2 was also sealed with epoxy putty and wrapped with shrink wrap. The effect of attenuation due to the nylon ball, epoxy putty and shrink wrap was similar to the attenuation caused by the hollow metallic rod present during the calibration, which was later removed from the bed. Therefore, no change was needed in calibration to take into account the effect of attenuation due to the nylon ball, epoxy putty and shrink wrap.



Figure 4-6: Nylon balls of different sizes



Figure 4-7: Model Agglomerate-1 (MA1)

4.1.3 Experimental Procedure

After the calibration of the RPT system was completed, model agglomerates were prepared and experiments were conducted by putting the model agglomerates in the fluidized bed. The model agglomerates were then tracked in the fluidized bed by the RPT system at two temperatures i.e. room temperature and 120 °C. At room temperature, agglomerates were tracked at 5 gas velocities for 300,000 events (approximately 45 min) for each velocity whereas at 120 °C, agglomerates were tracked at 3 gas velocities as mentioned below.

At Room Temperature: 0.06 m/s, 0.10 m/s, 0.35 m/s, 0.50 m/s and 0.60 m/s

At 120 °C: 0.06 m/s, 0.35 m/s (300,000 events) and 0.60 m/s (50,000 events)

4.2 Results and Discussion

4.2.1 Results for Model Agglomerate-2 (12500 μm)

Location coordinates obtained from the empirical equations using the data for MA2 were plotted with gas bubble flow distribution as shown in Figures 4-8 to 4-15. The solid line in

the figures for tracer locations corresponds to the bubble flow distribution on the secondary y-axis.

The results show that the model agglomerate segregated at all velocities at both room temperature and 120 °C when the bed was fully fluidized. Figures 4-8, 4-9 and 4-13 show that the model agglomerate did not move at 0.06 m/s and 0.10 m/s indicating a de-fluidized region in the bed which makes sense given the low bubble fraction in that region. MA2 spent more time in the region with low bubble flow. Regions with high bubble flow seem to have a lower agglomerate presence. Since overlapping points appear as one in this type of graph, the probability distribution of agglomerate presence was plotted instead of locations in separate graphs as shown in Figures 4-16 to 4-23.

The fluidized bed was divided into 220 cells (11 rows x 20 columns) each representing a 6 cm x 6 cm area of the bed. The probability of MA2 presence in each cell was calculated from the frequency of appearance for each case using the location data presented in Figures 4-8 to 4-15. Combining all the cells provides the probability distribution of MA2 presence in the whole bed. The probability distribution shows the data density which cannot be shown by plotting the location coordinates. It is clear from the probability distribution that the model agglomerate was more likely to be found in the low bubble fraction region in the fluidized bed.

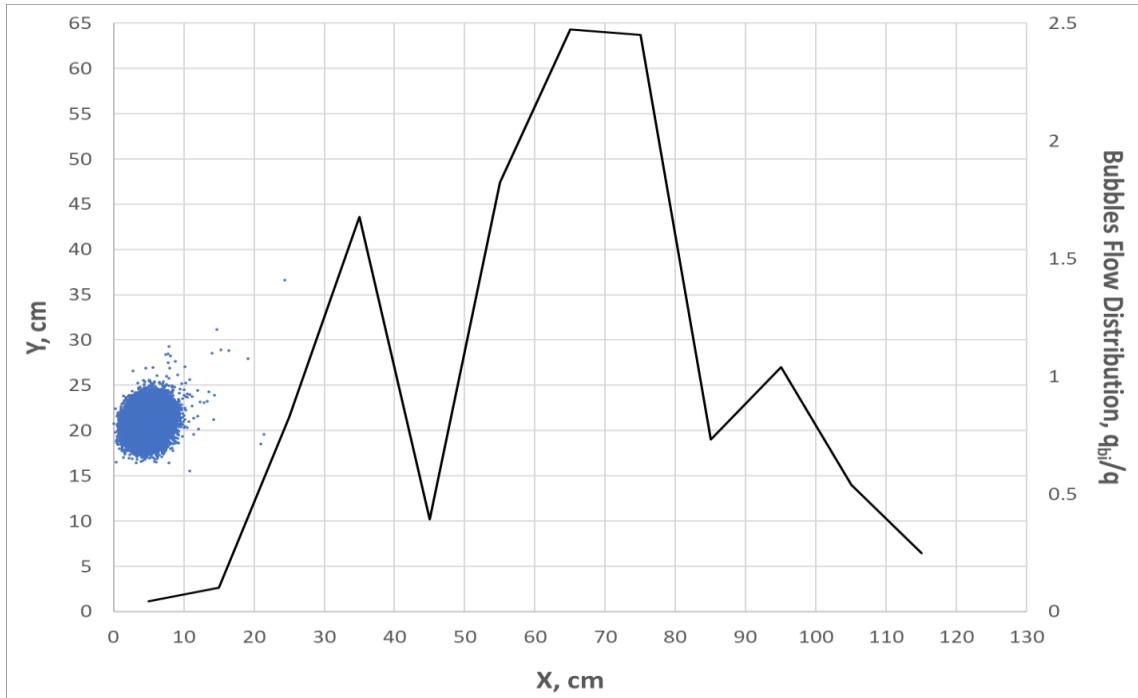


Figure 4-8: Tracer locations and gas bubble flow distribution for MA2 at 0.06 m/s and room temperature

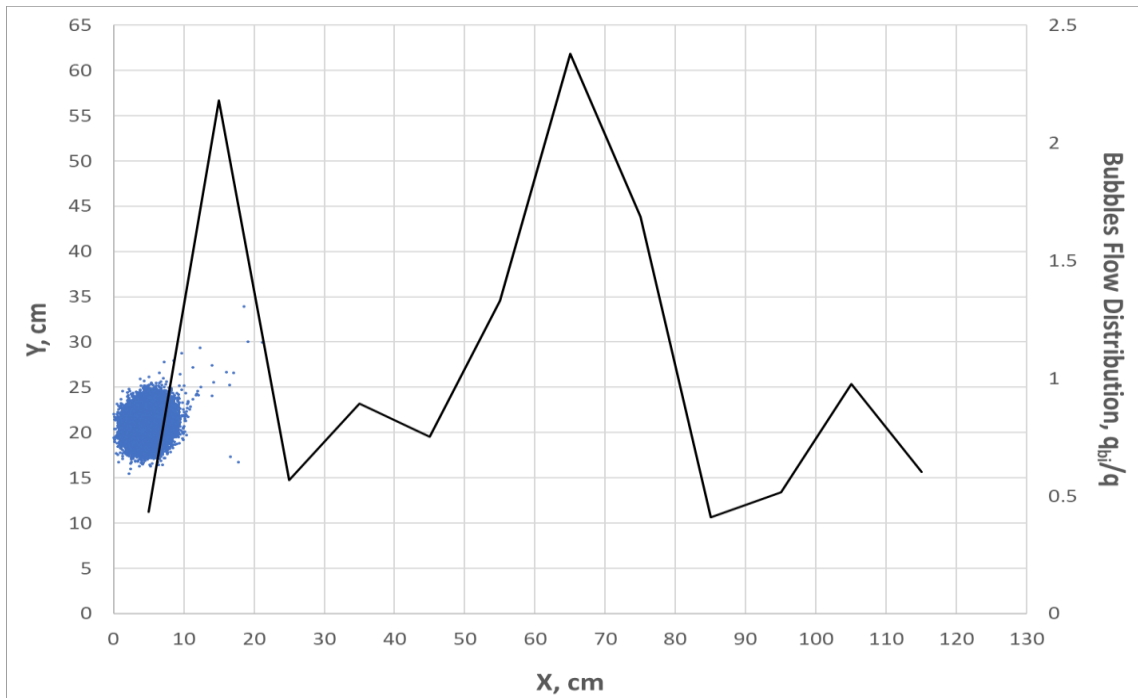


Figure 4-9: Tracer locations and gas bubble flow distribution for MA2 at 0.10 m/s and room temperature

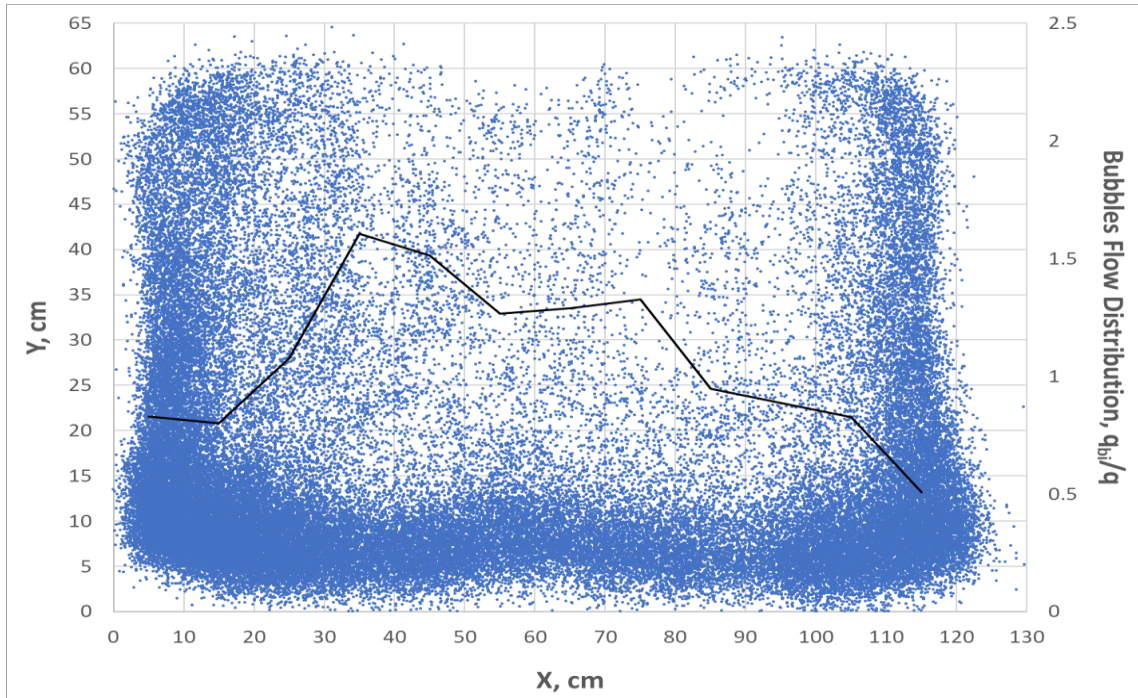


Figure 4-10: Tracer locations and gas bubble flow distribution for MA2 at 0.35 m/s and room temperature

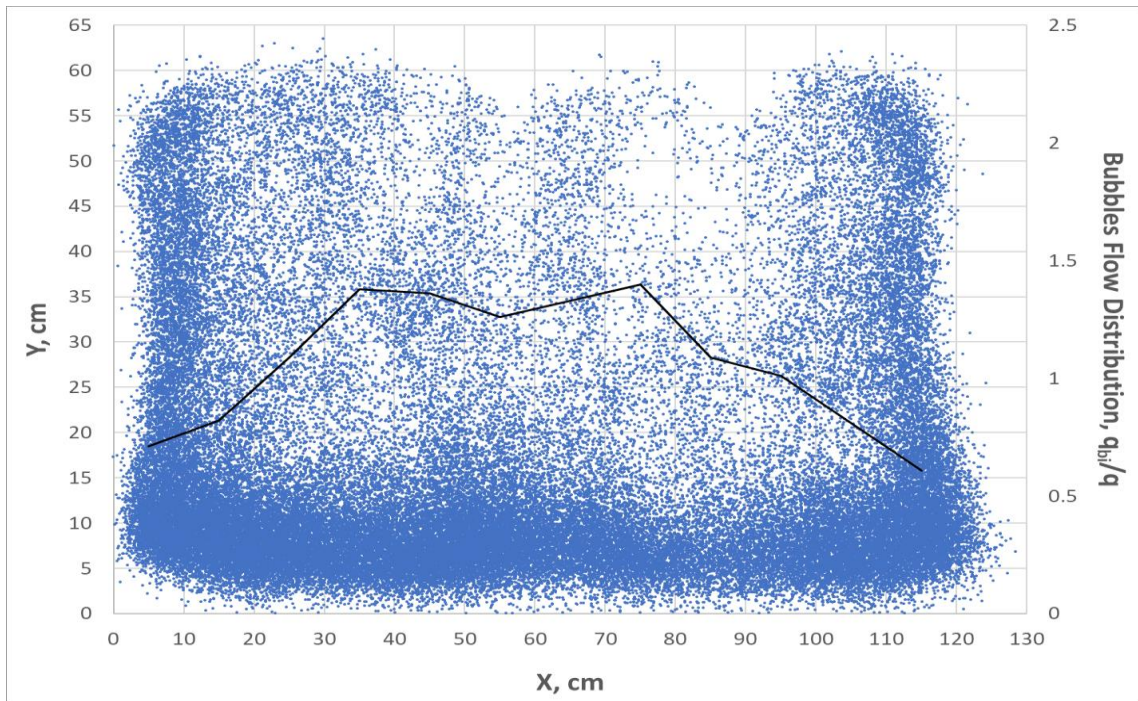


Figure 4-11: Tracer locations and gas bubble flow distribution for MA2 at 0.50 m/s and room temperature

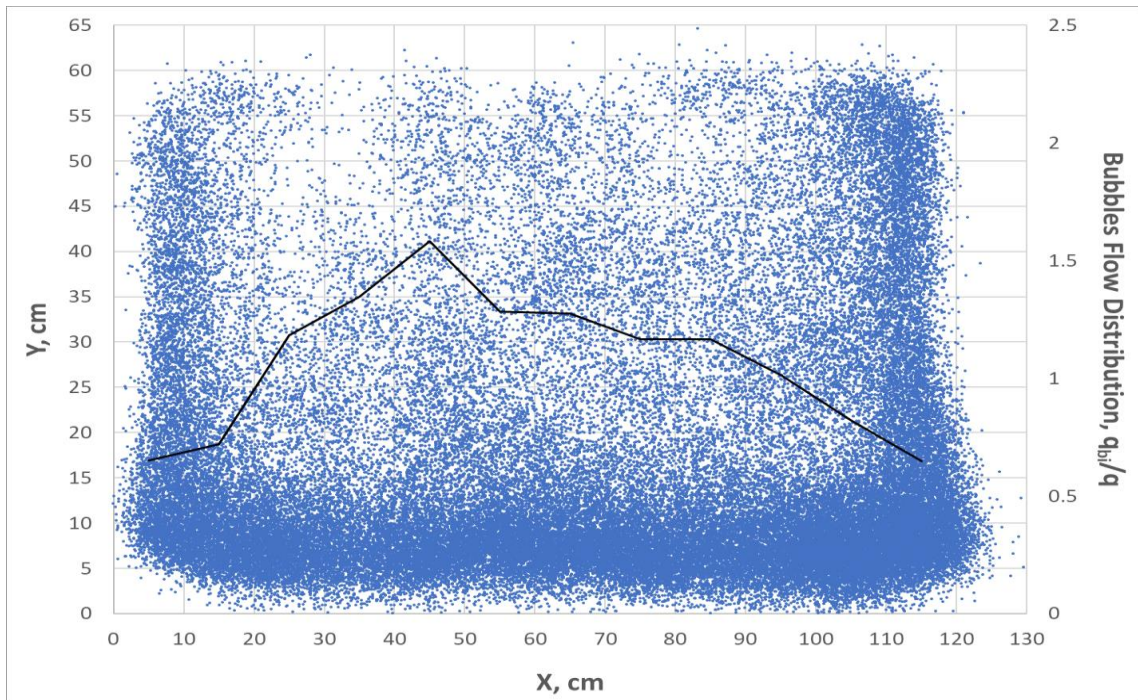


Figure 4-12: Tracer locations and gas bubble flow distribution for MA2 at 0.60 m/s and room temperature

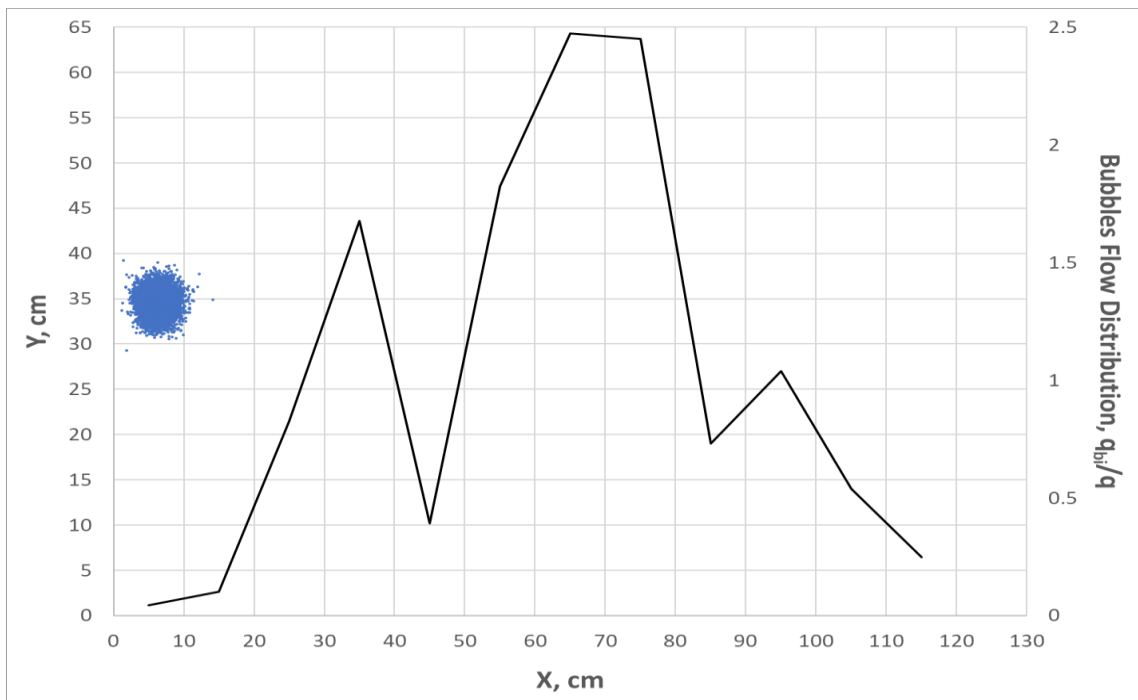


Figure 4-13: Tracer locations and gas bubble flow distribution for MA2 at 0.06 m/s and 120 °C

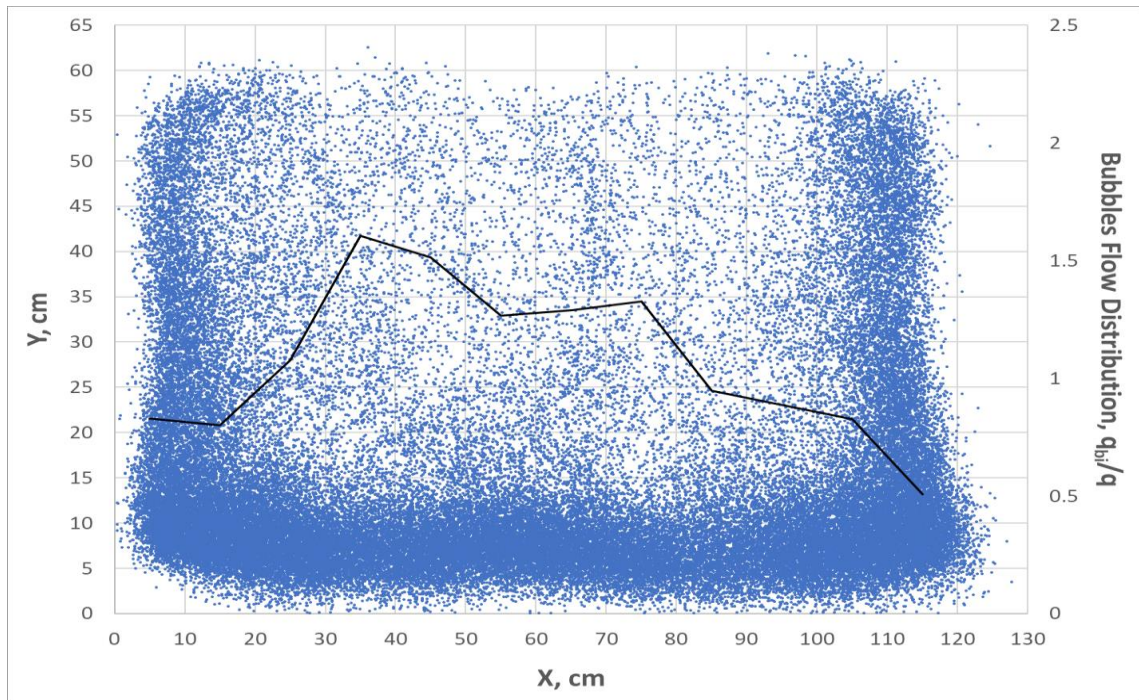


Figure 4-14: Tracer locations and gas bubble flow distribution for MA2 at 0.35 m/s and 120 °C

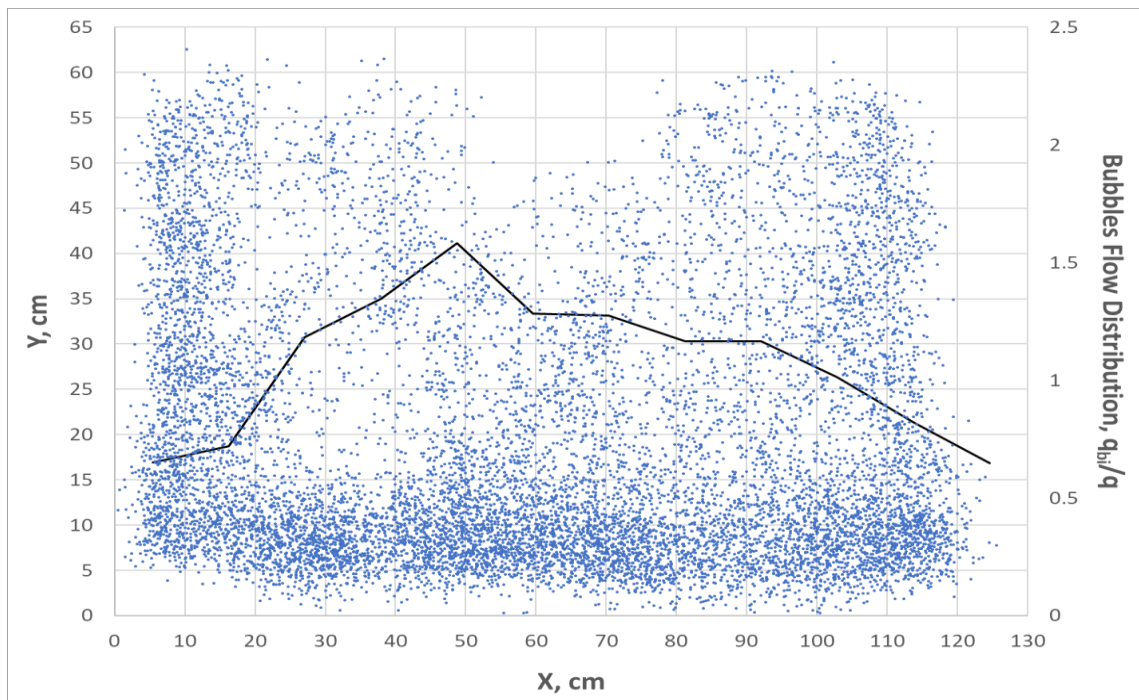


Figure 4-15: Tracer locations and gas bubble flow distribution for MA2 at 0.60 m/s and 120 °C

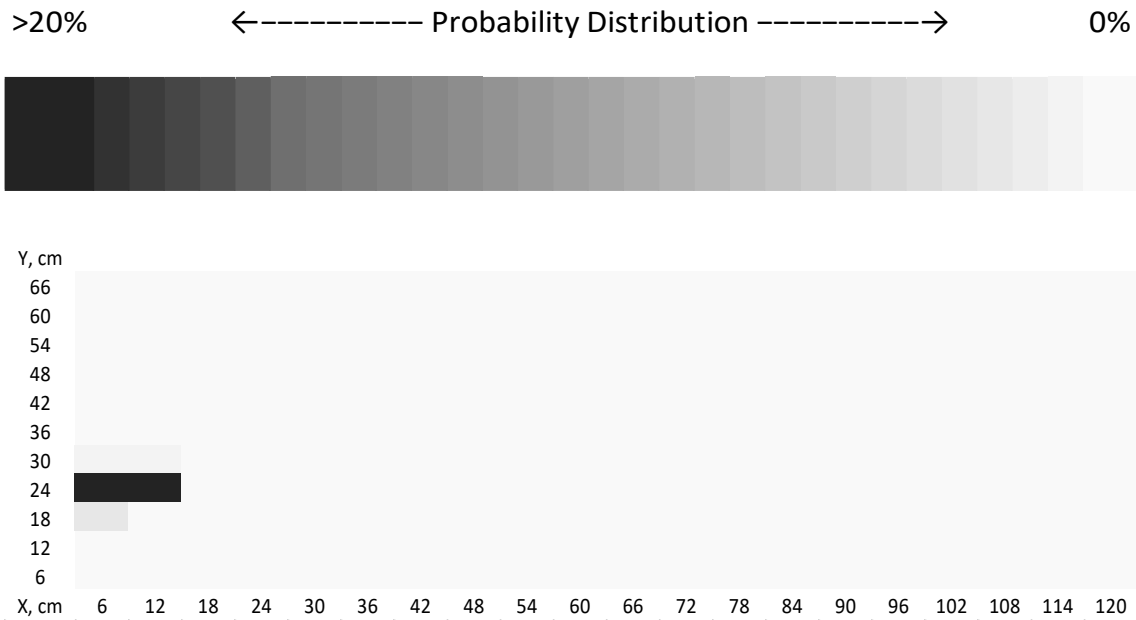


Figure 4-16: Probability distribution of particle presence for MA2 at 0.06 m/s and room temperature

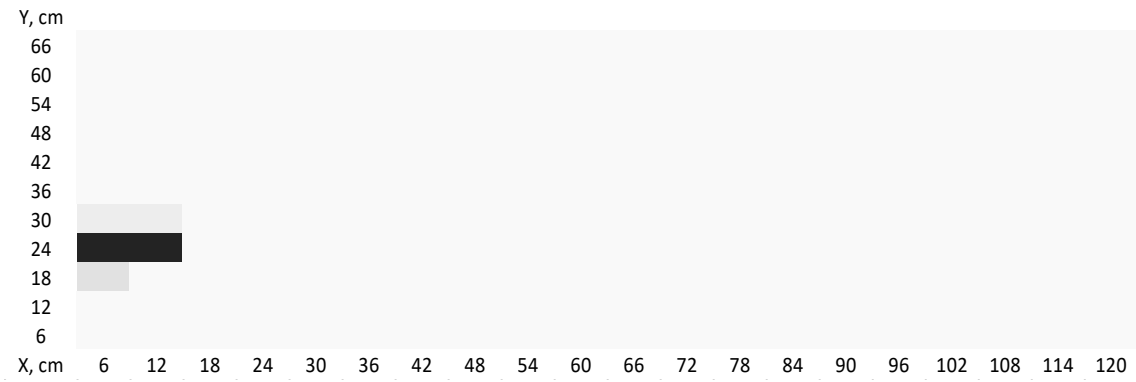


Figure 4-17: Probability distribution of particle presence for MA2 at 0.10 m/s and room temperature

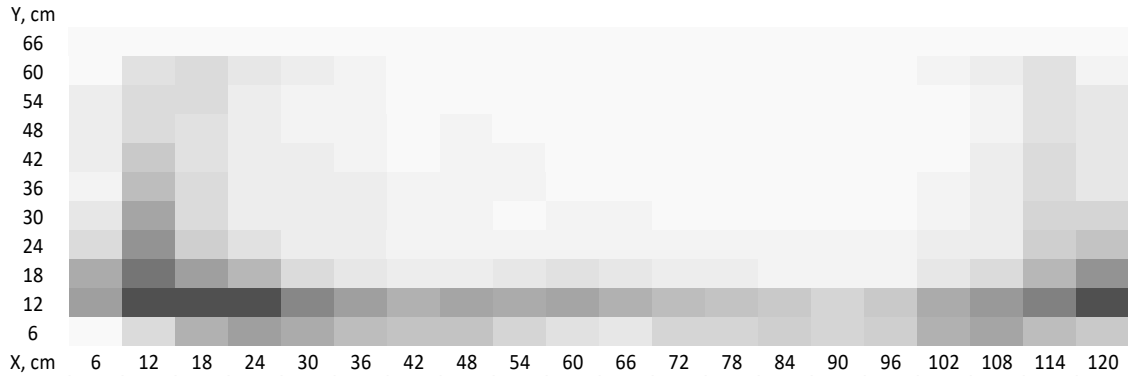


Figure 4-18: Probability distribution of particle presence for MA2 at 0.35 m/s and room temperature

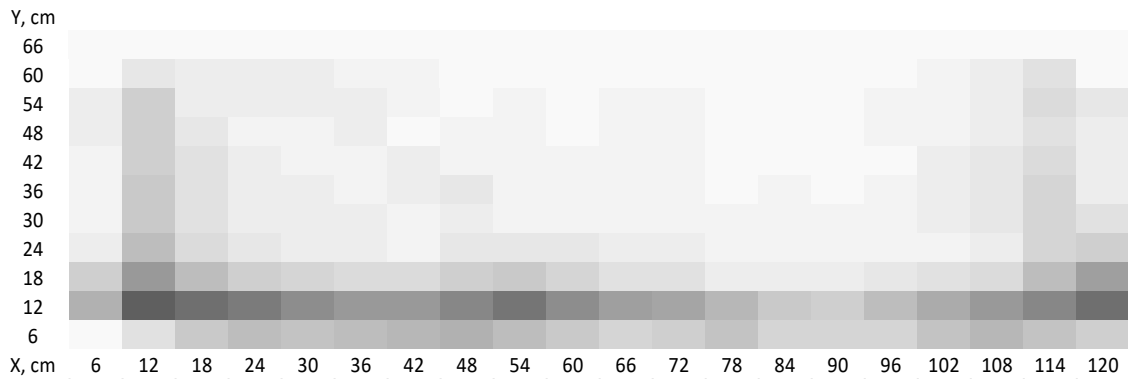


Figure 4-19: Probability distribution of particle presence for MA2 at 0.50 m/s and room temperature

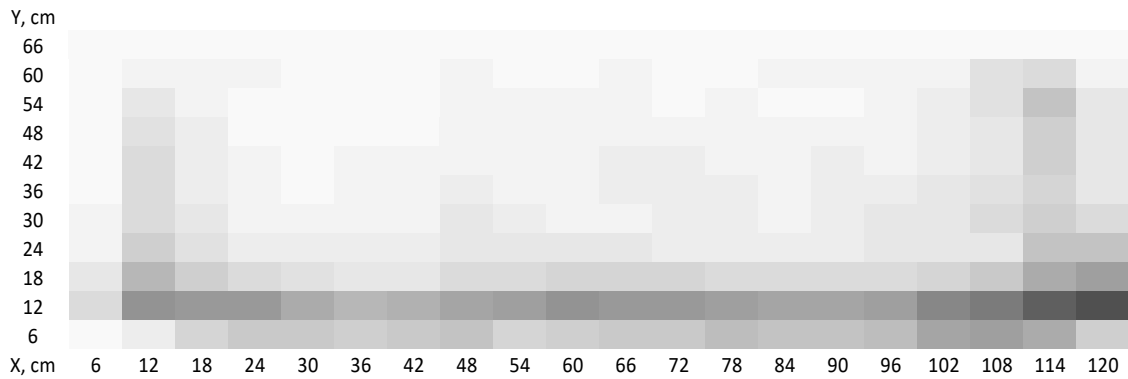


Figure 4-20: Probability distribution of particle presence for MA2 at 0.60 m/s and room temperature

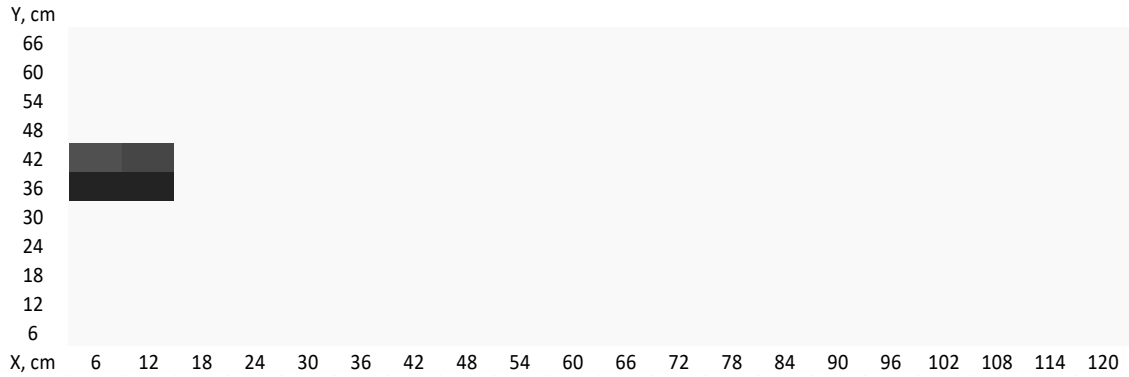


Figure 4-21: Probability distribution of MA2 presence at 0.06 m/s and 120 °C

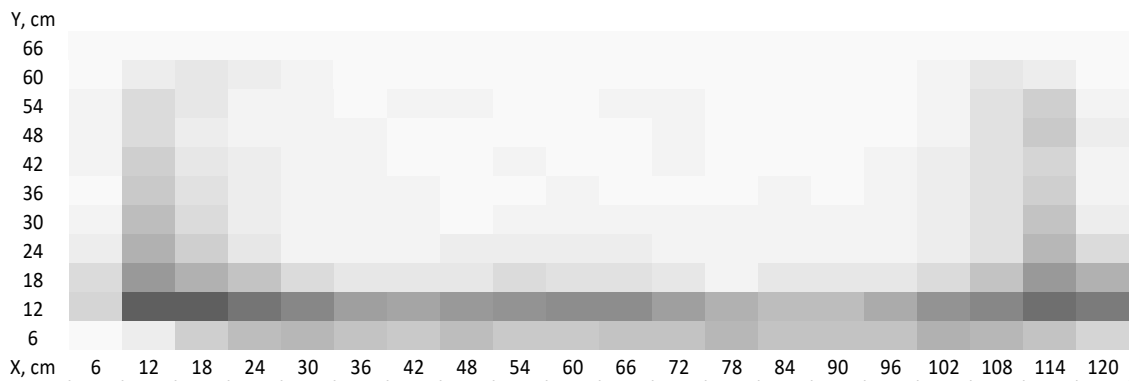


Figure 4-22: Probability distribution of MA2 presence at 0.35 m/s and 120 °C

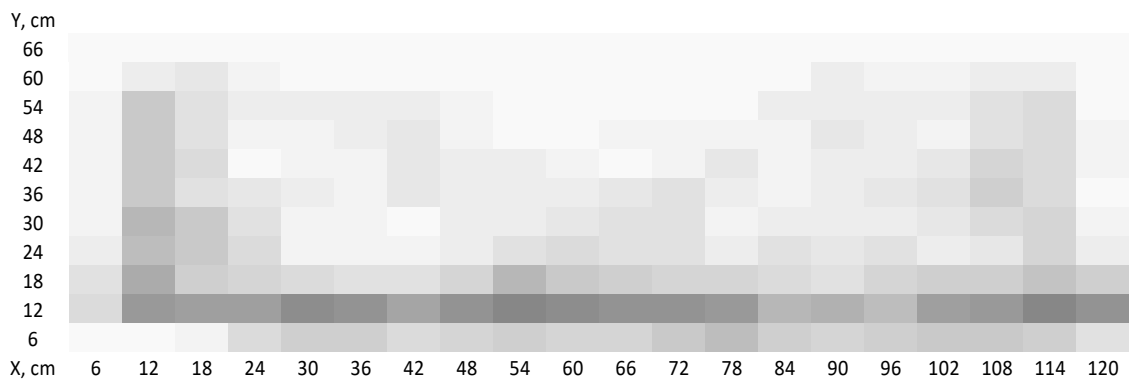


Figure 4-23: Probability distribution of MA2 presence at 0.60 m/s and 120 °C

4.2.2 Results for Model Agglomerate-1 (5500 μm)

Location coordinates obtained from the empirical equations using the data for MA1 were plotted with gas bubble flow distribution as shown in Figures 4-24 to 4-31. The solid line

in the figures for tracer locations corresponds to the bubble flow distribution on the secondary y-axis. The agglomerate again did not move at 0.06 m/s indicating poor gas distribution in the bed. Comparison of Figures 4-24 and 4-29 shows that the right side of the bed was not fully fluidized at 0.06 m/s. Although the agglomerate moved for 0.10 m/s, it seems like it was stuck near the gas distributor. Further analysis showed that the agglomerate did not move for a time in this region and then moved, however, it got stuck again in the same region after some time but was released afterwards. The results show that the model agglomerate segregated at a lower velocity (0.35 m/s) at both room temperature and 120 °C. However, it segregated in the top region at higher velocities i.e. 0.50 m/s and 0.60 m/s. Segregation in the top region for mid-size agglomerates was not seen in the runs with liquid injection. However, the agglomerates were collected after the de-fluidization of the bed whereas the results here show agglomerate presence in the fluidized bed. It might be because agglomerates at the top sunk when the bubbles in the fluidized bed escaped after de-fluidization changing some of the agglomerates distribution in the de-fluidized bed compared to the fluidized bed.

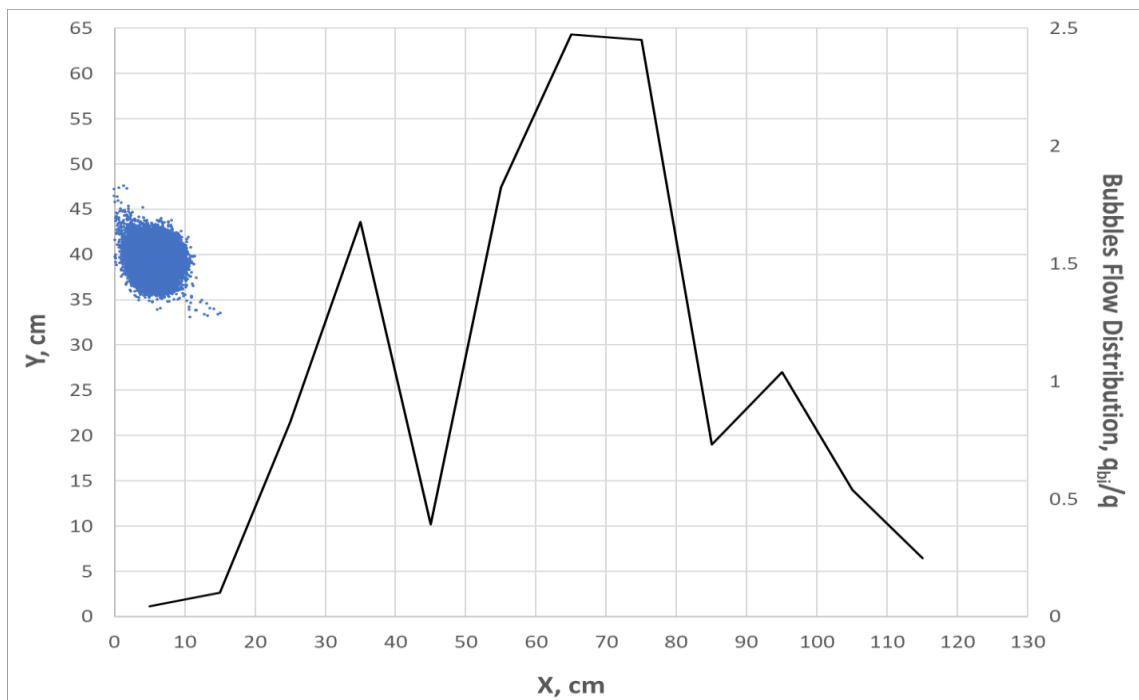


Figure 4-24: Tracer locations and gas bubble flow distribution for MA1 at 0.06 m/s and room temperature

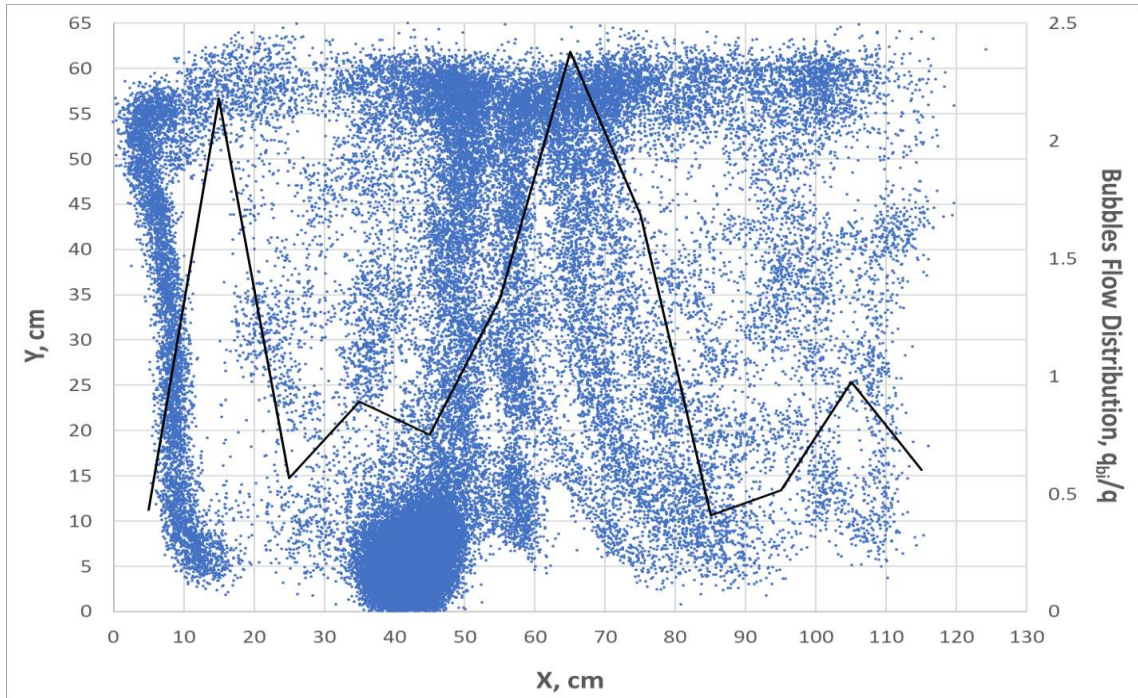


Figure 4-25: Tracer locations and gas bubble flow distribution for MA1 at 0.10 m/s and room temperature

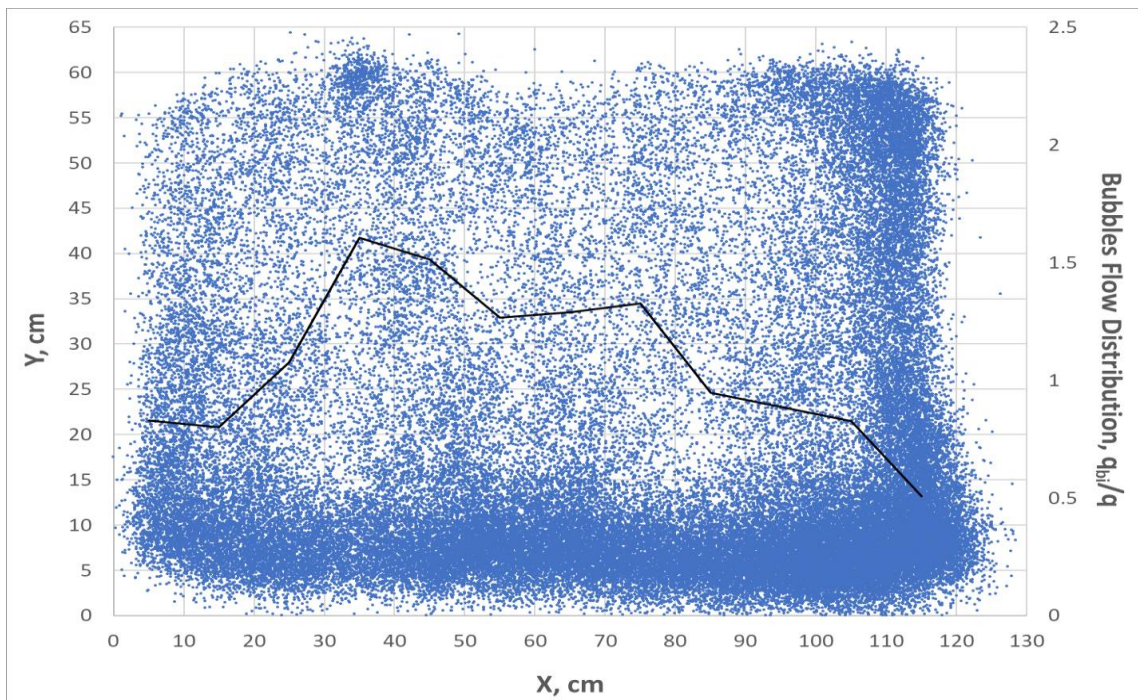


Figure 4-26: Tracer locations and gas bubble flow distribution for MA1 at 0.35 m/s and room temperature

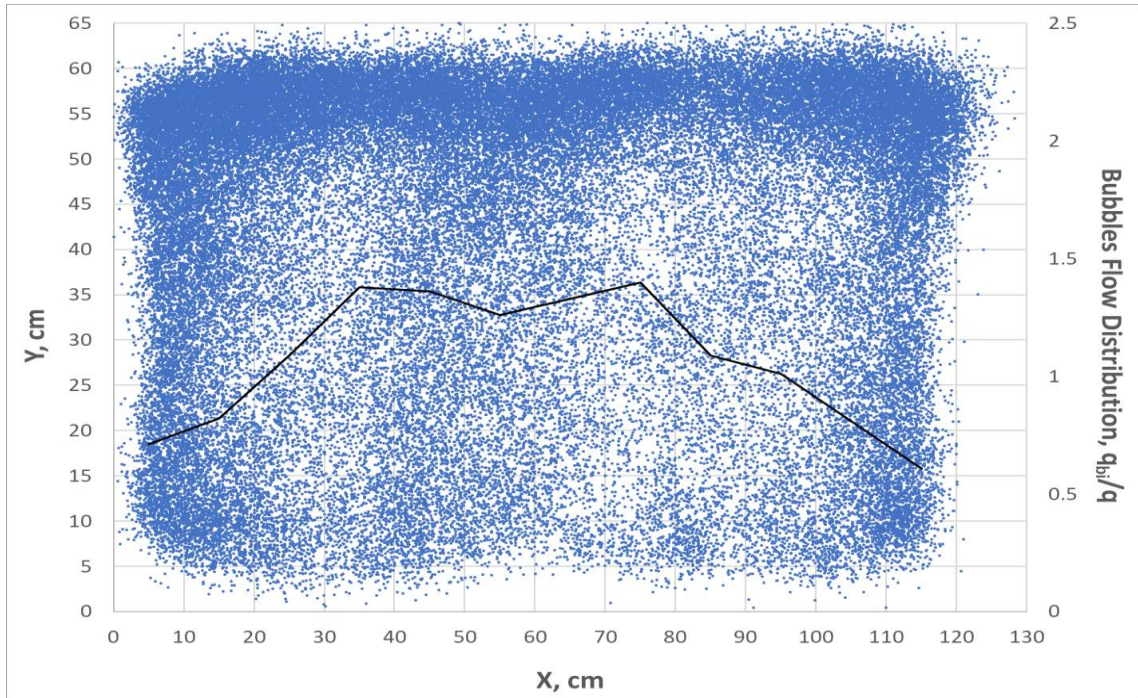


Figure 4-27: Tracer locations and gas bubble flow distribution for MA1 at 0.50 m/s and room temperature

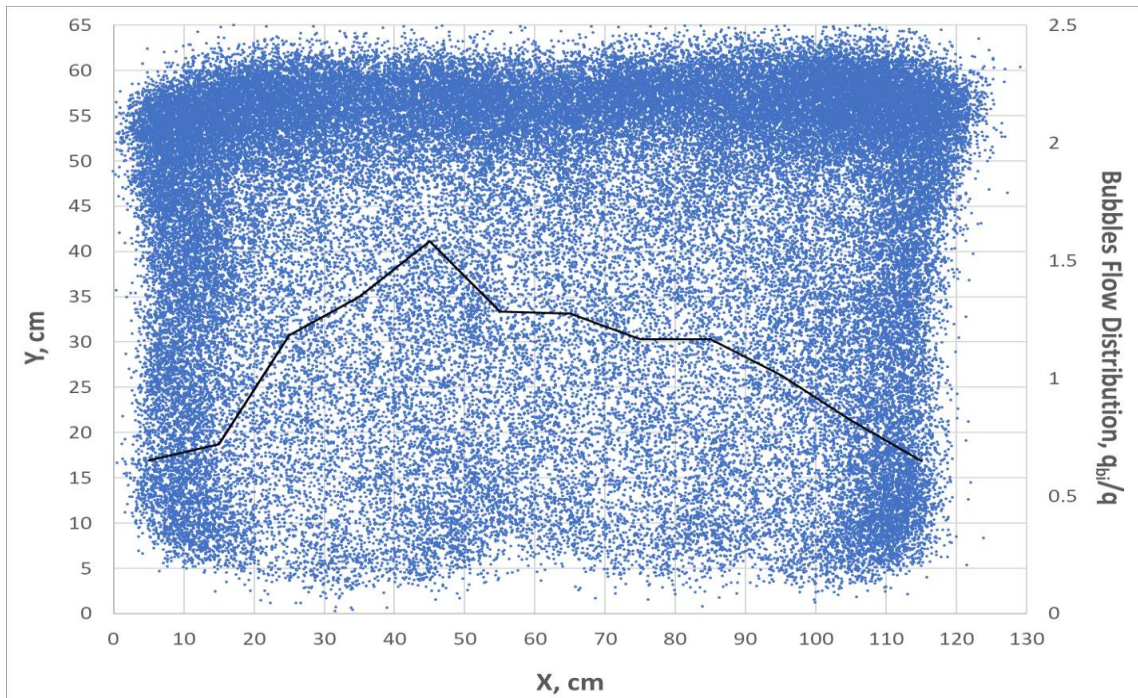


Figure 4-28: Tracer locations and gas bubble flow distribution for MA1 at 0.60 m/s and room temperature

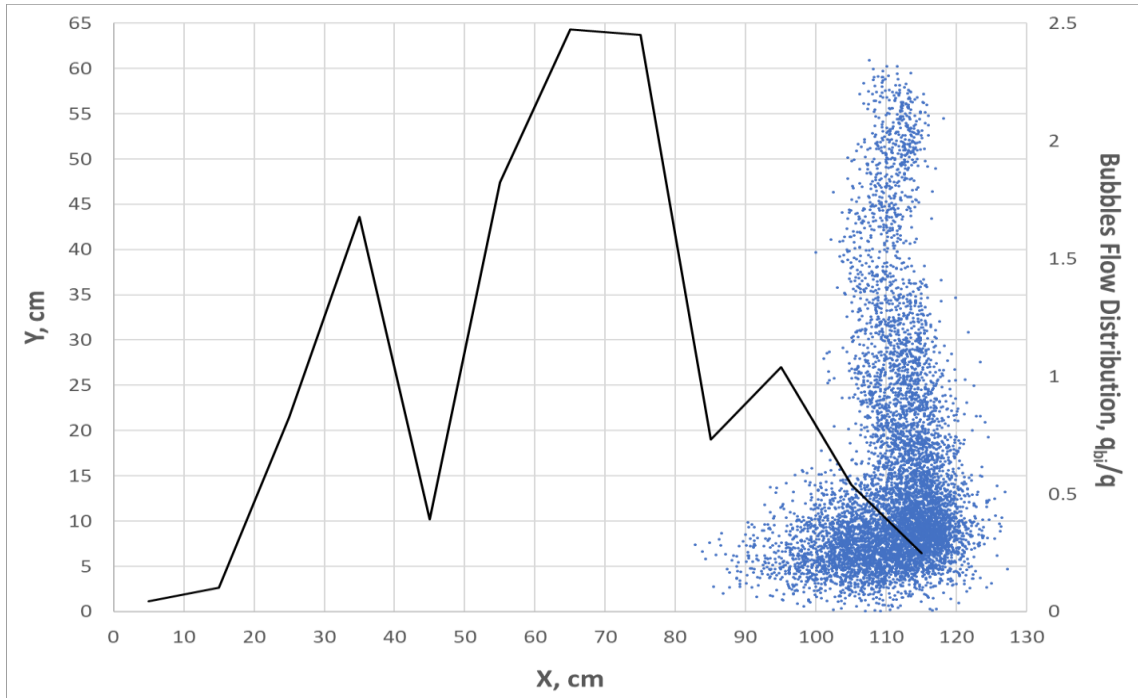


Figure 4-29: Tracer locations and gas bubble flow distribution for MA1 at 0.06 m/s and 120 °C

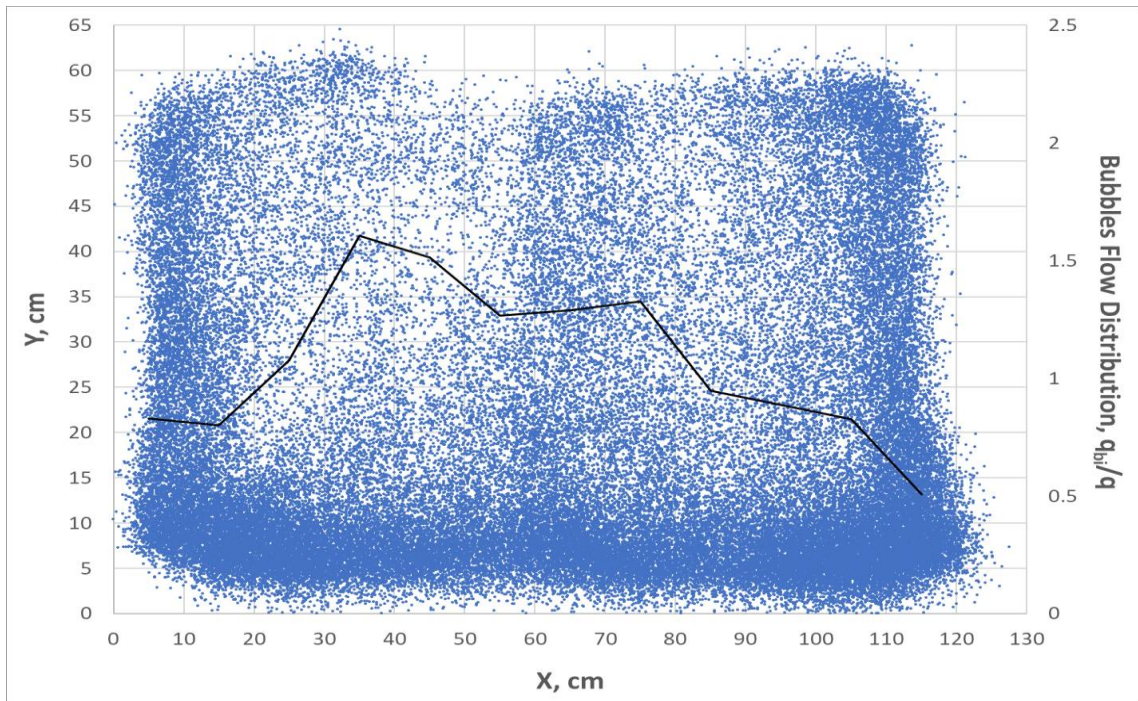


Figure 4-30: Tracer locations and gas bubble flow distribution for MA1 at 0.35 m/s and 120 °C

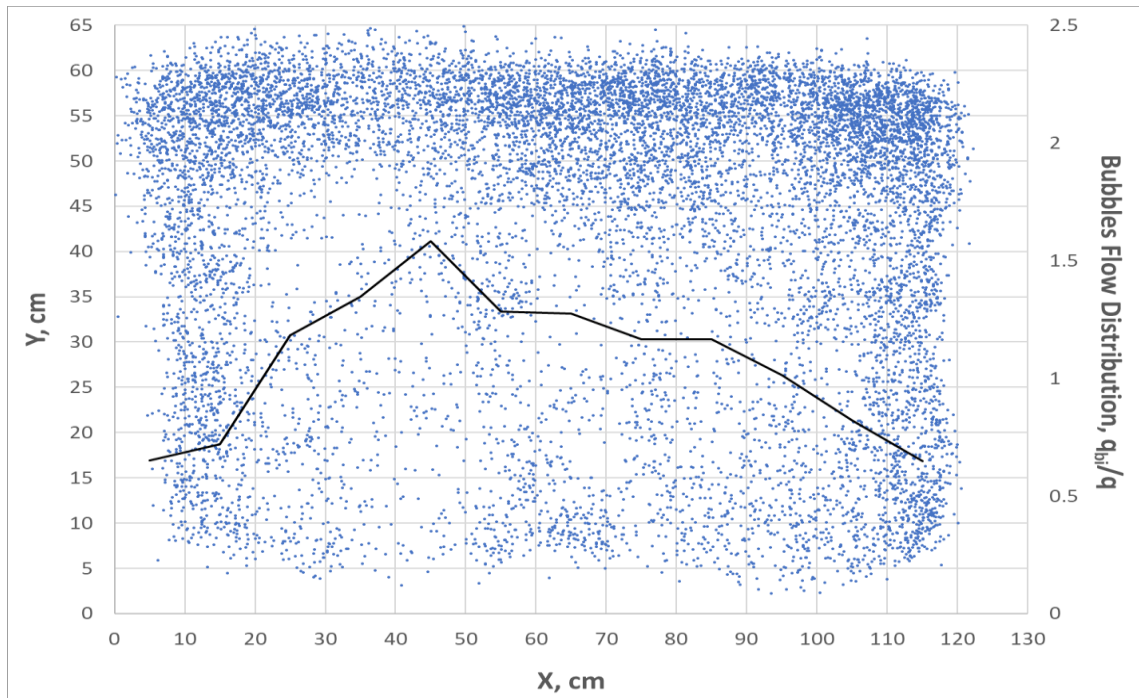
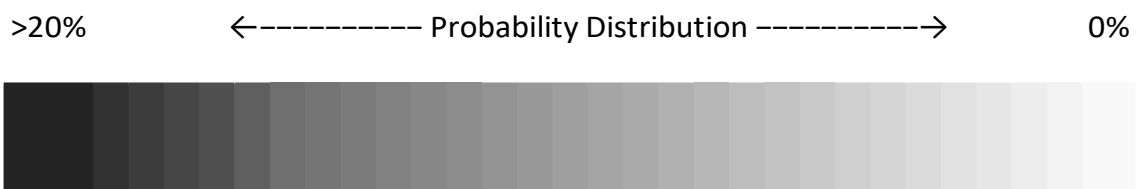


Figure 4-31: Tracer locations and gas bubble flow distribution for MA1 at 0.60 m/s and 120 °C

The probability distribution of agglomerate presence for MA1 at different gas velocities is shown in Figure 4-32 to Figure 4-39. It is observed that MA1 was more likely to be found near the top region at high velocities (0.50 m/s and 0.60 m/s). However, it was more likely to be found near the bottom at lower velocities indicating segregation of MA1.



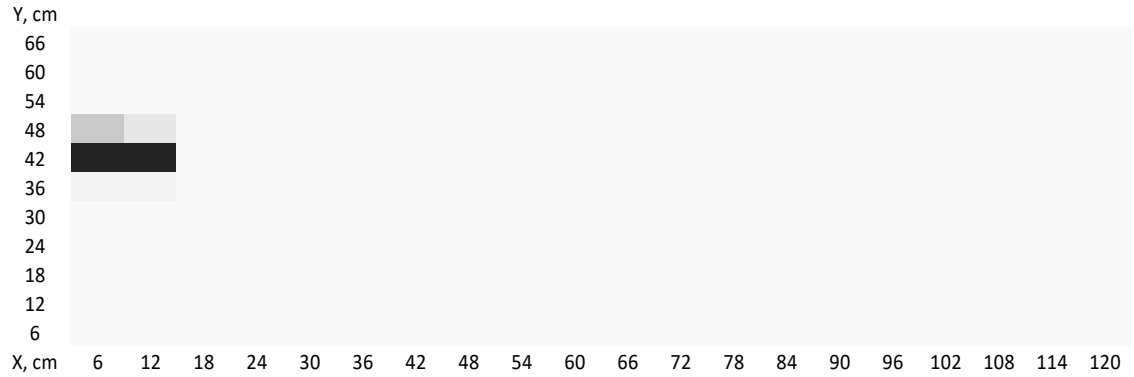


Figure 4-32: Probability distribution of particle presence for MA1 at 0.06 m/s and room temperature

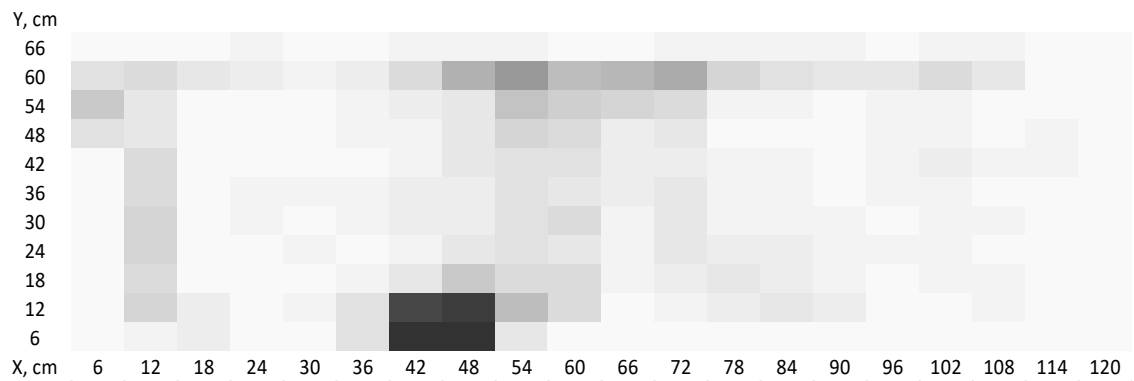


Figure 4-33: Probability distribution of particle presence for MA1 at 0.10 m/s and room temperature

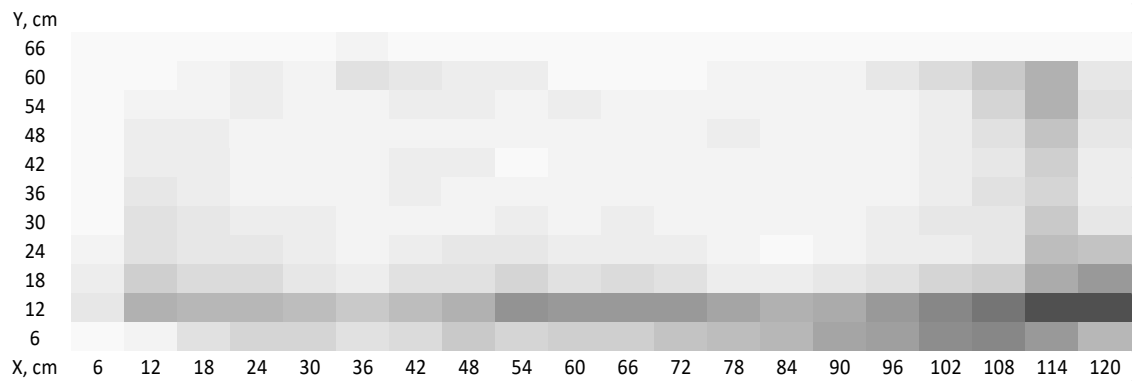


Figure 4-34: Probability distribution of particle presence for MA1 at 0.35 m/s and room temperature

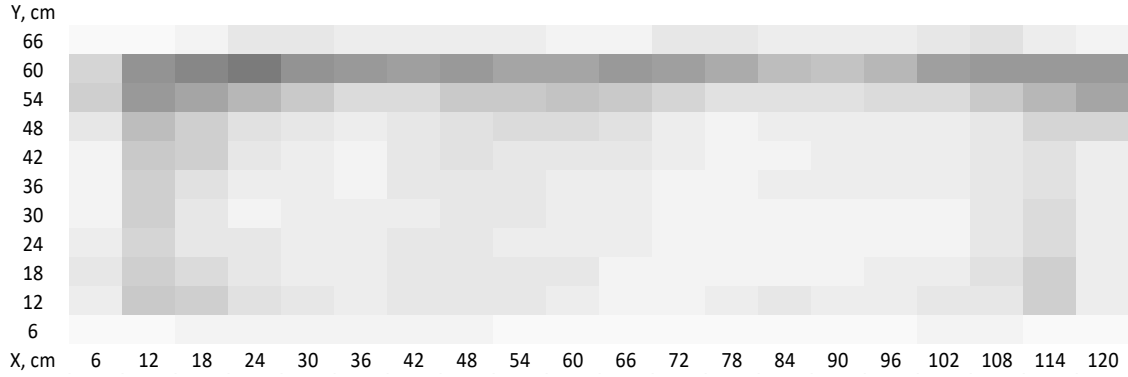


Figure 4-35: Probability distribution of particle presence for MA1 at 0.50 m/s and room temperature

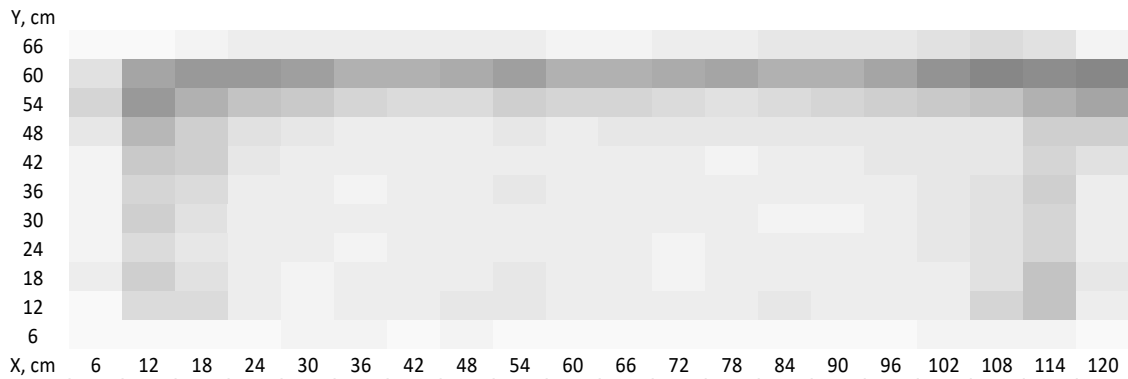


Figure 4-36: Probability distribution of particle presence for MA1 at 0.60 m/s and room temperature

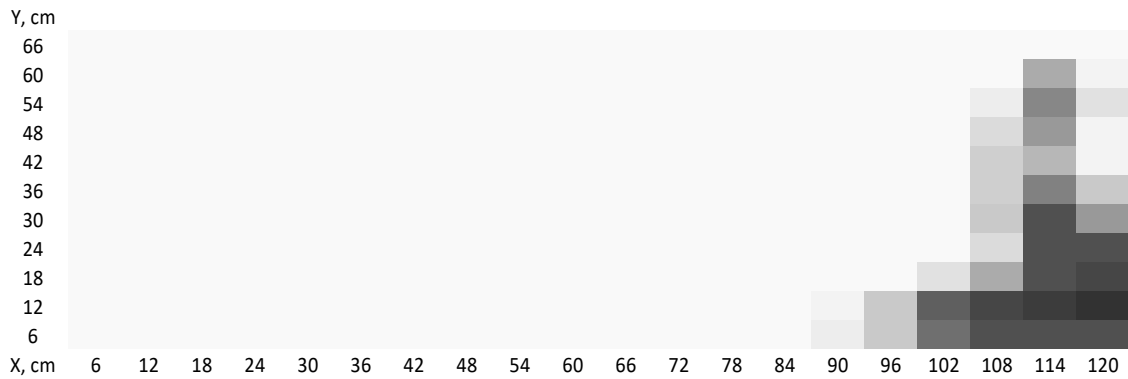


Figure 4-37: Probability distribution of MA1 presence at 0.06 m/s and 120 °C

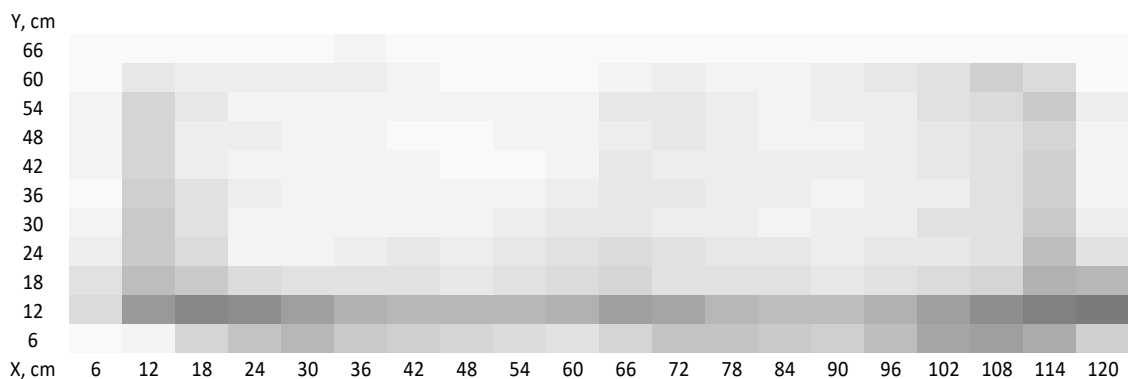


Figure 4-38: Probability distribution of MA1 presence at 0.35 m/s and 120 °C

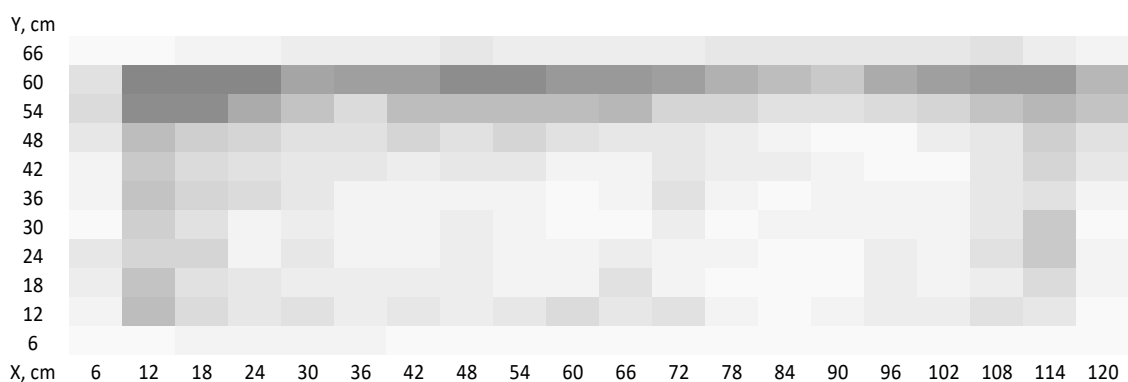


Figure 4-39: Probability distribution of MA1 presence at 0.60 m/s and 120 °C

4.2.3 Comparison of Results Obtained with Agglomerates formed by Liquid Injection Experiments with RPT Results

Indices of segregation for top and bottom were calculated for each run from the probability distribution of agglomerate presence in the fluidized bed except for 0.06 m/s and 0.10 m/s. Table 4-3 shows a comparison for index of segregation for the bottom between RPT and runs with liquid injection for MA2. The indices of segregation were defined in Chapter 3 (Section 3.3): a large value of an index of segregation indicates strong segregation.

V_g (m/s)	From Liquid Injection (at 120 °C)	From RPT of MA2	
		At Room Temp.	At 120 °C
0.35	2.4724	2.7495	2.4377
0.50	-	2.6632	-
0.60	1.6449	2.1462	2.0096

Table 4-2: Index of Segregation for bottom (IS_B) compared for different cases for a fluidization time of 4 min

Table 4-2 shows that segregation decreased with increases in gas velocity. There was some difference in index of segregation from liquid injection and index of segregation from RPT at 0.60 m/s. The reason for this difference might be that indices of segregation from RPT were obtained for a fluidized bed whereas indices of segregation from liquid injection were calculated for a de-fluidized bed: there was likely a change in the location of the agglomerates as the bed transitioned from fluidized to de-fluidized state.

Figures 4-40 and 4-41 show a comparison of index of segregation for the bottom for RPT and liquid injection (Gum Arabic or GA) experiments. For the 12500 μm agglomerate size, the results obtained with RPT and GA experiments were similar for both top and bottom indices of segregation. For the 5500 μm agglomerate, the index of segregation for the bottom obtained from RPT was lower than the index of segregation obtained from liquid injection experiments. The proportions of agglomerates obtained from the probability graphs (Figures 4-42 and 4-43) indicate that the vertical distribution of presence of agglomerate was similar to the actual presence of agglomerate (from GA experiments) for 12500 μm agglomerates, but differed for the 5500 μm . This variation in index of segregation and vertical distribution for 5500 μm agglomerates corresponds to the fact that 5500 μm agglomerates spent more time in the upper region of the bed (higher probability of presence in the upper region, Figure 4-43) as opposed to the 12500 μm agglomerate. Therefore, when the bed was slumped, the proportion of 5500 μm agglomerates increased in the lower region after de-fluidization as the bed slumped due to escaping bubbles.

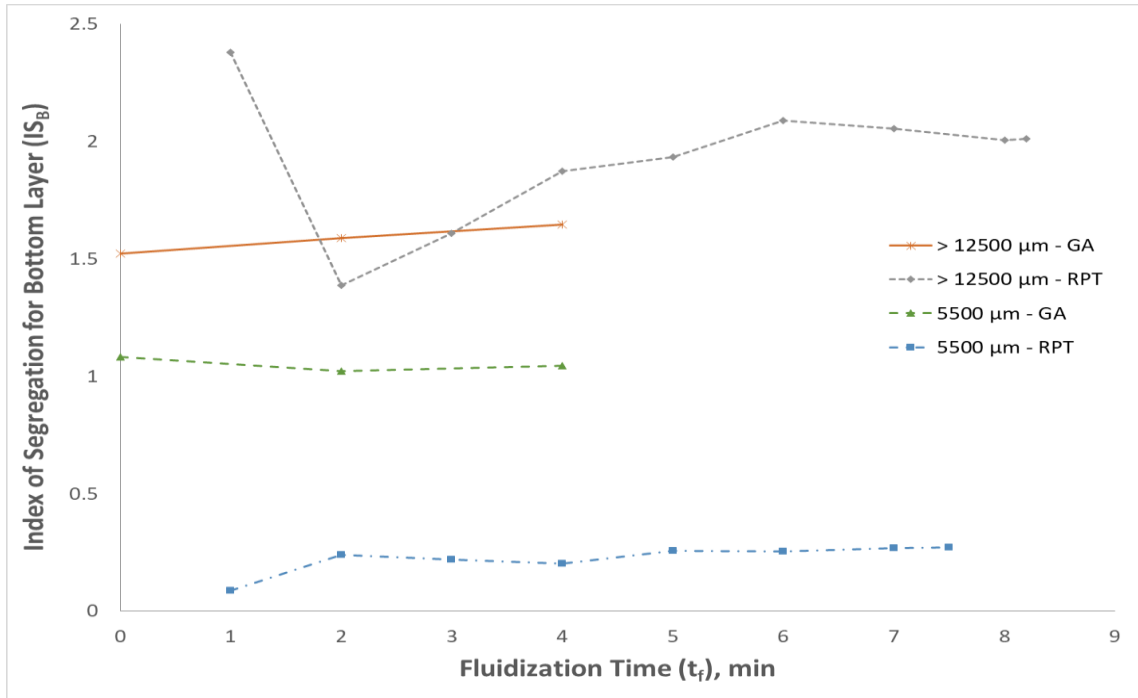


Figure 4-40: Index of Segregation for Bottom vs. fluidization time at 0.60 m/s

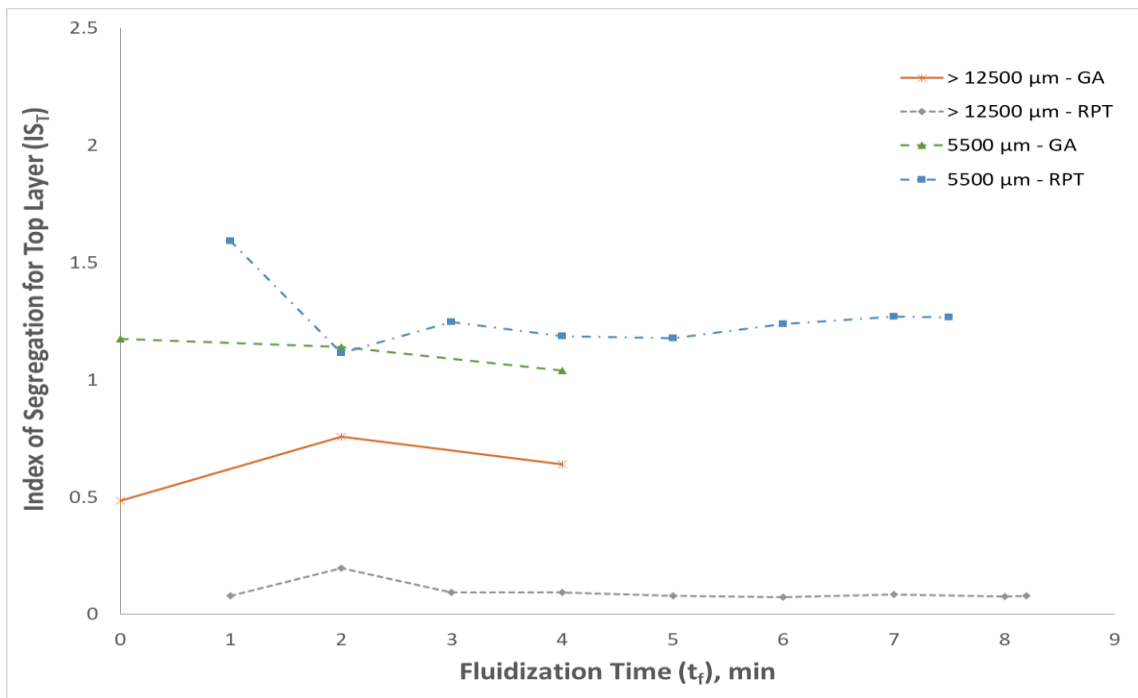


Figure 4-41: Index of Segregation for Top vs. fluidization time at 0.60 m/s

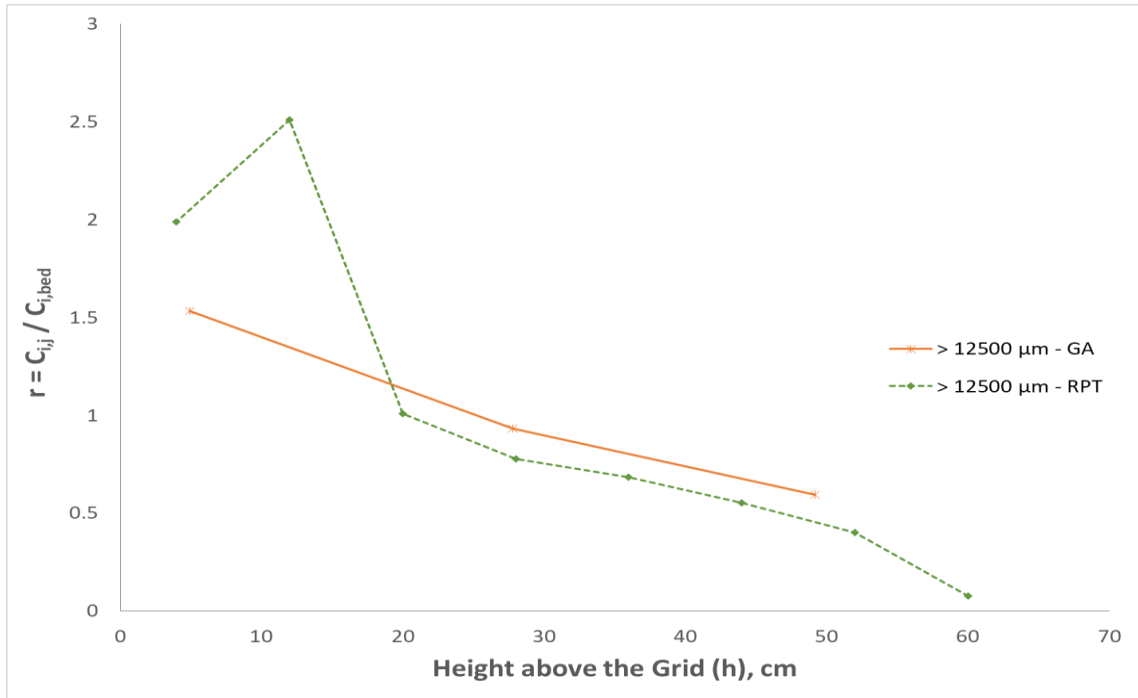


Figure 4-42: Vertical distribution of 12500 μm at 0.60 m/s

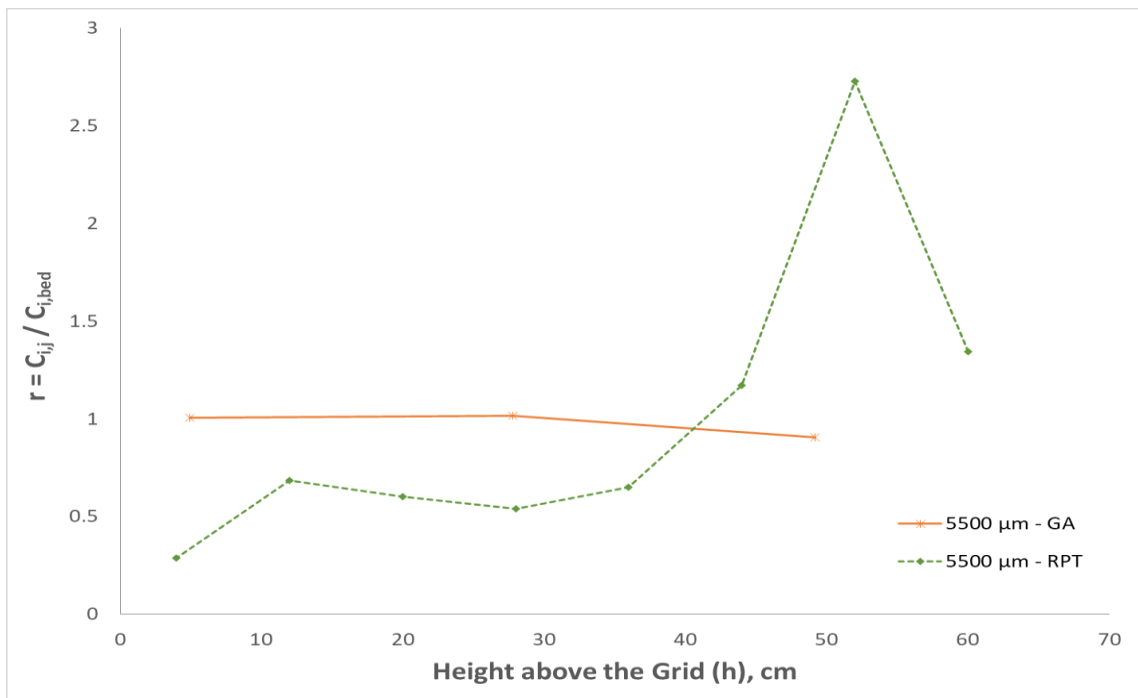


Figure 4-43: Vertical distribution of 5500 μm at 0.60 m/s

Figures 4-44 to 4-47 show the comparison of lateral distribution of agglomerates from RPT and liquid injection (GA) experiments. The lateral presence of agglomerate in the fluidized bed from RPT shows the effect of presence of bubbles in the region (Figures 3-30 to 3-33). The higher the bubble fraction in a region, the lower the agglomerate presence in that region. However, the ratio of the average agglomerate presence in the right side of the bed to the left side of the bed was close to 1 which means the average agglomerate presence in both halves was similar. This corresponds to the results of the liquid injection experiments in Section 3.3.2 (Figures 3-20 to 3-23) and gas bubble distribution provided in Section 3.3.4 which showed that the average proportion of actual agglomerates and the gas bubble flow in both halves of the bed was similar as well.

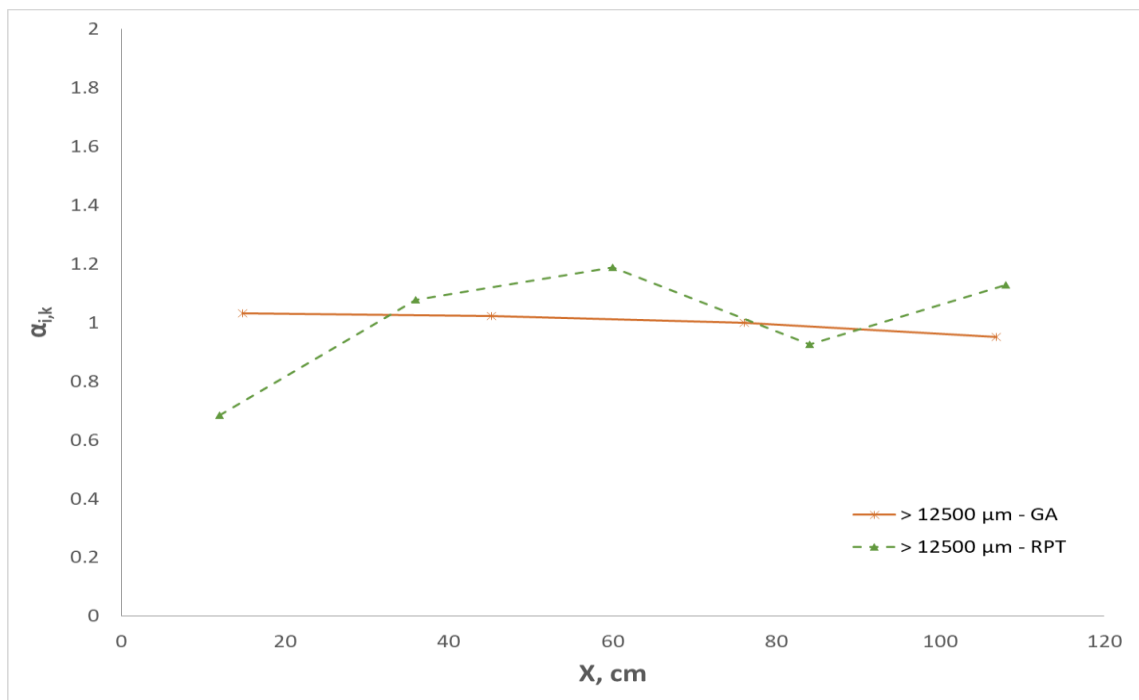


Figure 4-44: Lateral distribution of 12500 μm in Bottom layer at 0.60 m/s

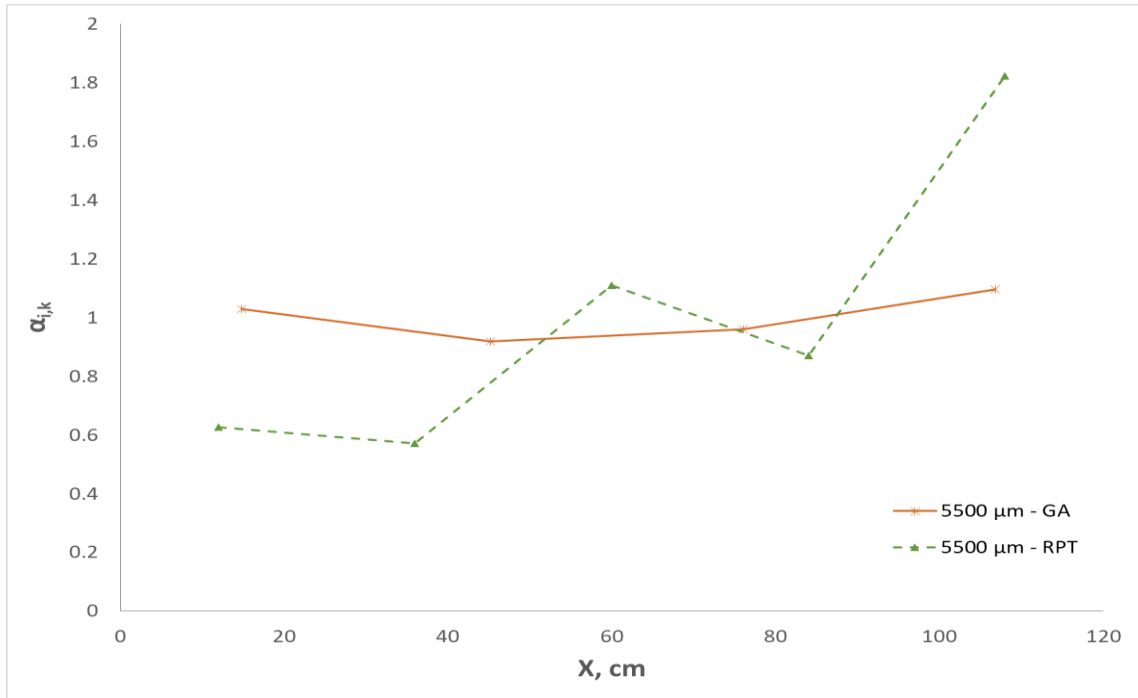


Figure 4-45: Lateral distribution of 5500 μm in Bottom layer at 0.60 m/s

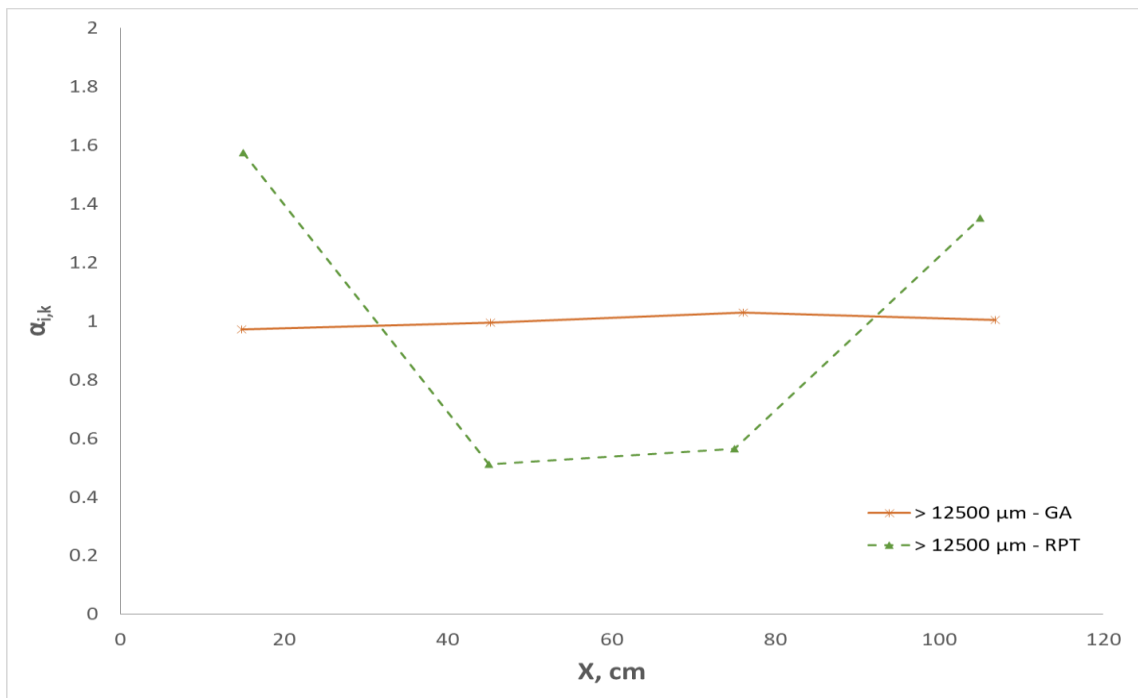


Figure 4-46: Lateral distribution of 12500 μm in Top layer at 0.60 m/s

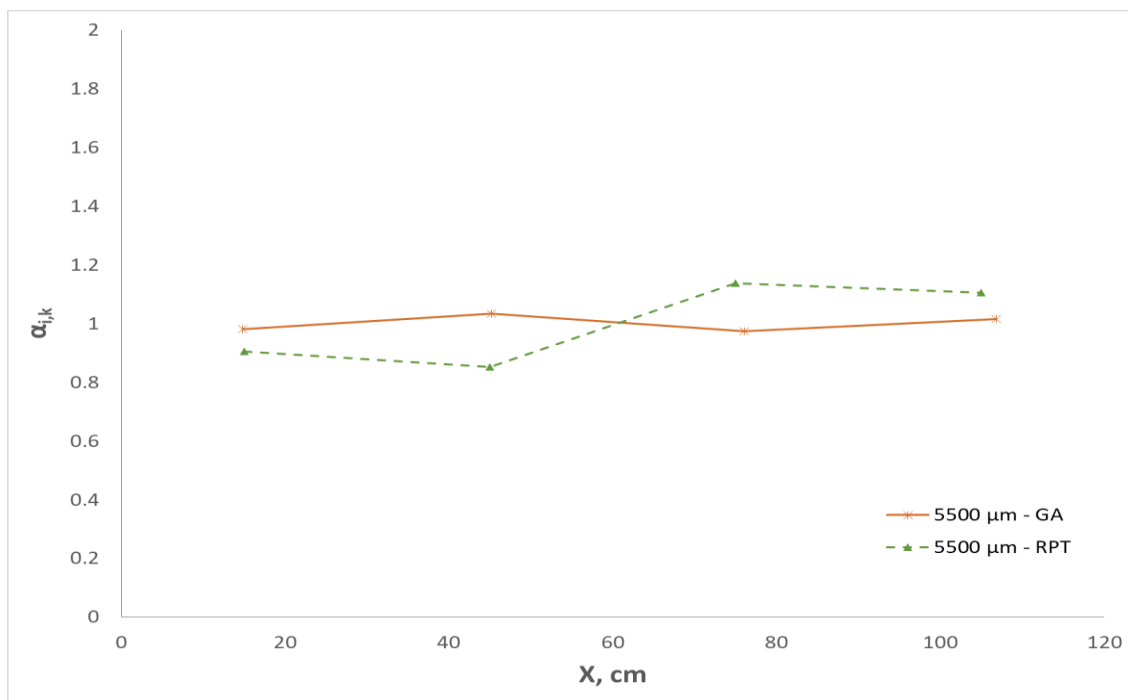


Figure 4-47: Lateral distribution of 5500 μm in Top layer at 0.60 m/s

4.3 Conclusion

Model agglomerates installed with a radioactive particle can be tracked in a fluidized bed using a calibrated Radioactive Particle Tracking (RPT) method. Empirical equations to determine location coordinates of agglomerates were developed from the calibration data. The calibration of the RPT system was a time-consuming task but it worked well for a 2D system.

Larger model agglomerates (12500 μm) spent more time near the bottom of the fluidized bed suggesting that large agglomerates segregate at high velocity. They were picked up by the bubbles, however, probability of presence of a large agglomerate was higher near the bottom of the fluidized bed. Segregation was reduced as the velocity in the fluidized bed was increased.

Smaller model agglomerates (5500 μm) spent more time near the top of the bed at high velocities, but segregated at low velocities. Hence, large agglomerates have a higher

tendency to segregate than the smaller particles. Segregation of agglomerates increased with a decrease in velocity.

Segregation and distribution results from Gum Arabic runs and results for gas bubble flow distribution from the tribo-electric method correlated with the results obtained from the RPT, validating the application of the RPT method.

Chapter 5

5 Study of the Impact of Radial Fluidization Gas Profile on Agglomerates Motion

The purpose of this chapter is to investigate how agglomerates behave when the two halves of the fluidized bed are subjected to two different gas velocities. One half of the bed has a higher gas velocity (and, hence, more gas bubbles) to simulate the core-annular flow observed in Fluid CokersTM.

5.1 Experimental Setup and Procedure

Studies described in this chapter used the same experimental setup and procedures for liquid injection experiments, triboelectric measurements and Radioactive Particle Tracking as in previous chapters. However, different gas velocities were generated in the two halves of the fluidized bed by adjusting the gas supply to the two sections of the gas distributor. The bed temperature was 120 °C.

Three cases were considered to obtain an average superficial gas velocity of 0.35 m/s as shown in Table 5-1. Although the wind-box is partitioned in two halves, there is no physical division of the bed solids in the fluidized bed. The fluidization gas from two halves can interact once it enters the fluidized bed. The results for the gas velocity of 0.35 m/s in both halves of the bed were considered as base case. The cases with different/uneven gas velocities in the two halves of the bed are further termed as “split velocity” cases.

Case	V_g in Left Section (m/s)	V_g in Right Section (m/s)	Average Superficial V_g (m/s)
Base Case	0.35	0.35	0.35
60L-10R	0.60	0.10	0.35
10L-60R	0.10	0.60	0.35

Table 5-1: Gas velocity provided by the two sections of the gas distributor

5.2 Results and Discussion

5.2.1 Gas Bubble Flow Distribution using Tribo-Electric Method

Figures 5-1 to 5-3 show the gas bubbles distribution for 3 heights for each case. Figures 5-2 and 5-3 show that more gas bubbles were present in the higher velocity side of the bed and that the gas bubbles distribution in the split cases was not perfectly symmetrical.

Figures 5-4 to 5-6 compare the gas bubbles distribution for a single row for all three cases. Figure 5-4 shows that the gas bubbles distribution is not as good for the bottom row (12 cm above the gas distributor) compared to the middle (32 cm above the gas distributor) and top (52 cm above the gas distributor) rows in Figures 5-5 and 5-6.

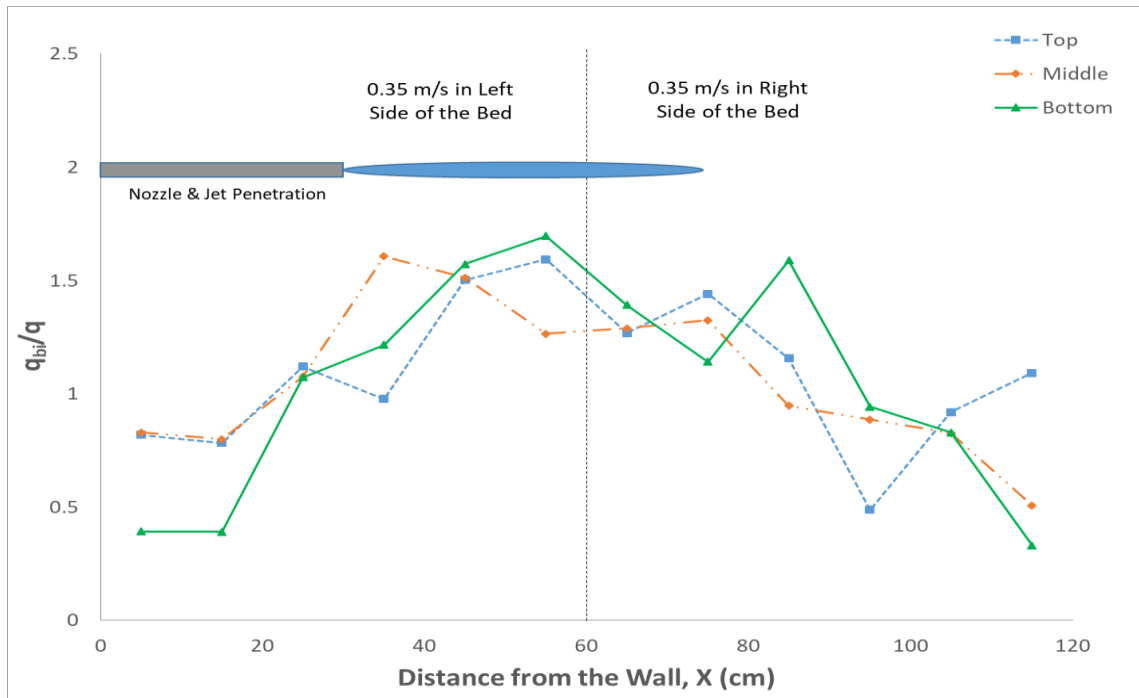


Figure 5-1: Gas bubble profile for $V_g = 0.35$ m/s in both halves of the fluidized bed (Bottom: $h = 12$ cm; Middle: $h = 32$ cm; Top: $h = 52$ cm)

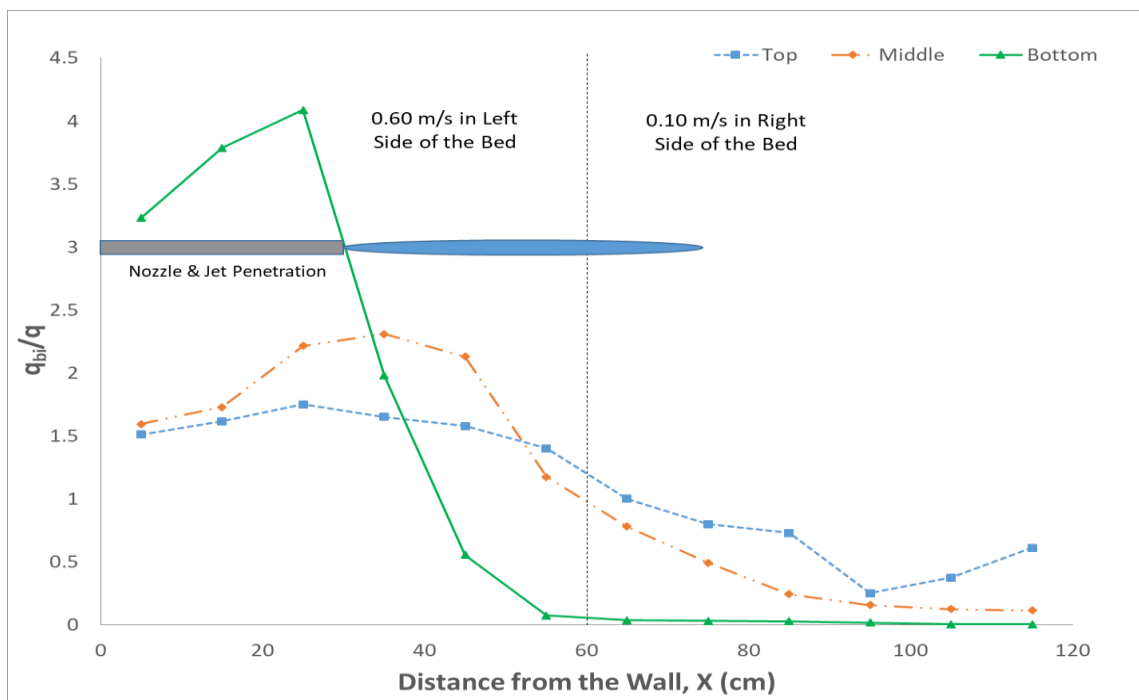


Figure 5-2: Gas bubble profile for 0.60 m/s in left and 0.10 m/s in right half of the fluidized bed (Bottom: $h = 12$ cm; Middle: $h = 32$ cm; Top: $h = 52$ cm)

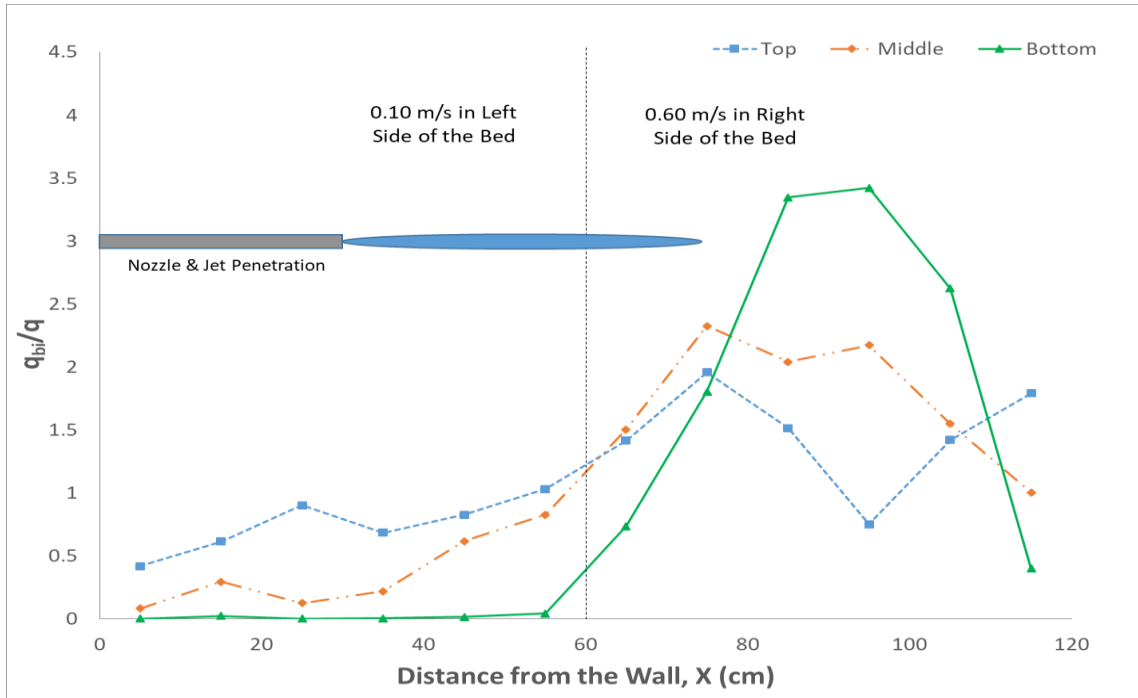


Figure 5-3: Gas bubble profile for 0.10 m/s in left and 0.60 m/s in right half of the fluidized bed (Bottom: $h = 12$ cm; Middle: $h = 32$ cm; Top: $h = 52$ cm)

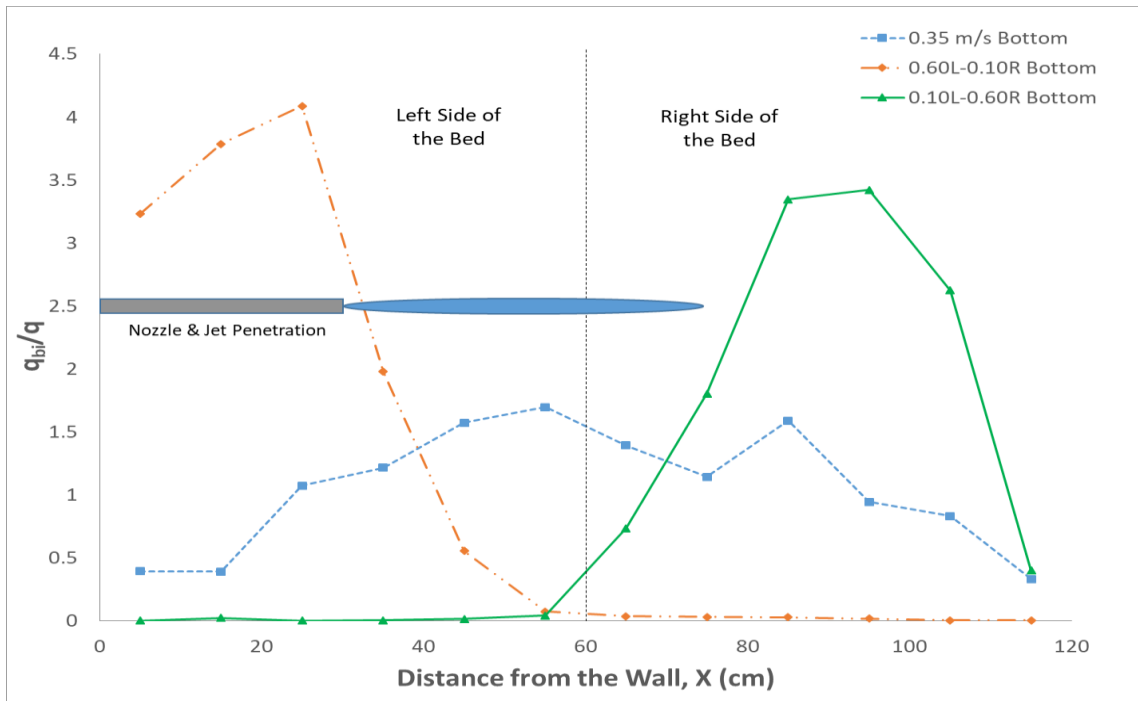


Figure 5-4: Gas bubble profile for Bottom row ($h = 12$ cm) for all velocities

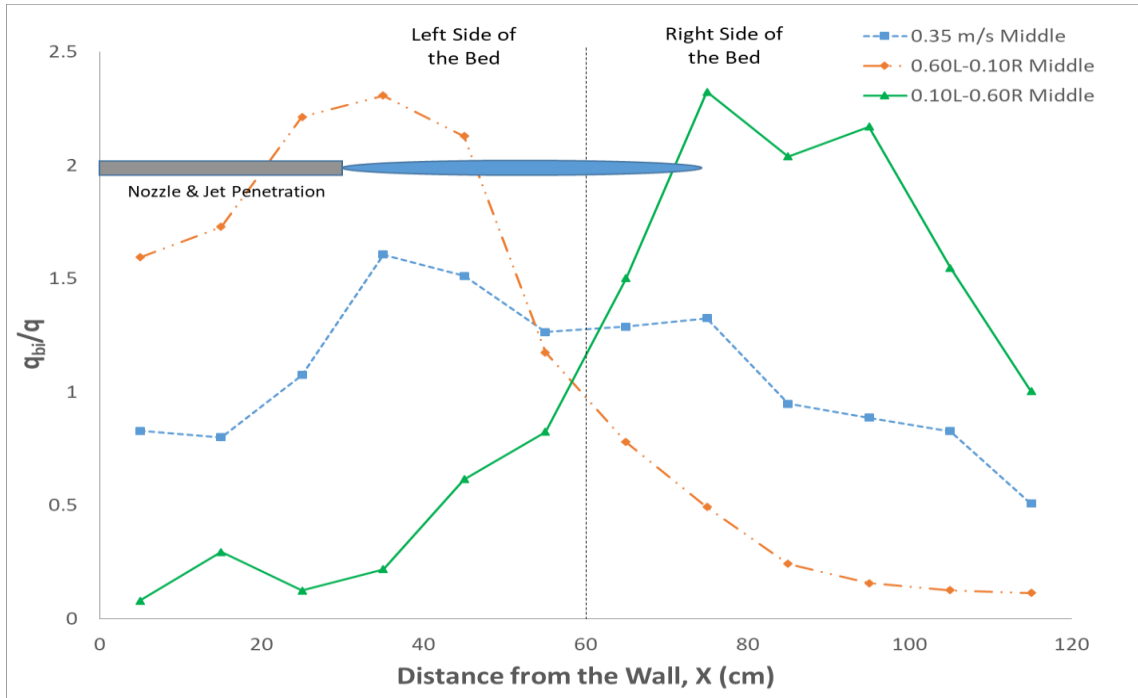


Figure 5-5: Gas bubble profile for Middle row ($h = 32$ cm) for all velocities

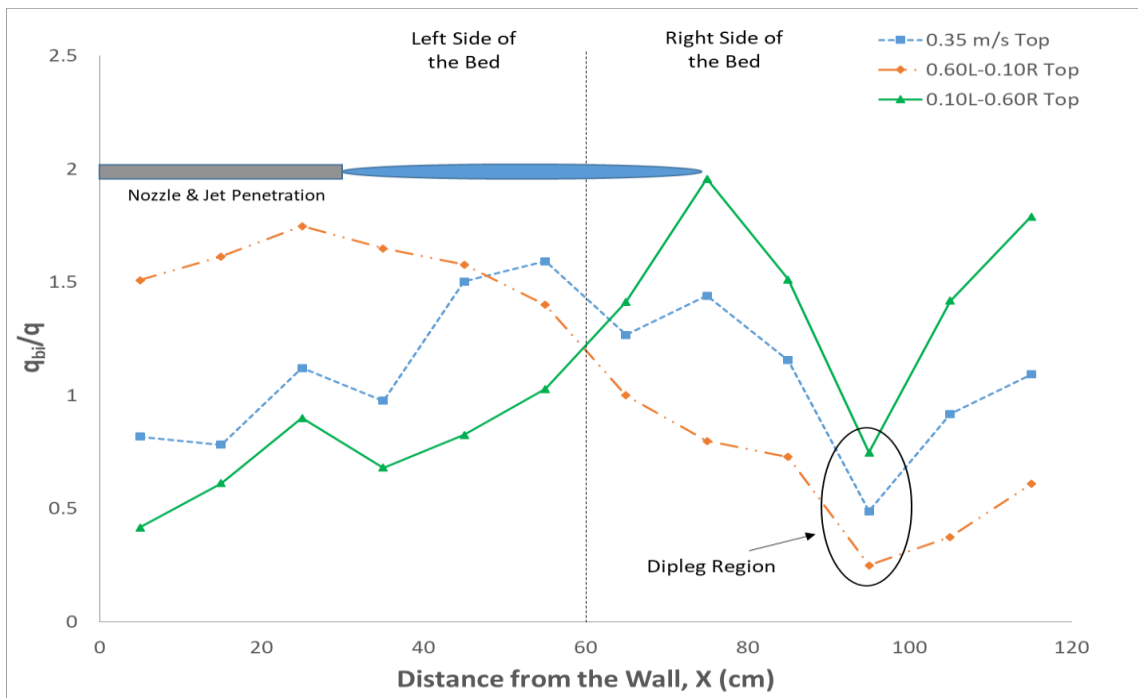


Figure 5-6: Gas bubble profile for Top row ($h = 52$ cm) for all velocities

5.2.2 Results for Liquid Injection Experiments

The experiments with liquid injection of gum Arabic solution show that uneven gas distribution (“split velocity”) caused a major increase in both agglomeration formation and subsequent agglomerate segregation, when compared to even gas distribution, with the same average superficial velocity on both sides of the bed. Figure 5-7 shows that more agglomerates were generated when the velocity in the jet tip region (right half of the bed) was lower.

Figure 5-8 shows that agglomerates larger than 3000 μm segregated more strongly near the bottom for split velocity cases, especially for agglomerates larger than 9500 μm . Segregation for agglomerates larger than 9500 μm was stronger near the bottom for 60L-10R case compared to 10L-60R case (Figure 5-8) which might be because the cumulative mass of agglomerates in the bed for 60L-10R case was higher than the 10L-60R case (Figure 5-7). Figure 5-9 shows the larger agglomerates were not as absent from the top layer when the gas distribution was split: this is expected as a split fluidization gas distribution induces stronger circulation currents that are more likely to circulate agglomerates to the top layer.

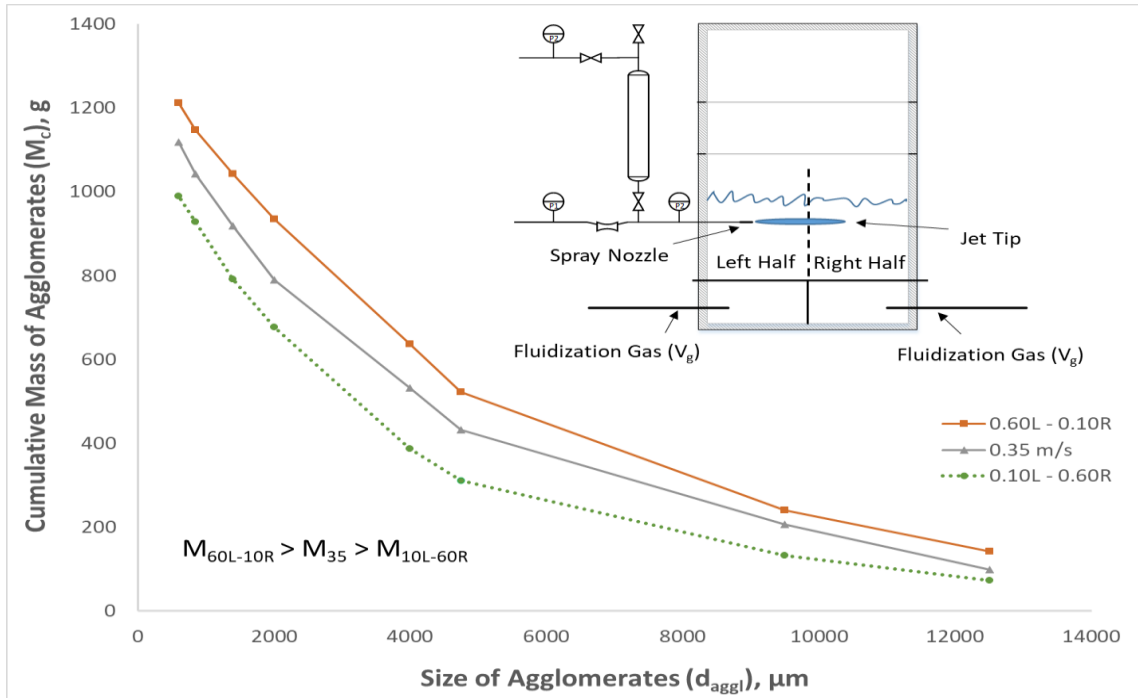


Figure 5-7: Cumulative mass of all collected agglomerates in the bed

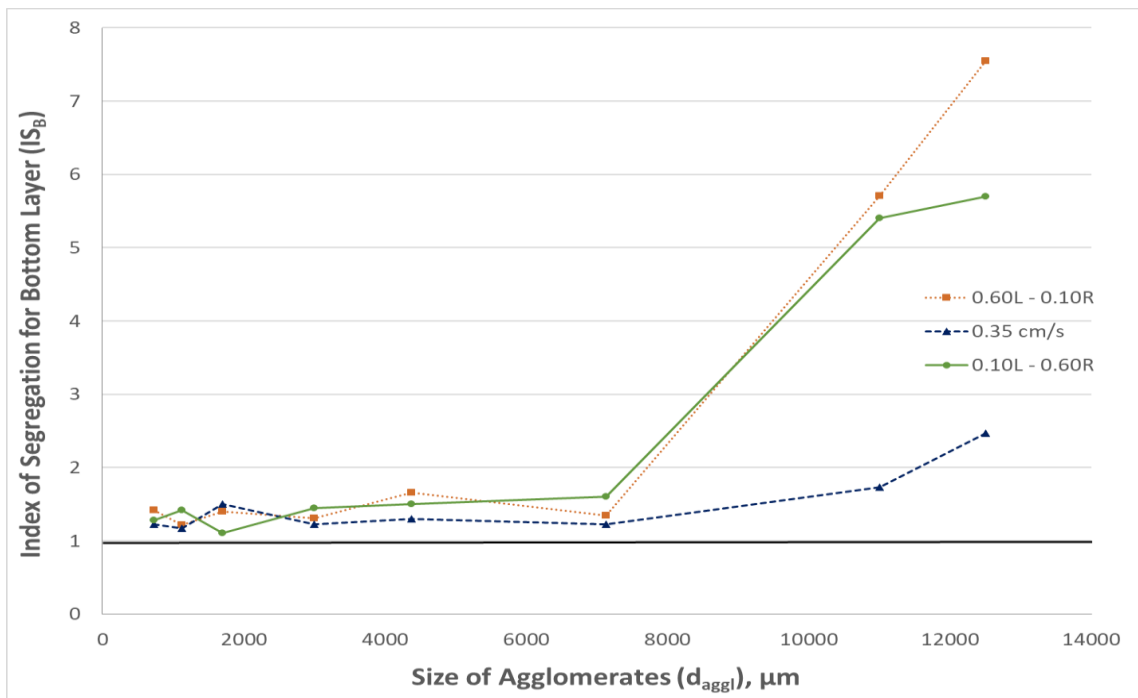


Figure 5-8: Index of Segregation for the Bottom layer

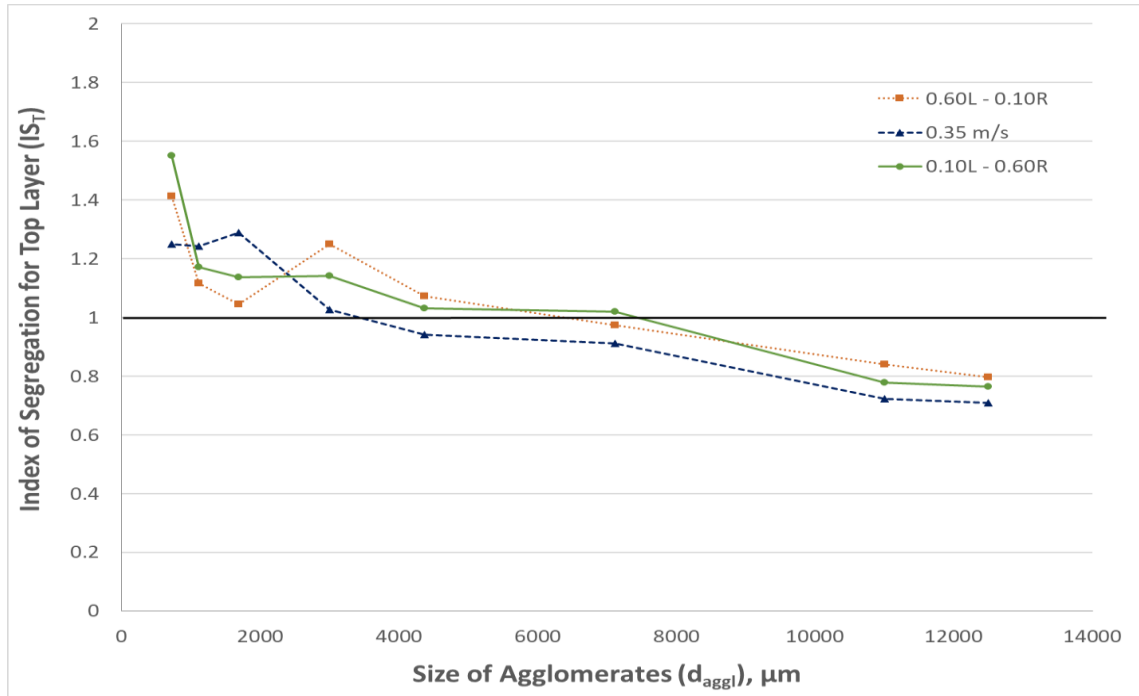


Figure 5-9: Index of Segregation for the Top layer

Agglomerates were well distributed laterally at 0.35 m/s in both halves of the bed (Figures 5-10 and 5-11). For split cases, lateral distribution of agglomerates (Figures 5-12 to 5-15) shows that a higher proportion of all agglomerates were present in the lower velocity side of the fluidized bed. This suggests that agglomerates were picked up by gas bubbles, which rose primarily through the higher velocity half of the bed, and then settled more slowly through the emulsion in the lower velocity half of the bed.

Density of agglomerates larger than 9500 μm was measured and found to be between 1380 kg/m^3 to 1475 kg/m^3 which is consistent with density of large agglomerates reported in Section-3.3.3.

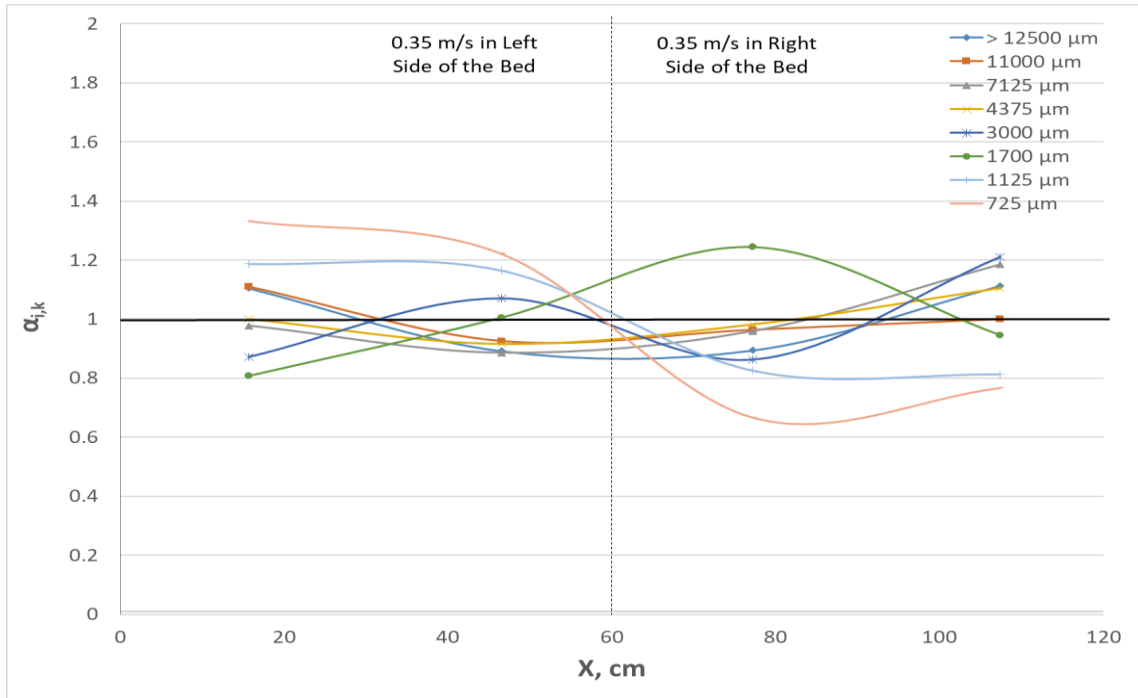


Figure 5-10: Lateral distribution of agglomerates for Bottom layer for 0.35 m/s in both halves of the bed

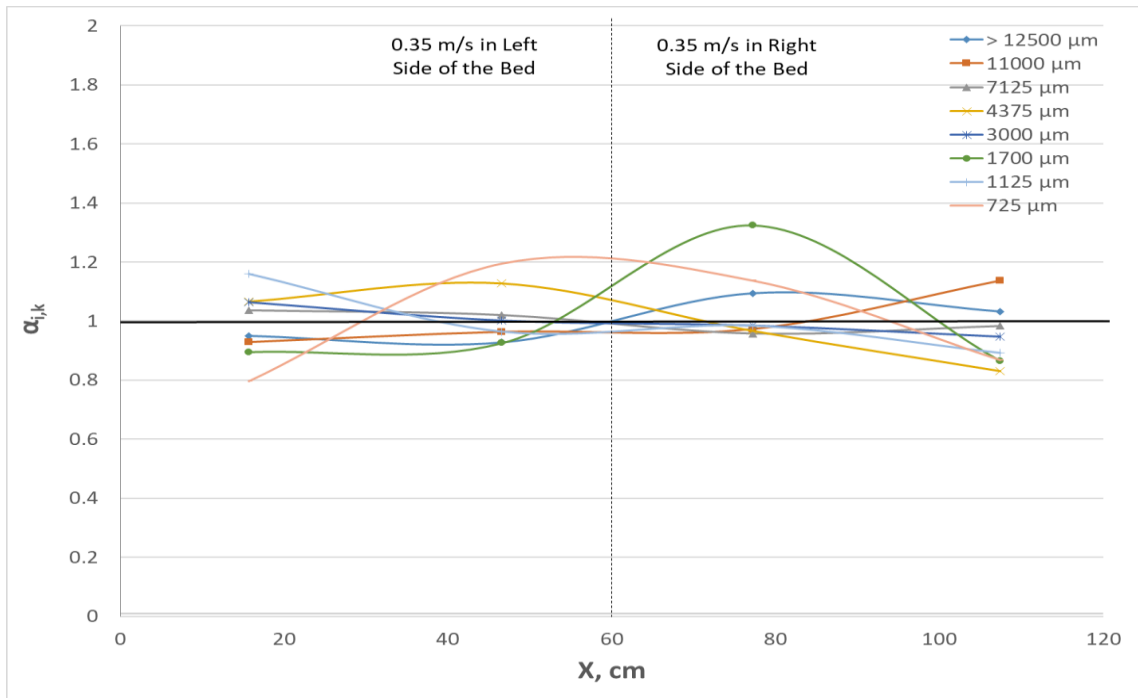


Figure 5-11: Lateral distribution of agglomerates for Top layer for 0.35 m/s in both halves of the bed

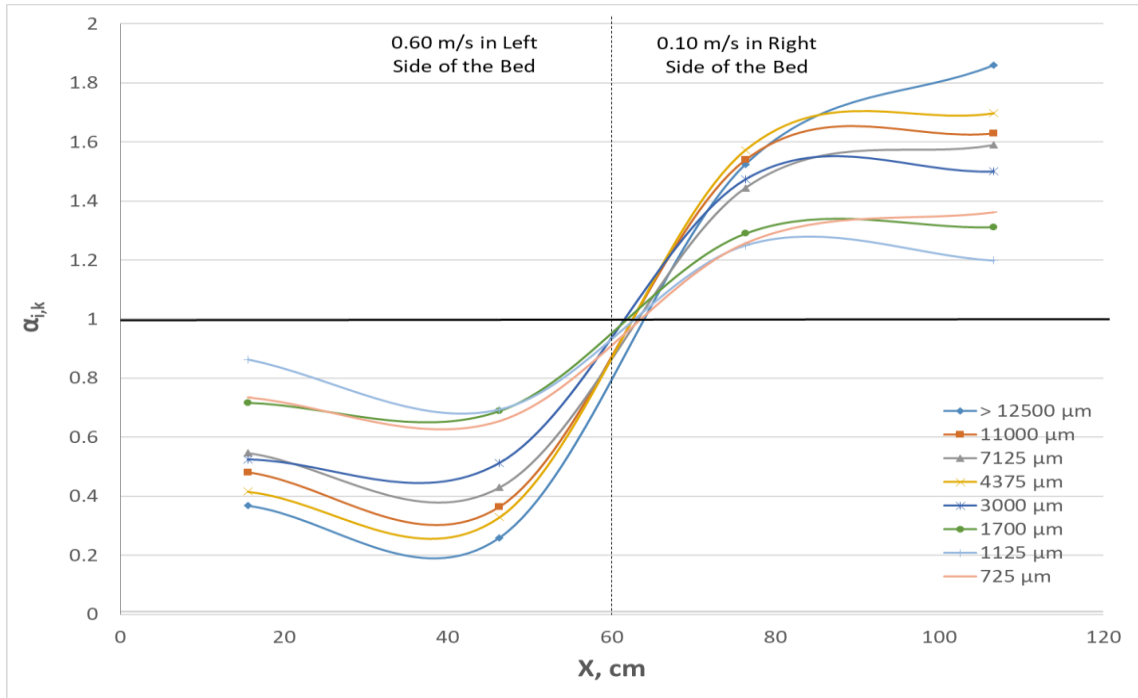


Figure 5-12: Lateral distribution of agglomerates for Bottom layer for 60L-10R

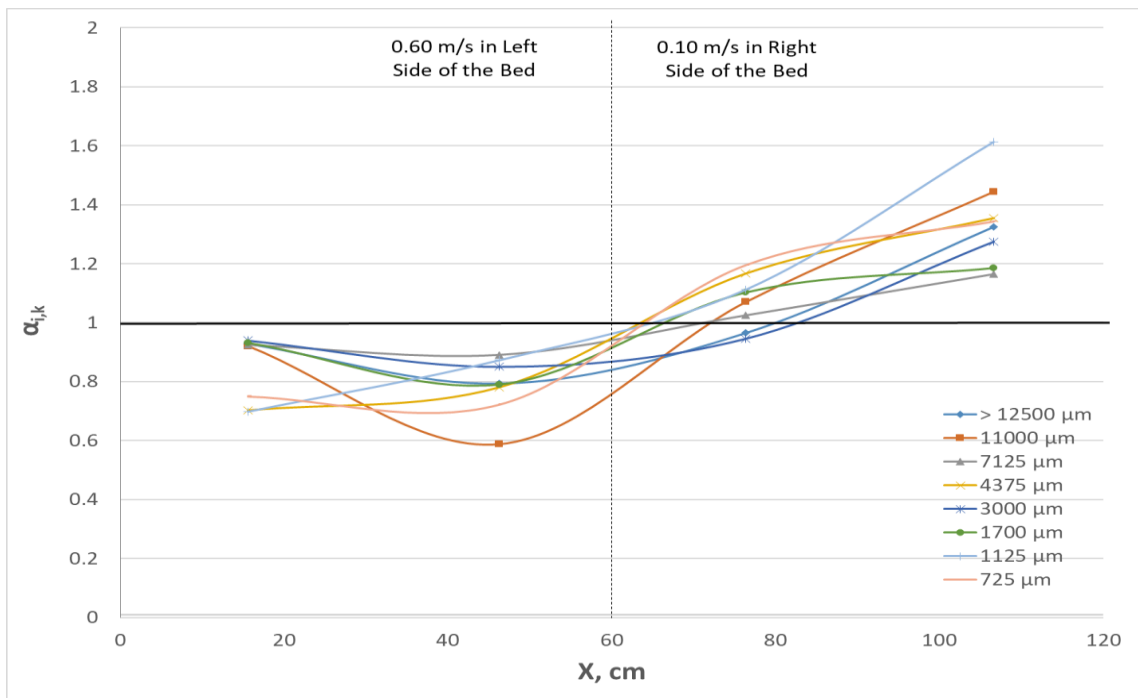


Figure 5-13: Lateral distribution of agglomerates for Top layer for 60L-10R

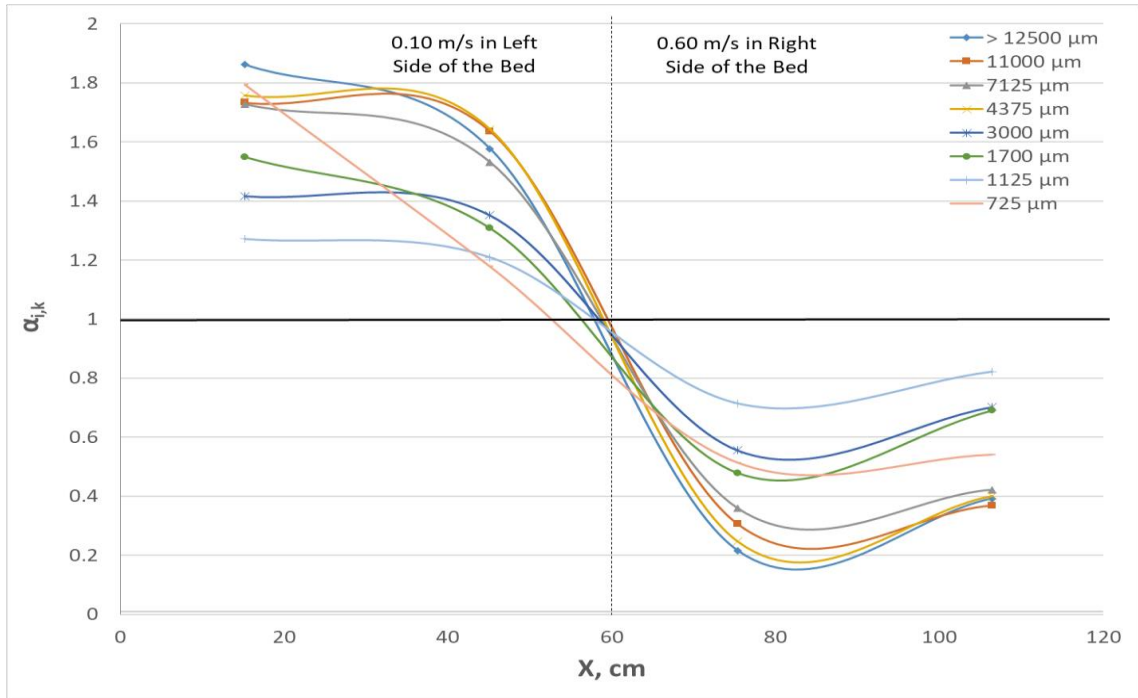


Figure 5-14: Lateral distribution of agglomerates for Bottom layer for 10L-60R

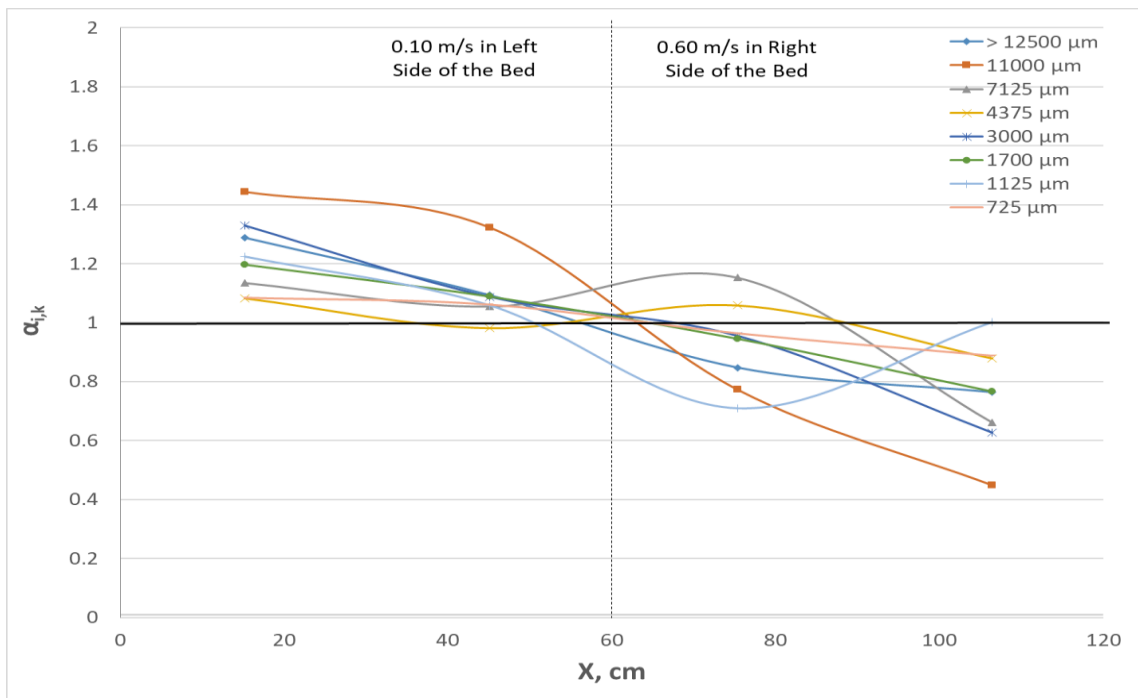


Figure 5-15: Lateral distribution of agglomerates for Top layer for 10L-60R

5.2.3 Results for Radioactive Particle Tracking

Location coordinates obtained from the empirical equations (Section 4.1.1.3) for MA2 (12500 μm and 1450 kg/m^3) were plotted with gas bubble flow distribution as shown in Figures 5-16 to 5-18. The solid line in the figures for tracer locations corresponds to the bubble flow distribution on the secondary y-axis.

The results show that the model agglomerate segregated in all cases. Figures 5-17 and 5-18 show the impact of core-annular behavior. The model agglomerate spent more time in the region with low bubble flow. Regions with high bubble flow seem to have lower agglomerate presence. Since the gas velocity in the two halves of the bed was switched for the split cases, mirrored results would be expected, but this was not the case because the gas distribution in the bed was not perfectly symmetrical as shown in Section 5.2.1.

Since overlapping points appear as one in this type of graph, probability distribution of agglomerate presence, as described in Section 4.2.1, was plotted in graphs shown in Figures 5-19 to 5-21. A shift in agglomerate presence is clear when Figure 5-19 is compared with Figures 5-20 and 5-21. Agglomerate presence greatly increased in the region of low flow as compared to the high flow region.

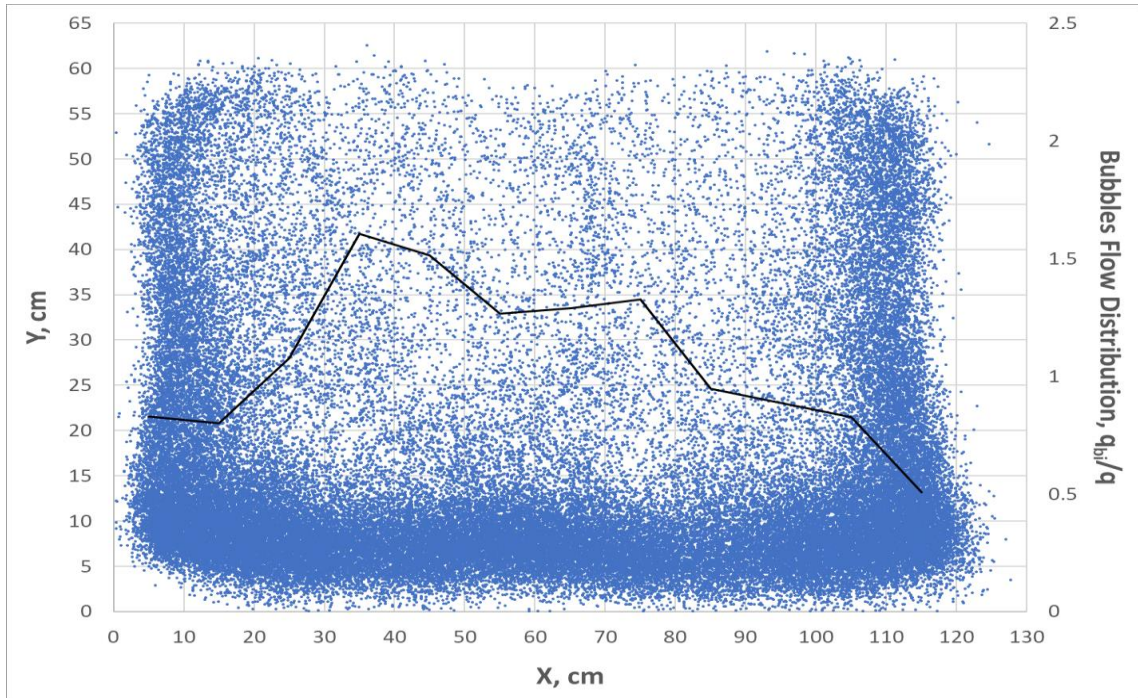


Figure 5-16: Tracer locations and gas bubble flow distribution for MA2 at 0.35 m/s in both halves of the bed

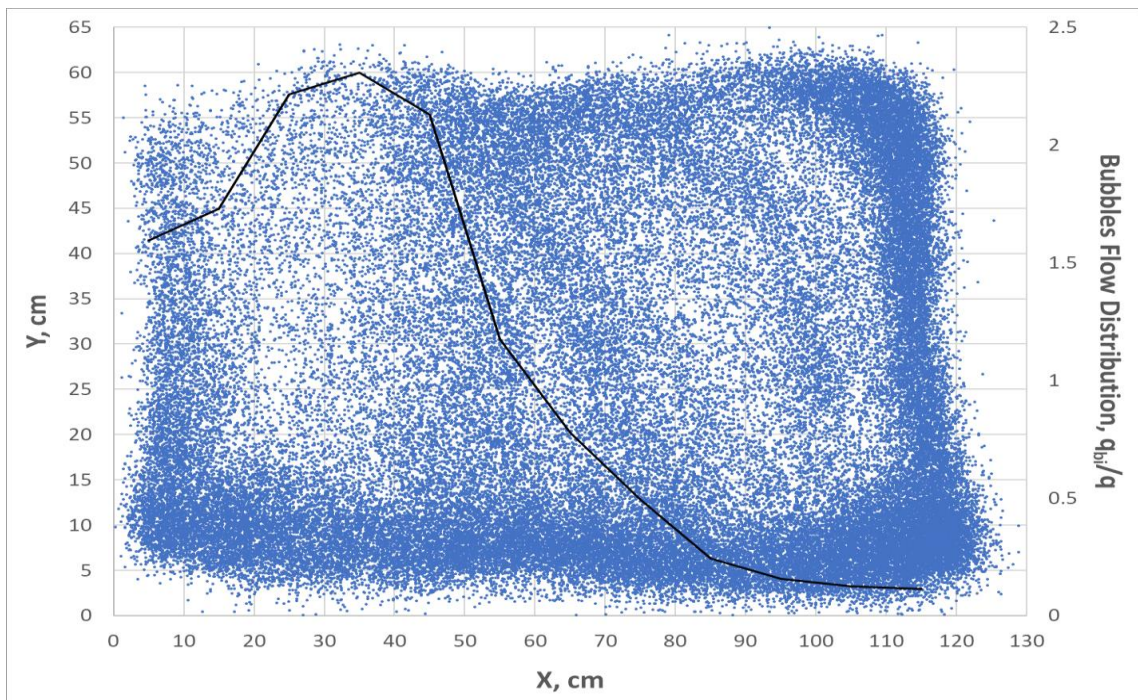


Figure 5-17: Tracer locations and gas bubble flow distribution for MA2 at 0.60 m/s in the left and 0.10 m/s in the right side of the bed

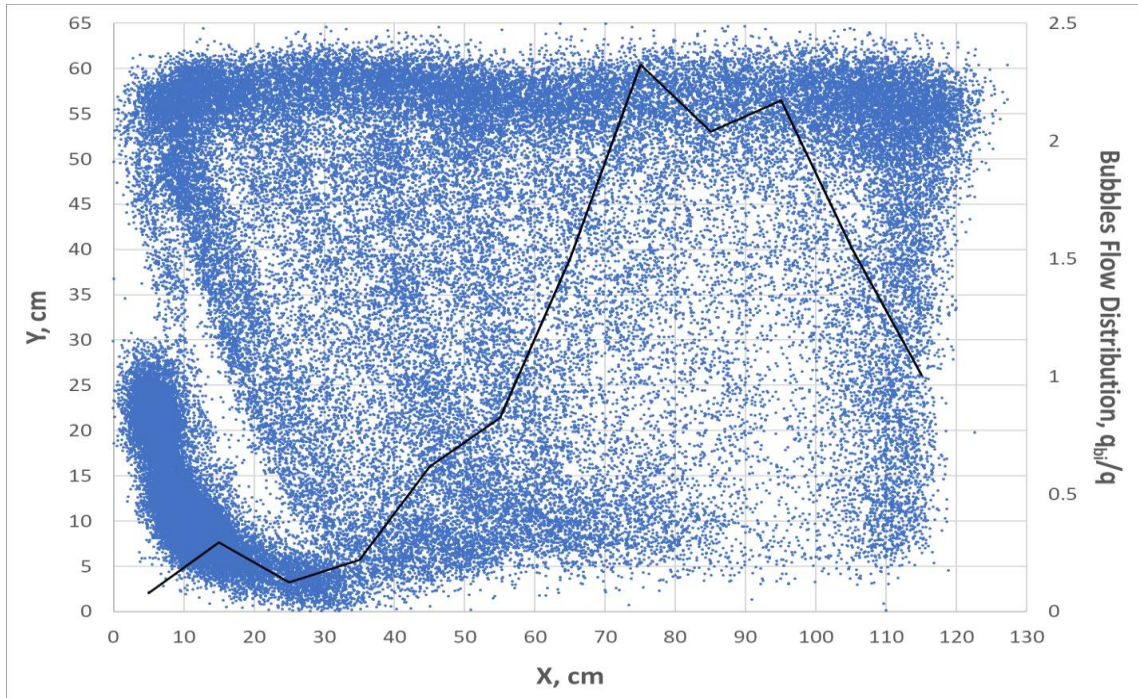


Figure 5-18: Tracer locations and gas bubble flow distribution for MA2 at 0.10 m/s in the left and 0.60 m/s in the right side of the bed

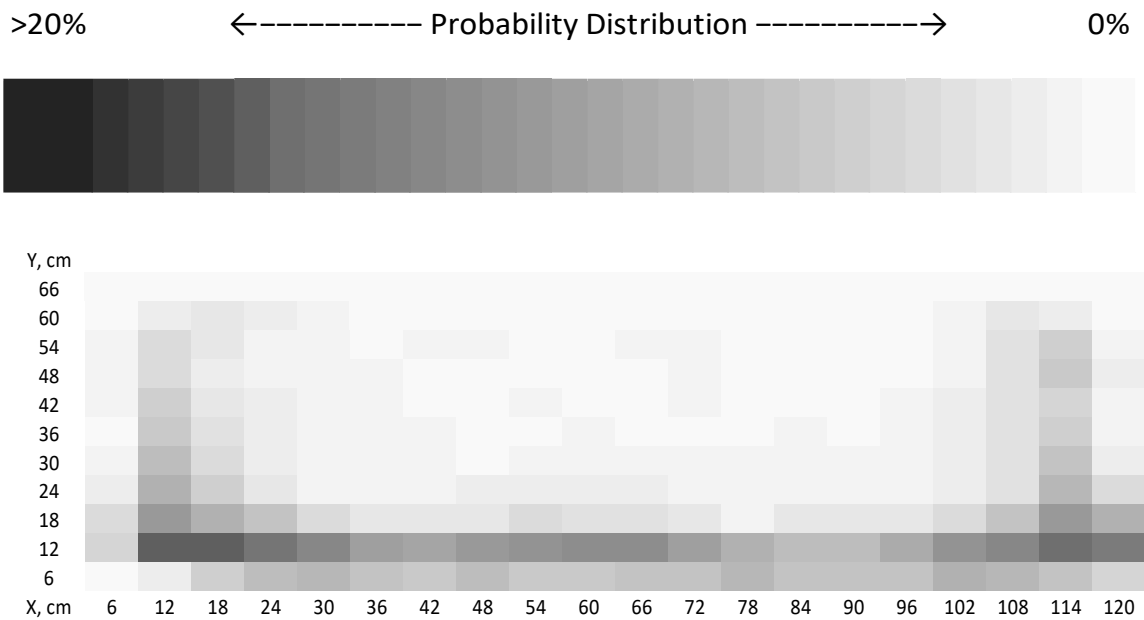


Figure 5-19: Probability distribution of particle presence for MA2 at 0.35 m/s in both halves of the bed

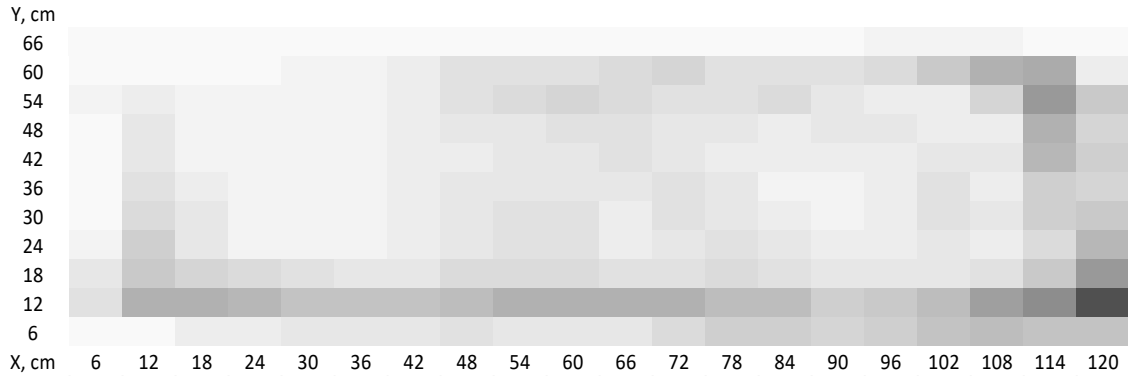


Figure 5-20: Probability distribution of particle presence for MA2 at 0.60 m/s in the left and 0.10 m/s in the right side of the bed

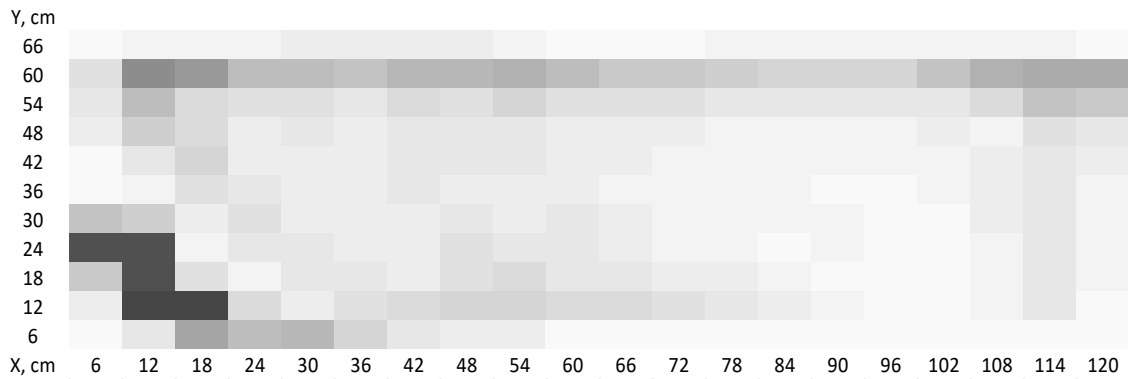


Figure 5-21: Probability distribution of particle presence for MA2 at 0.10 m/s in the left and 0.60 m/s in the right side of the bed

Similar behavior to the MA-2 agglomerate is observed for the MA-1 agglomerate (5500 μm and 1450 kg/m^3) when comparing the RPT results. The agglomerate segregated in all cases with a positive shift in agglomerate presence in the region of low bubble flow (Figures 5-22 to 5-27).

For both MA-2 and MA-1, the agglomerate presence increased towards the extreme sides of the bed when tested in the core-annular structure. It makes sense, as the regions with highest presence (the darkest shade on the figure) should have the lowest bubble flow. We have seen in Figures 5-2 and 5-3 that the regions in the bottom row at 0.10 m/s had the lowest bubble fraction and these are the same regions with highest agglomerate presence.

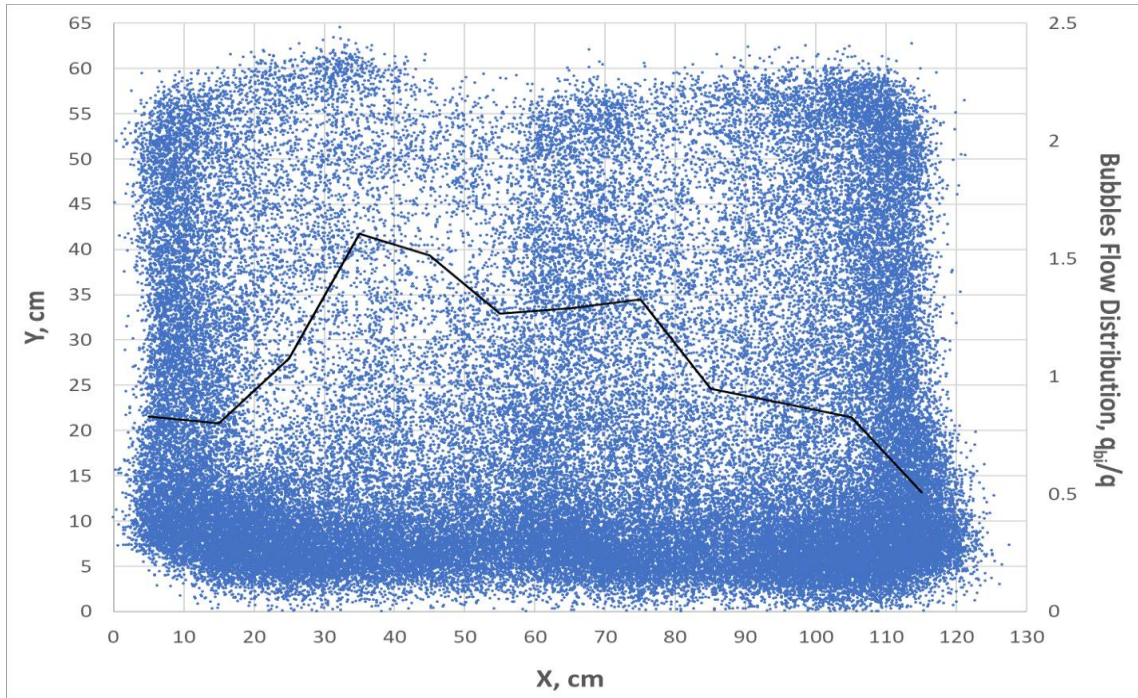


Figure 5-22: Tracer locations and gas bubble flow distribution for MA1 at 0.35 m/s in both halves of the bed

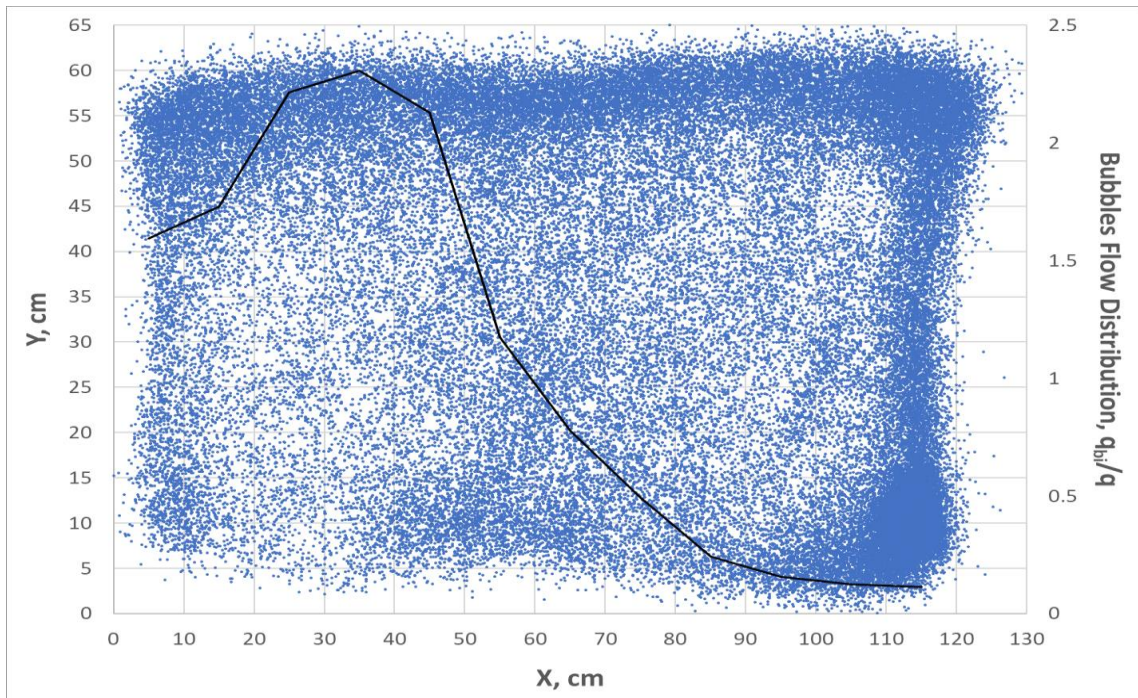


Figure 5-23: Tracer locations and gas bubble flow distribution for MA1 at 0.60 m/s in the left and 0.10 m/s in the right side of the bed

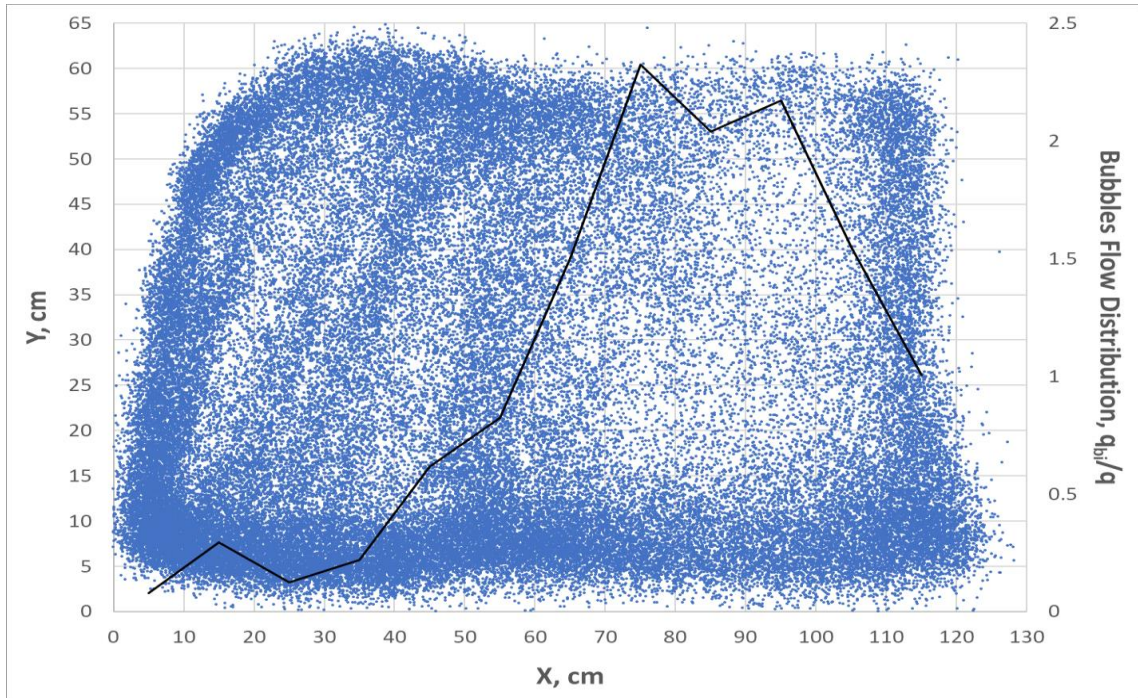


Figure 5-24: Tracer locations and gas bubble flow distribution for MA1 at 0.10 m/s in the left and 0.60 m/s in the right side of the bed

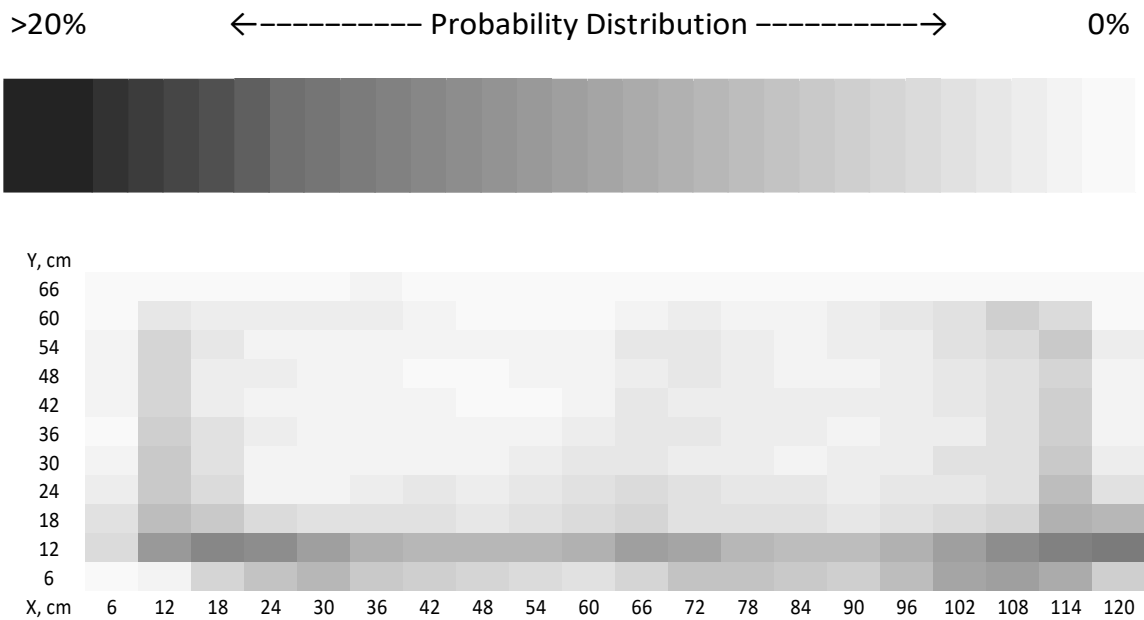


Figure 5-25: Probability distribution of particle presence for MA1 at 0.35 m/s in both halves of the bed

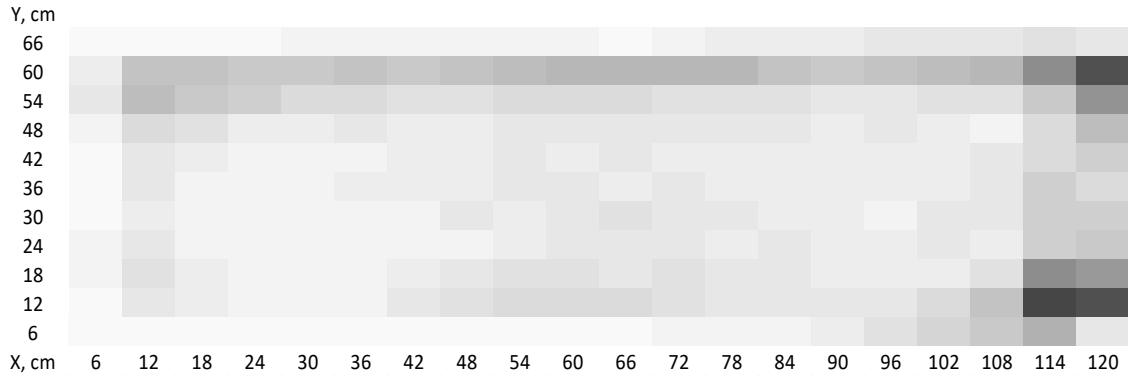


Figure 5-26: Probability distribution of particle presence for MA1 at 0.60 m/s in the left and 0.10 m/s in the right side of the bed

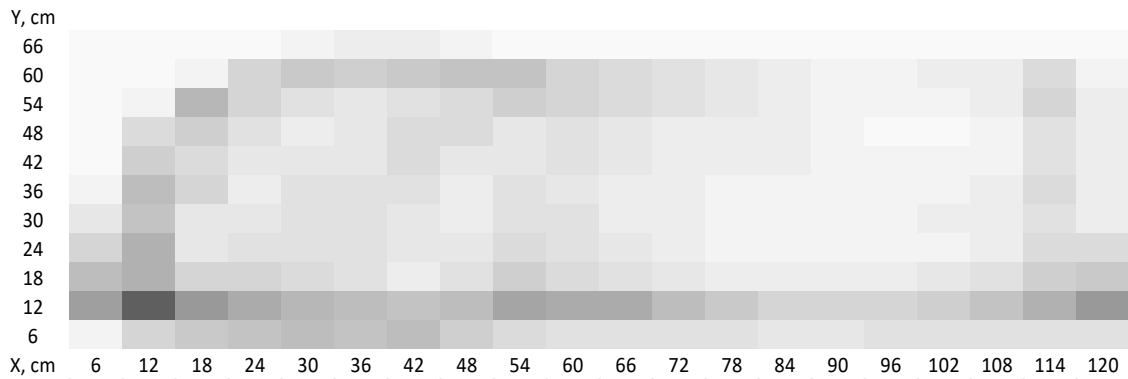


Figure 5-27: Probability distribution of particle presence for MA1 at 0.10 m/s in the left and 0.60 m/s in the right side of the bed

5.2.4 Comparison of Results obtained with Agglomerates formed by Liquid Injection Experiments, and Radioactive Particle Tracking

The indices of segregation were defined in Chapter 3 (Section 3.3): a large value of an index of segregation indicates strong segregation. The bottom index of segregation, as defined in Equation (3.4), was calculated for each RPT case from the probability distribution of agglomerate presence in the fluidized bed. Table 5-2 compares the bottom index of segregation values for RPT and liquid injection runs, for MA2. There is a good general agreement: both methods indicate that segregation is greatly enhanced by an uneven gas distribution, especially for the 10L-60R configuration.

Case	From Liquid Injection	From RPT
Base Case	2.4724	2.7495
60L-10R	5.6961	4.8618
10L-60R	7.5455	6.2793

Table 5-2: Index of Segregation for bottom (IS_B) compared for MA2

The proportions of agglomerates obtained from the probability graphs for both 12500 μm and 5500 μm (Figures 5-28 to 5-33) indicate that the vertical distribution of agglomerates obtained from RPT is similar to the results obtained from liquid injection experiments. Table 5-2 and Figures 5-28 to 5-33 show that segregation increased significantly when different gas velocities were present in the two halves of the bed.

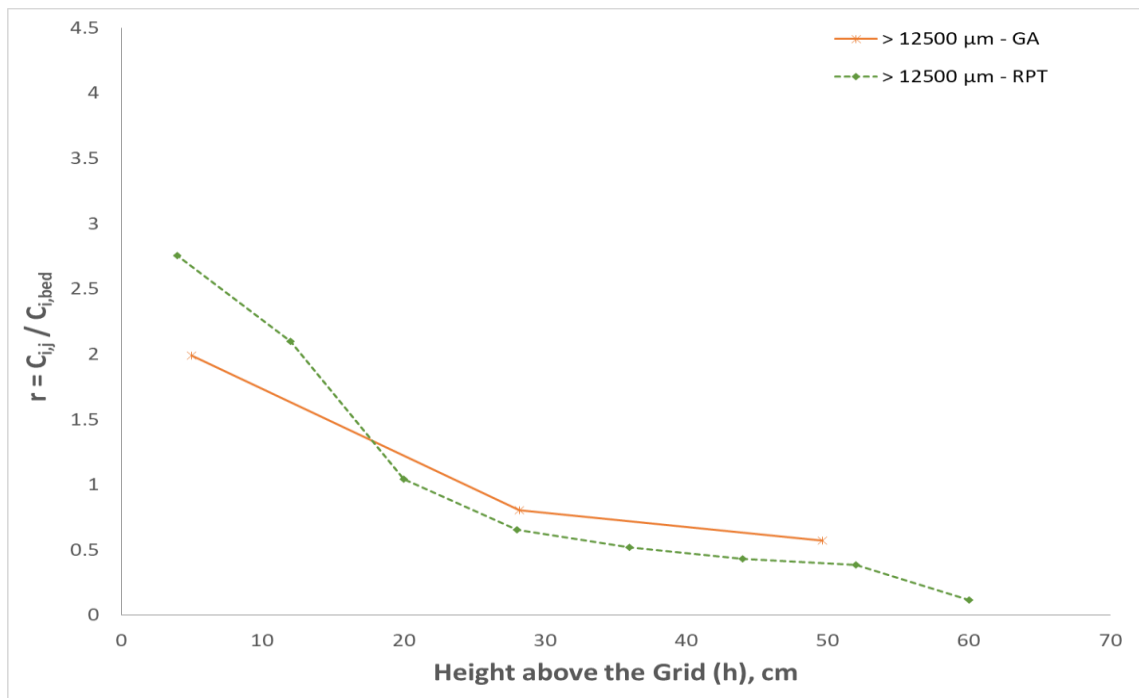


Figure 5-28: Vertical distribution of 12500 μm for the base case (0.35 m/s gas velocity in both sides of the bed)

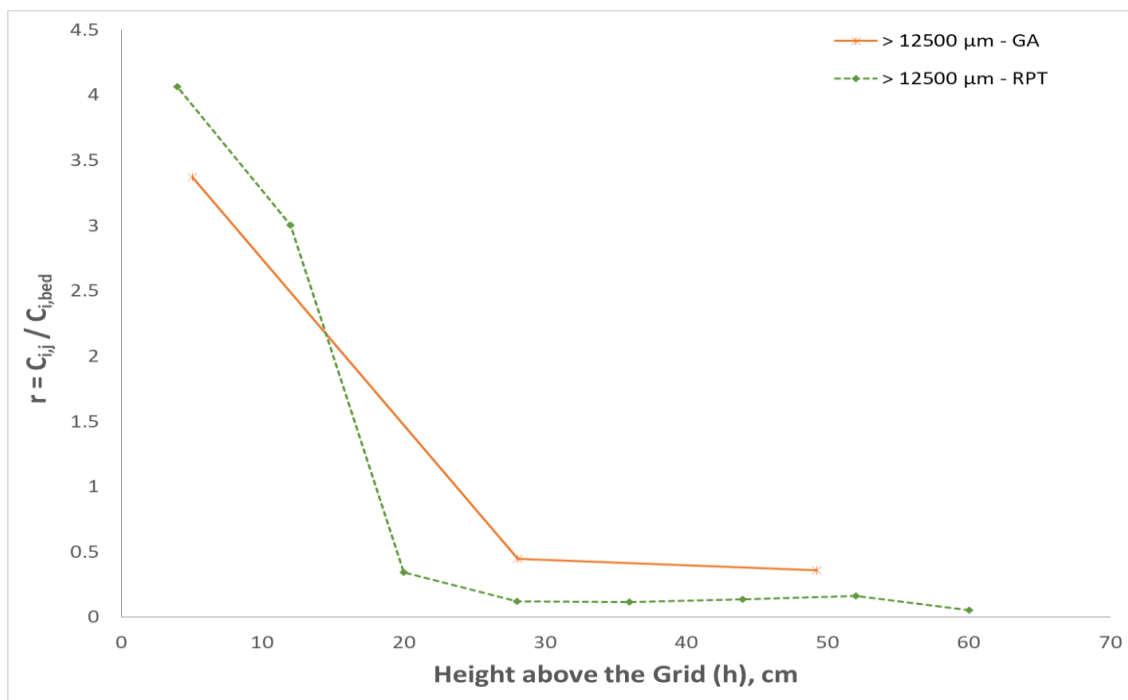


Figure 5-29: Vertical distribution of 12500 μm for the 60L-10R case (0.60 m/s gas velocity in the left side of the bed and 0.10 m/s in the right side of the bed)

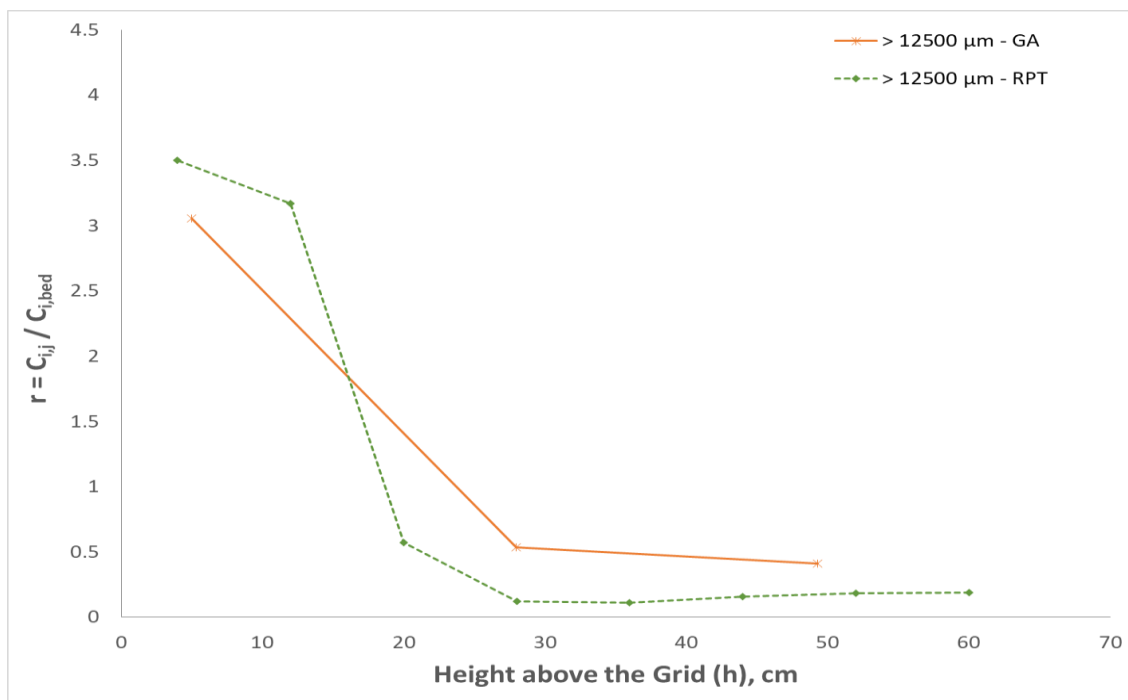


Figure 5-30: Vertical distribution of 12500 μm for the 10L-60R case (0.10 m/s gas velocity in the left side of the bed and 0.60 m/s in the right side of the bed)

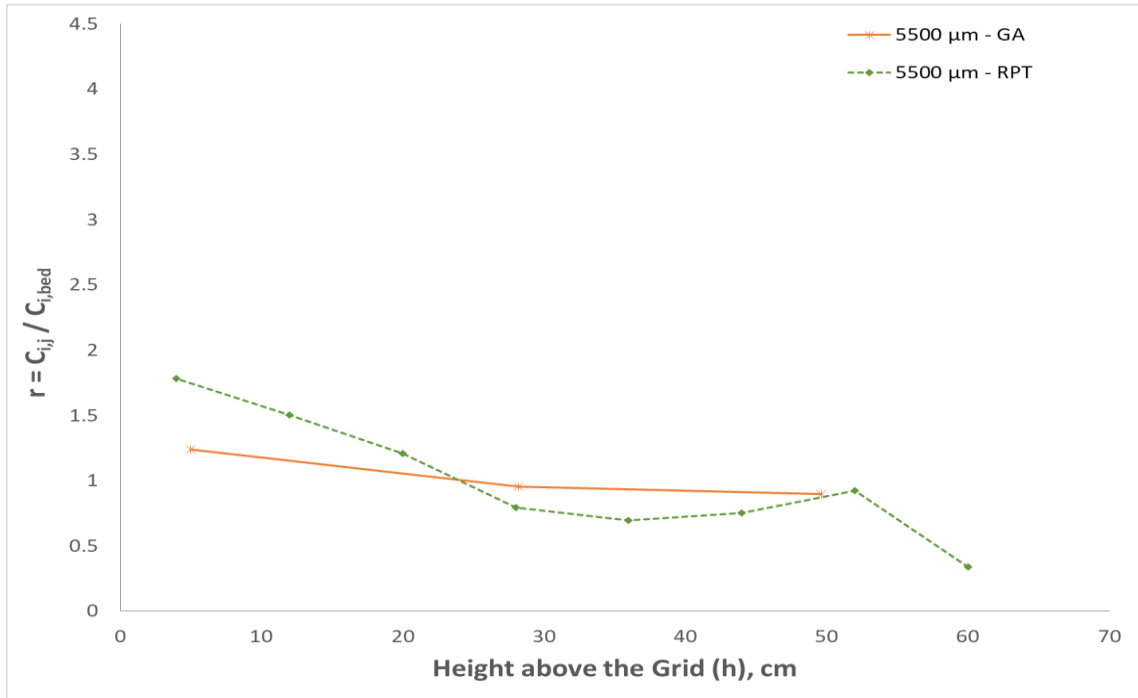


Figure 5-31: Vertical distribution of 5500 μm for the base case (0.35 m/s gas velocity in both sides of the bed)

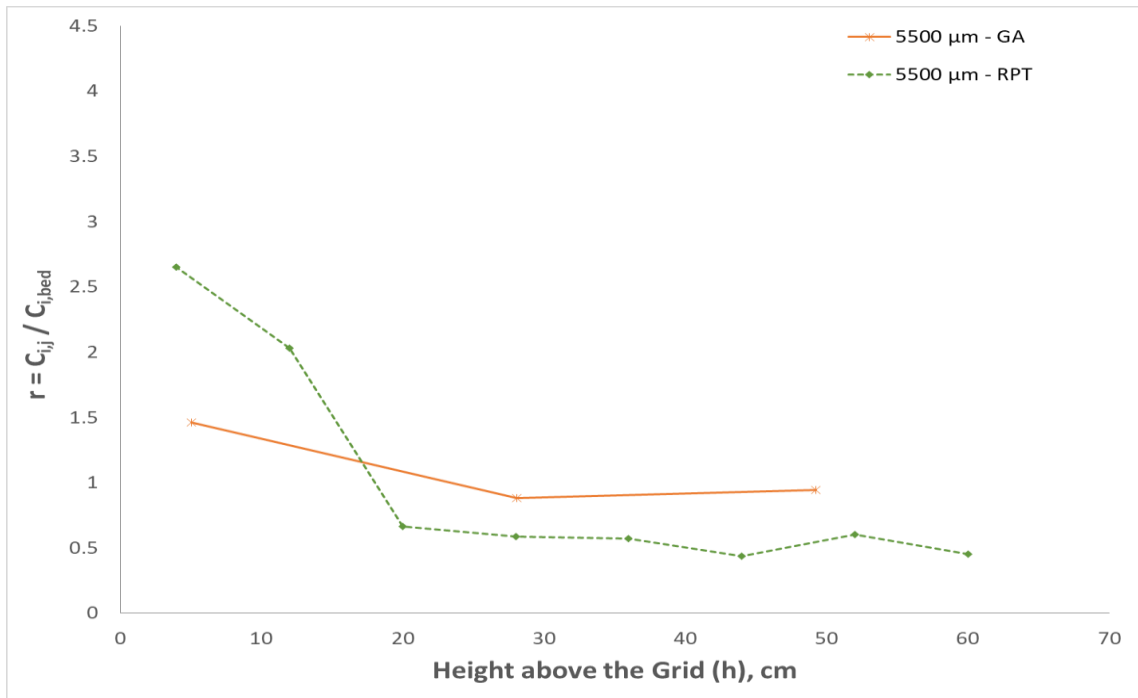


Figure 5-32: Vertical distribution of 5500 μm for the 60L-10R case (0.60 m/s gas velocity in the left side of the bed and 0.10 m/s in the right side of the bed)

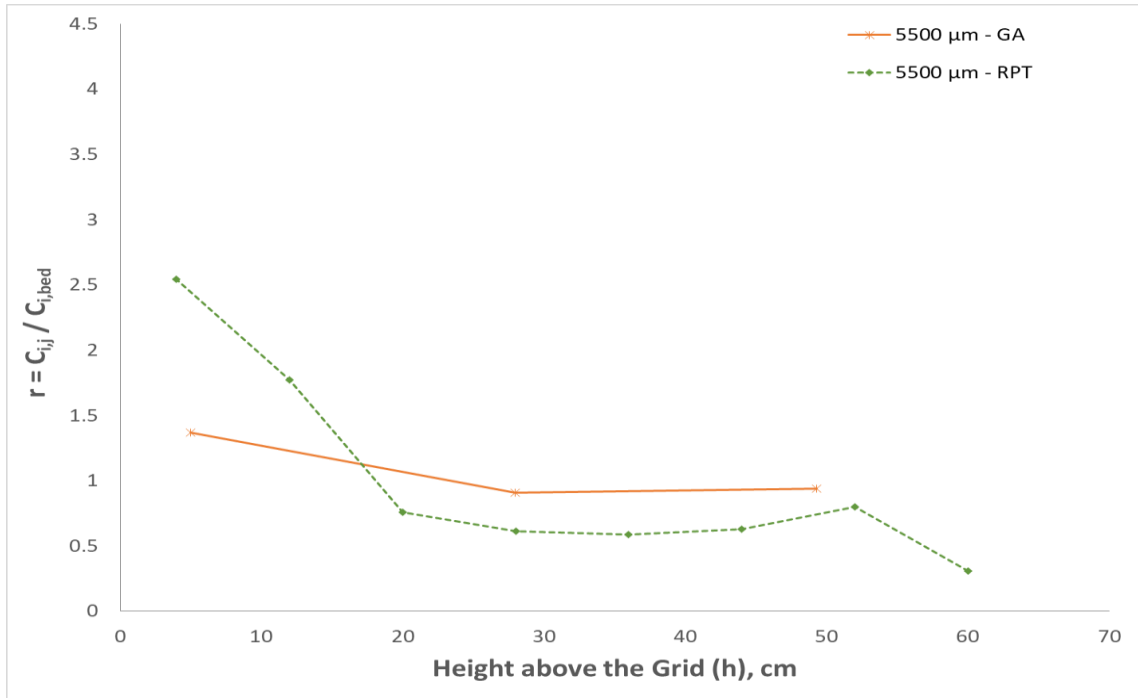


Figure 5-33: Vertical distribution of 5500 μm for the 10L-60R case (0.10 m/s gas velocity in the left side of the bed and 0.60 m/s in the right side of the bed)

Figures 5-34 to 5-39 compare the lateral distribution of agglomerates from RPT and liquid injection (gum Arabic or GA) experiments. Both methods provided similar results for lateral distribution of agglomerates. The lateral presence of agglomerates for both 12500 μm and 5500 μm in the fluidized bed at 0.35 m/s, as shown in Figures 5-34 and 5-37, are in line with results for lateral distribution at 0.60 m/s (Section 4.2.3) showing that the agglomerates distribution in both halves was similar for even distribution of gas. Both liquid injection (GA) experiments and RPT (Figures 5-34 to 5-39) show that the proportion of agglomerates increased significantly in the region of lower gas velocity for the uneven distribution of gas for model agglomerates.

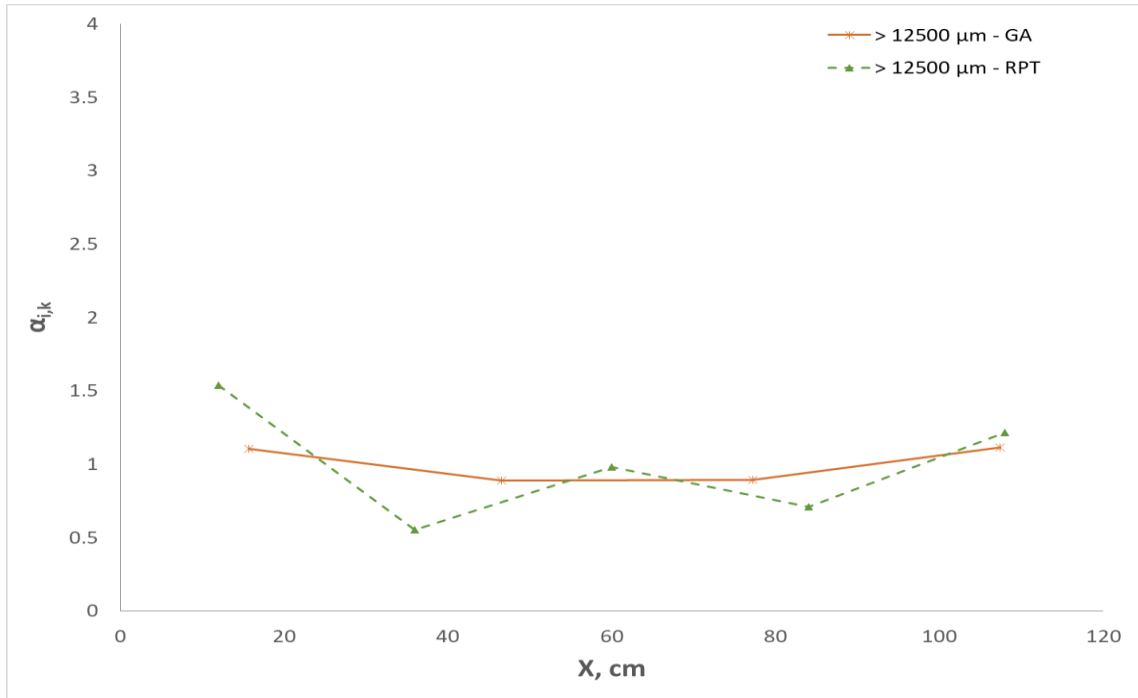


Figure 5-34: Lateral distribution of 12500 μm in Bottom layer for the base case (0.35 m/s gas velocity in both sides of the bed)

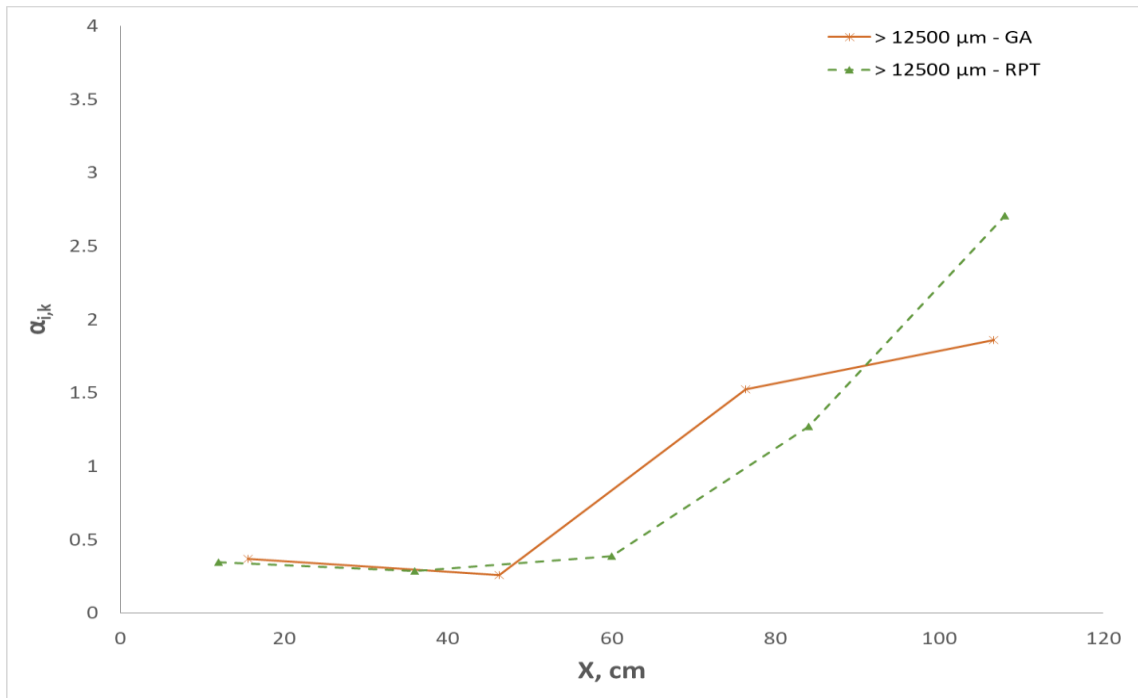


Figure 5-35: Lateral distribution of 12500 μm in Bottom layer for the 60L-10R case

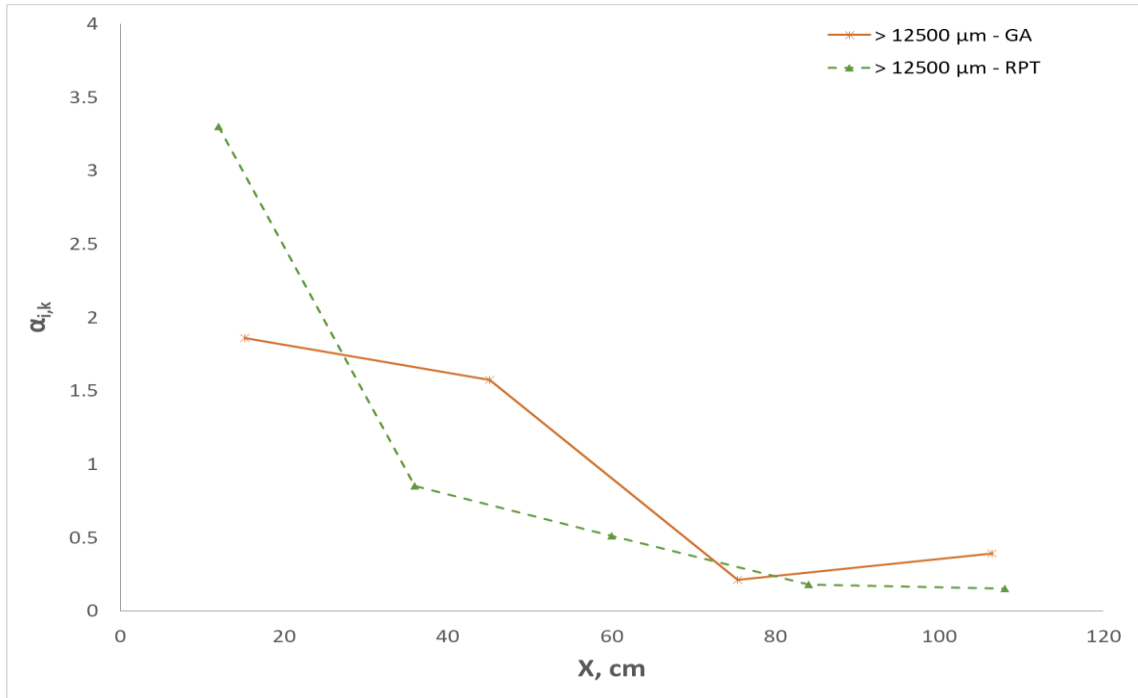


Figure 5-36: Lateral distribution of 12500 μm in Bottom layer for the 10L-60R case

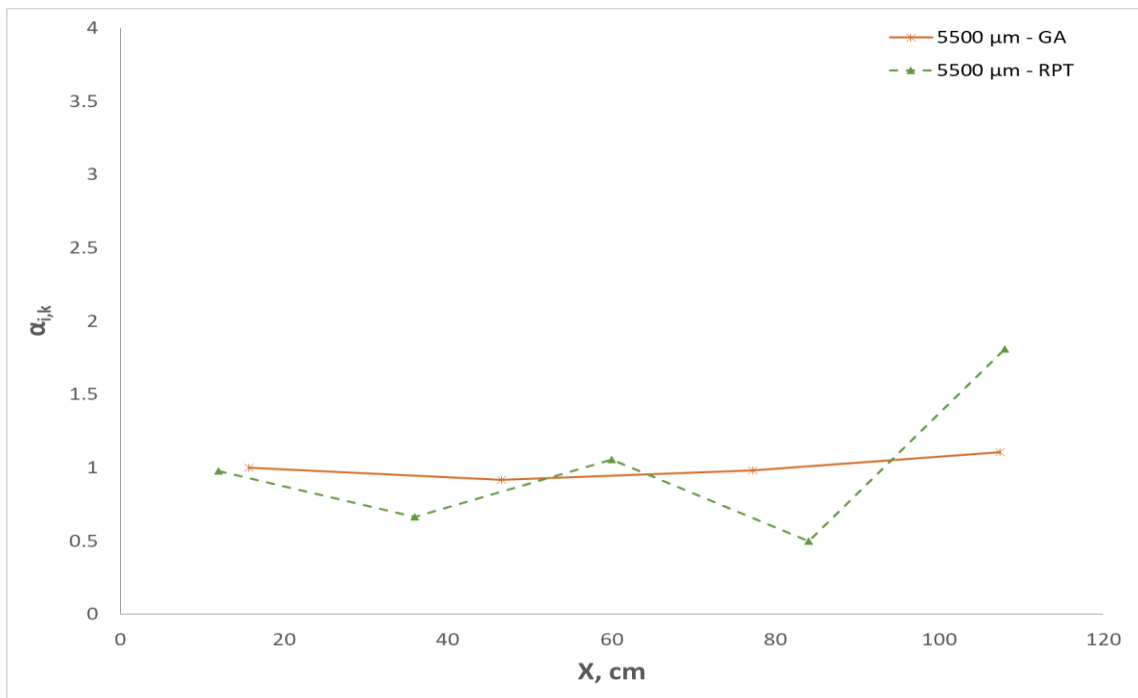


Figure 5-37: Lateral distribution of 5500 μm in Bottom layer for the base case (0.35 m/s in both halves of the bed)

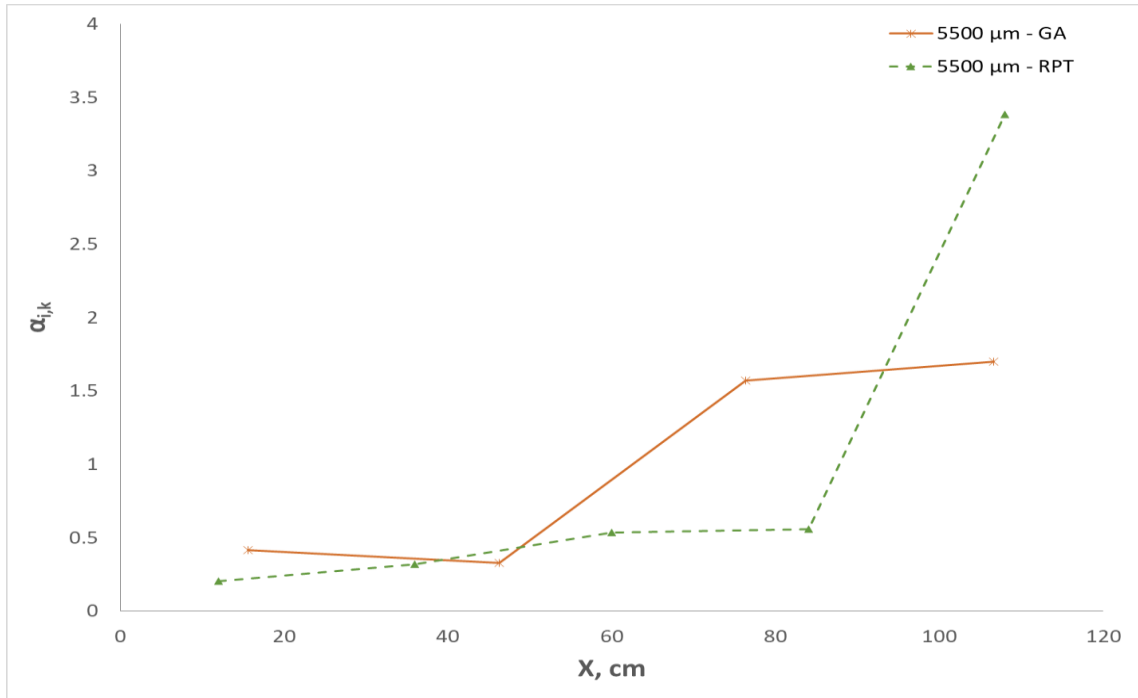


Figure 5-38: Lateral distribution of 5500 μm in Bottom layer for the 60L-10R case

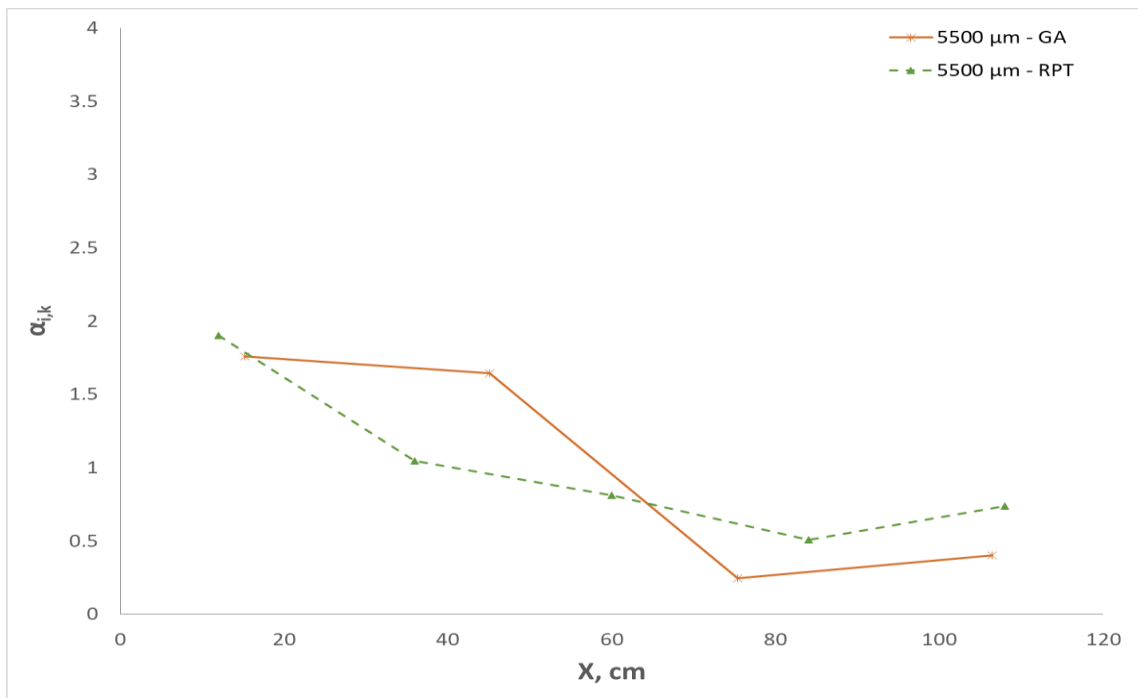


Figure 5-39: Lateral distribution of 5500 μm in Bottom layer for the 10L-60R case

5.3 Conclusion

For split velocity cases, the gas bubble distribution in the fluidized bed measured by the triboelectric method showed that the gas distribution was not perfectly symmetrical (mirror image of each other) and had a profound impact on the agglomerates generation and distribution. With liquid injection, more agglomerates were generated when the gas bubbles fraction was lower in the side of the bed where the jet tip was present.

The density of agglomerates was determined for agglomerates larger than 4000 μm and was found to be between 1380 kg/m^3 to 1475 kg/m^3 . Segregation and distribution results from Gum Arabic runs correlated well with the RPT results for the larger model agglomerate, which had a density of 1450 kg/m^3 .

Both liquid injection experiments and Radioactive Particle Tracking (RPT) showed that agglomerates segregated in the region of low bubble flow near the bottom of the bed for all cases; but the concentration gradients and, hence, the segregation were greatly enhanced by the split gas velocity. While agglomerates were distributed evenly between both halves of the bed for an even gas distribution, with an uneven gas distribution, a higher proportion of all agglomerates were present in the lower velocity side.

Chapter 6

6 Conclusions and Recommendations

Important conclusions of this thesis are summarized below followed by recommendations for future research work.

6.1 Conclusions

- Model agglomerates installed with a radioactive source can be successfully tracked in a fluidized bed using Radioactive Particle Tracking (RPT) with the help of empirical equations developed from the calibration data obtained by moving the radioactive source to many fixed locations throughout the fluidized bed.
- A solution of gum Arabic dissolved in water with blue dye (tracer) was used as a binding solution to generate agglomerates to determine the properties of the model agglomerates to be used for RPT method. Results showed that large agglomerates ($> 9500 \mu\text{m}$) are important for segregation. The segregation of large agglomerates decreased with fluidization velocity. The density of agglomerates was between 1350 kg/m^3 and 1450 kg/m^3 .
- A tribo-electric method was used to measure the gas bubble flow distribution in the fluidized bed. The ratio of the distributor pressure to the bed pressure drop was relatively low, at 8.2 % and 10.5 %, respectively, for the lower fluidization velocities of 0.06 and 0.10 m/s and, consequently, the gas bubble distribution was not as uniform in the lower bed region as for the higher fluidization velocities. Gas distribution became less erratic with the increase in gas velocity, however, more gas bubbles were present in the mid-section of the bed and fewer bubbles near the sides of the fluidized bed. For split cases, different (uneven) gas velocities were introduced in the two halves of the bed. Gas bubble distribution significantly increased in the half with higher gas velocity as compared to the case where uniform gas velocity was present in both halves (average of the two velocities for the split case was considered for the uniform velocity case).

- The larger model agglomerate (12500 μm) segregated near the bottom of the fluidized bed even at high velocities such as 0.60 m/s. However, segregation was reduced with increasing gas velocity in the fluidized bed. On the other hand, the smaller model agglomerate (5500 μm) only segregated at velocities lower than 0.35 m/s, confirming that larger agglomerates have a higher tendency to segregate. As expected, the extent of segregation at a given fluidization velocity was found to be greater for the larger agglomerate. Distribution of gas bubble flow in the bed showed a higher probability of model agglomerates being present in the regions with lower bubble flow.
- Core-annular flow was simulated by introducing different gas velocities in the two halves of the bed. It was found that the split in fluidization velocity greatly increased the agglomerate segregation near the bottom of the bed. Liquid injection experiments showed that more agglomerates were generated when the gas velocity was lower in the region where the tip of the spray nozzle jet was present. RPT and liquid injection results showed that both vertical and horizontal segregation increased in the bed for split cases. As in the experiments with a uniform gas flow distribution, agglomerates spend most time in the regions of low bubble flow.
- The vertical distribution of agglomerates found with the RPT method was similar to the liquid injection experiments for both uniform velocities in both halves of the fluidized bed and in the split case. The lateral distribution of agglomerates was, however, slightly different in some cases indicating escaping bubbles during slumping of the bed may affect the distribution of agglomerates in the liquid injection experiments.

6.2 Recommendations

- It would be useful to set up a calibration system to quickly move the radiative tracer at defined locations through the bed. This would greatly speed up the calibration process while providing information to determine the highest tracer velocity that can be reliably measured.

- The maximum gas velocity studied in this research work was 0.60 m/s. Higher gas velocities should be studied, since higher gas velocities are present in commercial units.
- Experiments in a cylindrical unit would confirm that the hydrodynamics of the rectangular unit used for this study provides a good approximation of the hydrodynamics of a cylindrical column.
- The Radioactive Particle Tracking (RPT) experiments were only conducted while the bed was fluidized, whereas in the liquid injection experiments, the agglomerates were collected after the bed was slumped which resulted in some differences in the agglomerates analysis from the two methods. For future studies, the RPT experiments should be conducted to monitor what happens when the bed is slumped.

References

- Ariyapadi, S., Holdsworth, D. W., Norley, C. J. D., Berruti, F., & Briens, C. (2003). Digital X-ray Imaging Technique to Study the Horizontal Injection of Gas-Liquid Jets into Fluidized Beds. *International Journal of Chemical Reactor Engineering*, 1(1). <https://doi.org/10.2202/1542-6580.1114>
- Ayatollahi, S. (2016). Particle Entrainment Studies From Dry and Wet Bed, (June), 202.
- Base, T. E., Chan, E. W., Kennett, R. D., & Emberley, D. A. (1999, December 21). Nozzle for atomizing liquid in two phase flow. Google Patents. Retrieved from <https://www.google.com/patents/US6003789>
- Bi, H.T, Grace, J.R., Lim, C.J., Rusnell, D., Bulbuc,, D., Mcnight, C.A, 2008. (2005). Hydrodynamics of the stripper Section of fluid cokers, 161–168. Retrieved from [doi:10.1002/cjce.5450830202](https://doi.org/10.1002/cjce.5450830202)
- Blaser, D. E., Chang, B. H., & Baker, C. L. (1986, May 6). Fluid coking with improved stripping. Google Patents. Retrieved from <https://www.google.com/patents/US4587010>
- Chaouki, J., Larachi, F., & Dudukovic, M. P. (1997). Noninvasive Tomographic and Velocimetric Monitoring of Multiphase Flows. *Industrial & Engineering Chemistry Research*, 5885(418), 4476–4503. <https://doi.org/10.1021/ie970210t>
- Geldart, D. (1973). Types of gas fluidization. *Powder Technology*, 7(5), 285–292. [https://doi.org/10.1016/0032-5910\(73\)80037-3](https://doi.org/10.1016/0032-5910(73)80037-3)
- Graf, H. G., & Janssen, H. R. (1985, May 21). Process for improving product yields from delayed coking. Google Patents. Retrieved from <https://www.google.com/patents/US4518487>
- Gray, M. R., Zhang, Z., McCaffrey, W. C., Huq, I., Boddez, L., Xu, Z., & Elliott, J. A. W. (2003). Measurement of adhesive forces during coking of Athabasca vacuum residue. *Industrial and Engineering Chemistry Research*, 42(15), 3549–3554. <https://doi.org/10.1021/ie020789h>

Hein, F. J. (2017). Geology of bitumen and heavy oil: An overview. *Journal of Petroleum Science and Engineering*, 154(November 2016), 551–563.

<https://doi.org/10.1016/j.petrol.2016.11.025>

House, P. (2007). *Interaction of Gas-Liquid Jets with Gas-Solid Fluidized Beds: Effect on Liquid-Solid Contact and Impact on Fluid Coker Operation. PhD Thesis.*

Jahanmiri, M. (2017). Use of a baffle to enhance the distribution of a liquid sprayed into a gas-solid fluidized bed. Master's diss.

Javier Sanchez, F. C. (2013). Hydrodynamics in Recirculating Fluidized Bed Mimicking the Stripper Section of the Fluid Coker, (January), 278.

Lin, J. S., Chen, M. M., & Chao, B. T. (1985). A novel radioactive particle tracking facility for measurement of solids motion in gas fluidized beds. *AIChE Journal*, 31(3), 465–473. <https://doi.org/10.1002/aic.690310314>

Luckenbanch, E. C. (1969, November 25). Reaction vessel. Google Patents. Retrieved from <https://www.google.com/patents/US3480406>

McDougall, S., Saberian, M., Briens, C., Berruti, F., & Chan, E. (2005). Effect of liquid properties on the agglomerating tendency of a wet gas-solid fluidized bed. *Powder Technology*, 149(2–3), 61–67. <https://doi.org/10.1016/j.powtec.2004.09.043>

Miller, R. W. (1996). *Flow measurement engineering handbook*. McGraw-Hill. Retrieved from <https://books.google.ca/books?id=0e9RAAAAMAAJ>

Morales, C. B. (2013). Development and Application of an Experimental Model for the Fluid Coking Process. *M.Sc Thesis*, (August).

Moslemian, D., Devanathan, N., Dudukovic, M. P., & Moslemian, D. (1992). Radioactive particle tracking technique for investigation of phase recirculation and turbulence in multiphase systems Radioactive recirculation particle tracking technique for investigation and turbulence in multiphase systems of phase, 4361(1992), 4361–4372. <https://doi.org/10.1063/1.1143736>

- Prociw, N. A. (2014). Effect of Nozzle Geometry on Jet Bed Interaction : Experiments with Commercial Scale Nozzles and Eroded Nozzles, (September), 150.
- Rados, N. (2003). Slurry Bubble Column Hydrodynamics.
- Reyes, L. A. P. (2015). Effect of Temperature and Successive Sprays on Liquid Distribution in Fluidized Beds. *Electronic Thesis and Dissertation Repository*, (August), 118. <https://doi.org/10.1016/j.powtec.2005.04.034>
- Schaefer, T., & Mathiesen, C. (1996). Melt pelletization in a high shearmixer. IX. Effects of binder particle size. *International Journal of Pharmaceutics*, 139((1-2)), 139–148. [https://doi.org/10.1016/0378-5173\(96\)04548-6](https://doi.org/10.1016/0378-5173(96)04548-6)
- Shehata, A. H., Aljohani, M. S., & Arabia, S. (2007). a Review of Nuclear Non-Intrusive Visualization Methods in Industry : Computed Tomography and. *4th Middle East NDT Conference and Exhibition, Kingdom of Bahrain*,.
- W. L. McCabe, J. C. Smith, P. H. (1993). UNIT OPERATION HANDBOOK.pdf.
- Weber, S. C. (2009). No Title.
- Wiens, J. S. (2010). Experimental and Modeling Study of a Cold-Flow Fluid Catalytic Cracking Unit Stripper.
- Yang, W. C. (2003). *Handbook of Fluidization and Fluid-Particle Systems*. Taylor & Francis. Retrieved from https://books.google.ca/books?id=n_UqkwcFbwkC

Appendices

Appendix A: Calibration for Sonic Nozzle Banks

The fluidized bed used in this study was fluidized by means of air which was supplied by two banks of sonic nozzles. Each bank supplied air to half of the bed, through a distribution grid provided at the bottom of the bed. To make sure that the air supply was not affected by the variation in downstream pressure (due to variation in bed height), 3 sonic nozzles of different sizes had been installed in each bank. Each bank comprised of 3 sonic nozzles (small, medium and large) that could be used in different combinations to achieve a wide range of gas fluidization velocities in the bed. Table A-1 represents the combinations that could be used to attain different desired flow rates.

Sonic Nozzle	1	2	3	4	5	6	7
Small	Open	Closed	Closed	Open	Open	Closed	Open
Medium	Closed	Open	Closed	Open	Closed	Open	Open
Large	Closed	Closed	Open	Closed	Open	Open	Open

Table A-1: Combinations of sonic nozzles that can be utilized to achieve a range of desired velocities

To proceed with the experiments, the nozzles were calibrated for all the combinations provided in Table A-1 so that the bed could be fluidized precisely at the desired velocity.

Measurements were taken for each combination shown in Table A-1 to get a calibration curve for the gas velocities at different upstream pressures. The upstream pressure was measured using a pressure transducer installed upstream of the sonic banks. The downstream pressure of the sonic nozzles for each bank was monitored by an analog pressure indicator to make sure that the air flow is sonic through the nozzles. A flow orifice plate was installed downstream of the sonic bank to measure the pressure difference. The pressure difference across the flow orifice plate was measured using a digital manometer

for high accuracy. The higher the pressure difference across the flow orifice plate, the higher the flow rate of the gas through the flow orifice plate for a given upstream pressure until choke flow occurs.

In summary, the following parameters were measured to generate the calibration curves,

1. Pressure upstream of the sonic bank (psig), P_1 , by analog pressure indicator
2. Voltage upstream of the sonic bank (V), by pressure transducer
3. Pressure difference across the flow orifice plate downstream of the sonic bank (psi), by digital manometer
4. Pressure downstream of the sonic bank (psig), P_2 , for monitoring only by analog pressure indicator

Calculation Steps:

1. Calculate pressure upstream of flow measuring orifice, where P_2 is close to atmospheric pressure,

$$P_1 = \Delta P + P_2$$

2. Calculate expansion factor using (McCabe & Smith, 1993),

$$Y = 1 - \frac{\Delta P}{\gamma P_1} (0.41 + 0.35 \beta^4)$$

3. Make corrections in density for pressure using gas laws
4. Find discharge coefficient for respective type of flow measuring orifice plate, which is corner taps in this case (Miller, 1996),

$$C_d = 0.5959 + 0.312\beta^{2.1} - 0.184\beta^8$$

5. Then find gas velocity through flow measuring orifice (McCabe & Smith, 1993),

$$V_g = \frac{C_d}{\sqrt{1 - \beta^4}} Y \sqrt{\frac{2 \Delta P}{\rho_g}}$$

6. Calculate Reynolds Number and find the iterated value of C_d based on gas velocity,

$$C_d = 0.5959 + 0.312\beta^{2.1} - 0.184\beta^8 + \frac{91.71\beta^{2.5}}{Re^{0.75}}$$

7. Gas mass flow rate can now be calculated by (using gas density at P_2),

$$m_g = V_g \rho_g A_{orifice}$$

8. Gas velocity in bed is calculated as,

$$V_{gbed} = \frac{m_g}{\rho_g A_{bed}}$$

9. Gas velocity in bed at 120 °C can be corrected for pressure and temperature using,

$$V_{gbed@120} = V_{gbed@20} \frac{P_{grid} T_{atm}}{P_{atm} T_{grid}}$$

Calibration Results

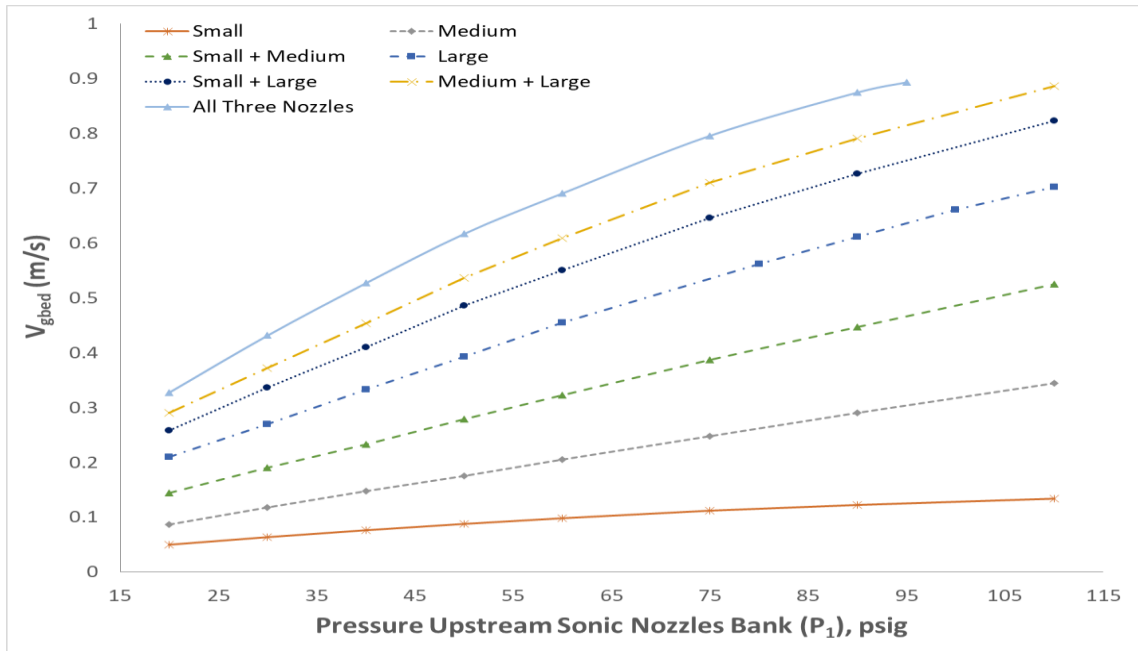


Figure A-1: Calibration curves for different combinations of sonic nozzles to supply fluidization gas to the right side of the bed

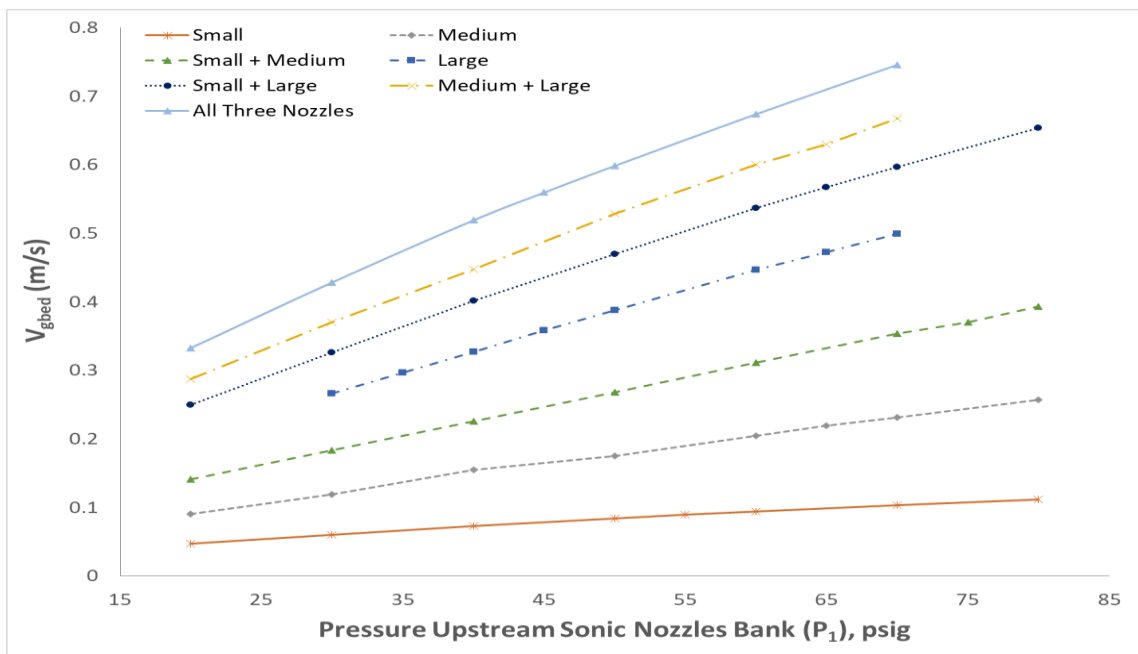


Figure A-2: Calibration curves for different combinations of sonic nozzles to supply fluidization gas to the left side of the bed

Curriculum Vitae

Name: Muhammad Owais Iqbal Bhatti

Post-secondary Education and Degrees: Master of Engineering Science (M.E.Sc.)
The University of Western Ontario
London, Ontario, Canada
Sep. 2015 – Sep. 2017

Bachelor of Engineering (B.E.)
University of Karachi
Karachi, Pakistan
Jan. 2007 – Dec. 2010

Honours and Awards: Western Graduate Student Scholarship
The University of Western Ontario
Merit Based Graduate Scholarship
2016-2017

Queen Elizabeth II Graduate Scholarship in Science and Technology (QEII – GSST)
The University of Western Ontario
Merit Based Graduate Scholarship
2016-2017

Related Work Experience Graduate Research Assistant
Institute for Chemicals and Fuels from Alternative Resources (ICFAR), The University of Western Ontario
Sep. 2015 – Aug. 2017

Teaching Assistant
The University of Western Ontario
CBE-3310 – Process Dynamics and Control
Jan. 2017 – Apr. 2017

Teaching Assistant
The University of Western Ontario
CBE-9550 - Advanced Particle and Fluidization Technology
Sep. 2016 – Dec. 2016

Process Engineer
ENAR Petrotech Services (Private) Limited
Karachi, Pakistan
Jan. 2011 to Aug. 2015